



HAL
open science

Mixtures of Bose and Fermi superfluids

I. Ferrier-Barbut

► **To cite this version:**

I. Ferrier-Barbut. Mixtures of Bose and Fermi superfluids. Physics [physics]. Ecole Normale Supérieure, 2014. English. NNT: . tel-01087312v2

HAL Id: tel-01087312

<https://theses.hal.science/tel-01087312v2>

Submitted on 21 Dec 2014 (v2), last revised 15 Apr 2016 (v3)

HAL is a multi-disciplinary open access archive for the deposit and dissemination of scientific research documents, whether they are published or not. The documents may come from teaching and research institutions in France or abroad, or from public or private research centers.

L'archive ouverte pluridisciplinaire **HAL**, est destinée au dépôt et à la diffusion de documents scientifiques de niveau recherche, publiés ou non, émanant des établissements d'enseignement et de recherche français ou étrangers, des laboratoires publics ou privés.



THÈSE de DOCTORAT de l'École Normale Supérieure
École Doctorale de Physique en Ile de France ED564
Spécialité : Physique

présentée par

Igor Ferrier-Barbut

pour obtenir le grade de docteur de l'École Normale supérieure

Mixtures of Bose and Fermi superfluids
Mélanges de superfluides de Bose et de Fermi

Soutenue le 31 Octobre 2014

Devant le jury composé de :

M.	S. Balibar	Président du Jury
Mme.	I. Bouchoule	Rapportrice
M.	F. Chevy	Directeur de thèse
Mme.	H. Perrin	Examinatrice
M.	C. Salomon	Directeur de thèse
M.	G. Shlyapnikov	Examineur
M.	S. Stringari	Rapporteur

Contents

Introduction	9
1 Bose-Einstein condensates and Fermi superfluids	15
1.1 Ideal Quantum Gases	15
1.2 The Local Density Approximation	17
1.3 S-wave Interactions and Feshbach Resonances	19
1.3.1 S-wave interactions	19
1.3.2 Feshbach resonances	20
1.3.3 Feshbach resonances in lithium	23
1.3.4 ${}^6\text{Li}$ - ${}^7\text{Li}$ interactions and Feshbach resonances	25
1.4 Interacting Bose-Einstein Condensates	25
1.4.1 Weakly interacting Bose-Einstein condensates	26
1.4.2 Approaching the unitary Bose gas	28
1.5 Fermi Superfluids in the BEC-BCS crossover	29
1.5.1 Stability of Fermi gases on Feshbach resonances	29
1.5.2 The BEC-BCS crossover	29
1.5.3 The equation of state	31
1.6 Superfluidity of Bose and Fermi gases	34
1.6.1 Landau's criterion for superfluidity	34
1.6.2 Landau's criterion for a mixture of Bose and Fermi superfluids	37
1.6.3 Beyond Landau's criterion	38
1.6.4 Some experiments on a critical velocity in superfluid dilute gases	39
1.6.5 Other hallmarks of superfluidity	40
2 Experimental set-up	43
2.1 Lithium isotopes, atomic structure	43
2.2 Laser cooling	45
2.2.1 Laser system	45
2.2.2 The lithium source	46
2.2.3 Double Magneto-Optical trap	46
2.2.4 Optical pumping	47
2.3 Magnetic trapping and radio-frequency evaporation	48
2.3.1 Quadrupole trap, magnetic transport and transfer to the Ioffe-Pritchard Trap	48
2.3.2 Doppler cooling of ${}^7\text{Li}$	50

2.3.3	Radio-frequency evaporative cooling of ^7Li	50
2.4	The hybrid optical dipole - magnetic trap (ODT)	51
2.5	Preparation of strongly interacting degenerate gases	53
2.5.1	Preparing a resonantly interacting Bose gas	53
2.5.2	Preparing a mixture of Bose and Fermi superfluids	55
2.6	Imaging	60
2.7	Calibrations	62
2.7.1	Imaging Calibration	62
2.7.2	Frequencies measurement	64
2.7.3	Magnetic field calibration	65
3	D_1 sub-Doppler cooling of ^7Li	67
3.1	Grey molasses cooling in a nutshell	67
3.2	Implementation on ^7Li	69
3.3	The Λ model.	71
3.4	The perturbative approach	73
3.5	The continued fractions approach	78
4	Three-body losses in strongly interacting Bose gases	83
4.1	Three-body losses	83
4.2	A glance at Efimov Physics	84
4.3	Results on the stability of a unitary Bose gas	86
4.4	Conclusion: stability domain of the strongly interacting Bose gas	90
5	Mixtures of Bose and Fermi superfluids	91
5.1	Two-body interactions in the $ 1_f\rangle$, $ 2_f\rangle$, $ 2_b\rangle$ mixture	92
5.2	Mean-field interactions and phase separation	93
5.3	Evidences for superfluidity	96
5.3.1	Thermometry of the mixture	96
5.3.2	Degeneracy points	97
5.3.3	Superfluidity of ^7Li	97
5.3.4	Superfluidity of ^6Li	98
5.3.5	Frictionless counter-flow	101
5.4	Coupled dipole modes, theory	104
5.4.1	Simple model for the BEC dipole frequency shift	104
5.4.2	Sum rules and coupled ^6Li - ^7Li dipole oscillations	105
5.5	Coupled dipole modes, experiments	109
5.5.1	Dipole modes excitation	110
5.5.2	Uncoupled oscillations	110
5.5.3	Coupled oscillations	111
5.5.4	Discussion of the model	114
5.6	Damping of the dipole modes and critical velocity	116
5.6.1	Damping at unitarity	117

5.6.2 Damping in the BEC-BCS crossover	120
5.6.3 Friction at finite temperature	122
5.7 Concluding remarks and prospects with Bose-Fermi superfluid mixtures . .	124
Conclusion	127
Appendix	129
References	171

Remerciements

En premier lieu, je souhaite remercier mes deux directeurs, Christophe et Frédéric. L'accueil chaleureux au sein de leur équipe ainsi que la proximité de nos interactions ont créé un cadre de confiance pour ma de thèse. Christophe nous fait bénéficier de son expérience et de son inspiration pour mener nos projets et s'est impliqué en salle de manip pour nous permettre de sauter le pas lors de choix difficiles. Fred a fait preuve d'une disponibilité rare, toujours prêt à tenir une discussion de physique, avec à coeur de décrire avec précision nos observations nous faisant bénéficier au passage de ses compétences pour la théorie.

Je souhaite ensuite remercier particulièrement chacun des membres du jury Sébastien Balibar, Sandro Stringari, Isabelle Bouchoule, Gora Shlyapnikov et Hélène Perrin, pour avoir jugé avec attention mes travaux et pour la richesse des échanges qui s'en sont suivis, pour les commentaires et corrections détaillés améliorant la qualité de ce manuscrit.

Les travaux présentés dans ce qui suit ont été le fruit d'un travail d'équipe, tout d'abord constituée de Benno Rem et Andrew Grier. Mes premiers pas sur une manip d'atomes froids ont été effectués en leurs compagnie, grâce à Nir Navon qui nous a donné les clés de l'expérience Lithium. Cela a été un plaisir d'évoluer avec et parallèlement à Benno, tout en s'imprégnant des connaissances d'Andrew, distillées avec patience. Nous avons plus tard accueilli dans nos rangs Marion Delehayé puis Sébastien Laurent, qui ont su tout deux faire preuve de la persévérance nécessaire à la difficile tâche de s'intégrer à notre équipe, prenant par la suite une place prépondérante dans nos travaux. En dehors de la science, j'ai beaucoup aimé la bonne ambiance régnant dans l'équipe, permettant de discuter de tout et de rien, de montagne et de ski, de séries télé, de vélos volés...

Nous avons bénéficié d'une collaboration étroite avec des théoriciens, en particulier Yvan Castin, Felix Werner, Dima Petrov et Sandro Stringari. En plus d'apprendre beaucoup à leur contact, j'ai particulièrement apprécié l'intérêt qu'ils ont porté à nos résultats expérimentaux et la qualité avec laquelle ils ont su les décrire théoriquement et trouver les pistes à explorer au delà.

Je souhaite aussi remercier les personnes qui ont passé plus ou moins de temps dans notre équipe, en particulier Lev avec qui cela a été un plaisir de travailler et d'apprendre, ainsi que Matthieu, Ulrich, Tim, Andrea. De même que les autres membres du groupe fermions, Thomas qui m'a offert plusieurs opportunités d'enseignement, Diogo, Franz, Norman, Daniel et les suivants.

L'environnement scientifique offert par le groupe atomes-froids du laboratoire est remarquable, j'ai profité des échanges avec ses différents membres. J'ai apprécié passer ces années en compagnie des autres doctorants et post-docs du groupe, Daniel, Matthias, Alexandre, Laurianne, Vincent, Laura, Tilman, Christof.

Le succès de nos expériences repose sur le support des services techniques et administratifs en général et dans le cas de notre dispositif de manière importante celui du service électronique du LKB qui connaît avec précision nos appareils électroniques et les répare efficacement.

J'ai la chance de compter parmi mes amis des physiciens, Fabien, Manu et Philippe et leur équipe, permettant de combiner discussions scientifiques éclairantes et bonnes soirées pendant ces années. Mes autres amis, dont beaucoup m'ont fait l'honneur d'assister à ma soutenance, m'ont permis m'épanouir en dehors de ma thèse pour conserver un équilibre sain. Parmi eux (sans hiérarchie) Max et Elisabeth, Vincent et Leah, Camille, Guit et Jeane, Elsa, Max, Cyssou, Antoine, Marc, Kev, Max, Thierry et Yana, Soso, Laura, Antoine, Jojo, Tom, Jérôme, Mumu, Yanou, Manu, la L.T. et d'autres...

Enfin je remercie ma mère pour son attention permanente, son soutien et ses conseils précieux pour les choix difficiles, Bernard, décelant avec brio quand ses conseils, toujours avisés, sont nécessaires, mes soeurs sources d'inspiration, notre relation a été un support fondamental, pour finir, Raphaëlle, pour avoir su prendre sa place naturellement dans tout ça, se rendant indispensable.

À mon père

Introduction

Quantum Physics associates a wave-like behaviour to all particles, and divides them into two families, bosons and fermions. As waves, particles interfere, these interferences differentiate bosons from fermions: when bosons interfere constructively, fermions do so destructively. This difference leads to distinct collective behaviours when many particles are prone to occupy the same energy levels, that is in the quantum degenerate regime. At the thermodynamical level, the ground state of a system of non-interacting identical particles depends on the nature of its constituents. At zero temperature, an ensemble of bosons will form a Bose-Einstein condensate (BEC), characterized by the occupation by all the bosons of the lowest energy level, while an ensemble of identical fermions will populate the lowest energy levels from bottom-up with exactly one particle per level, forming a so-called Fermi sea. Adding to quantum statistical effects, the interactions between the constituents can strongly modify the ground state. For this reason, depending on these interactions, both an ensemble of interacting bosons and of fermions can undergo the transition to a superfluid state (superconducting for charged particles) at low temperature. This superfluid state is characterized by unusual flow properties, with at low velocities, a zero viscosity, or electrical resistance for charged particles.

Historically, the discovery of this state constituted the first observations of manifestations of Quantum Physics at the thermodynamical level, and marked the start of the exploration of the quantum many-body problem. The first experimental observations date back from the works of Kamerlingh Onnes [*Kamerlingh Onnes, 1913*] and the liquefaction of helium in 1908. These led to the discovery of an ensemble of unusual phenomena in bosonic liquid helium 4 at temperatures below 2.17 K. With the experiments of Kapitza [*Kapitza, 1938*] on the one hand and Allen and Misener on the other hand [*Allen and Misener, 1938*] these effects were understood to be due to a phase transition to a superfluid state. In parallel, in 1911 using the same cryogenic techniques, Kamerlingh Onnes had discovered the superconducting state, a macroscopic signature of Quantum Mechanics in an ensemble of fermions - the electrons in a metal. In 1972, helium 3, the fermionic twin to helium 4, was discovered to be superfluid at very low temperatures (below 2.6 mK) [*Osheroff et al., 1972*], bridging between helium 4 and superconducting metals. London in 1938 had interpreted superfluidity of ^4He in terms of Bose-Einstein condensation, noting that the experimental critical temperature for superfluidity was close to the theoretical critical temperature for condensation. Nonetheless, the non-interacting picture was insufficient to yield a faithful description, and only interacting models could succeed, with for example two-fluids hydrodynamics or the Bogolyubov description. The interactions bear an even higher importance for fermionic ensembles, as was

realized by Bardeen, Cooper and Schrieffer (BCS) [Bardeen et al., 1957a, Bardeen et al., 1957b]. It is the possibility for fermions to bind in pairs thanks to an attractive interaction that causes the transition to a superconducting (superfluid) state.

Search for double superfluidity in liquid helium mixtures

Once superfluidity was obtained for both liquid ^4He and ^3He , researchers have tried to obtain a doubly superfluid mixture in liquid helium. However, ^3He and ^4He interact strongly with each other. As a consequence, phase separation occurs and the density of dilute ^4He in liquid ^3He drops rapidly to zero for decreasing temperature, before ^3He becomes superfluid [Edwards and Daunt, 1961]. In the opposite situation, a small fraction (X) of ^3He can remain diluted in superfluid ^4He at zero temperature [Edwards et al., 1965], $X = 6\%$ at saturated vapor pressure pressure and $X = 9\%$ at 25 bars. This is illustrated in figure 1 taken from [Rysti, 2013] where temperature is represented on the vertical axis and ^3He fraction X on the horizontal axis, where the region in which the mixed ^3He - ^4He phase is stable at room pressure is shown in green and blue. The only possibility to realize a double superfluid is then in the dilute phase of ^3He . The possibility for a phase transition to a super-

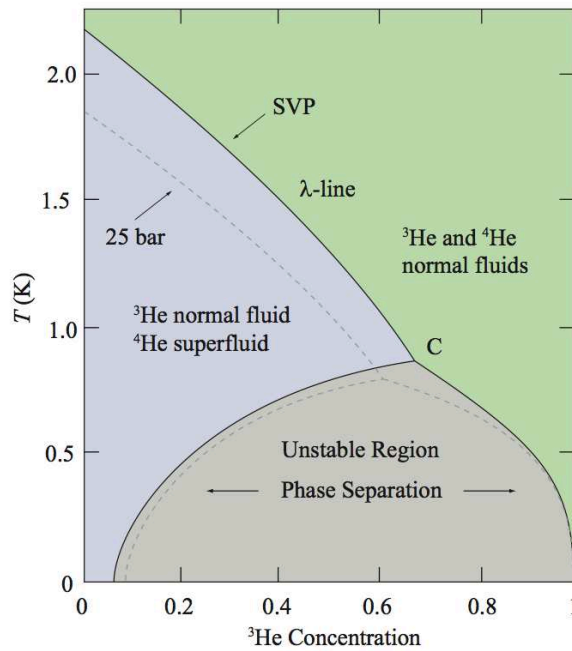


Figure 1: Phase diagram of ^3He - ^4He solutions taken from [Rysti, 2013], the region of stability for the mixed ^3He - ^4He phase at saturated vapor pressure (SVP) is shown in green and blue. The green region corresponds to both liquids being normal liquids, and the blue region corresponds to superfluid ^4He and normal ^3He . The grey region corresponds to a phase separation between pure ^3He and a dilute solution of ^3He in ^4He . Pure liquid ^3He is superfluid under $T_c = 2.6$ mK.

fluid state of fermions diluted into bosons was first demonstrated using a hard sphere model in [Cohen and van Leeuwen, 1961]. Using Landau's Fermi liquid theory, Bardeen, Baym and Pines [Bardeen et al., 1967] have carried the first calculation of the critical temperature for superfluidity of dilute ^3He in superfluid ^4He , demonstrating that this temperature was very low, of the order of a few μK . The cause of this very low temperature is the high diluteness of ^3He . The cooling technique that cooled down helium mixtures to the lowest temperature so far is adiabatic nuclear demagnetization of a copper sample in contact with helium, with a record of $97 \mu\text{K}$ obtained in 1994 [Oh et al., 1994]. However the cooling power of this technique decreases exponentially with temperature and it seems that it has reached its limit. With this temperature record, double superfluidity remains elusive as of today. The search for this state has however not yet been given-up, and researchers have designed a new cooling technique: adiabatic melting of solid ^4He [Tuoriniemi et al., 2002]. The lowest temperature achieved with this method is $300 \mu\text{K}$ but since this limit was due to technical problems, better performances are still hoped-for. Finally with a refined knowledge of the ^3He - ^3He interaction in ^4He , [Rysti et al., 2012] calculate a critical temperature for superfluidity of ^3He in superfluid ^4He as high as $T_c \simeq 45 \mu\text{K}$, within possible reach. The exponential dependence of T_c in interactions parameter can however induce large errors on this prediction.

Bose-Fermi mixtures in ultracold atoms

Apart from liquid helium and solids, the field of many-body quantum physics tackles nowadays numerous physical systems, including exotic systems like neutron stars, and superfluidity has now been observed in diverse situations [Bennemann and Ketterson, 2013]. In 1995 after the first realization of Bose-Einstein condensation in ultracold dilute gases of rubidium and sodium [Anderson et al., 1995, Davis et al., 1995], cold atom experiments joined-in as a valuable test-bench for theories, owing to their capability of studying a wide variety of systems. Cold atom set-ups allow to trap bosonic and fermionic isotopes of many different elements. The absence of defects, their very high diluteness and low temperatures allow for a simple description of the interactions, enabling a direct comparison with theories. Of particular interest for this thesis, they offer the possibility to address different interaction regimes, from the truly ideal textbook case to highly correlated states of matter in the strongly-interacting regime.

Four years after the first observation of Bose-Einstein condensation, quantum degeneracy was reached in a dilute gas of the fermionic isotope of potassium, ^{40}K [DeMarco, 1999]. It did not take long for experimentalist to simultaneously cool mixtures of bosonic and fermionic isotopes of lithium close to quantum degeneracy [Schreck et al., 2001a, Truscott et al., 2001], and the first observation of a mixture of a Bose-Einstein condensate with a Fermi sea was obtained in 2001 in the ultracold Fermions team at ENS [Schreck et al., 2001b]. Since these seminal works, a rich variety of Bose-Fermi mixtures have been produced, table 1 provides an extensive list of such experimental realizations.

Species	Reference(s)
${}^6\text{Li}(\text{f}) - {}^7\text{Li}(\text{b})$	[Schreck <i>et al.</i> , 2001b, Truscott <i>et al.</i> , 2001]
${}^{23}\text{Na}(\text{b}) - {}^6\text{Li}(\text{f})$	[Hadzibabic <i>et al.</i> , 2002]
${}^{40}\text{K}(\text{f}) - {}^{87}\text{Rb}(\text{b})$	[Roati <i>et al.</i> , 2002, Modugno <i>et al.</i> , 2002]
${}^6\text{Li}(\text{f}) - {}^{87}\text{Rb}(\text{b})$	[Silber <i>et al.</i> , 2005]
${}^3\text{He}^*(\text{f}) - {}^4\text{He}^*(\text{b})$	[McNamara <i>et al.</i> , 2006]
${}^6\text{Li}(\text{f}) - {}^{40}\text{K}(\text{f}) - {}^{87}\text{Rb}(\text{b})$	[Taglieber <i>et al.</i> , 2008]
${}^6\text{Li}(\text{f}) - {}^{85,87}\text{Rb}(\text{b})$	[Deh <i>et al.</i> , 2008, Deh <i>et al.</i> , 2010]
${}^{84,86,88}\text{Sr}(\text{b}) - {}^{87}\text{Sr}(\text{f})$	[Tey <i>et al.</i> , 2010, Stellmer <i>et al.</i> , 2013]
${}^6\text{Li}(\text{f}) - {}^{174}\text{Yb}(\text{b})$	[Hara <i>et al.</i> , 2011, Hansen <i>et al.</i> , 2011]
${}^{170,174}\text{Yb}(\text{b}) - {}^{173}\text{Yb}(\text{f})$	[Sugawa <i>et al.</i> , 2011]
${}^{40}\text{K}(\text{f}) - {}^{41}\text{K}(\text{b}) - {}^6\text{Li}(\text{f})$	[Wu <i>et al.</i> , 2011]
${}^{161}\text{Dy}(\text{f}) - {}^{162}\text{Dy}(\text{b})$	[Lu <i>et al.</i> , 2012]
${}^{23}\text{Na}(\text{b}) - {}^{40}\text{K}(\text{f})$	[Park <i>et al.</i> , 2012]
${}^6\text{Li}(\text{f}) - {}^{133}\text{Cs}(\text{b})^{(\dagger)}$	[Repp <i>et al.</i> , 2013, Tung <i>et al.</i> , 2013]
${}^{52}\text{Cr}(\text{b}) - {}^{53}\text{Cr}(\text{f})$	[Laburthe-Tolra, 2014]

Table 1: Bose-Fermi mixtures realized in dilute ultracold gases to present, the bosonic (b) or fermionic (f) nature of each isotope is indicated in parentheses. Helium isotopes are trapped in a metastable state. ^(†) The Li-Cs mixture has been cooled close to quantum degeneracy.

These experiments were designed for different aims. Modugno *et al.*, in [Modugno *et al.*, 2002] have demonstrated that an attractive interaction between a BEC of ${}^{87}\text{Rb}$ and a Fermi sea of ${}^{40}\text{K}$ can lead to a collapse of the Fermi sea thus exhibiting the first spectacular effect of Bose-Fermi interactions in a degenerate mixture. The most recurrent motivation is the prospect of tuning the interactions between bosons and fermions using the tool of Feshbach resonances, a way to control finely the two-body interactions. This tunability has been shown in many combinations: Li-Li [Zhang *et al.*, 2005], Na-Li [Stan *et al.*, 2004], K-Rb [Inouye *et al.*, 2004, Ferlaino *et al.*, 2006, Ospelkaus *et al.*, 2006a, Zaccanti *et al.*, 2006], Li-Rb [Deh *et al.*, 2008, Deh *et al.*, 2010], K-K [Wu *et al.*, 2011], Na-K [Park *et al.*, 2012], Li-Cs [Repp *et al.*, 2013, Tung *et al.*, 2013] and could be further explored with other ones such as Li-K or He-He [Goosen *et al.*, 2010]. Feshbach resonances further allow to form bound pairs of atoms, offering the possibility of creating polar fermionic molecules, [Wu *et al.*, 2012]. The alkaline-earth like elements ytterbium (Yb) and strontium (Sr) have fermionic isotopes with a SU(N) symmetry in the ground state^(a) which open prospects of interesting hamiltonians, further extended by the coupling to a bosonic component. Mixed with lighter atoms, heavy elements like Sr, Yb or caesium (Cs) allow to study large mass-imbalance effects for example in few-body bound states [Pires *et al.*, 2014, Tung *et al.*, 2014]. Placing a Bose-Fermi mixture

^(a)In the ground state the nuclear spin decouples from electronic state, realizing a SU(N) symmetry with N the degeneracy of the ground state.

in a lattice, one can study the on-site localization of the bosons driven by the interactions with the fermions [*Ospelkaus et al., 2006b, Günter et al., 2006, Best et al., 2009*], resembling the famous superfluid-Mott transition of bosons, or even the dual Mott phase of bosons and fermions with either attractive or repulsive interactions [*Sugawa et al., 2011*]. Finally Bose-Fermi mixtures composed of atoms with a magnetic dipole moment could form exotic phases of matter. It is the case of chromium, and with a stronger dipole moment, the lanthanide elements erbium and dysprosium.

In none of the above-cited Bose-Fermi mixtures experimentally obtained, both components were superfluid. First, fermionic superfluidity requires a sufficiently strong and attractive interaction, this has limited so far the achievement of superfluidity to only two species, the alkalis lithium (${}^6\text{Li}$) and potassium (${}^{40}\text{K}$). Second one needs the bosonic component to form a stable superfluid in the conditions of fermionic superfluidity, which further eliminates number of candidates. Finally the boson-fermion interaction must not destabilize the mixture, further narrowing the search. There remains a few possible solutions in the multitude of available choices.

In this thesis we will present experiments on dilute ultracold gases of lithium 7 - a boson - and lithium 6 - a fermion. Lithium isotopes have the virtue to present Feshbach resonances. The main original result of this work is the observation of a mixture of a superfluid of ${}^6\text{Li}$ and a Bose-Einstein condensate of ${}^7\text{Li}$. We will show how the usage of Feshbach resonances allows to create a stable, superfluid BEC with weakly repulsive interactions. By the right choice of internal states this BEC can be mixed with a superfluid of ${}^6\text{Li}$, avoiding phase-separation. The interactions in the Fermi superfluid can be tuned also with a Feshbach resonance. In the strongly attractive-limit, we create a mixture of two Bose-Einstein condensates, one made of atoms and the other of molecules. In the weakly-attractive limit we obtain a mixture of a Bose superfluid with a Fermi superfluid in the BCS regime, realizing the long-sought goal of liquid helium mixtures of a mixture of Bose and Fermi superfluids.

Outline

- The first chapter of this manuscript presents the theoretical aspects of degenerate gases of ${}^6\text{Li}$ and ${}^7\text{Li}$. It introduces the two-body interactions present in our gases, with a description of Feshbach resonances. Then the theory of Bose-Einstein condensation and Fermi superfluids in the presence of these interactions is overviewed. A particular attention is given to the manifestations of superfluidity in these systems, and especially the critical velocity for frictionless flow, characteristic of this state.

- The second chapter covers the experimental techniques employed to produce and study these gases, describing the cooling techniques and precise preparations employed to obtain our ultracold samples. A possible improvement of the cooling procedure using grey molasses on the D_1 line is described in chapter 3, with a theoretical investigation of the cooling process employed.
- In the fourth chapter, we report on an investigation of Bose gases under strong interactions. Using Feshbach resonances we were able to place gases of bosons in a situation of resonant two-body interaction to investigate the stability of such gases against three-body inelastic collisions which are the dominant cause atom losses. This study outlines the limit of stability of strongly-interacting Bose gases.
- The final chapter is dedicated to the experimental realization of a mixture of Bose and Fermi superfluids, and the study of this system. We present the conditions of stability of this mixture, demonstrating that they are fulfilled with our system. We demonstrate the superfluidity of both components and show that the characteristic frictionless flow is observed. Then we explore the properties of this system, presenting a measurement of the interaction between the two components using collective oscillations. We finish by exploring the critical velocity for counter-flow motion, a property specific to superfluids.

“Vous avez peur de quoi?

Vous avez peur de qui?

Peur? Mais vous allez perdre les gars!” Aimé Jacquet

Chapter 1 |

Bose-Einstein condensates and Fermi superfluids

The study of the manifestations of Quantum Mechanics at the thermodynamical level is a central motivation of the field of ultracold gases. In the present chapter, we will briefly give some important background for the description of dilute Bose and Fermi gases. First, in the case of non-interacting quantum particles, revealing the effects of quantum statistics, then in the more interesting situation of interacting particles. We will summarize the important theoretical and experimental results constituting the state-of-the-art of research on these systems, and address the interesting phenomena that arise and in particular superfluidity.

1.1 | Ideal Quantum Gases

Let us start by the simple case of a classical gas of non-interacting particles of mass m . We will work in the grand-canonical ensemble, because, as we will see in 1.2, it yields useful relations for experimental observables such as in-trap density. The gas is described by the classical Boltzmann distribution $f(\epsilon)$, which represents the probability for a particle to occupy a state with energy ϵ at a chemical potential μ and at a temperature T .

$$f(\epsilon) = e^{-\beta(\epsilon-\mu)} \quad (1.1)$$

with $\beta = 1/k_{\text{B}}T$. For particles in free-space this yields:

$$n\lambda_{\text{dB}}^3 = e^{\beta\mu} \quad (1.2)$$

where n is the density and $\lambda_{\text{dB}} = \sqrt{2\pi\hbar^2/mk_{\text{B}}T}$ is the thermal de Broglie wavelength. Eq. (1.2) is the equation of state (EoS) of a classical gas in the grand-canonical ensemble, by using the Gibbs-Duhem relation $\frac{\partial P}{\partial \mu} = n$ one recovers the usual ideal gas expression $P = nk_{\text{B}}T$.

In the case of a quantum gas made of identical particles, the different quantum statistics between bosons and fermions result in two different energy distributions (f_{B} for bosons and f_{F} for fermions):

$$f_{\text{B}}(\epsilon) = \frac{1}{e^{\beta(\epsilon-\mu)} - 1} \quad (1.3)$$

$$f_{\text{F}}(\epsilon) = \frac{1}{e^{\beta(\epsilon-\mu)} + 1}. \quad (1.4)$$

In turn, they lead to [Landau and Lifchitz, 1966b]:

$$n_B \lambda_{dB}^3 = g_{3/2}(e^{\beta\mu}) \quad (1.5)$$

$$n_F \lambda_{dB}^3 = -g_{3/2}(-e^{\beta\mu}) \quad (1.6)$$

^(a) which are respectively the EoS of an ideal gas of bosons and fermions.

Taking the limit of high temperature or low fugacity z ($z = e^{\beta\mu}$) for the expressions above, one recovers the classical Boltzmann gas relations. However at low temperature (1.3) and (1.4) lead to a marked difference with the classical behavior. For fermions, the occupation probability (1.4) is always smaller than one, two identical fermions cannot occupy the same state. The Fermi energy is defined by $E_F = \mu(T = 0, N_f)$ where N_f is the total number of fermions ($T_F = E_F/k_B$). The shape of $f_F(\epsilon)$ is dictated by the ratio T/T_F . When this ratio is large f_F is close to (1.1) while at zero temperature all states with energy $\epsilon \leq E_F$ are occupied with probability 1 and all states above E_F are empty. We thus see that the temperature T_F sets the scale for the apparition of quantum statistics effects (quantum degeneracy). The Fermi energy can be calculated using

$$N = \sum_i f_F(\epsilon_i, T = 0, \mu = E_F). \quad (1.7)$$

For a homogeneous system in a box, it yields:

$$E_F = \frac{\hbar^2}{2m} (6\pi^2 n)^{2/3} \quad (1.8)$$

The state of a Fermi gas at zero-temperature is called a Fermi sea. Although very different from a classical gas, it does not, however, constitute a new phase of the system.

In the bosonic case the physical condition $f_B > 0$ imposes that $\mu < \epsilon_0$ with ϵ_0 the ground state energy. Then for all states with energy $\epsilon \geq \epsilon_0$ the occupation number is bounded, but when $\mu \rightarrow \epsilon_0$, the occupation probability of the ground state diverges. Thus there is a critical number of bosons for which all states are fully occupied and any additional particle necessarily fills the ground state^(b), marking the transition from an ideal gas (1.5) to a Bose-Einstein condensate (BEC). The temperature scale for quantum degeneracy and Bose-Einstein condensation $T_{c,b}$ is found by setting

$$\sum_{i \neq 0} f_B(\epsilon_i, T_{c,b}, \mu = \epsilon_0) = N \quad (1.9)$$

using a straightforward calculation, it yields that Bose-Einstein condensation is reached for

$$(n \lambda_{dB}^3)_c = \zeta(3/2) \quad (1.10)$$

where $\zeta(x)$ is the Riemann function. The critical parameter for BEC is then found to be the phase-space density $n \lambda_{dB}^3$, the critical temperature at a given density is $k_B T_{c,b} \simeq 3.3 n^{2/3} \hbar^2 / m$.

^(a) g_s are the polylogarithm functions defined by $g_s(z) = \sum_{k=1}^{\infty} z^k / k^s$.

^(b) This conclusion holds only if the sum in 1.9 excluding the ground state converges, which is verified in the homogeneous case.

Contrarily to the fermions case, the transition to a BEC does constitute a phase transition, peculiar in nature since its cause is purely statistical.

After homogeneous systems, we now consider the experimentally relevant cases of N_f fermions in two equally populated spin states and N_b bosons in one spin state in a 3D harmonic potential with frequencies $\omega_x, \omega_y, \omega_z$,

$$V_{\text{ext}}(\mathbf{r}) = \sum_i \frac{m_\alpha}{2} \omega_i^2 r_i^2, \quad (1.11)$$

where the index $\alpha = \text{b, f}$ denotes either bosons or fermions. T_F and $T_{\text{c,b}}$ can be straightforwardly obtained using (1.7, 1.9) in the presence of the external potential [Pitaevskii and Stringari, 2003]:

$$k_B T_F = \hbar \bar{\omega} (3N_f)^{1/3} \quad (1.12)$$

$$k_B T_{\text{c,b}} = \hbar \bar{\omega} (N_b / \zeta(3))^{1/3} \quad (1.13)$$

where $\bar{\omega} = (\omega_x \omega_y \omega_z)^{1/3}$ is the mean trapping frequency. These temperatures are the references for quantum degeneracy of harmonically trapped gases.

The ideal gas case considered until here is in many occasions far from the experimental reality where interactions can have a relevant effect. Before turning to the addition of quantum interaction effects on top of quantum statistics, let us introduce the local-density approximation (LDA).

1.2 | The Local Density Approximation

This approximation simplifies the treatment of harmonically trapped systems. We will see that it allows to express easily local variables in trapping potentials, even when interactions are present as long as the thermodynamics of the homogeneous case is known. It is valid for slowly varying density and trapping potential.

The LDA assumption is that at each position \mathbf{r} there exists a mesoscopic volume over which the local system is at equilibrium and homogeneous. All small volumes being in contact, they can exchange heat and are thus at thermal equilibrium with temperature T . The mesoscopic volumes can also exchange particles imposing a constant chemical potential μ_0 over the whole system. The LDA then treats a small local volume as a homogeneous system with a local chemical potential $\mu_\alpha(\mathbf{r})$ shifted by the external potential (α denotes the particle type considered) :

$$\mu_\alpha(\mathbf{r}) = \mu_0 - V_{\text{ext}}(\mathbf{r}) \quad (1.14)$$

$$n_\alpha(\mathbf{r}) = n_\alpha(\mu_\alpha(\mathbf{r}), T) = n_\alpha(\mu_0 - V_{\text{ext}}(\mathbf{r}), T) \quad (1.15)$$

It is now clear that the use of the grand-canonical ensemble is appropriate, and from the knowledge of the equation of state in the form $n_\alpha(\mu_\alpha, T)$, the global chemical potential μ_0 and temperature, one can reconstruct the local density and all other thermodynamics variables. For example the density distribution of a Boltzmann gas in a harmonic potential containing N particles can be easily obtained by inserting (1.14) into (1.2) and setting $N = \int d^3r n(\mathbf{r})$:

$$n(\mathbf{r}) = N \left(\frac{m\bar{\omega}}{2\pi k_B T} \right)^{3/2} e^{-V_{\text{ext}}(\mathbf{r})/k_B T} \quad (1.16)$$

In general, when there are several particle types, Eq. (1.14) is still valid but μ_α depends on the density of the different species present:

$$\mu_\alpha(\mathbf{r}) = \sum_{\beta} \mu_{\alpha\beta}(n_\beta(\mathbf{r}), T) = \mu_{\alpha,0} - V_{\text{ext}}(\mathbf{r}) \quad (1.17)$$

where $\mu_{\alpha\beta}$ is the contribution to the chemical potential of species α due to the presence of species β .

In-situ pressure measurement

An additional – and experimentally handy – consequence of the LDA is that the doubly-integrated density \bar{n} in a harmonic trap is proportional to the pressure. Indeed recalling the Gibbs-Duhem formula $n = \left(\frac{\partial P}{\partial \mu} \right)_T$ and using (1.14) it can be shown that :

$$P(\mu_z, T) = \frac{m\omega_x\omega_y}{2\pi} \bar{n}(z) = \frac{m\omega_x\omega_y}{2\pi} \iint n(x, y, z) dx dy \quad (1.18)$$

with $\mu_z = \mu_0 - \frac{m}{2}\omega_z^2 z^2$. Since $\bar{n}(z)$ is easily accessible experimentally, (1.18) is used to measure the equation of state of a harmonically trapped system in the form $P(\mu, T)$, lying at the basis of many thermodynamics studies for Bose and Fermi gases in three dimensions [Nascimbène *et al.*, 2010, Navon *et al.*, 2010, Navon *et al.*, 2011]. In two dimensions similar relations can be obtained and have been used for thermodynamics studies of 2D Bose gases [Hung *et al.*, 2011, Yefsah *et al.*, 2011]. Another way of extraction of the equation of state using the LDA has been employed, through the measure of the pressure and of the compressibility $dn/d\mu$ by means of a precise knowledge of the trapping potential [Ku *et al.*, 2012, Desbuquois *et al.*, 2014]. This method spares the need of the knowledge of the global chemical potential μ_0 . Finally, the local density approximation can be used in addition with the measurement of local density fluctuations to extract thermodynamic observables and the equation of state, as has been successfully implemented for one-dimensional Bose gases [Esteve *et al.*, 2006].

1.3 | S-wave Interactions and Feshbach Resonances

With this basis, we now turn to the description of interactions and their consequences. At ultracold temperatures in alkali gases, two-body collisions occur generally in the s-wave channel and have a short-range character. This section then outlines the minimum background from theory of two-body elastic collisions^(c) useful for the description of properties of Bose and Fermi gases under our experimental conditions.

1.3.1 S-wave interactions

The general hamiltonian for a collision problem is written in the center-of-mass frame

$$\hat{H} = \hat{H}_0 + V_{\text{int}}(\hat{\mathbf{r}}) \quad (1.19)$$

\hat{H}_0 is the free hamiltonian $\hat{H}_0 = \frac{\hat{p}^2}{2\mu}$ with reduced mass μ . The interaction potential $V_{\text{int}}(\hat{\mathbf{r}})$ in the case of lithium represents the Van der Waals interaction with the characteristic $1/r^6$ attractive tail and short range $1/r^{12}$ repulsion. The solutions to the Schrödinger equation with the above hamiltonian are decomposed as a sum of spherical harmonics factorized in an angular and a radial part, each term l corresponding to a partial wave with angular momentum $l\hbar$. The radial wave-function then satisfies a Schrödinger equation with an effective potential:

$$V_{\text{eff}}(r) = V_{\text{int}}(r) + \frac{\hbar^2 l(l+1)}{\mu r^2} \quad (1.20)$$

The second term represents an effective repulsive barrier for all partial waves with $l > 0$. In the case of lithium, the height of this barrier is of order $k_B \times 4$ mK. Below this typical temperature, p-waves ($l = 1$) and higher-orders are suppressed leaving only s-wave collisions $l = 0$, since the typical temperatures of our samples are much lower (between a few hundred μ K and 100 nK), our gases are in the s-wave regime of two-body collisions. We will give the solutions to the collision problem in this ultracold – low energy – regime.

The general method to find eigenstates of (1.19) is to express the two-body wave-function as a sum of a plane wave with wave-vector k (unperturbed free particles) and a spherical wave (scattered particles):

$$\psi(\mathbf{r}) \propto e^{ikz} + \frac{f(\theta, k)}{r} e^{ikr} \quad (1.21)$$

$f(\theta, k)$ is the amplitude of the wave-function that is in the scattered state, it is called the scattering amplitude. In the s-wave regime, by symmetry f is independent of θ , and at low-

^(c)Inelastic collisions might occur, when energy stored in the internal degrees of freedom is relaxed into kinetic energy for the atoms accompanied by a change of internal structure. However since they induce heating and losses we prepare our gases in internal states (spin states) which are protected by conservation laws against inelastic collisions

energy tends to [Landau and Lifchitz, 1966a]:

$$f(k) \underset{k \rightarrow 0}{=} \frac{-a}{1 + i k a - a r_e k^2} \underset{ka \rightarrow 0}{=} -a \quad (1.22)$$

a is called the scattering length and r_e the effective range. Thus in the limit

$$k r_e \ll 1, \quad (1.23)$$

the only parameter describing the interactions is the scattering length a . This means that the details of the potential do not affect the low-energy two-body physics. As a consequence, the low-temperature scattering properties of many different species are actually described by a unique hamiltonian, that can be derived using any model potential, as long as it reproduces $f = -a$. In particular one can chose a “universal” zero-range potential, approximating the interaction by a contact interaction:

$$V(\mathbf{r}) = \frac{4\pi\hbar^2 a}{m} \delta(\mathbf{r}) \quad (1.24)$$

where $\delta(\mathbf{r})$ is the usual Dirac function^(d).

From the knowledge of f , one can obtain the scattering cross section σ :

$$\frac{d\sigma}{d\Omega} = \begin{cases} |f(k, \theta)|^2 & \text{distinguishable particles} \\ |f(k, \theta) + \epsilon f(k, \pi - \theta)|^2 & \text{identical particles} \end{cases} \quad (1.25)$$

Where $\epsilon = 1(-1)$ for identical bosons (fermions). Again, f is independent of θ in the s-wave channel, so for distinguishable particles, the scattering cross section σ is deduced from (1.22), $\sigma = 4\pi a^2$. When considering identical particles, quantum statistics play a role, constructive interferences for bosons lead to an amplified cross-section $\sigma_b = 8\pi a^2$, while destructive interferences cancel-out s-wave scattering for fermions yielding $\sigma_f = 0$. These interference effects are inverted when considering p-waves, such that identical fermions can interact in this channel but as seen earlier such scattering is strongly inhibited (except in the case of a resonant enhancement). Thus in the low energy regime, two distinguishable spin-states are in general required for collisions to occur in a Fermi gas, this is in particular true for the systems considered in this work.

1.3.2 Feshbach resonances

Magnetic Feshbach Resonances

From the above discussion, one might get the impression that the scattering properties between two atoms are immutable with in particular a fixed scattering length. However to study the effects of interactions it is very useful to be able to control them - varying a . This

^(d)See [Cohen-Tannoudji, Claude, 1999] for details of the choices of interaction potential, the $\delta(\mathbf{r})$ potential has to be regularized for the calculation of some physical quantities.

control knob is a specificity of cold atom experiments, and arises from the internal degrees-of-freedom of the atoms. So far we have discussed the orbital wave-function and left out the spin wave-function, assuming it was fixed. Taking the internal structure into account allows for different spin states and hence different interacting potentials. This new degree of freedom gives rise to the so-called Feshbach resonances (FR), which are the most standard way to tune the two-body interactions in ultracold gases. A precise description of them can be found in [Chin *et al.*, 2010], we will again here summarize only the features that are necessary in the frame of our experiments.

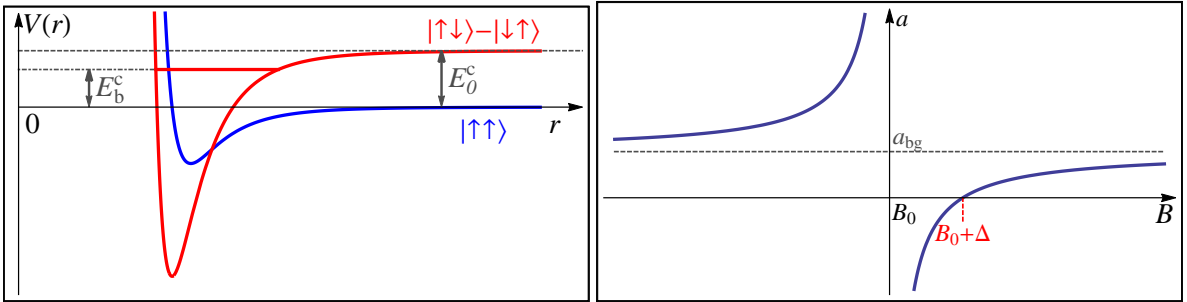


Figure 1.1: Schematic representation of a Feshbach resonance, the left panel shows the interaction potential in the open (closed) channel in blue (red). The open channel in this simplified example is a triplet state and the closed channel is the singlet state, since these two have different total spin their relative energy E_0^c can be modified using an external magnetic field B . Thus the energy of the bound state E_b^c depends on B . On the right panel, the resulting dependence of scattering length a in B is represented.

Feshbach resonances take place in collision events in which two atoms in their respective initial spin state can be coupled to different output states by the collision (see fig. 1.1). The initial spin state configuration is called the entrance/open channel and the different states to which they can be coupled constitute the closed channel. The coupling between the two channels is usually of the hyperfine kind, but can also be induced, for example by radio-frequency or optical radiation. The reference energy (the threshold) is the zero of the entrance channel potential at infinite separation r . The zero energy E_0^c in the closed channel depends on its spin configuration and can be varied using an external parameter, namely the magnetic field B in the case hyperfine coupling. From now on we will consider only this case of magnetic Feshbach resonances.

Furthermore, the closed channel potential can feature a bound state with energy E_b^c which for some value of B crosses the zero energy of entrance channel (see fig. 1.1). When this occurs, scattering in the open channel is enhanced, leading to a divergence of a . The width Δ in magnetic field of this resonance depends on the coupling strength between the two channels. This coupling leads to a dressing of the bound state in the closed channel by the open channel. The scattering length a as function of B takes the form:

$$a(B) = a_{\text{bg}} \left(1 - \frac{\Delta}{B - B_0} \right) \quad (1.26)$$

The unitary regime

Naively one might think that at $B = B_0$, σ diverges with a , but recalling (1.22) we get

$$\sigma = \begin{cases} \frac{4\pi a^2}{1+k^2 a^2} \xrightarrow{k|a| \gg 1} \frac{4\pi}{k^2} & \text{distinguishable.} \\ \frac{8\pi a^2}{1+k^2 a^2} \xrightarrow{k|a| \gg 1} \frac{8\pi}{k^2} & \text{identical bosons.} \end{cases} \quad (1.27)$$

In the limit $k|a| \ll 1$, we recover the expressions given earlier, and a is the only parameter characterizing interactions. In the other limit $k|a| \gg 1$, σ saturates to a value obtained by replacing a by $1/k$, which is the largest cross-section compatible with the conservation of probability density. This situation in which a diverges ($1/a = 0$) and drops out of the problem is called the unitary regime, or unitarity.

The shallow bound state

In the vicinity of a Feshbach resonance, the dressed bound state exists only on the side where $a > 0$. Close to the resonance position it is strongly dressed by the open channel and its binding energy takes the universal form:

$$E_b = -\frac{\hbar^2}{ma^2} \quad (1.28)$$

Since this energy is much weaker than the binding energy of dimers formed in the bare interatomic potential, we will refer to the dimer as the shallow dimer and to the latter as deeply-bound dimers. The spatial extent of the wave-function of the shallow dimer is proportional to a . The expression (1.28) should be used with care, it is correct (as the main contribution to E_b) only provided $|r_e| \ll |a|$. The validity of this assumption varies between the different resonances, calling for a classification.

Feshbach resonances are thus usually separated into two kinds, ‘broad’ or ‘narrow’ resonances. We give here a simple image of how these kinds are defined:

For broad resonances one can assume $|r_e| \ll |a|$ over a large fraction of the width Δ around B_0 , in narrow ones this assumption is valid only in a region of width $\zeta\Delta$ around B_0 with $\zeta \ll 1$. For broad resonances the bound state is strongly dressed by the open channel and (1.28) is a good approximation over the whole width Δ while it is true only in a range of width $\zeta\Delta$ for narrow ones, we shall call this range the universal region.

More specifically, the classification of resonances into ‘broad’ and ‘narrow’ kinds is dictated by a parameter called $s_{\text{res}}^{(e)}$, its expression cannot be given here without entering into unnecessary molecular physics considerations, see [Chin *et al.*, 2010] for more details. s_{res} is called the resonance strength, it takes into account the strength of the coupling between the two channels as well as characteristics of the molecular bound state in the closed channel. Resonances with $s_{\text{res}} > 1$ ($s_{\text{res}} < 1$) are the ones conventionally called broad (narrow)

^(e)Rigorously these two kinds should be called ‘entrance channel dominated’ and ‘closed channel dominated’ because there exists exceptions where resonances with a large width Δ are actually closed channel dominated.

resonances.

In studies of few-body properties [Gross *et al.*, 2011, Dyke *et al.*, 2013, Julienne and Hutson, 2014], finite-range corrections are actually easily measured experimentally. As we shall see in details in section 4, few-body effects are a cause of atom losses in ultracold gases. Indeed it is the formation of small atomic clusters containing $2, 3, \dots, N$ atoms which eventually leads to the construction of the solid state which constitutes the true ground state of atomic ensembles at ultracold temperatures. Provided few-body losses are weak, it was shown by [Giorgini *et al.*, 1999] for bosons that the many-body properties remain dictated to a good approximation by the universal expressions depending only on a such that finite-range effects can be neglected. When a becomes very large, resonant few-body effects can appear and modify the properties of the gas. This is expected for the strongly-interacting Bose gas as we will discuss below. In the case of fermions, the Feshbach resonances of ${}^6\text{Li}$ in which we are interested in this work are very broad with a strong universal character and the effective range can be neglected. Furthermore, for spin-1/2 fermions the Pauli exclusion principle hampers few-body losses.

The following paragraph lists the different Feshbach resonances at our disposal in lithium isotopes to realize interacting quantum systems.

1.3.3 Feshbach resonances in lithium

A number of s-wave Feshbach resonances exist in the different spin states of ${}^6\text{Li}$ and ${}^7\text{Li}$. We denote $|1_f\rangle$ ($|1_b\rangle$) the absolute ground state of ${}^6\text{Li}$ (${}^7\text{Li}$), $|2_f\rangle$ ($|2_b\rangle$) the second-to-lowest and so forth. We will focus on the ground and first excited states of each species as they are the ones used in the experiment. The most accurate results obtained on the characterization of FRs in ${}^6\text{Li}$ were published in [Zürn *et al.*, 2013] and in ${}^7\text{Li}$ in [Gross *et al.*, 2011, Navon *et al.*, 2011, Dyke *et al.*, 2013], we summarized them in table 1.1 and represented their $a(B)$ dependence in fig. 1.2.

One of the most famous example of a broad Feshbach resonance is the one in ${}^6\text{Li}$ between $|1_f\rangle$ and $|2_f\rangle$ located at 832G, with a resonance strength of $s_{\text{res}} = 59$, that has allowed numerous studies of strongly interacting Fermi gases and the exploration of the BEC-BCS crossover. In ${}^7\text{Li}$ two resonances widely used are the ones listed in table 1.1, they are actually intermediate between narrow and broad ($s_{\text{res}} = 0.8$). But with $\zeta \sim 0.3$, they still exhibit a universal behavior over a large range of magnetic field (few tens of G) [Chin *et al.*, 2010, Julienne and Hutson, 2014] and are suitable for few- and many-body physics studies.

Experimentally, for the study of interactions in many-body systems we aim at using the universal region of a Feshbach resonance. The limit then is the magnetic-field stability achieved on the experiment which has to be narrower than the width of the universal region.

State	s_{res}	ζ	$B_0(\text{G})$	$\Delta(\text{G})$	$a_{\text{bg}}(a_0)$
$ 1_b\rangle$	0.81	0.31	737.8(2)	-171	-21
$ 2_b\rangle$	~ 1	$\simeq 0.3$	893.7(4)	-237.8	-18.24
$ 2_b\rangle$	$\ll 1$	$\ll 1$	845.5(5)	4.5	-18.24
$ 3_b\rangle$	$\lesssim 1$?	~ 1040	~ 170	~ -15

States	s_{res}	$B_0(\text{G})$	$\Delta(\text{G})$	$a_{\text{bg}}(a_0)$
$ 1_f\rangle - 2_f\rangle$	59	832.18(8)	-262.3(3)	-1582(1)
$ 1_f\rangle - 3_f\rangle$	29	689.68(8)	-166.6(3)	-1770(5)
$ 2_f\rangle - 3_f\rangle$	46	809.76(5)	-200.2(5)	-1642(5)

Table 1.1: Some Feshbach resonances position and width in the ground states of ${}^7\text{Li}$ (top) and ${}^6\text{Li}$ (bottom). a_0 is the Bohr radius. $\zeta \gg 1$ for all ${}^6\text{Li}$ resonances listed here. The data on the ${}^7\text{Li}$ $|3_b\rangle$ state Feshbach resonance comes from a private communication with Servaas Kokkelmans.

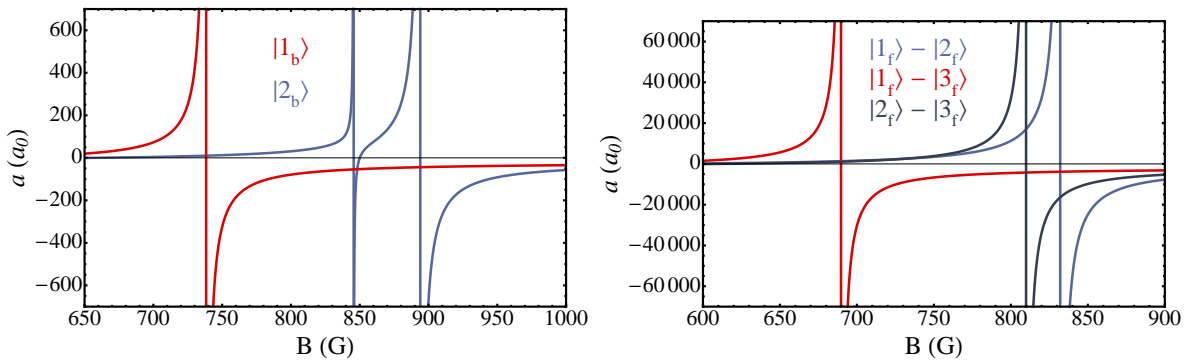


Figure 1.2: Scattering length dependence of the different states of ${}^7\text{Li}$ (left) and ${}^6\text{Li}$ (right) corresponding to the data given in tab. 1.1. The resonance in the $|3_b\rangle$ state is not represented here since it has not been measured experimentally and is not known with great precision. Note the difference of a factor 100 in the vertical scales between left and right panels reflecting the much higher strength of ${}^6\text{Li}$ resonances with respect to ${}^7\text{Li}$ ones.

1.3.4 ${}^6\text{Li}$ - ${}^7\text{Li}$ interactions and Feshbach resonances

The main result of this work is the observation of a mixture of Bose and Fermi superfluids with ${}^7\text{Li}$ and ${}^6\text{Li}$. For the discussion of interactions between these superfluids, we need to know the scattering properties of ${}^6\text{Li}$ - ${}^7\text{Li}$ collisions. In the low-temperature regime, ${}^6\text{Li}$ and ${}^7\text{Li}$ atoms collide only in s-waves^(f). The scattering cross-section is given by $\sigma_{67} = 4\pi a_{67}^2 / (1 + a_{67}^2 k^2)$ as is usual for distinguishable atoms, with a_{67} the scattering length, which depends on the internal states involved. At high magnetic field, the background scattering length (a_{bf}) for all combinations of the internal states of interest ($|1_{\text{b}}\rangle$, $|2_{\text{b}}\rangle$, $|3_{\text{b}}\rangle$, $|1_{\text{f}}\rangle$, $|2_{\text{f}}\rangle$, and $|3_{\text{f}}\rangle$) is $a_{\text{bf}} = 41 a_0$. This value is typically smaller than the intra-isotope scattering lengths, to magnify the effect of presence of each superfluid on the other, it would then be preferable to increase this scattering length. It can be done using inter-isotope Feshbach resonances.

	$ 1_{\text{b}}\rangle$	$ 2_{\text{b}}\rangle$	$ 3_{\text{b}}\rangle$
$ 1_{\text{f}}\rangle$	226 G, 246 G[150 mG], 540 G, 540 G	287 G, 317 G[300 mG], 604 G	365 G, 674 G[220 mG],
$ 2_{\text{f}}\rangle$	256 G, 276 G, 578 G, 588 G	314 G, 344 G, 640 G	394 G, 699 G[120 mG],
$ 3_{\text{f}}\rangle$	305 G, 609 G,	374 G[140 mG], 661 G,	727 G[60 mG]

Table 1.2: Position and width of the Feshbach resonances in ${}^6\text{Li}$ - ${}^7\text{Li}$ collisions, for the different internal states. The estimated width is indicated between square brackets, extracted from theoretical calculations, when it is smaller than 50 mG it is not indicated.

${}^6\text{Li}$ - ${}^7\text{Li}$ resonances exist, they have been predicted theoretically in the group of S. Kokklemans, we use their results here. All of them are narrower than 1 G, and the majority is narrower than the magnetic field fluctuations on our setup ($\sim 50 - 100$ mG). The positions of the resonances in collisions between $|1_{\text{f}}\rangle$ and $|1_{\text{b}}\rangle$ have been calculated in [von Kempen *et al.*, 2004] and measured in [Zhang *et al.*, 2005]. The resonances in other combinations of states are known using calculations of S.K. privately communicated to our group. We have summarized their positions and width when known in table 1.2.

1.4 | Interacting Bose-Einstein Condensates

Using the background in collision theory presented above, we can explore the properties of Bose and Fermi quantum gases in the presence of s-wave short-range interactions. These interactions are characterized only by the scattering length a which can be tuned on

^(f)The Van der Waals radius is very close to that of ${}^7\text{Li}$ or ${}^6\text{Li}$ collisions ($R_{\text{vdw}} \simeq 31a_0$ [von Kempen *et al.*, 2004]) so the p-wave barrier is essentially of the same height as in ${}^6\text{Li}$ - ${}^6\text{Li}$ and ${}^7\text{Li}$ - ${}^7\text{Li}$ collisions.

a Feshbach resonance to high values and at unitarity to $1/a = 0$. This section is dedicated to the description of interacting Bose gases, first in the weakly-interacting regime where the thermodynamical state of a Bose gas is well established. As the weakly-interacting regime is realized on the tail of a Feshbach resonance we will next briefly discuss the regime of strong interaction reached when getting closer to resonance.

1.4.1 Weakly interacting Bose-Einstein condensates

The weakly-interacting Bose gas is described in second-quantization by the following hamiltonian obtained for a contact interaction (1.24):

$$\hat{H} = \int \left(\frac{\hbar^2}{2m} \hat{\psi}^\dagger \nabla^2 \hat{\psi} + \frac{g}{2} \hat{\psi}^\dagger \hat{\psi}^\dagger \hat{\psi} \hat{\psi} \right) d\mathbf{r} \quad (1.29)$$

with g the coupling constant

$$g = 4\pi\hbar^2 a/m. \quad (1.30)$$

obtained in the Born approximation, a is the scattering length defined above and m the mass of the bosons. This Hamiltonian is valid when $kr_e \ll 1$, it can be solved using a mean-field prescription: $\hat{\psi} = \psi_0 + \delta\hat{\psi}$ with $\langle \delta\hat{\psi} \rangle = 0$ and $\psi_0 \in \mathbb{C}$. This implies that the $U(1)$ symmetry of the hamiltonian^(g) is broken in agreement with the general theory of phase transitions. The order parameter of this phase is then $\psi_0 = \sqrt{n}$. In the mean-field approximation the energy can be easily obtained:

$$E_0 = \frac{1}{2} N n g \quad (1.31)$$

with n the density of bosons. Using the thermodynamical relations $P = -\left(\frac{\partial E}{\partial V}\right)_{T,N}$, $\mu = \left(\frac{\partial E}{\partial N}\right)_{T,V}$ one deduces

$$P = gn^2/2 \quad (1.32)$$

$$\mu = gn \quad (1.33)$$

Additionally the condition for mechanical stability $\frac{\partial n}{\partial P} \geq 0$ imposes $a \geq 0$, so that a uniform Bose-Einstein condensates can exist only for positive a . The writing of the equation of state in the form (1.33) is very practical for in-trap calculations, because using LDA (1.14) one can directly obtain the density distribution of a BEC containing N_b bosons in a harmonic trap at zero temperature. It reads:

$$n(\mathbf{r}) = \frac{1}{g} \left(\mu_0 - \sum_i \frac{m\omega_i^2}{2} r_i^2 \right) \quad (1.34)$$

$$\mu_0 = \frac{\hbar\bar{\omega}}{2} \left(15N_b a \sqrt{\frac{m\bar{\omega}}{\hbar}} \right)^{2/5} \quad (1.35)$$

^(g)(1.29) is invariant under the transformation $\psi(\mathbf{r}) \rightarrow e^{i\alpha} \psi(\mathbf{r})$

where the central chemical potential μ_0 is obtained by integration over the volume. The spatial extent of a BEC in direction r_i called the Thomas-Fermi radius R_i can be directly extracted from (1.34) yielding

$$R_i = \sqrt{\frac{\hbar \bar{\omega}}{m\omega_i \omega_i}} \left(15N_b a \sqrt{\frac{m\bar{\omega}}{\hbar}} \right)^{1/5}. \quad (1.36)$$

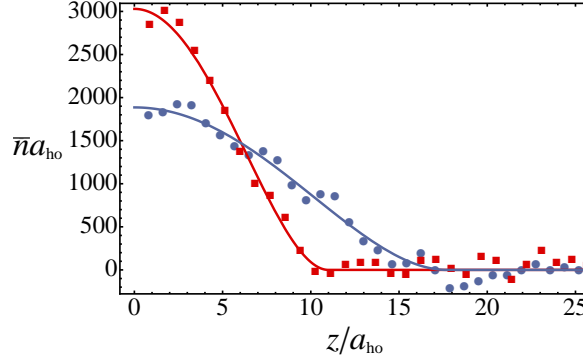


Figure 1.3: Examples of two BEC containing 22×10^3 atoms at two different scattering lengths. Doubly integrated density profiles in units of the harmonic oscillator length in the z direction $a_{\text{ho}} = \sqrt{\hbar/m\omega_z}$ here $\simeq 10 \mu\text{m}$ with $\omega_z = 2\pi \times 15.5 \text{ Hz}$. Data taken in the $|2_b\rangle$ state of ^7Li close to the 845.5 G Feshbach resonance (red squares: 832.0(5) G, blue circles: 845.0(5) G). Using fits with eq. (1.34) (solid lines) of the red squares (blue circles) profile we find a scattering length of $a = 60(10) a_0$, ($a = 500(50) a_0$), in agreement with theoretical expectations for the respective magnetic fields. In the first case the maximal density is $n_{\text{max}} \simeq 2 \times 10^{13} \text{ cm}^{-3}$ (corresponding to $na^3 \simeq 4 \times 10^{-7}$), in the latter $n_{\text{max}} \simeq 5 \times 10^{12} \text{ cm}^{-3}$ ($na^3 \simeq 10^{-5}$).

This is one example of a readily measurable prediction from the mean-field approximation, illustrated in the two experimental profiles at two different scattering lengths displayed in figure 1.3. It is valid for a $T = 0$ BEC, and to describe finite-temperature effects, the Hartree-Fock approximation [Pitaevskii and Stringari, 2003] treats (1.29) accounting for a non-zero population of the excited states $\mathbf{p} \neq 0$.

Even at zero-temperature, quantum fluctuations can induce non-zero population in the excited states. A full expansion of (1.29) to second order in $\delta\hat{\Psi}$ using the Bogolyubov method yields the well known dispersion relation for the elementary excitations of a BEC:

$$\epsilon(\mathbf{q}) = \sqrt{\left(\frac{q^2}{2m}\right)^2 + c^2 q^2} \quad (1.37)$$

where the speed of sound is found to be $c = \sqrt{gn/m}$. Furthermore, the inclusion of fluctuations of the BEC field around its MF value (and using a renormalized coupling constant), yields the Lee-Huang Yang correction for the ground state energy (see for example [Landau and Lifchitz, 1966a, Pitaevskii and Stringari, 2003]), first calculated in the context of hard-sphere bosons [Lee et al., 1957]:

$$E_0 = \frac{1}{2} N n g \left(1 + \frac{128}{15\sqrt{\pi}} \sqrt{na^3} \right) \quad (1.38)$$

In the variables (μ, n) this EoS is

$$\mu = gn \left(1 + \frac{32}{3\sqrt{\pi}} \sqrt{na^3} \right). \quad (1.39)$$

The small dimensionless parameter that quantifies the corrections is found to be $\sqrt{na^3}$, thus the MF approximation in 3D is asymptotically valid in the weakly-interacting regime. Until very recently no departure from mean-field had been observed in dilute gases. The use of Feshbach resonances has allowed for the measurement of the LHY correction, first in the excitation spectrum of a BEC using Bragg spectroscopy [Papp *et al.*, 2008] and then using the direct measure of the EoS, backed-up by a Quantum Monte-Carlo theory [Navon *et al.*, 2011].

1.4.2 Approaching the unitary Bose gas

In experimental studies of thermodynamics of the homogeneous Bose gas, the measurement of the LHY correction constituted the first step away from the weakly-interacting regime. However, in [Navon *et al.*, 2011] the highest reported value of the diluteness parameter na^3 was about $(na^3)_{\max} \lesssim 0.03$, so beyond-mean field effects remained a small correction to the weakly interacting state. Using a Feshbach resonance one can tune na^3 to much larger values^(h) and especially to $na^3 > 1$.

When a is increased, correlations induced by interactions grow. By going to the resonance position one can reach the regime $na^3 > 1$ and unitarity for $1/a = 0$. Values of na^3 larger than 1 do not mean that the inter-particle distance is smaller than the interaction range because a does not represent the range of the interactions, on a broad Feshbach resonance the effective range (r_e) remains small. Rather, the coherent length increases, so that when $na^3 > 1$, coherent few-body effects take place, amplified by bosonic statistics.

The description of the unitary Bose gas ($1/a = 0$) is a theoretical challenge under intense investigation [Li and Ho, 2012, Yin and Radzihovsky, 2013, Piatecki and Krauth, 2014, Smith *et al.*, 2014, Jiang *et al.*, 2014, Rossi *et al.*, 2014]. At unitarity since $1/a = 0$, two-body effects should drop-out of the description of the gas, and higher-order effects should play a role. The most recent theoretical works indeed suggest a phase diagram governed by three-body effects inducing a liquid phase [Piatecki and Krauth, 2014].

Experimental efforts for the obtention of a unitary Bose gas have been hindered by the intrinsic instability of strongly interacting Bose gases. This instability is caused by three-body losses depleting the gases, these losses have an a^4 dependence [Fedichev *et al.*, 1996] and so increase sharply when approaching resonance. Chapter 4 of this work describes experimental studies of stability of resonantly-interacting Bose gases, for a higher level of detail see also [Rem, 2013].

^(h)in [Navon *et al.*, 2011] the highest scattering length used was about $5000 a_0$, using ^7Li resonances it can be stabilized to values up to $|a| \gtrsim 40000 a_0$.

1.5 | Fermi Superfluids in the BEC-BCS crossover

We continue our description of interacting dilute quantum gases by reviewing interacting fermions. We have discussed earlier the case of an ideal Fermi gas, which is realized in ultracold gases with a single spin component. The addition of a second component allows for s-wave collisions, and many-body effects can play a major role. The use of Feshbach resonances is crucial for that matter. We will thus review in this section the physics of atomic Fermi gases containing two spin states ($|\uparrow\rangle, |\downarrow\rangle$)⁽ⁱ⁾ in equal population, with a Feshbach resonance between them.

1.5.1 Stability of Fermi gases on Feshbach resonances

Before entering into details of Fermi gases on a Feshbach resonance, let us consider their stability. As we discussed in 1.4, this issue is crucial for zero-temperature Bose gases. First, homogeneous BECs are mechanically unstable when $a < 0$ eliminating half of the accessible range. Second, 3-body recombination dramatically shortens their lifetime when approaching the strongly-interacting regime at the center of the resonance. On the opposite, Fermi gases exhibit a precious stability over most of the range of interactions accessible. The fundamental difference with bosons arises from fermionic statistics with the Pauli exclusion principle. On the macroscopic level it creates the so-called Fermi pressure, famous for preventing neutron stars from gravitational collapse, which protects ultracold Fermi gases from a mechanical collapse. On the microscopic level, Fermi statistics reduces relaxation processes to bound states which would imply association of two atoms with the same spin. Thus in a gas containing two spin states, dimers can be formed but three-body processes are strongly hampered. The main loss mechanism for $a > 0$ has been shown to be dimer-dimer collisions with a relaxation rate γ decreasing with increasing interactions: $\gamma \propto a^{-2.55}$ [Petrov *et al.*, 2004]. As a result the lifetime of Fermi gases on Feshbach resonances is long compared to equilibration as was demonstrated experimentally in [Bourdel *et al.*, 2003, Regal *et al.*, 2004a]. This confirms that Fermi gases can span the different regimes of interactions accessible on a Feshbach resonance, we will qualitatively describe these regimes in the following.

1.5.2 The BEC-BCS crossover

The zero-temperature Fermi gas on a Feshbach resonance realizes the so-called BEC-BCS crossover [Zwinger, 2012]. The experimental realization of such a crossover, proposed early by Leggett, and Nozières and Schmitt-Rink [Leggett, 1980, Nozières and Schmitt-Rink, 1985], has been extremely valuable for the advance of the fermionic many-body problem. It first makes the connection between Bardeen-Cooper-Schrieffer superfluidity of conventional superconductors on the one end, and Bose-Einstein condensation at the other end. Second, in the midst of the resonance, the regime where the scattering length becomes larger than

⁽ⁱ⁾In ultracold gases of neutral atoms, the different spin states are internal states, for example different Zeeman sub-levels.

the inter-particle distance ($na^3 > 1$) can be studied, contrarily to the actual situation on Bose gases. At its center lies the unitary Fermi gas. Ultracold Fermi gases are thus used as a quantitative test bench for many-body theories benefitting from their high controllability and the - apparent - simplicity of their constituents.

At zero temperature when the scattering length describes fully the two-body interactions, the only additional parameter describing the gas is the Fermi energy $E_F = \hbar^2 k_F^2 / 2m$. k_F is the Fermi wave vector proportional to the inverse of the inter-particle distance ($k_F = (3\pi^2 n)^{1/3}$) in a homogeneous system. All measurable quantities are function of one universal dimensionless parameter $1/k_F a$ which is formally equivalent to the parameter na^3 introduced for bosons^(j).

For small and positive scattering length ($1/k_F a > 1$), fermions pair-up into the bosonic universal shallow dimer with binding energy \hbar^2 / ma^2 . The gas is thus in the strongly attractive limit^(k), but due to the Pauli exclusion principle the interaction between dimers is repulsive, with effective dimer-dimer scattering length $a_d = 0.6a$ [Petrov et al., 2004]. These dimers then form a Bose-Einstein condensate at zero temperature as was observed experimentally by [Greiner et al., 2003, Jochim et al., 2003b, Zwierlein et al., 2003, Regal et al., 2004b, Bourdel et al., 2004]. It was shown in [Leyronas and Combescot, 2007] that the equation of state of the dimer gas is that of a BEC, including the Lee-Huang-Yang correction. This has been demonstrated experimentally on the lithium experiment [Navon et al., 2010], in a study of the thermodynamics of the Fermi gas through the BEC-BCS crossover. This BEC limit is asymptotically valid when the dimers are effectively tightly bound, that is for $1/k_F a \gg 1$. When the size of the dimers become of the order of the inter-particle distance $1/k_F a \sim 1$, the repulsive Bose gas picture does not hold anymore.

On the opposite side of resonance, a is small and negative, that is the interaction is weakly attractive. In this limit, it was shown first by Cooper [Cooper, 1956] that fermions with opposite momentum and opposite spin can form a bound state, called a Cooper pair^(l). The pairing mechanism here is not a two-body mechanism as is the case for the bound state for $a > 0$, but is due to the presence of the many-body Fermi sea which stabilizes the bound state by reducing fluctuations. The binding energy of these pairs is equal to Δ where Δ is called the gap, because it creates a gap in the quasi-particles excitations energy, located at the Fermi surface. Using a variational wave-function for the ground state, Bardeen, Cooper and Schrieffer have shown that for arbitrarily weak attractive interaction fermions

^(j)At $T \neq 0$ two parameters are required : T/T_F and $1/k_F a$

^(k)We call this a strongly-attractive limit in the sense that the fermions form a bound state, if the formation of these molecules is avoided, one realizes the so-called 'upper-branch' with a repulsive interaction ($a > 0$) but this branch is unstable.

^(l)Cooper derived the existence of bound states in the frame of electrons in metals, to explain conventional superconductivity. In this system, demonstrating the existence of an attractive interaction mediated by the ion lattice was an important breakthrough by Bardeen and Pines and Fröhlich [Frohlich, 1952, Bardeen and Pines, 1955] while it is 'trivial' in the case of a gas of neutral atoms.

form a superfluid (superconductor in the case of electrons) when Cooper pairing is present [Bardeen *et al.*, 1957a, Bardeen *et al.*, 1957b].

The Fermi gas on a Feshbach resonance thus indeed realizes the two limiting cases of the BEC-BCS crossover with on both ends a well understood weakly-interacting limit. In the close vicinity of the Feshbach resonance the Fermi gas is in the very interesting strongly-correlated regime, with at its center the unitary Fermi gas (UFG). Apart from the interest of creating a strongly-correlated system, this regime shares characteristics with high- T_c superconductors [Randeria *et al.*, 1989, Sá de Melo *et al.*, 1993]. They are indeed thought to realize a state where Cooper pairs have a size of the order of the inter-particle distance.

1.5.3 The equation of state

The unitary Fermi gas is the prime example of the realization of a strongly-correlated state of matter with ultracold gases. It exhibits unique properties, among which universality: since $1/k_F a = 0$, all quantities are proportional to that of a non-interacting Fermi gas^(m). For instance the chemical potential of the zero-temperature unitary Fermi gas is :

$$\mu = \xi E_F \quad (1.40)$$

where ξ is called the Bertsch parameter. Theoretically, the description of the UFG is a challenge since no small parameter is available to perform a perturbative theory. Thus the measurement of ξ constitutes a benchmark for many-body theories, permitting a direct comparison between theory and experiment. It has been measured experimentally with high precision in [Nascimbène *et al.*, 2010, Ku *et al.*, 2012, Van Houcke *et al.*, 2012] converging to a value:

$$\xi = 0.37(1). \quad (1.41)$$

The knowledge of ξ yields the equation of state of the zero-temperature unitary Fermi gas. Over the crossover, in the grand canonical ensemble, the pressure (measured in experiments) can be expressed as follows:

$$P(\mu, a) = 2P_0(\tilde{\mu})h(\delta) \quad (1.42)$$

$$\tilde{\mu} = \mu + \frac{\hbar^2}{2ma^2} \Theta\left(\frac{1}{a}\right) \quad (1.43)$$

$$\delta = \frac{\hbar}{a\sqrt{2m\tilde{\mu}}} \quad (1.44)$$

$$P_0(\mu) = \frac{1}{15\pi^2} \left(\frac{2m}{\hbar^2}\right)^{3/2} \mu^{5/2} \quad (1.45)$$

^(m)Contrarily to the unitary Bose gas where three body effects are thought to play a role, they empirically do not enter the description of a unitary Fermi gas since few-body effects are diminished by the Pauli exclusion principle.

where P_0 is the pressure of a non-interacting single-component Fermi gas and the factor 2 accounts for the presence of two spin states, and $\Theta(x)$ is the Heaviside function. The shifted chemical potential $\tilde{\mu}$ is equal to μ for $a < 0$ (BCS) side, for $a > 0$ (BEC side) it is the chemical potential corrected by the binding energy of the dimer, ensuring $\tilde{\mu} > 0$. δ measures the strength of the interactions, it generalizes $1/k_{\text{F}}a$ in the grand-canonical ensemble, and $h(\delta)$ is the dimensionless pressure.

We can derive simple limits for $h(\delta)$: First the BCS equation of state: when $a \rightarrow 0^-$ then the pressure is that of a non-interacting Fermi gas yielding

$$\lim_{\delta \rightarrow -\infty} h(\delta) = 1 \text{ (BCS)}. \quad (1.46)$$

At unitarity, the expression is the same but rescaled by a numerical factor, using (1.40) we have $n \propto (\mu/\xi)^{3/2}$ and thus by integration with respect to μ using the Giggs-Duhem relation we obtain $P = 2P_0/\xi^{3/2}$ so that

$$h(0) = \xi^{-3/2} \text{ (Unitarity)}. \quad (1.47)$$

On the BEC side in first approximation we can use the mean field EoS of bosons seen in the previous section: $P = \mu_{\text{d}}^2/2g_{\text{dd}}$ where $\mu_{\text{d}} = 2\tilde{\mu}$ is the chemical potential of the dimers and $g_{\text{dd}} = 2\pi\hbar^2 a_{\text{d}}/m$ is the dimer-dimer coupling constant ($a_{\text{d}} = 0.6a$). We then get

$$\lim_{\delta \rightarrow \infty} h(\delta) = \frac{15\pi}{2.4} \delta \text{ (BEC)}, \quad (1.48)$$

the LHY correction can be easily included in the same fashion, see [Navon, 2011].

Using the direct measurement of the pressure as a function of the chemical potential, the equation of state of the Fermi gas in the crossover has been measured in [Navon *et al.*, 2010]. The data obtained was fitted using an expansion in terms of Padé approximants, which allow from the data to find the best approximation of the EoS with a rational function of a given order, yielding an analytical description for the experimentally measured EoS. The Padé approximants were constrained using known theoretical limits such as the LHY expression. A comprehensive description of the equation of state is given in [Navon, 2011]. The explicit expression of the dimensionless pressure h is⁽ⁿ⁾:

$$h(\delta) = \begin{cases} \frac{\beta_1 + \beta_2 \delta + \beta_3 \delta \log(1+\delta) + \beta_4 \delta^2 + \beta_5 \delta^3}{1 + \beta_6 \delta^2} & \delta < 0 \text{ (BCS)} \\ \frac{\delta^2 + \alpha_1 \delta + \alpha_2}{\delta^2 + \alpha_3 \delta + \alpha_4} & \delta > 0 \text{ (BEC)} \end{cases} \quad (1.49)$$

This result can be compared to the different existing theories, and is in remarkable agreement with the early Nozières Schmitt-Rink calculation and in very good agreement with a fixed-node Monte-Carlo method [Astrakharchik *et al.*, 2004], see a full comparison with theories in [Zwinger, 2012].

⁽ⁿ⁾ $\alpha_1 = -1.137$, $\alpha_2 = 0.533$, $\alpha_3 = -0.606$, $\alpha_4 = 0.141$, $\beta_1 = 3.78$, $\beta_2 = 8.22$, $\beta_3 = 8.22$, $\beta_4 = -4.21$, $\beta_5 = 3.65$, $\beta_6 = 0.186$.

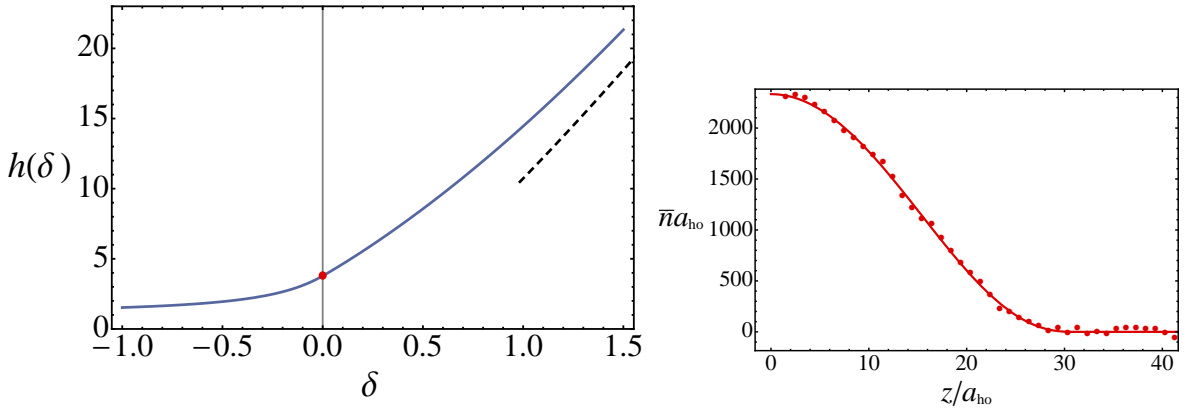


Figure 1.4: Left: experimental equation of state of the Fermi gas in the BEC-BCS crossover (1.49) (blue line). The dashed black line is the expression obtained for h by performing a Legendre transform from the LHY expression of the energy (1.38) to calculate the pressure [Nascimbène, 2010, Navon, 2011], yielding a fair agreement with the experimental EoS. The right panel is a doubly integrated density profile (red circles) of one spin state for a unitary Fermi gas, formed by a spin-balanced mixture of $|1_f\rangle - |2_f\rangle$ at 832 G containing 1.7×10^5 atoms in each spin state, fitted with the EoS (full line) of a unitary Fermi gas (red circle in left panel). In units of the harmonic oscillator length $a_{ho} = \sqrt{\hbar/m\omega_z} \simeq 10 \mu\text{m}$.

In the whole BEC-BCS crossover, the spin-balanced Fermi gas is superfluid at $T = 0$. There is no additional phase-transition between the BEC and BCS regimes (which is why it is called a crossover). On the BEC side, the critical temperature for superfluidity is weakly dependent on $a^{(o)}$. For $1/k_F a < 1$, T_c can be approximated in the BCS theory which predicts an exponential dependence on $1/k_F a$: $T_c/T_F \propto \exp(-\pi/2k_F|a|)$.

To conclude on the BEC-BCS crossover, the phase diagram of Fermi gases is not restricted to zero temperature. The finite-temperature unitary Fermi gas has been studied in depth [Nascimbène *et al.*, 2010, Ku *et al.*, 2012] and the EoS is now very precisely known in excellent agreement with a diagrammatic Monte-Carlo theory [Van Houcke *et al.*, 2012]. In addition, these studies demonstrated the existence of a phase transition to the superfluid state with a critical temperature $T_c = 0.167(13) T_F$ [Nascimbène *et al.*, 2010, Ku *et al.*, 2012, Navon *et al.*, 2013]. The nature of the normal (non-superfluid) phase is still a debated issue, thermodynamics studies indicate a Fermi-liquid behaviour [Nascimbène *et al.*, 2011], while some theories propose a ‘pseudogap’ phase induced by the pre-formation of pairs above the critical temperature. Additionally, another parameter easily tuneable in experiments is the ratio in spin states populations. In the case of imbalanced gases, an instability occurs for large imbalances destroying superfluidity. At zero-temperature this limit in terms of chemical potential imbalance is called the Clogston-Chandrasekhar limit. In a homogeneous unitary Fermi gas the critical imbalance is $x_c = 0.44$, with $x = n_\downarrow/n_\uparrow$ and for a harmonically trapped gas, this limit is given by $P_c = 0.77$, where the polarization P is de-

^(o)For atomic BECs, the corrections to T_c induced by interactions are very weak, see [Baym *et al.*, 2001] for example, and have been recently measured for an atomic BEC in a harmonic trap [Smith *et al.*, 2011].

fined by $P = (N_{\uparrow} - N_{\downarrow}) / (N_{\uparrow} + N_{\downarrow})$ [Lobo et al., 2006, Zwierlein et al., 2006, Partridge et al., 2006, Nascimbène et al., 2009].

1.6 | Superfluidity of Bose and Fermi gases

After giving an account of the thermodynamical properties of interacting Bose and Fermi gases, we turn to the description of superfluidity and its manifestations in these systems. Both interacting Bose-Einstein condensate and Fermi gases in the BEC-BCS crossover are superfluid at zero temperature, and a description of the superfluid state will be useful later in the study of a mixture of such superfluids and their relative motion.

Superfluidity in general refers to an ensemble of phenomena related to flow properties. Its most famous manifestation is ‘flow without friction’. The first experimental signatures of frictionless flow were seen as the drop of resistance in a piece of superconducting metal [Kamerlingh Onnes, 1913], and in liquid helium, Kapitza, Allen and Misener observed a drop of viscosity below 2.18 K [Kapitza, 1938, Allen and Misener, 1938]. It refers to a state in which the (super)fluid has a non-zero velocity with respect to an external body in contact with it, without any dissipation. This state is not the ground state as demonstrated in [Leggett, 2001], it is actually metastable, with a macroscopically long life-time. A spectacular consequence of flow without friction is the existence of persistent currents in a toroidal (ring shaped) geometry. Such long-lived currents were measured in superconducting rings, where their lifetime could be inferred to be longer than 10^5 years [File and Mills, 1963]. In ultracold atoms, persistent currents were observed in single-component BECs contained in a ring trap, and the life-time of the current was shown to be limited only by the lifetime of sample itself, extending up to two minutes [Ryu et al., 2007, Beattie et al., 2013].

1.6.1 Landau's criterion for superfluidity

Flow without friction is allowed in a superfluid below a certain critical velocity v_c . The famous expression of v_c obtained by Landau [Landau, 1941b, Landau, 1941a] reads:

$$v_c = \text{Min}_{\mathbf{p}} \left(\frac{\epsilon(\mathbf{p})}{p} \right) \quad (1.50)$$

where $\epsilon(\mathbf{p})$ is the dispersion relation of elementary excitations.

Let us derive this expression formally: we consider an object of mass M in contact with a superfluid and moving with respect to it at a velocity \mathbf{v} . This object is slowed-down by

the creation of an excitation in the superfluid. The initial energy and momentum in the superfluid's frame are:

$$E_i = \frac{Mv^2}{2}, \quad \mathbf{P}_i = M\mathbf{v}, \quad (1.51)$$

and the final ones:

$$E_f = \frac{Mv'^2}{2} + \epsilon(\mathbf{p}), \quad \mathbf{P}_f = M\mathbf{v}' + \mathbf{p}. \quad (1.52)$$

\mathbf{v}' is the velocity of the impurity after the creation process, \mathbf{p} is the momentum of the excitation with energy $\epsilon(\mathbf{p})$. The conservation laws^(p) lead to

$$\mathbf{p} \cdot \mathbf{v} = \frac{p^2}{2M} + \epsilon(\mathbf{p}) \quad (1.53)$$

Hence for the process to be energetically allowed the velocity of the impurity must obey:

$$v \geq v_c = \text{Min}_{\mathbf{p}} \left(\frac{\frac{p^2}{2M} + \epsilon(\mathbf{p})}{p} \right) \quad (1.54)$$

Let us first consider the excitation to be a motion of the entire superfluid. Each particle of the superfluid carries a momentum (\mathbf{q}) we then have $\mathbf{p} = N\mathbf{q}$ and $\epsilon(\mathbf{p}) = Nq^2/2m$ where N is the number of particles constituting the superfluid. Then applied to (1.54) we find the surprising result $v_c = 0$, this result in fact is in agreement with the statement that the frictionless motion of a superfluid is a metastable state. However setting in motion the entire superfluid requires a strong coupling of the object to the superfluid. For a weakly coupled object, the interaction of the object with the entire superfluid is a high-order process, the first excitations created will rather be the low-lying elementary excitations. Landau's criterion is found by considering that the object has a very high mass such that the associated term does not contribute to v_c , and we indeed finally find (1.50). This formula was obtained considering a superfluid flowing inside its container for which the limit $M \rightarrow \infty$ is valid [Landau, 1941b, Landau, 1941a]. We must differentiate it with the case of a light impurity.

Relation (1.50) applied to a weakly-interacting Bose gas where $\epsilon(\mathbf{p}) = \epsilon^B(\mathbf{p})$ is the Bogolyubov dispersion relation (1.37) leads to the well-known result that the critical velocity is the speed of sound c_b

$$v_c = c_b = \sqrt{gn/m}. \quad (1.55)$$

For the Fermi gas in the BEC-BCS crossover, there exist two excitation branches, one of them is a collective excitation with bosonic statistics. At low momenta the dispersion relation of this branch is linear:

$$\epsilon_b^F(\mathbf{p}) \underset{p \rightarrow 0}{=} p c_f, \quad (1.56)$$

where c_f is the speed of sound in the Fermi gas. Another kind of excitation is the destruction of a pair, this process forms two excitations with dispersion relation :

$$\epsilon_{qp}(\mathbf{p}) = \sqrt{\left(\frac{p^2}{2m} - \mu\right)^2 + \Delta^2}. \quad (1.57)$$

^(p)We consider here a translation-invariant system.

Since they are created in pairs, their total momentum and energy are not constrained and they form a continuum. We note the lower limit of this continuum $\epsilon_f^F(\mathbf{p}) = \epsilon_{qp}(\mathbf{q}_1) + \epsilon_{qp}(\mathbf{q}_2)$ with $\mathbf{q}_1 + \mathbf{q}_2 = \mathbf{p}$. From (1.57) one easily sees that $\epsilon_f^F(\mathbf{p}) \geq 2\Delta$ (with an equality for $p < \sqrt{2m\mu}$). Finally the Landau critical velocity in a Fermi gas is:

$$v_c = \text{Min}_{s=f,b} \left(\frac{\epsilon_s^F(\mathbf{p})}{p} \right) \quad (1.58)$$

Thus, depending on the exact dispersion relations of the two branches, $\epsilon_b^F(\mathbf{p})$ and $\epsilon_f^F(\mathbf{p})$, it can be either more favorable to create one type of excitations or the other. In a theoretical study of these elementary excitations using BCS theory, Combescot *et al.* [Combescot *et al.*, 2006] have studied the critical velocity in the crossover. They have shown that on the BEC side, the critical velocity is due to the emission of phonons, as one would expect for a BEC since the pair binding energy is large. On the BCS side, the sound velocity increases while the pair binding energy $\Delta \propto \exp(-2/\pi k_F a)$ drops and pair breaking is favored, finally the transition between these two mechanisms happens very close to the unitary limit as shown in figure 1.5.

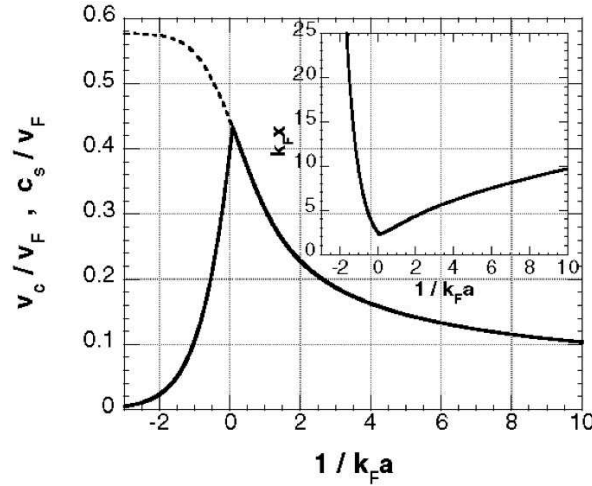


Figure 1.5: Critical velocity for (solid line) a Fermi gas as a function of $1/k_F a$ calculated using (1.58) and the dispersion relations for the elementary excitations as obtained in [Combescot *et al.*, 2006]. The sound velocity on the BCS side is shown in dashed line. (The inset shows the healing length of a Fermi superfluid in the crossover.)

In the case of a finite-mass impurity, the presence of the associated term $p^2/2M$ modifies noticeably which branch gives the lowest v_c , as shown in [Castin *et al.*, 2014] using BCS theory and the random phase approximation. Figure 1.6 (a) is a phase diagram representing the branch giving the lowest critical velocity (bosonic or fermionic) in the BEC-BCS crossover and as a function (in y axis) of M/m where M (m) is the mass of the impurity (superfluid Fermi particles). The unit on the x axis Δ/μ is equivalent to the interaction parameter $1/k_F a$ with $1/k_F a = 0$ for $\Delta/\mu = 1.162$, $1/k_F a < 0$ for $\Delta/\mu < 1.162$. In the region F the critical

velocity from (1.54) is due to fermionic excitations, in the region B_1 it is due to bosonic excitations but for a momentum p where $\epsilon_b^P(p)$ is not linear anymore, it is rather very close to $\epsilon_f^F(p)$. Last, in the region B_2 it is due to bosonic excitations and the linear part dominates, that is $v_c = c_f$.

Taking the limit $M \rightarrow \infty$ we find the result of [Combescot et al., 2006] that the critical velocity changes from the fermionic excitation branch to the speed of sound close to unitarity ($\Delta/\mu = 1.162$), on the other hand when the impurity has a mass M close to that of the superfluid particles, the critical velocity is given by the speed of sound in a much broader region of the crossover.

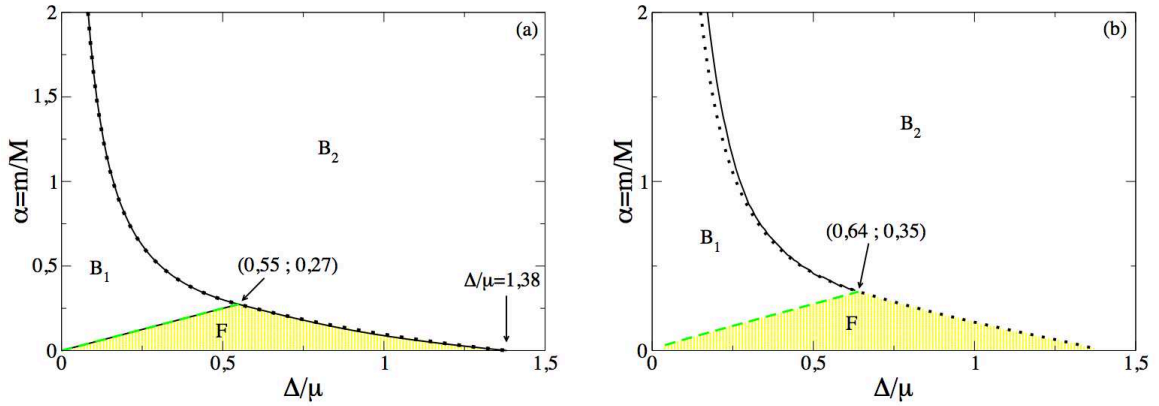


Figure 1.6: Left: phase diagram for the critical velocity of an impurity embedded in a Fermi superfluid. On the horizontal axis: Δ/μ equivalent to $1/k_F a_f$ ($1/k_F a_f > 0$ for $\Delta/\mu > 1.162$). Vertical axis: mass ratio $\alpha = m/M$ where M (m) is the mass of the impurity (superfluid Fermi particles). In the region named B_2 we have $v_c = c$, in the B_1 region the critical velocity is due to bosonic excitations but in a momentum range where their dispersion relation is very close to the fermionic excitations's dispersion relation. In the F region (yellow), v_c is given by fermionic excitations. Right: critical velocity for a BEC in a Fermi superfluid, the regions are labelled identically. The chemical potential of the BEC μ_b is weak compared to the Fermi energy of the fermions, $\mu_b/E_F = 0.1$.

1.6.2 Landau's criterion for a mixture of Bose and Fermi superfluids

In the last chapter of this thesis we present the first experimental results on the critical velocity of motion for a BEC moving inside a Fermi superfluid. Let us calculate this critical velocity using Landau's argument, we thus calculate the minimal velocity for the emission of elementary excitation, valid for weakly coupled superfluids. We note $\epsilon^B(\mathbf{p})$ the dispersion relation of excitations in the BEC and $\epsilon_s^F(\mathbf{p})$ that in the Fermi superfluid where s refers to the two possible branches. We consider two superfluids in relative motion with velocity v . The slowing-down of the whole superfluids is not allowed in the weak coupling limit, such that v is not changed in the emission process. We write the initial and final conditions in the

frame of the Fermi superfluid:

$$E_i = \frac{M_B v^2}{2}, \quad \mathbf{P}_i = M_B \mathbf{v} \quad (1.59)$$

$$E_f = \frac{M_B v^2}{2} + \epsilon_s^F(\mathbf{p}) + \epsilon^B(\mathbf{q}) + \mathbf{q} \cdot \mathbf{v}, \quad \mathbf{P}_f = M_B \mathbf{v} + \mathbf{q} + \mathbf{p}. \quad (1.60)$$

M_B is the total mass of the Bose superfluid, the term $\mathbf{q} \cdot \mathbf{v}$ is simply the Doppler shift of the excitation in the BEC. The conservation laws then lead to the critical velocity:

$$v_c = \text{Min}_{\substack{\mathbf{p} \\ s=f,b}} \left(\frac{\epsilon^B(\mathbf{p}) + \epsilon_s^F(\mathbf{p})}{p} \right). \quad (1.61)$$

We see that this critical velocity is the same as (1.54) but replacing a free particle energy by the dispersion relation of the other superfluid. The analysis of the critical velocity of a BEC moving inside a Fermi superfluid can be thus obtained by expansion of the analysis of a finite-mass impurity, this is performed in [Castin *et al.*, 2014]. The result is displayed in 1.6 (b), for the case of a BEC with a chemical potential $\mu_b = E_F/10$ where E_F is the local Fermi energy of the Fermi superfluid. In this limit the phase diagram is weakly modified, with respect to a finite mass impurity. On the BEC side of the crossover, the first excitations created are phonons, leading to a critical velocity from (1.61) $v_c = c_b + c_f$.

1.6.3 Beyond Landau's criterion

The critical velocity calculated from Landau's criterion must be handled with care. First it describes a homogeneous superfluid. Already in an inhomogeneous system such as a trapped gas, the geometry of the superfluid modifies the dispersion relation of elementary excitations with respect to the homogeneous case [Zaremba, 1998, Stringari, 1998]. In turn this reduces strongly the critical velocity compared to the naive expectation of the sound velocity given the density n at the center of the cloud: $v_c \neq \sqrt{gn(0)/m}$ [Fedichev and Shlyapnikov, 2001]. So already, taking finite-size and geometry effects into account changes the expected value of the critical velocity, however this is still within the scope of Landau's criterion.

As said before, Landau's criterion is valid in the weak coupling limit. Experimentally, the 'impurities' are rarely weakly coupled. For a strong coupling, higher-order excitations can be created. Notoriously 'hydrodynamic' excitations such as vortices and solitons can appear. Creation of vortices or solitons is dependent on the geometry of the problem, if we consider a superfluid moving inside a container, its proportions and form will influence the creation of defects. Identically the shape and size of a moving defect will determine its critical velocity [Frisch *et al.*, 1992]. It is known for instance that in most cases critical velocities measured in liquid helium cannot be described by Landau's criterion and that turbulence sets in, see for example [Wilks and Betts, 1987]. Only in experiments performed with moving ions inside ^4He , the critical velocity measured is in agreement with Landau's criterion, where the dispersion relation presents a roton minimum [Allum *et al.*, 1976, Allum *et al.*, 1977]. An

argument originally formulated by Feynman treats a vortex or a vortex ring as an elementary excitation (replacing the momentum \mathbf{p} by the moment of inertia I) in order to salvage Landau's criterion [Feynman, 1955]. It is valid only in a cylindrical geometry and in general this cannot be applied and a specific hydrodynamic analysis is required.

In dilute ultracold gases, homogeneous systems have been created only very recently [Gaunt *et al.*, 2013] and so far all experiments studying superfluid flow have been performed on inhomogeneous gases. Most searches for superfluid flow have been performed by moving an impurity created by a laser beam (with infinite effective mass) focused at the position of the ultracold gas. The laser creates a potential usually large with respect to inter-particle distance, and the impurity created this is not necessarily weakly coupled. The local density approximation can be used to calculate the local density in the region where the laser creates an additional potential and then extract the local critical velocity [Watanabe *et al.*, 2009] from Landau's criterion. A possible instability due to vortex creation can be investigated analytically in simple cases [Frisch *et al.*, 1992] or using for instance hydrodynamic numerical simulations [Stießberger and Zwerger, 2000]. We review the experimental results obtained until present in the following.

1.6.4 Some experiments on a critical velocity in superfluid dilute gases

On dilute Bose-Einstein condensates, a critical velocity for the motion of a laser impurity has been first observed in [Raman *et al.*, 1999, Onofrio *et al.*, 2000, Raman *et al.*, 2001]. The observed critical velocity lies around $0.3 c_{b,0}$ where $c_{b,0}$ is the sound velocity at the center of the cloud. Considering the inhomogeneity of the gas perturbed by the laser, this value of the critical velocity did not allow for a comparison with theory and so could not determine the dissipation mechanism. Other measurements realized on a superfluid ring stirred by a laser showed the influence of the barrier height on the critical velocity in good agreement with a model using Landau's criterion and accounting for a reduced density at the barrier position [Wright *et al.*, 2013]. The creation of vortices by a moving laser beam was first observed in [Inouye *et al.*, 2001]. In an elegant experiment, Neely *et al.* demonstrated the formation of vortices by a moving laser impurity in an oblate geometry [Neely *et al.*, 2010] with a critical velocity in very good agreement with numerical simulations ($v_c \simeq 0.1c$). The creation of solitons by a moving elongated potential barrier was observed in [Engels and Atherton, 2007]. Finally, in a two-dimensional Bose gas the existence of a critical velocity has been experimentally proved by stirring a laser at constant radius, the two-dimensional geometry allowing to probe a constant density [Desbuquois *et al.*, 2012].

It is clear in the experiments on Bose-Einstein Condensates listed above that the usage of a laser as an impurity does not realize the weak-coupling limit required for Landau's criterion to be applicable. To make a more weakly coupled impurity, [Chikkatur *et al.*, 2000] have used a stimulated Raman process to turn condensate atoms into impurities expelled by the trapping potential. They have measured the energy dissipated by the impurities as a

function of their velocity, and observed a dramatic reduction for velocities under the speed of sound of the condensate. The critical velocity of microscopic, weakly-coupled impurities is thus in agreement with Landau's criterion, identically to the case of liquid ^4He where the motion of ions agreed with this criterion.

In ultracold Fermi gases, two measurements of a critical velocity have been performed, one using a moving one-dimensional optical lattice creating a periodic potential [Miller *et al.*, 2007] in an elongated gas and very recently a tightly-focused attractive laser beam stirring a gas in an oblate trap [Weimer *et al.*, 2014]. In the first reference, the measured critical velocity at unitarity is in rough agreement with the Landau criterion predictions displayed in figure 1.5. The qualitative behavior in the crossover agrees with the different mechanisms for damping between BEC and BCS sides. The measured v_c drops sharply on the BCS side as one expects for pair breaking since the gap is exponentially reduced and is slightly reduced on the BEC side in agreement with phononic excitations. The setup used in [Weimer *et al.*, 2014] allowed for a better control of the systematic errors rendering possible a quantitative comparison with theory from [Combescot *et al.*, 2006]. In the whole crossover, the measured critical velocity is reduced with respect to theory, a feature they attribute to probing lower density regions along the stirrer axis, which is well accounted-for by numerical simulations on the BEC side. Up to this reduction, in the crossover the critical velocity follows the theoretical expectations.

1.6.5 Other hallmarks of superfluidity

A striking phenomenon due to superfluidity is the quantization of circulation in a rotating superfluid:

$$\oint \mathbf{v} \cdot d\mathbf{l} = p h/m, \quad p \in \mathbb{Z}. \quad (1.62)$$

This is due to the fact that the velocity field of a superfluid is related to the phase ϕ of the order parameter^(q) $\mathbf{v} = \nabla\phi h/m$. Since the phase is single-valued up to factors 2π , circulation is quantized, giving rise to vortices in rotating superfluids. Vortices in rotating dilute Bose and Fermi gases have been observed [Madison *et al.*, 2000, Zwierlein *et al.*, 2005], confirming the superfluid nature of these systems.

Another hallmark of superfluidity is the existence of second sound. This second sound mode, in addition to the usual 'first sound', is predicted by two-fluids hydrodynamics treating the normal and superfluid fraction as separate fluids, the superfluid fraction carrying no entropy. These solutions depend on the thermodynamic properties of the superfluid and provide a sensitive test for measurements of the equation of state. It is

^(q)The order parameter characterizing the superfluid phase is $\langle\psi\rangle$ for bosons as we have seen, for fermions it is $\langle\psi_\uparrow\psi_\downarrow\rangle$ [Leggett, 2006]. To connect to the Bose case, the fermion order parameter can be seen as the mean value of the annihilation operator for a pair.

worth noting that in the case of liquid helium, since $C_p \simeq C_V^{(r)}$, the thermal expansion coefficient $\alpha = -\frac{1}{n} \left(\frac{\partial n}{\partial T} \right)_P$ is small and first and second sound are two uncoupled modes. In dilute gases this is not true so a coupling between these modes arises [Hu *et al.*, 2010]. As a second consequence, the second sound excitation carries a density modulation enabling its observation by usual imaging techniques. This way second sound excitations have been unambiguously observed recently in a unitary Fermi gas [Sidorenkov *et al.*, 2013]. These measurements were in good agreement with the previously measured EoS and also provide the best measurement so far for the superfluid fraction.

Conclusion

To summarize this chapter, we have aimed at presenting ultracold Bose and Fermi gases, from a point of view that will serve for the results presented in the following chapters. We presented the theory of ultracold Bose and Fermi gases that are studied in our experiments. In the final section we gave a special attention to the superfluidity of these gases because the final part of this work presents novel studies of features of superfluidity in a mixture of Bose and Fermi superfluids. In the next chapter, we detail how such systems are obtained experimentally on our setup.

^(r) $C_p = \left(\frac{\partial U}{\partial T} \right)_P, C_V = \left(\frac{\partial U}{\partial T} \right)_V$

Chapter 2 |

Experimental set-up

“Young people must break machines to learn how to use them.” Henry Cavendish

The experimental set-up on which we prepare quantum degenerate gases of lithium has been running now for more than 15 years and several generations of PhD students. The details of the apparatus have been presented in many theses starting from Gabriele Ferrari’s in 2000. Thorough presentations of the set-up can be found in [Ferrari, 2000, Schreck, 2002] and [Tarruell, 2009]. As during my thesis we have not modified profoundly the apparatus, we will review the main elements. A later chapter is dedicated to a laser cooling scheme that was first implemented on potassium by the other team of the LKB ultracold Fermi group and that we have transposed to lithium atoms.

2.1 | Lithium isotopes, atomic structure

Lithium has two stable isotopes ${}^7\text{Li}$, a boson and ${}^6\text{Li}$, a fermion. The natural abundances are 92.5% for ${}^7\text{Li}$ and 7.5% for ${}^6\text{Li}$, their masses $m_6 = 6.015 \text{ u}$ and $m_7 = 7.016 \text{ u}$ with u the atomic mass unit $\text{u} = 1.661 \times 10^{-27} \text{ kg}$ [Heavner et al., 2001, Nagy et al., 2006].

Lithium is the third element in the periodic table, and the lightest of the alkali metals (considering that Hydrogen is not an alkali). Alkalis have a single electron in their outermost electronic shell (a s -shell), so they have a simple atomic structure. ${}^6\text{Li}$ has a nuclear spin of $I = 1$, ${}^7\text{Li}$ of $I = 3/2$. The energy levels at zero magnetic field of ${}^6\text{Li}$ and ${}^7\text{Li}$ are represented in figure 2.1, the optical transition from the $2s$ orbital to the $2p$ is at 671 nm. The fine structure splitting between the $2^2P_{1/2}$ ^(a) and the $2^2P_{3/2}$ state is about 10 GHz. Incidentally, the isotope shift of the $2S \rightarrow 2P$ transition is also of 10 GHz, and the D_1 line ($2^2S_{1/2} \rightarrow 2^2P_{1/2}$) of ${}^7\text{Li}$ is almost tuned with the D_2 line ($2^2S_{1/2} \rightarrow 2^2P_{3/2}$) of ${}^6\text{Li}$. The natural linewidth of the optical transitions is $\Gamma = 2\pi \times 5.9 \text{ MHz}$ for both isotopes, from which we can conclude that the hyperfine levels of the $2^2P_{3/2}$ are not resolved since their splitting is smaller than the linewidth Γ (see fig. 2.1).

^(a)spectroscopic notation: $n^{2s+1}L_J$, n is the principal quantum number, s is the total electrons spin (1/2 for Li), L is the orbital angular momentum of the electrons and $J = L + S$, finally $F = I + J$.

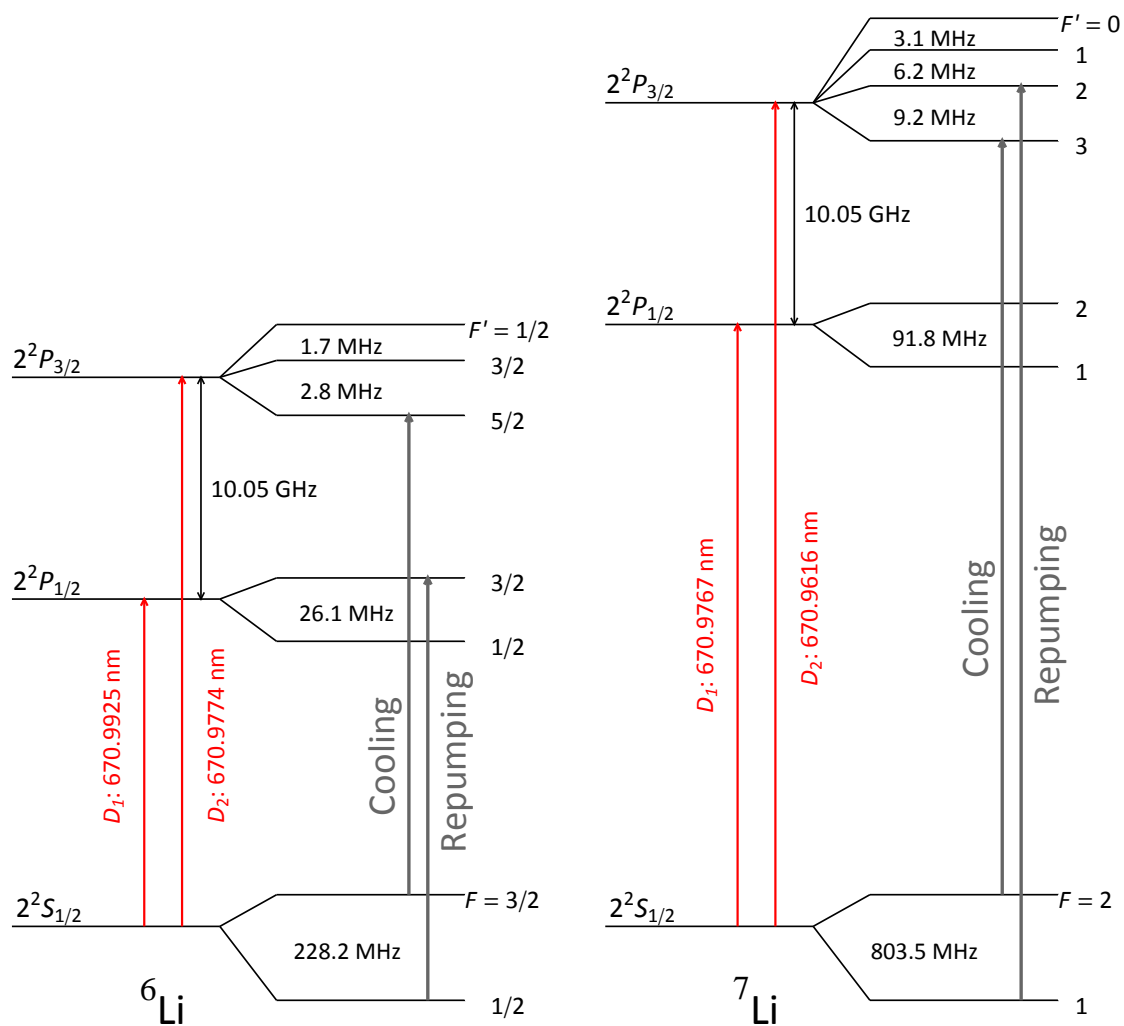


Figure 2.1: Level schemes of ${}^7\text{Li}$ and ${}^6\text{Li}$, the most accurate measurements of the optical transitions, fine and hyperfine splittings can be found in [Sansonetti et al., 2011]. Note the near perfect tuning between the ${}^7\text{Li}$ D_1 and ${}^6\text{Li}$ D_2 lines. The transitions used for cooling and repumping in the magneto-optical trap are indicated in grey, see main text.

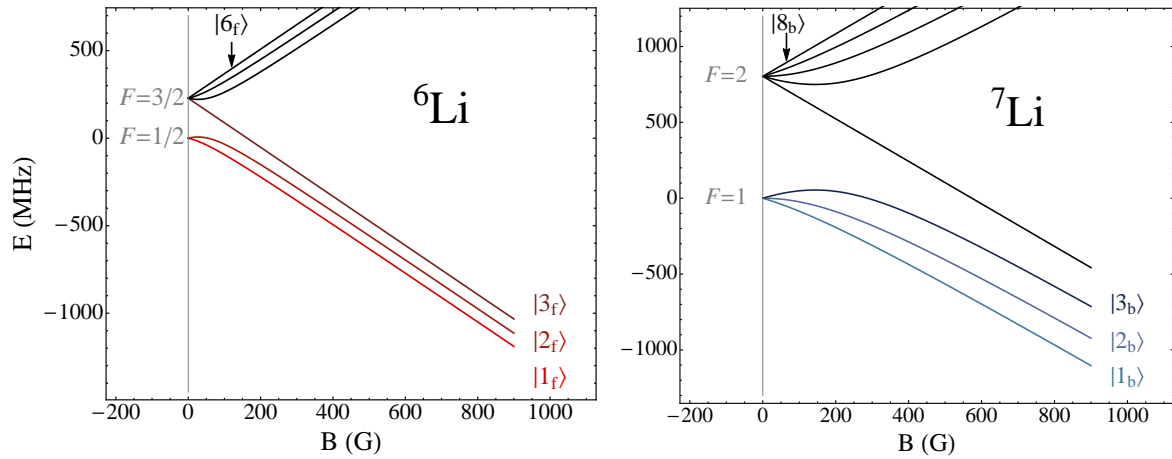


Figure 2.2: Magnetic field dependence of the energy levels of ${}^6\text{Li}$ (left) and ${}^7\text{Li}$ (right). The energy reference is taken to be the energy of the $F = 1/2$, $F = 1$ manifolds at zero field. For simplicity the states are labeled here $|1_s\rangle$, $|2_s\rangle$, ... and the index s indicates the isotope (b for ${}^7\text{Li}$ and f for ${}^6\text{Li}$). At low field, $|1_f\rangle$ connects to $|F = 1/2, m_F = 1/2\rangle$ and $|6_f\rangle$ to $|F = 3/2, m_F = 3/2\rangle$ for ${}^6\text{Li}$ and for ${}^7\text{Li}$: $|1_b\rangle$ connects to $|F = 1, m_F = 1\rangle$ and $|8_b\rangle$ to $|F = 2, m_F = 2\rangle$. During the magnetic trapping stages, the atoms are polarized in $|6_f\rangle$ and $|8_b\rangle$. At the beginning of the optical trapping stage, they are transferred to the absolute ground states $|1_f\rangle$ and $|1_b\rangle$ by a radio-frequency rapid adiabatic passage.

2.2 | Laser cooling

2.2.1 Laser system

The laser system is based on a master-oscillator – power-amplifier scheme, we use three master lasers for frequency references, locked using saturated-absorption spectroscopy. One master laser is locked on the D_2 line of ${}^7\text{Li}$. Two other masters are locked on ${}^6\text{Li}$ transitions, one on the D_1 line and one on the D_2 line, the latter is also used for a frequency reference close to the D_1 transition of ${}^7\text{Li}$. The lasers on the experiment are laser diodes, originally built for DVD drives^(b). The diodes have a spectrum centered at 660 nm and can output in normal conditions up to 120 mW in continuous mode. To obtain light on the transitions of lithium at 671 nm, the diodes are heated-up to approximately 70 °C to dilate the diode’s cavity, without reducing significantly the diode’s performances.

The power-amplifying diodes are injection-locked to the master lasers. To mitigate the effects of drifts of the geometric alignment of the laser beams, all laser outputs are coupled in optical fibers, decoupling the alignments of the input and output beams. This fiber coupling causes an optical power loss from 30% to 50% depending on the quality of the fiber injection. To compensate for this loss we use the diodes at or above the limit of their power ability, shortening their lifetime. To improve the stability of the experiment, we

^(b)Model HL6545MG from Hitachi, now available at Thorlabs.

have increased the power available in some beams where power is crucial using tapered amplifiers (TA).

2.2.2 The lithium source

Our samples are loaded from a saturated vapor in an oven where lithium (with natural abundances) is kept at 390 °C. At this temperature lithium is liquid^(c), and the saturated vapor pressure is sufficient. To cool and trap lithium to degeneracy temperatures, we first use laser cooling, addressing its atomic transitions. From the oven, the vapor is collimated using a tube of length 9 cm and inner diameter 6 mm. The tube is heated-up at a temperature of 510 °C at the junction with the oven and 190 °C on its output end. The temperature in the tube is thus above the melting point avoiding solid chunks from forming^(d).

2.2.3 Double Magneto-Optical trap

At the output of the tube we use a spin-flip Zeeman slower, with cooling light on the D_2 line of both isotopes. At the end of the Zeeman slower, the atoms have a mean velocity of about 50 m/s. From this jet we load a magneto-optical trap (MOT) of both isotopes. By turning on or off their respective cooling light, we can also selectively trap only ${}^6\text{Li}$ or ${}^7\text{Li}$ in the MOT. The MOT is performed in a glass cell, by three pairs of counter-propagating beams, represented in figure 2.3. The cooling light for ${}^7\text{Li}$ and ${}^6\text{Li}$ is tuned to the D_2 line and we use the cycling transitions $F = 2 \rightarrow F' = 3$ and $F = 3/2 \rightarrow F' = 5/2$ for ${}^7\text{Li}$ and ${}^6\text{Li}$ respectively (these transitions are used in the Zeeman slower as well). Due to the rather narrow hyperfine structure of the excited state, the open transitions $F = 2 \rightarrow F' = 2$ and $F = 3/2 \rightarrow F' = 3/2$ are also excited and a strong repumper is needed to pump atoms fallen into the lower hyperfine manifolds ($F = 1$, $F = 1/2$) back in the cooling cycle. For ${}^6\text{Li}$, this repumping is done using the D_1 transition $F = 1/2 \rightarrow F' = 3/2$. To avoid having near resonant light for ${}^6\text{Li}$, we repump ${}^7\text{Li}$ using the D_2 $F = 1, F' = 2$ transition, as indicated in figure 2.1^(e). The cooling beam is detuned by $\delta = -5\Gamma$ for ${}^7\text{Li}$ and -4Γ for ${}^6\text{Li}$, the repumpers are detuned respectively by -4Γ and -2Γ . All frequencies are mixed in each beam, which have a $1/e^2$ diameter of $\simeq 1.5$ cm. The maximum intensity per frequency is $I \simeq 3.5$ mW/cm², except for the ${}^7\text{Li}$ cooling frequency which is amplified by a TA and is about $I \simeq 5.5$ mW/cm². This corresponds to $I \simeq I'_{\text{sat}}/50$ for the cooling beams, where $I'_{\text{sat}} = I_{\text{sat}}(1 + (2\delta/\Gamma)^2)$ is the saturation intensity at the beams detuning and

^(c)the melting temperature is 180.6 °C and the boiling point is at 1342 °C.

^(d)Some liquid drops can form inside the tube, in principle the temperature gradient is such that these drop move opposite to the gradient thanks to a temperature-dependent surface tension [Tarruell, 2009]. However we have run several times into a clogging of this tube, the solution in this case is to heat the tube to temperatures as high as 600 °C to evaporate the liquid.

^(e)The repumping transitions in the spin-flip region of the Zeeman slower are identical as in the MOT

$$I_{\text{sat}} = 2.4 \text{ mW/cm}^2.$$

In normal conditions, the magneto-optical trap is loaded in 40 s and contains a few 10^9 ${}^7\text{Li}$ atoms and $\simeq 10^8$ ${}^6\text{Li}$ atoms^(f). The temperature of the two isotopes in the MOT is about 3 mK, roughly the same for the two isotopes. Following the MOT stage, we perform a compressed-MOT (CMOT), which consists in reducing the cooling beams detunings down to -2Γ in 8 ms and a lowering of the repumpers intensity to $I = 0$. This results in a denser cloud of atoms, 100% pumped in the lowest hyperfine manifolds. The temperature of this cloud is $600 \mu\text{K}$ for both isotopes, the intensities and frequencies are chosen to minimize this temperature under the constraint of keeping 100% of the atoms. This temperature is higher than the lowest temperature expected for Doppler cooling in the simplified model of a two-level atom: $T_D = \hbar\Gamma/2k_B = 140 \mu\text{K}$. The reason for this is that the two-level model is too simple because the upper hyperfine states are unresolved, furthermore at high density multiple photon scattering takes places.

The low cooling efficiency for lithium represents an experimental difficulty in the prospect of cooling to quantum degeneracy. It imposes high capture efficiency for the trapping potential collecting the atoms after the laser cooling stage. To improve the laser cooling efficiency and provide a better starting point for the subsequent evaporative cooling, several solutions exist. One can use different transitions, with a narrower linewidth, this solution was implemented in [Duarte *et al.*, 2011] using the $2S_{1/2} \rightarrow 3P_{3/2}$ transition, with a wavelength of $\lambda = 323 \text{ nm}$ and a linewidth $\Gamma = 2\pi \times 754 \text{ kHz}$. This has proved successful, but requires a new laser system at a wavelength at which lasers have weak power and short lifetimes. To overcome these limitations, we have implemented and investigated a new laser cooling scheme addressing the D_1 line at $\lambda = 671 \text{ nm}$, developed for potassium by the Fermix team in our group [Rio Fernandes *et al.*, 2012]. We dedicated a chapter to present our work. However due to the usage of two isotopes and the close tuning of ${}^7\text{Li}$ and ${}^6\text{Li}$ lines, the full implementation of this scheme on our experiment would have implied important changes to our laser system. Since the experiment was functional without this scheme we have decided not to use it, but a number of experimental groups have now implemented our method [Salomon *et al.*, 2013, Nath *et al.*, 2013, Burchianti *et al.*, 2014].

2.2.4 Optical pumping

At the end of the MOT – CMOT sequence, the atoms are polarized in the lowest hyperfine manifolds. The next stage of the sequence consists in magnetic trapping. Maxwell's equations forbid the creation of trapping potentials by maxima of magnetic field. As a consequence, only internal states which energy increases with magnetic field can be trapped purely magnetically ("low field seekers"). In the lowest hyperfine manifolds, one state per isotope (the $|F = 1, m_F = -1\rangle$ for ${}^7\text{Li}$ and the $|F = 1/2, m_F = -1/2\rangle$ for ${}^6\text{Li}$) has a positive

^(f)When the oven tube is clogged, loading can take up to 100 s and the numbers are divided by $\simeq 5$.

slope as shown in figure 2.2. However the maximum depth realizable by a magnetic trap is too low: $300 \mu\text{K}$ for ${}^6\text{Li}$, 2.6 mK for ${}^7\text{Li}$ and these states are unsuitable for magnetic trapping. We therefore have to transfer the atoms to the upper hyperfine manifold in which we can realize very deep traps. Furthermore we need to use internal states which are protected against inelastic collisions, this is ensured using the maximally-stretched states : $|F = 2, m_F = 2\rangle$ ($|8_b\rangle$) and $|F = 3/2, m_F = 3/2\rangle^{(g)}$ ($|6_f\rangle$). We polarize the atoms in these states by an optical-pumping sequence. During this sequence, we use a beam in which two frequencies are mixed with σ^+ polarization and a weak magnetic field (10 G) parallel to the beam propagation axis. One frequency realizes the ‘hyperfine pumping’ of ${}^7\text{Li}$, transferring the atoms from $F = 1$ to $F = 2$, with a frequency tuned to the $F = 1 \rightarrow F' = 2$ D_2 transition at zero field. The role of the other frequency is twofold, first it pumps ${}^7\text{Li}$ in the $|2, 2\rangle$ Zeeman sub-level, second it does the hyperfine pumping for ${}^6\text{Li}$ ($F = 1/2$ to $F' = 3/2$). The optimal frequency (maximizing the pumping efficiency on both isotopes) of this second beam is detuned by -45 MHz from the $F = 2 \rightarrow F' = 2$ D_1 transition of ${}^7\text{Li}$ and 25 MHz $F = 1/2 \rightarrow F' = 3/2$ D_2 transition for ${}^6\text{Li}$. ${}^6\text{Li}$ is not polarized in the $|3/2, 3/2\rangle$, because the number of ${}^6\text{Li}$ atoms is not a limiting factor and the remaining atoms in the other sublevels are expelled in the later stages. The optical pumping sequence lasts $300 \mu\text{s}$, the beam has a $1/e^2$ radius of 5 mm on the atoms and a total power of 3 mW per frequency.

2.3 | Magnetic trapping and radio-frequency evaporation

2.3.1 Quadrupole trap, magnetic transport and transfer to the Ioffe-Pritchard Trap

Once the atoms are optically pumped, a quadrupole magnetic trap is turned-on in 2 ms using the MOT coils with opposite currents between the coils. The atoms are then transported in the vertical direction to a small appendage of the glass cell see figure 2.3. This transport is done with two sets of coils: the MOT coils and the Feshbach coils. The zero of the magnetic field is moved by decreasing current in the MOT coils to zero and simultaneously ramping up current in the Feshbach coils, in 500 ms . At the end of transport the atoms lie in the center of the Feshbach coils pair, the overall efficiency of this transport is about 40% , most of the losses are due to the cutting of the density distribution by the appendage walls.

From the quadrupole trap created by the Feshbach coils, the atoms are transferred to a Ioffe-Pritchard trap. This trap is realized by four Ioffe bars which generate a strong field gradient confining the atoms in the radial direction. The axial confinement is provided by the Pinch coils that create a curvature of the magnetic field along the trap symmetry axis.

^(g)By conservation of angular momentum, the stretched states are protected against spin-relaxation during a collision.

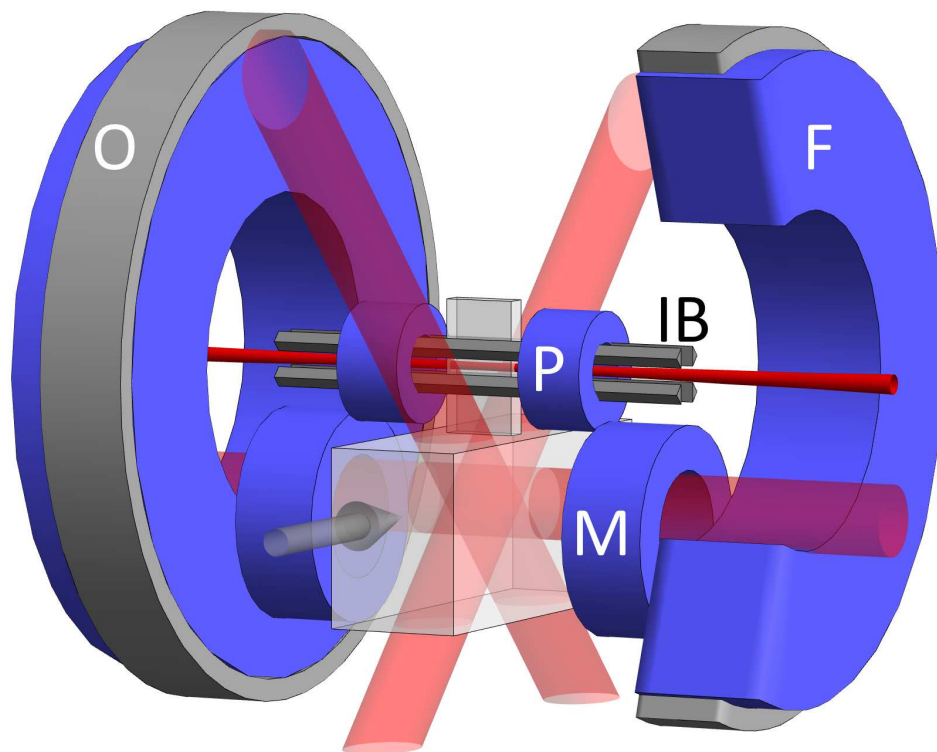


Figure 2.3: Scheme of the experiment in the glass cell region, the MOT coils (M) lie in the lower part of the cell where the atoms are collected from the Zeeman slower jet (grey arrow). The MOT beams are shown in light red. The Pinch (P), Feshbach and Offset (O) coils (F) are centered on the appendage,. The Ioffe bars (IB) create a strong confinement in the radial direction (perpendicular to the bars and the symmetry axis of the Feshbach and Pinch coils). The dipole trap laser propagates along the long direction of the upper trap, shown in opaque red.

The Feshbach coils can also be used (with parallel currents) to adjust the field offset, and an additional pair of coils: the Offset coils are designed to finely adjust this offset. The transfer from the quadrupole trap to the Ioffe-Pritchard trap cannot be done adiabatically since it involves field-reversals in some regions. This transfer is done by an instantaneous turn-on of the Ioffe bars' current, followed by a fast switch-on of the Pinch coils. The efficiency of this transfer is hard to quantify because due to the large size and high optical density of the cloud at this stage, we cannot count the atom number reliably.

2.3.2 Doppler cooling of ${}^7\text{Li}$

Once the atoms are confined in the Ioffe-Pritchard trap, the ratio between the currents in the Pinch and Feshbach coils can be varied to adjust the offset field and the confinement.

In the tightly confined Ioffe trap, the cloud has an initial temperature of $T \simeq 3$ mK. Unfortunately, the collisional cross-section of ${}^7\text{Li}$ is cancelled at momenta corresponding to a temperature of 6 mK and is still weak at 3 mK [Tarruell, 2009]. The collision rate γ is given by

$$\gamma = n\sigma v, \quad (2.1)$$

for one atom with velocity v in a cloud of density n , σ is the scattering cross-section. So a low scattering cross-section results in low collision rates and very slow thermalization, whereas a fast thermalization is essential for the success of evaporative cooling.

To solve this problem we use the last part of laser cooling on ${}^7\text{Li}$ in the sequence: a simple Doppler cooling. This cooling is implemented with a single propagating beam in the axial direction detuned to the red of the $F = 2, m_F = 2 \rightarrow F' = 3, m_F = 3 D_2$ transition, with an adjustable polarization. The use of a single propagating beam is allowed since the quadrupole trap redistributes partially the momentum in three dimensions. Since the direction and amplitude of the magnetic field vary in space, so does the energy of the internal levels of the atoms. The right detuning for Doppler cooling in these conditions is thus rather complex to calculate and we optimize empirically the polarization, power and detuning of the cooling light. Doppler cooling cools down to temperatures of about 300 μK , with a loss of 25 % of the ${}^7\text{Li}$ atoms, it is essential for an efficient evaporation.

2.3.3 Radio-frequency evaporative cooling of ${}^7\text{Li}$

After Doppler cooling, we can safely start the evaporation of ${}^7\text{Li}$. This evaporation is done with a radio-frequency knife tuned on the transition $|2, 2\rangle \rightarrow |1, 1\rangle (|8_b\rangle \rightarrow |1_b\rangle)$, the energetic atoms turned into the $|1, 1\rangle$ state are expelled by the magnetic field. The frequency of this transition is much higher than the ${}^6\text{Li}$ hyperfine splitting (228 MHz) and is thus selective on ${}^7\text{Li}$. ${}^6\text{Li}$ is then sympathetically cooled by collisions with ${}^7\text{Li}$, with no loss of ${}^6\text{Li}$ required. This sympathetic cooling is a very efficient way of producing high number cold samples of

${}^6\text{Li}$, it circumvents the necessity to have two fermionic spin states present to allow for s-wave collisions. Sympathetic cooling can also be implemented using a second species as a coolant.

Radio-frequency evaporation is performed in 22 s, lowering the frequency from 1050 MHz down to 840 MHz. The temperatures and numbers in the final state are as follows: when ${}^6\text{Li}$ is absent we trap up to 2.5×10^6 ${}^7\text{Li}$ atoms, at a temperature of $8 \mu\text{K}$. When ${}^6\text{Li}$ is present, since it is initially in strong minority, it does not impede evaporative cooling of ${}^7\text{Li}$ at the beginning of evaporative cooling, however when the numbers of ${}^7\text{Li}$ become comparable to that of ${}^6\text{Li}$, the thermal load it represents is higher than what the heat capacity of ${}^7\text{Li}$ can take out and ${}^7\text{Li}$ numbers drop sharply with little decrease in temperature. The amount of ${}^6\text{Li}$ in the Ioffe trap and thus the final temperature achievable can be freely adjusted by varying the power of the ${}^6\text{Li}$ cooling light. In normal conditions we have up to 2.5×10^6 ${}^6\text{Li}$ atoms, in equilibrium with 5×10^5 ${}^7\text{Li}$ atoms at a temperature of $12 \mu\text{K}$. The temperatures quoted are for a Ioffe trap with frequencies $\omega_r = 3.1 \text{ kHz}$, $\omega_z = 70 \text{ Hz}$ ^(h). Using these frequencies the phase space densities at the center of the cloud $n(0)\lambda_{\text{dB}}^3 = N(\hbar\omega/k_{\text{B}}T)^3$ are: $\simeq 10^{-1}$ for ${}^7\text{Li}$ alone, and for the mixture : $\simeq 10^{-1}$ for ${}^6\text{Li}$ and $\simeq 2 \times 10^{-2}$ for ${}^7\text{Li}$.

2.4 | The hybrid optical dipole - magnetic trap (ODT)

The phase space densities at the end of evaporation in the Ioffe-Pritchard trap are close to quantum degeneracy, and evaporating more we could reach the Bose-Einstein condensation threshold for ${}^7\text{Li}$. But since the background scattering length in the $|2, 2\rangle$ state is negative : $a_{\text{bg}} = -27 a_0$, reaching this threshold would result in a collapse. Furthermore, in the Ioffe trap, the magnetic field offset and the trap confinement cannot be adjusted independently. For these reasons, we transfer the atomic clouds to a hybrid optical – magnetic trap (dipole trap or ODT).

The optical trapping relies on the dipole force [Grimm *et al.*, 2000], which dominates at large detunings over the radiation pressure force used for laser cooling. The dipole potential takes the form

$$U_{\text{dip}} = \frac{3\pi c^2 \Gamma}{2\omega_0^3 \Delta} I(\mathbf{r}), \quad (2.2)$$

where c is the speed of light in vacuum, ω_0 is the bare frequency of the atom's transition with linewidth Γ , $\Delta = \omega_1 - \omega_0$ is the light detuning and $I(\mathbf{r})$ is the light intensity profile. For our trap we use an Ytterbium fiber laser with wavelength $\lambda_1 = 2\pi c/\omega_1 = 1073 \text{ nm}$, in a gaussian TEM_{00} mode:

$$I(\mathbf{r}) = \frac{2P}{\pi w(z)^2} e^{-2r^2/w(z)^2} \quad (2.3)$$

where P is the total laser power and $w(z)$ is the $1/e^2$ radius of the beam at position z along

^(h)These frequencies have not been measured for a long time and might have drifted since then.

the propagation axis. $w(z)$ is given by the laser waist at focus w_0 : $w(z) = w_0\sqrt{1 + (z/z_R)^2}$, ($z_R = \pi w_0^2/2\lambda$). The potential created is attractive ($\Delta < 0$) and cylindrically symmetric. Close to the focus ($r \ll w_0, z \ll z_R$), it takes the harmonic form:

$$U_{\text{dip}} \simeq -U_0 + \frac{1}{2}m(\omega_r^2 r^2 + \omega_z^2 z^2) \quad (2.4)$$

where $U_0 = 3c^2\Gamma P/2\omega_0^3|\Delta|w_0^2$ is the potential depth, and the frequencies are $\omega_r = \sqrt{4U_0/mw_0^2}$, $\omega_z = \omega_r\lambda/\sqrt{2\pi}w_0$. The waist of our laser is

$$w_0 = 27(2) \mu\text{m},$$

so that using our parameters, the axial trapping frequency is very weak at low power ($\omega_z/2\pi < 24$ Hz for a laser power $P < 1$ W). To increase the confinement we add an axial magnetic trapping created by the Pinch coils. To create an attractive potential we can either trap low-field seekers with a field minimum, or create a field saddle-point with a maximum in the axial direction and a minimum transversely. This saddle potential is created by running an opposite current in the Feshbach coils with respect to the Pinch coils. The radially repulsive potential it creates is very weak compared to the optical potential and can be neglected. The trap resulting from the dipole laser and the magnetic field is thus still cylindrically symmetric. In the axial direction the potential is highly harmonic and can be measured with high precision, the frequency is freely adjustable by the current in the Pinch coils. The depth in the transverse direction is adjustable by the laser power.

We load the atom cloud from the Ioffe trap to the dipole trap adiabatically in 20 ms, the typical loading efficiency is about 80% with the numbers and temperatures quoted above. The laser power in the initial ODT is about 8 W, resulting in a radial frequency of $\omega_r \simeq 2\pi \times 8$ kHz, and an axial frequency dominated by the optical potential $\omega_z \simeq 2\pi \times 75$ Hz, the associated trap depth is $U_0 \simeq 200 \mu\text{K}$. The atoms are kept in the ODT with an offset field created by the Offset coils of 13 G. The temperature of the cloud in this trap depends now on the isotope, for ${}^7\text{Li}$, since the trap depth is different to the depth in the Ioffe at the end of RF evaporation, there can be some evaporation in the ODT if this trap is shallower. We usually indeed observe a slight atom loss accompanied by cooling of ${}^7\text{Li}$ after loading the dipole trap. The case of ${}^6\text{Li}$ is different: since there are no collisions and ${}^7\text{Li}$ is in minority at this stage, there is no thermalization possible for ${}^6\text{Li}$, and no evaporation initially in the ODT. In this regime the temperature of the ${}^7\text{Li}$ gas results from the competition between a thermalization with the large heat load of the ${}^6\text{Li}$ cloud and the evaporation through ${}^7\text{Li}$ - ${}^7\text{Li}$ collisions⁽ⁱ⁾. The resulting temperatures are different for the two isotopes, the bosons stabilize at a trap ratio $\eta = U_0/k_B T \simeq 6$ corresponding to $T \simeq 35 \mu\text{K}$ while ${}^6\text{Li}$ fills the trap up to a higher potential energy: $\eta \simeq 4.5$, $T \simeq 45 \mu\text{K}$.

⁽ⁱ⁾As a result of this continuous evaporation, the lifetime of the ${}^7\text{Li}$ cloud is short at this stage.

2.5 | Preparation of strongly interacting degenerate gases

After the transfer to the optical dipole trap, we modify the internal state of the atoms to place them in states with Feshbach resonances. ${}^7\text{Li}$ atoms are transferred from the $|2, 2\rangle$ state to the $|1, 1\rangle$ ($|8_b\rangle \rightarrow |1_b\rangle$), and ${}^6\text{Li}$ from $|3/2, 3/2\rangle$ to $|1/2, 1/2\rangle$ ($|6_f\rangle \rightarrow |1_f\rangle$). This transfer is done using a radio-frequency rapid adiabatic passage (RAP) across the RF transitions.

A rapid adiabatic passage in a two-level system consists in dressing the levels by a strong field with Rabi frequency Ω , and sweeping the field detuning δ across the resonance, sufficiently slowly such that the atoms follow the dressed state to end up in the other level, having absorbed or emitted a photon. The transition probability is given by the Landau-Zener formula:

$$P_{\text{tr}} = 1 - e^{-2\pi\Omega^2/\dot{\delta}} \quad (2.5)$$

where $\dot{\delta}$ is the detuning variation speed.

For the RAPs here we fix the frequency of the RF radiation at 827 MHz for ${}^7\text{Li}$ and 240 MHz for ${}^6\text{Li}$, the magnetic field offset is then swept from 13 G to 4 G in 50 ms, crossing resonance. The efficiency of the resulting transfer is found to be above 85% for both species. At this point we can ramp the magnetic field to high values using the Feshbach coils (in reverse direction to the Pinch coils).

Depending on the systems we mean to study, different routes are followed from here. We will describe in the following the “recipes” for the preparation of two different systems: a strongly interacting Bose gas, with which we studied the lifetime of a resonant Bose gas, and a mixture of a Bose-Einstein condensate and a Fermi superfluid in the BEC-BCS crossover.

2.5.1 Preparing a resonantly interacting Bose gas

First we describe how we proceed to obtain a Bose gas with which we studied 3-body recombination of resonantly interacting bosons (presented in chapter 4). Three-body recombination is studied by monitoring atom losses as a function of time. We performed these studies using ${}^7\text{Li}$ only, and we used the Feshbach resonance in the absolute ground state $|1_b\rangle$, which connects to the $|1, 1\rangle$ state at low field.

To cool the gas to the temperatures of interest, we complete a last forced evaporation in the ODT, the efficiency of this evaporation depends on the scattering rate which is proportional to a^2 . The background scattering length of the $|1_b\rangle$ at low field is small and negative ($a = -21 a_0$), so to increase the collision rate, we ramp the magnetic field to values close to the Feshbach resonance in the $|1_b\rangle$. On the other hand, three-body losses increase like a^4 for bosons. A compromise has to be found between a high scattering rate and low losses. The value of the scattering length that we use to satisfy this is $a = 190 a_0$, at 721 G. The ramp to this field is done in 350 ms using the Feshbach coils. At this field, we perform the last

evaporative cooling of the sequence, by lowering the laser power and thus the trap depth. The trap depth is lowered to an arbitrary value with which we set the final temperature of the cloud. The duration of the evaporation sequence depends on the final temperature needed, the maximum duration is 3s to obtain pure BECs with 20 000 atoms and laser power down to low values (about 100 mW). For the studies of three-body recombination, we used non-condensed Bose gases, at temperatures between $1 \mu\text{K}$ and $15 \mu\text{K}$.

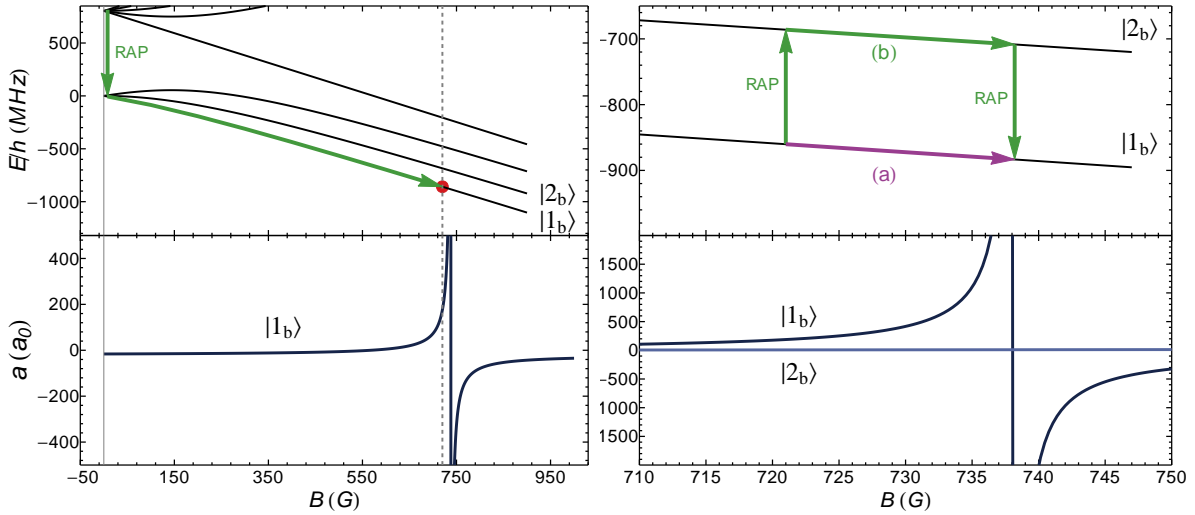


Figure 2.4: Experimental sequences for the preparation of resonantly interacting Bose gases of ^7Li . Top panels represent the internal energy of the atoms as a function of magnetic field, the bottom panels represent the scattering length in the different states.

Left: the arrow indicates the evolution of the internal state of the atoms, from the loading in the optical dipole trap to the beginning of the last forced evaporative cooling. The atoms are transferred to the $|1_b\rangle$ state by a rapid adiabatic passage (RAP) at low field, then the field offset is ramped to 721 G (dashed grey line) where evaporation is performed.

Right: Transfer of the cloud to a strongly-interacting field (here to unitarity) after evaporation. The two different strategies are schematically represented, either a direct field ramp to the desired field (a) or a transfer to the weakly interacting $|2_b\rangle$ state (b) to prevent losses during the ramp.

Following evaporation, we set the scattering length to the desired value, by a last field ramp. Since we typically need ramps of a few Gauss to a few tens of Gauss, we use the Offset coils for this last ramp, these coils are limited in current but have a much lower impedance than the Feshbach coils and can produce faster ramps.

As the scattering length is increased towards resonance, further evaporative losses take place, induced by several factors. First, the two-body scattering rate increases so that more atoms can be expelled from the trap by collisions, thus evaporation is more efficient. Second, three-body losses are amplified as well, and since in a harmonic trap these losses lead inevitably to a heating of the cloud [Weber *et al.*, 2003], the temperature increases, also inducing evaporation.

However, to conduct studies of three-body recombination, it is preferable to cancel evaporation which is a two-body process, to isolate three-body losses. To reduce evaporation when increasing a , we increase the trap depth simultaneously with the field ramp. For an adiabatic increase of the laser power, the phase-space density $n(0)\lambda_{\text{dB}}^3 = (\hbar\bar{\omega}/k_{\text{B}}T)^3$ is conserved and the trap depth U_0 is proportional to the laser power P such that the ratio between temperature and trap depth η increases with laser power like $\eta \propto P^{2/3}$. Since there is heating induced by three-body losses during the ramp, this dependence is only an indication.

The goal of our experiment is to determine the temperature dependence of three-body losses close to unitarity. In consequence, we need the temperature to be constant in time once the final ramp is done. The final trap depth is chosen to satisfy this condition, ending-up with trap ratios between $\eta = 6$ and $\eta = 8$. The time of the ramp is 500 ms, which is the fastest ramp such that the Offset coils do not produce an inductive field overshoot at the end of the ramp. We further wait 5 ms after the ramp to leave time for the field to stabilize. With this method, we ensure that the temperature remains stable and that losses are due primarily to three-body processes at the desired field. During the 500 ms of the ramp, a fraction of the atoms is lost, leading to numbers at the end of the ramp between $N = 10^5$ at 1 μK to $N = 5 \times 10^5$ at 15 μK .

In order to prevent for losses during the ramp, we used a second strategy, which consisted in transferring the atoms to a weakly-interacting state (the $|2_{\text{b}}\rangle^{(j)}$) during the field ramp (fig. 2.4). The atoms are transferred from the $|1_{\text{b}}\rangle$ to the $|2_{\text{b}}\rangle$ by a rapid adiabatic passage at a field where both states are weakly interacting, then the field is ramped to the desired value, finally they are transferred back to the $|1_{\text{b}}\rangle$. This method prevents three-body losses during the ramp. However it relies on the efficiency of both transfers. Furthermore the second RF transfer is done from a weakly-interacting state to a strongly-interacting one which modifies the transfer probability. Altogether the numbers obtained are comparable to the ones obtained with a direct ramp and we used this only for a few data sets.

The study of the stability of the unitary Bose gas performed with gases prepared by the method presented above are reported in chapter 4, in [Rem et al., 2013] (see appendix C) and in [Rem, 2013].

2.5.2 Preparing a mixture of Bose and Fermi superfluids

This section explains how we obtained a mixture of a BEC with a strongly-interacting Fermi superfluid starting from the thermal gas loaded in the optical dipole trap. Two necessary conditions for this superfluid mixture to be stable is that the bosons have a positive scattering length and the fermions be at the vicinity of a Feshbach resonance. These requirements are fulfilled if we obtain a mixture composed of ^7Li in the $|2_{\text{b}}\rangle$ state and ^6Li mixed in the $|1_{\text{f}}\rangle$ and $|2_{\text{f}}\rangle$ states at fields around 832 G. We present in what follows how this mixture is produced

^(j)the $|2_{\text{b}}\rangle$ connects at low field to the $|1, 0\rangle$.

in our apparatus.

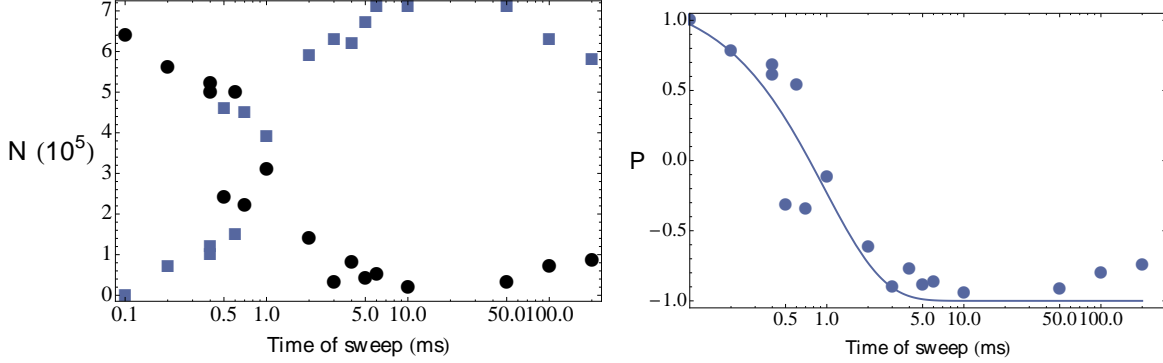


Figure 2.5: Transfer efficiency of ${}^7\text{Li}$ from $|1_b\rangle$ to $|2_b\rangle$ at 656 G. The frequency of the RF radiation is swept from 170.9 MHz to 170.7 MHz. Left: total number of atoms in $|1_b\rangle$ (black circles) and $|2_b\rangle$ (blue squares) as a function of the sweep time (in log scale). Right: polarization $P = (N_1 - N_2)/(N_1 + N_2)$ as a function of sweep time, fitted with eq. (2.5), blue line. The transfer reaches its highest efficiency at $t = 10$ ms, and coherence is partially lost after 100 ms.

Spin states preparation, ${}^7\text{Li}$ transfer

The initial conditions in the dipole trap are given in section 2.4, the mixture is composed initially of ${}^7\text{Li}$ and ${}^6\text{Li}$ in their absolute ground state at low magnetic field, obtained by a rapid adiabatic passage from the magnetically trapped states. First, the magnetic field offset is increased to 656 G in 150 ms. This field value is chosen to be far under the position of the Feshbach resonance in the $|1_b\rangle$ state, avoiding losses and heating that would be caused by crossing the magnetic field position of this resonance. At this field, we transfer the ${}^7\text{Li}$ atoms to the $|2_b\rangle$ state by a new rapid adiabatic passage. The frequency of the transition $|1_b\rangle \rightarrow |2_b\rangle$ at 656 G is $\nu_{12} = 170.8$ MHz. The RAP is implemented by applying a radio-frequency radiation during 10 ms, with a sweep of the frequency from 170.9 MHz to 170.7 MHz in this time. The efficiency of the transfer versus sweep time is represented in figure 2.5. A too fast sweep results in a non-adiabaticity of the transfer (expressed in eq. (2.5)), with a fraction of the atoms remaining in $|1_b\rangle$. Using a fit with equation (2.5), we find a Rabi frequency $\Omega = 2\pi \times 2.3$ kHz. The typical transfer efficiency at 10 ms is above 90%. When the sweep time is too long, coherence is lost leading to a decoherent mixture at long times. This decoherence may be explained in our case by field fluctuations or atoms collisions, which are spin-state dependent.

Spin states preparation, ${}^6\text{Li}$ spin mixture

Once the ${}^7\text{Li}$ transfer is achieved, the offset field is ramped in 100 ms to 835 G, in the close vicinity of the ${}^6\text{Li}$ Feshbach resonance at 832 G. During this ramp, the remaining atoms in the

$|1_b\rangle$ state of ${}^7\text{Li}$ are lost due to the crossing of its Feshbach resonance. At 835 G, we prepare the spin-mixture of ${}^6\text{Li}$. The resonance frequency for the transition $|1_f\rangle \rightarrow |2_f\rangle$ at this field is found to be between 76.25 MHz and 76.3 MHz. We implement a partial Landau-Zener (LZ) sweep (a full LZ sweep corresponding to what we call a rapid adiabatic passage). In order to adjust the spin polarization $P = (N_1 - N_2)/(N_1 + N_2)$ of the cloud, according to eq. (2.5) we can vary the sweep time (changing δ) or the power of the radio-frequency radiation (changing the Rabi frequency Ω). The dependence of polarization on the sweep time for a sweep of 100 kHz around resonance is shown in figure 2.6. We also show the total number of atoms $N = N_1 + N_2$ as a function of sweep time, where we see an atom number loss due to transfer in the $|2_f\rangle$ state. This loss is caused by the turn-on of s-wave collisions between distinguishable spin states leading to evaporation of the fermions mixture. It is accompanied by a temperature decrease to $T = 30 \mu\text{K}$.

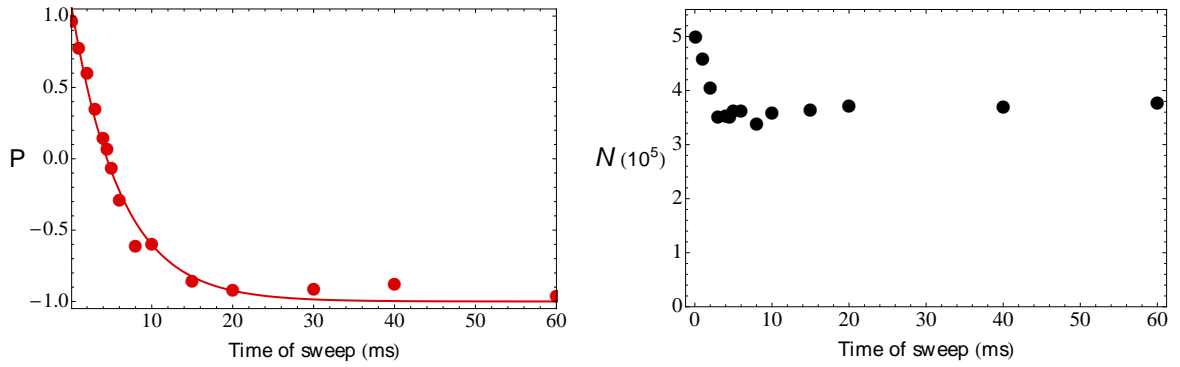


Figure 2.6: Transfer efficiency of ${}^6\text{Li}$ from $|1_f\rangle$ to $|2_f\rangle$ at 835 G. The frequency of the field is swept 100 kHz across the transition frequency. Left: polarization (circles) as a function of sweep time fitted with eq. (2.5), giving a Rabi frequency of $\Omega = 2\pi \times 650$ Hz. Right: total number of ${}^6\text{Li}$ atoms $N = N_1 + N_2$ as a function of sweep time, showing evaporation due to collisions between distinguishable spin states.

For the production of a superfluid mixture, we prepare a spin-balanced ($P = 0$) cloud of ${}^6\text{Li}$, but we can also vary the spin-polarization to create unbalanced degenerate Fermi gases. The mixture thus prepared is the starting point of the last evaporative cooling. It is composed of $N_b = 2 \times 10^5$ ${}^7\text{Li}$ bosons in the $|2_b\rangle$ state and a mixture of ${}^6\text{Li}$ fermions in the $|1_f\rangle$ and $|2_f\rangle$ states with total number $N_f = 1.5 \times 10^6$, at 835 G. The temperature of the mixture is about $30 \mu\text{K}$, ${}^7\text{Li}$ is in thermal equilibrium with ${}^6\text{Li}$ due to inter-isotope collisions with scattering length $a_{bf} = 41 a_0$. If we mean to study the mixture on the BCS side of the Feshbach resonance of ${}^6\text{Li}$, we need to cross the narrow resonance of $|2_b\rangle$ at 845 G. If we cross this resonance when the ${}^7\text{Li}$ cloud is in the BEC state, it collapses. To avoid collapse, for studies of the BCS side the evaporation is done at 860 G, after a 50 ms field ramp using the Offset coils.

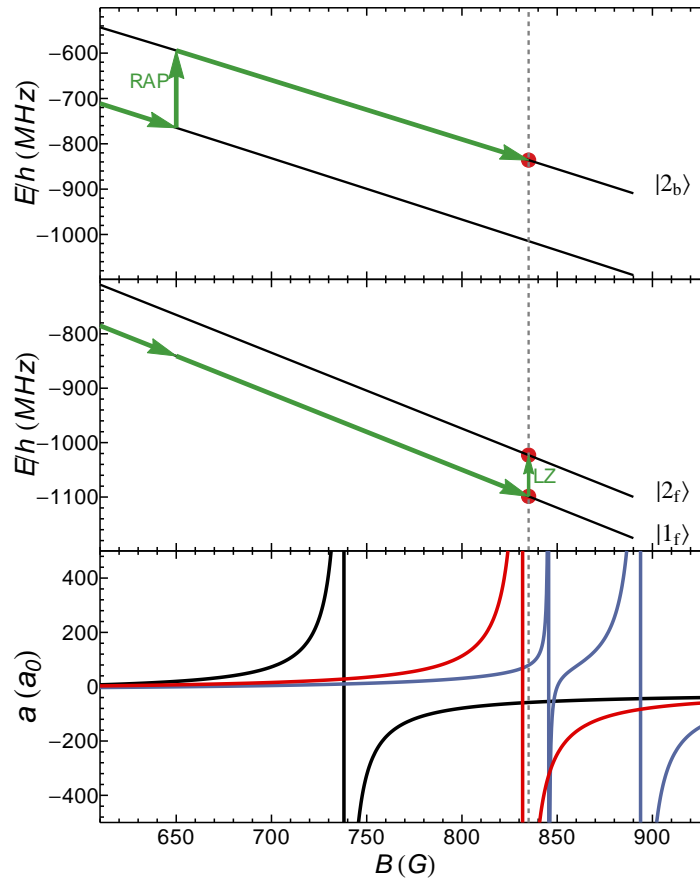


Figure 2.7: Schematic representation of the preparation sequence for the superfluid mixture. Top panel, magnetic field dependence of the ${}^7\text{Li}$ energy levels and the sequence 'trajectory' in green arrows. Middle panel, same for ${}^6\text{Li}$.

Both isotopes are transferred at low magnetic field to their absolute ground state by a rapid adiabatic passage (not shown), then the field is ramped-up to 656 G in 150 ms. ${}^7\text{Li}$ is transferred to the $|2_b\rangle$ at 656 G, then the field is ramped to 835 G in 100 ms and the spin-mixture of ${}^6\text{Li}$ is prepared by adjusting the Landau Zener efficiency of a RF sweep across the $|1_f\rangle \rightarrow |2_f\rangle$ transition at 835 G. At this field evaporation is performed. The mixture at the beginning of the last evaporation is schematically represented by red circles.

The bottom panel shows the different scattering lengths a in the states involved, black and blue curves show a in the $|1_b\rangle$ and $|2_b\rangle$ states of ${}^7\text{Li}$ and the red curve shows $a/100$ for $|1_f\rangle$ - $|2_f\rangle$ collisions of ${}^6\text{Li}$.

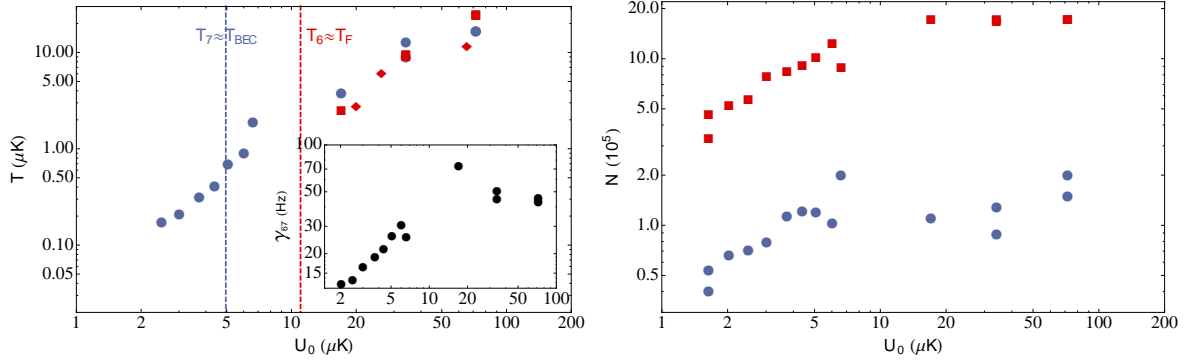


Figure 2.8: Left: Temperature of the ^7Li (blue symbols) and ^6Li (red symbols) during the evaporation at 835 G. The red diamonds are measured using a time of flight image in the axial direction, the red squares and blue circles are measured using the in-situ imaging in the radial direction (the imaging system and temperature measurement are explained in section 2.6). The dashed lines show the depth at which we reach Fermi degeneracy (red) and Bose-Einstein condensation (blue). Inset: Scattering rate of one ^7Li atom at the center of the ^6Li cloud as a function of trap depth. We observe a drop of the scattering rate at low trap depth leading to slow cross-thermalization.

Right: Total number of atoms of each species (red: ^6Li , blue: ^7Li) as a function of trap depth during evaporation. Note the very small loss of ^7Li (a factor ~ 2) in the process, demonstrating that cooling is ensured by ^6Li .

Thermalization and evaporation

At 835 G, and $30 \mu\text{K}$, ^6Li exhibits a unitarity-limited scattering rate, in the conditions given above, $\gamma_{66} \simeq 10 \text{ kHz}$ with γ_{66} the fermion-fermion collision rate. The thermalization of ^6Li is thus very fast. The collision rate of one ^7Li boson with fermions at the center of the Fermi cloud is $\gamma_{67} \simeq 70 \text{ Hz}$ and is higher than the boson-boson collision rate at this stage $\gamma_{77} \simeq 15 \text{ Hz}$. γ_{67} gives the timescale for thermalization of ^7Li with ^6Li . So inversely to the situation of the evaporation in the Ioffe trap, ^6Li constitutes the coolant. However, the evaporation of the mixture is forced by lowering the laser power, thus lowering the trap depth for both species. In consequence ^7Li can undergo evaporation and if the trap depth is lowered too fast, ^7Li will be lost before it cools down.

We optimized the trap lowering ramp by monitoring both ^7Li and ^6Li and verifying cross-thermalization. The total evaporation ramp lasts for 3.2 s and the final trap depth is about $U_0 \simeq 2 \mu\text{K}$. In figure 2.8 we display the number and temperature evaporation of both species. We observe that ^6Li and ^7Li are at thermal equilibrium during the initial steps of evaporation. Furthermore we observe a very high efficiency of the dual species-evaporation on both species in the initial steps, showing very little atom losses.

At low trap depth, as displayed in figure 2.8, the cross-species scattering rate γ_{67} drops. As a consequence, the thermalization between ^7Li and ^6Li takes longer and longer. We observe that in the last stages, when stopping evaporation, a slow thermalization dynamics takes place on ^7Li (see fig. 2.9 for a fast evaporation to a shallow trap) which can be explained

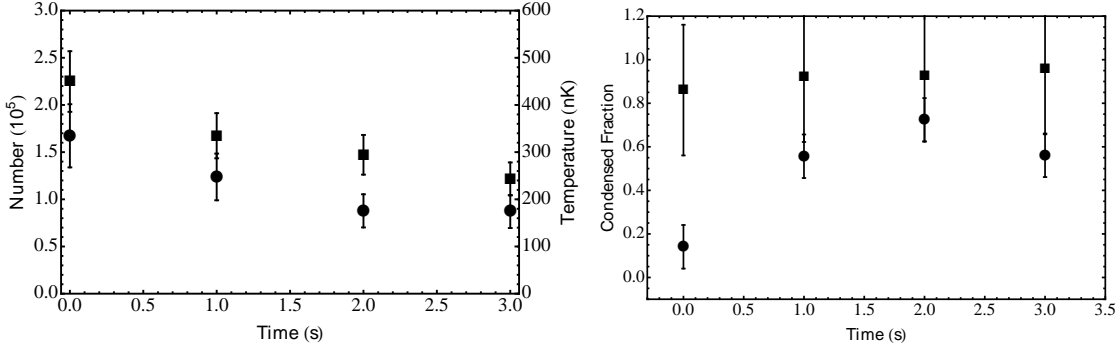


Figure 2.9: ^7Li thermalization dynamics after a fast evaporation (2 s) to a trap depth ($U_0 \simeq 2 \mu\text{K}$). Left: temperature (squares) and number (circles) as a function of time. Right: condensed fraction N_0/N as a function of time, comparison between the measured one (circles) and the one calculated from temperatures and numbers (squares).

by a partial cross-thermalization. The condensate fraction of ^7Li grows significantly in one second, accompanied by a temperature decrease by 40% and an atom loss of the same order. We make a comparison between the condensed fraction measured using the density profile and the one calculated from the ideal Bose gas prediction $N_0/N = 1 - (T/T_c)^3$ using the temperature and numbers measured. At initial times $t \lesssim 1$ s the observed condensate fraction disagrees with the expectation, signalling that thermalization is not yet achieved.

In order to ensure cross-thermalization, we systematically wait at least 700 ms at the end of evaporation before running experiments on the mixture. Once we have obtained a degenerate mixture, we vary the magnetic field to the desired value where we want to perform the experiment. The ramp to this field is done during the last wait time.

2.6 | Imaging

The atomic density profiles that we have presented until here, from which we extract experimental observables, have been obtained using absorption imaging. This technique is based on the recording of the optical density of the atomic cloud on resonant light. The intensity of a light beam propagating along the z direction through an atomic cloud is given by the Beer-Lambert law:

$$I(x, y) = I_0(x, y)e^{-OD(x, y)}, \quad (2.6)$$

where OD is the optical density and I_0 is the initial beam intensity. The optical density is

$$OD(x, y) = \sigma \int dz n(x, y, z), \quad (2.7)$$

where n is the cloud's atomic density and σ is the absorption cross-section of one atom. Thus recording the light intensity of a beam on a CCD camera yields the integrated density

in the propagation direction, the intensity I_0 is recorded in the absence of atoms and the ratio I/I_0 gives the optical density. At resonance the theoretical expression of the cross-section is $\sigma = 6\pi(\lambda/2\pi)^2 \times C$ where C is the Clebsh-Gordan coefficient for the absorption transition and light polarization. However we cannot rely on this expression since experimental imperfections can reduce the cross-section, for instance if the imaging light's spectral width is not narrower compared to the atomic natural linewidth, the absorption at resonance is reduced. We thus have to measure the cross-section experimentally.

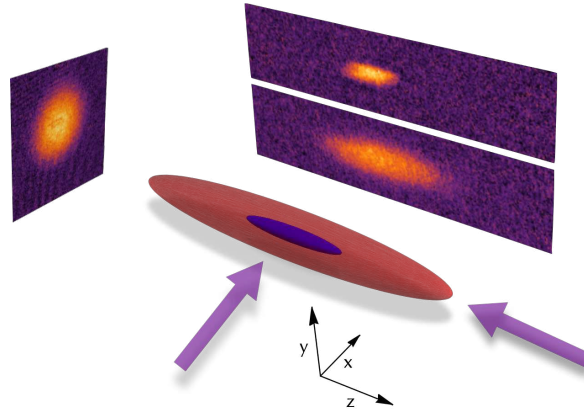


Figure 2.10: Schematic representation of the imaging system. The imaging directions are indicated by the purple arrows, we show three different optical density images, obtained from a Bose-Fermi mixture. A BEC of in the $|2_b\rangle$ state is imaged in the radial direction, together with one spin-state of a degenerate Fermi gas, the other fermions spin state is imaged in time of flight in the axial direction.

In the dipole trap, there are two directions of propagation used for imaging: one along the trap symmetry axis (z direction), parallel to the magnetic field, with σ^+ polarization, and one along its radial direction with π polarization (fig. 2.10). The axial imaging can yield ‘time of flight’ pictures, which are obtained after release and expansion of the cloud. The radial imaging can be used while the atoms are in the trap - ‘in situ imaging’- or after a time of flight. In the non-degenerate regime, we can infer the cloud’s temperature by the radius of the cloud: In situ, according to (1.16) the axial gaussian width is given by

$$\sigma_z = \sqrt{k_B T / m\omega_z^2} \quad (2.8)$$

thus fitting the observed distribution with a gaussian yields the temperature of the cloud. In the other direction, after a long time of flight, the spatial distribution reflects the initial momentum distribution and we can also obtain the temperature this way.

The imaging resolution in the radial direction, about $5 \mu\text{m}$ is not much smaller than the cloud’s radial size, as a consequence, the image obtained by this imaging does not reflect the real optical density because it is spread in the radial direction. Thus only the doubly integrated density is accurate. A further consequence of this low resolution is that this

imaging can be used only in the linear-absorption regime: $I/I_0 \simeq 1 - OD$: The convolution of the optical density by the resolution smearing conserves the total atom number only in this linear regime [Nascimbène, 2010]. A solution to circumvent this limitation is to do a short time of flight, the cloud expands radially much faster than axially thanks to the high aspect ratio of our trap ($\omega_r/\omega_z > 10$) and the optical density can be reduced without modifying the axial distribution.

Using acousto-optic modulators, we are able to shift the light frequency to the transitions frequency at high field, this shift is of the order of $\mu_B \times B \simeq 1.2$ GHz at $B = 850$ G where μ_B is the Bohr magneton. This way we can image the atom cloud directly at high magnetic field, and thanks to the energy splitting of the internal states our imaging is spin-selective, furthermore when in the Paschen-Back regime the imaging transitions are closed transitions. Our CCD cameras (Pixelfly QE) are able to acquire two subsequent images with a short time separation (as short as $3 \mu s$), allowing to image two spin-states in the same imaging direction^(k). In total we can image two states in situ and up to two other states in time of flight in the axial direction. When imaging several spin states of the same cloud, precautions must be taken in order to avoid significant heating by the first imaging pulse [Nascimbène, 2010, Navon, 2011], which would distort the density distribution. When imaging both states of a strongly interacting ^6Li Fermi gas this limits the duration of the pulses to $40 \mu s$. When imaging the ^7Li Bose gas and one fermion state in situ, it is safer to image the bosons first since they are in minority and can only weakly perturb the fermions.

2.7 | Calibrations

2.7.1 Imaging Calibration

We have written earlier that the absorption cross-section of the atoms on the imaging light differs from the ideal case and thus must be calibrated experimentally. The knowledge of this cross-section allows to back-out the number of atoms in the line of sight - the 1D integrated density. To calibrate it, one has to find an independent way of extracting the integrated density, by measuring variables to which it is related. For instance one could measure the two- or three-body losses decay time, which, involving two- or three-atom collisions depends on the local atomic density. Since part of our work has been to explore three-body losses, we perform an independent calibration, with which we calibrate the doubly-integrated density. The doubly-integrated density is the observable we use in the experiment, and from the knowledge of the trap frequencies and the equation of state of the gas it can be related to the 1D integrated density.

^(k)When two fermionic atoms are paired, the imaging frequency is shifted by the binding energy. However this has a significant effect only if the binding energy is large compared to the imaging transition linewidth which is not verified in the experiments we report in this thesis.

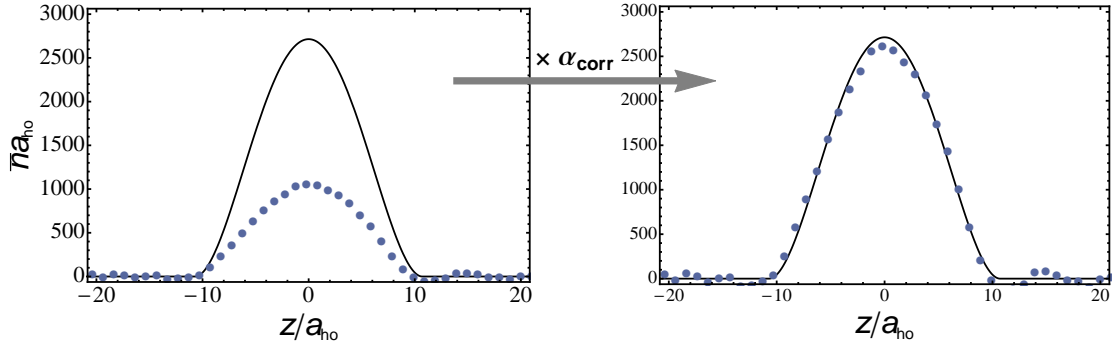


Figure 2.11: Calibration of the doubly integrated density for the $|2_b\rangle$ state: the left picture shows data points obtained by an integration of the optical density measured, the black curve is the theoretical profile that is calculated from the extent of the cloud (Thomas-Fermi radius), the trap frequencies and the scattering length. Using this curve we correct our doubly integrated density (right).

This calibration is obtained by the in-situ imaging of degenerate interacting gases. From the equations of state of interacting Bose and Fermi gases seen in the first chapter of this work, and using the local density approximation, the density profiles of degenerate gases depend on the total atom number contained in the gas. In the case of a Bose gas, the Thomas-Fermi radius of a BEC in a harmonic trap given by equation (1.36) depends on the total number of atoms present in the cloud, contrary to the case of an ideal thermal gas where it depends only on temperature. This radius can be measured with good precision, this way we get a calibration factor (α_{corr}) for the integrated density as represented in figure (2.11) and obtain an absolute measurement of the doubly integrated density and of the total atom number. This calibration depends not only on the imaging light absorption cross-section but also on the measure of the radial extent of the BEC that will depend on the imaging magnification⁽¹⁾ and the parameters that enter expression (1.36): the trap frequencies and the scattering length (obtained from the magnetic field), all these parameters can be measured independently. We can then back-out the experimental absorption cross-section.

An alternative method we also use to calibrate the total number for bosons is to compare the temperature at the onset of BEC to the critical temperature calculated using eq. (1.13).

By these two methods we get for bosons:

In the $|1_b\rangle$ state : using the Thomas Fermi radius radius : $\alpha_{\text{corr}} = 2.4(5)$.

In the $|2_b\rangle$: using the TF radius $\alpha_{\text{corr}} = 2.8(5)$, and using the critical temperature: $\alpha_{\text{corr}} = 2.7(5)$. The origin of such a large α_{corr} is not fully understood. A reduction of detectivity by a factor ~ 1.7 is due to a finite spectral width of the probe light but this factor is still far from the reductions $\alpha_{\text{corr}} \geq 2.4$ measured.

To calibrate ${}^6\text{Li}$ imaging at high field, we use a balanced Fermi superfluid at unitarity, its equation of state has been measured and calculated with great precision giving a Thomas-

⁽¹⁾The magnification of our imaging is measured by monitoring the free fall of gases under the effect of gravity.

Fermi radius in the i direction: $R_i = \xi^{1/4} k_F \hbar / m \omega_i$ where $\xi = 0.37$ is the Bertsch parameter and $k_F = \sqrt{2m\bar{\omega}(3N_f)^{1/3}/\hbar}$ is the Fermi wave-vector of the trapped gas with total atom number N_f .

Using the same procedure as for bosons we measure $\alpha_{\text{corr}} = 1.9(5)$.

2.7.2 Frequencies measurement

A precise and accurate knowledge of the trap frequencies is essential for nearly all measurements on our gases. We use two different ways to measure the trap frequencies: center-of-mass (CoM) oscillations or parametric excitation. CoM oscillations consist in displacing the center of gravity of the cloud away from the center of the trap and letting it evolve, if the cloud remains in the harmonic region of the trap the CoM oscillates at the trap frequencies (fig. 2.12). Trap anharmonicities cause damping of this motion.

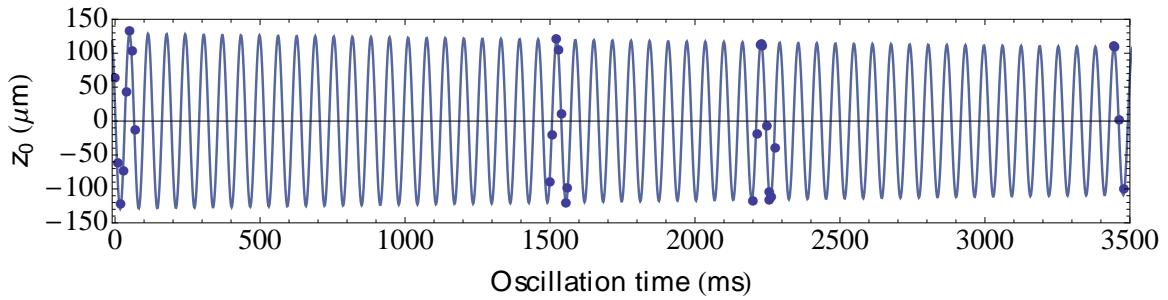


Figure 2.12: Oscillation of a BEC in the ODT in the axial direction. The fit by a damped sine function shows excellent agreement, with a long damping time (≥ 20 s), showing the high harmonicity of the magnetic confinement.

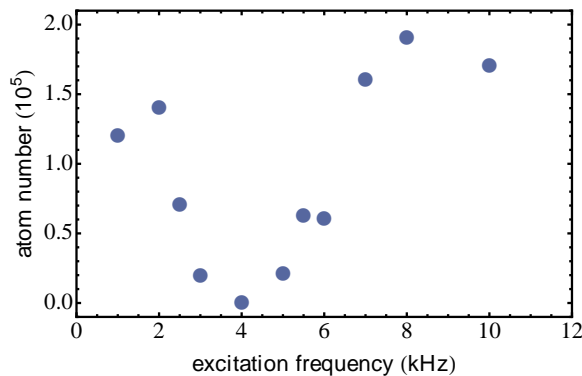


Figure 2.13: Atom number left in the dipole trap after a parametric excitation, for a trap depth of $U_0 \simeq 12 \mu\text{K}$.

To apply a parametric excitation on the cloud we can for example weakly modulate the trap power. The response to this excitation is measured as a heating or the atom loss it causes (fig. 2.13). The resonance frequency is twice the trap frequency provided the

gas is not superfluid and in the collisionless regime $\omega/\gamma \gg 1$ where ω is the weakest trap frequency and γ is the collision rate. In the opposite case: the hydrodynamic regime reached for $\omega/\gamma \ll 1$ or when the gas is superfluid, the response frequency is modified [Pitaevskii and Stringari, 2003, Riedl et al., 2008] and it is safer to use center-of mass oscillations^(m).

In the dipole trap, the radial confinement is provided by the laser, and the axial confinement is dominated by the magnetic field at weak laser powers. The harmonicity of the magnetic confinement is much higher than the laser confinement, this results in higher precision on the knowledge of the axial confinement at low power (typically $\delta\omega_z/\omega_z \lesssim 10^{-2}$) compared to the radial confinement (10^{-1}).

2.7.3 Magnetic field calibration

Another essential calibration on the experiment is that of the magnetic field. The value of the magnetic field fixes the scattering lengths and the imaging transitions frequency of the atoms, and a precise knowledge of these values is essential. The magnetic field is calibrated on our experiment by measuring the frequency of hyperfine transitions of ^7Li , whose field-dependence is known with great precision. The usual transition we use is $|1_b\rangle \rightarrow |2_b\rangle$ which has a frequency of the order of 175 MHz and a field dependence of ~ 40 kHz/G. For a more precise measure we use the transition $|2_b\rangle \rightarrow |5_b\rangle$ ⁽ⁿ⁾, with a higher field sensitivity (~ 2.7 MHz/G).

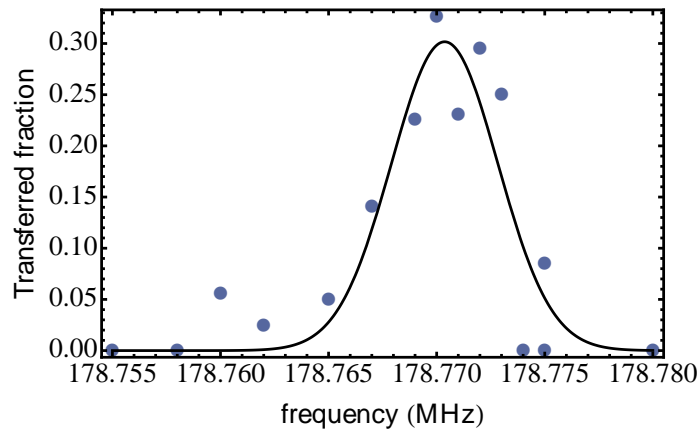


Figure 2.14: Example of magnetic field measurement by radio-frequency transfer from the $|1_b\rangle$ state to the $|2_b\rangle$ state by monitoring the population transfer. The central frequency is extracted by a gaussian fit to the data, yielding here a magnetic field $B = 837.5(1)$ G.

The magnetic field measurement consists in monitoring the fraction of atoms transferred

^(m)Note that our spin-balanced Fermi gas at 835 G is already in the hydrodynamic regime at the beginning of the last evaporation.

⁽ⁿ⁾The $|5_b\rangle$ state connects to the $|F = 2, m_F = 1\rangle$ at low field.

for a pulse of fixed frequency (Fig. 2.14). This acquisition takes typically one hour, the field stability during this time, given by the width of the transfer spectrum is $\Delta B \leq \pm 100$ mG. The field stability on time scales of two days can be higher, up to 0.3 G, and for measurements requiring a precise knowledge of the field we have to calibrate the field every day.

Summary

In summary we have presented how degenerate quantum gases of lithium are prepared, starting from a dilute hot vapor, using first laser cooling then evaporative cooling. Once the atoms are placed in the optical trap, the magnetic field is freely adjustable, this allows us to control the two-body interactions inside the gas. By choosing the constituents of the gas we can study different many-body systems of bosons and fermions. Using these preparation schemes we prepared Bose gases with a resonant two-body interaction with which we studied three-body recombination at unitarity as presented in chapter 4. Next, we have prepared doubly-superfluid mixtures of bosons and fermions, we report on the results about these studies in chapter 5. But first, next chapter is dedicated to a novel laser cooling method which opens possibility for improvements of the set-up both in terms of sample size and cycle rate.

Chapter 3 |

D_1 sub-Doppler cooling of ^7Li

In chapter 2 we quote a temperature at the end of the MOT–CMOT phase of $600\ \mu\text{K}$ on our experiment. Some other experimental teams report temperatures down to $300\ \mu\text{K}$ with the same cooling technique, but these results remain far from the expected temperature of Doppler cooling on a two-level atom: the Doppler temperature $T_D = \hbar\Gamma/2k_B = 140\ \mu\text{K}$. This poor cooling efficiency is explained by the fact that the upper hyperfine states of lithium on the D_2 line are unresolved. Thus the model of Doppler cooling on one cycling transition is too simple and the result of this model does not apply. Ironically, in the past the two-level model has also showed too simple to predict temperatures of laser-cooled samples, but in the other direction: it predicted higher temperatures than measured [Lett *et al.*, 1988]. The origin of these low temperatures lied in the multi-level structure of the atoms as well as the polarization gradients present in the cooling light, [Dalibard and Cohen-Tannoudji, 1989], the story of these discoveries is now a classics of atomic physics history that led to the discovery of Sisyphus cooling.

In potassium isotopes, the typical temperature reached in a MOT is about $150\ \mu\text{K}$ close to the Doppler temperature, but the usual sub-Doppler cooling by the Sisyphus mechanism is absent, due also to a narrow hyperfine structure. To solve this problem, the other team of the LKB ultracold Fermi gases group has used a technique close to Sisyphus cooling: ‘grey molasses cooling’ to lower the obtained temperature [Rio Fernandes *et al.*, 2012]. Grey molasses cooling was designed after Sisyphus cooling was discovered more than twenty years ago [Grynberg and Courtois, 1994, Weidemüller *et al.*, 1994], and soon implemented on caesium and rubidium [Boiron *et al.*, 1995, Esslinger *et al.*, 1996].

Grey molasses cooling is explained in the references cited above and in good details in [Cohen-Tannoudji, Claude, 1996] (in french), we will outline its working principle here, and focus on the effect of the Λ configuration present with the cooling and repumping beams, which we have explored [Grier *et al.*, 2013].

3.1 | Grey molasses cooling in a nutshell

Grey molasses cooling relies on the existence of bright and dark states due to a degeneracy of the ground state. Owing to quantum interferences, the dark state is not coupled to

the excited state by the laser and as such its energy is not light shifted. Bright states are not transparent to light, as a consequence they experience a light shift proportional to the light intensity^(a). These bright and dark states depend on the transition considered and the light polarization. For a simplified picture we will consider a model with three levels, two ground states and one excited state with width Γ . This system is shone by one standing light wave, with detuning Δ with respect to the frequency of the ground-excited transition, for which one of the two ground levels is a dark state, the other one being bright.

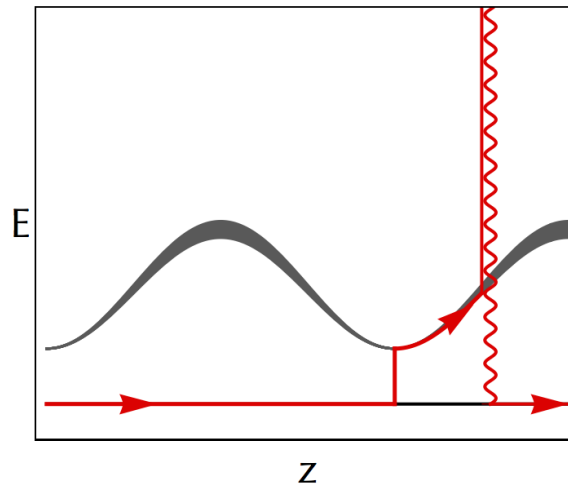


Figure 3.1: A grey molasses cycle. The bright state is dressed by the light standing wave, with a space variation of the light-shift and optical-pumping rate (linewidth), represented here for a wave with $\delta > 0$. First the atom is coupled from a dark state to a bright state at a minimum of the potential created by the light shift. Second it climbs up a potential hill before being pumped back to a dark state through the excited state.

The grey molasses principle is represented in figure 3.1. First, the atoms trapped in a dark state leave this state to a bright state. This mechanism can be due for example to the fact that the atom does not follow adiabatically the dark state in which case it is referred-to as motional coupling, or to an off-resonant Raman. The important point is that the coupling out of the dark state has the highest probability where the bright state is closest to the dark state. For positive detuning $\Delta > 0$, the light-shift is positive and increases with intensity such that the two states are closest at the bottom of the potential hill. After being transferred into the bright state, the atoms start climbing the hill and convert their kinetic energy into potential energy. Finally, when the atom reaches the top of the hill, it is optically pumped back to the dark state. To understand why, we can use the dressed atom formalism, in which the bright state is dressed by the light and acquires an excited state character. Since the excited state has a linewidth Γ , this dressing results in a finite width for the bright states $\Gamma' = \Gamma(\Omega(z)/\Delta)^2$ where $\Omega(z)$ is the Rabi frequency associated to the standing wave, which is proportional to the square root of its intensity. The space-varying light-shift and linewidth

^(a)The light shift is precisely the potential that is used for optical trapping by a dipole trap.

are represented in figure 3.1 together with the full cycle. The net result of this cycle is a kinetic energy loss when climbing up a light-shift potential hill, this energy being carried by the spontaneous photon emitted at the end of the cycle. This kinetic energy loss for one atom results in a temperature decrease for an atomic ensemble.

To apply this technique, one thus needs a transition which contains at least one dark state, shone with a light with positive detuning. The existence of a dark state is ensured provided the light addresses a transition $F \rightarrow F'$ with $F' \leq F^{(b)}$, in which case the bright and dark states emerge from the Zeeman degeneracy in the lower manifold. Both for potassium and lithium, since the upper states are unresolved the use the D_2 line, induces excitation of other transitions, forcing to use the D_1 line.

The application of this technique on the D_1 line of potassium was a success and led to a temperature $T = 20 \mu\text{K}$ much lower than the Doppler temperature. Following this success, we decided to use it on ${}^7\text{Li}$ in order to improve our experiment performances, as reported below and in the corresponding article [Grier *et al.*, 2013] (in appendix C).

3.2 | Implementation on ${}^7\text{Li}$

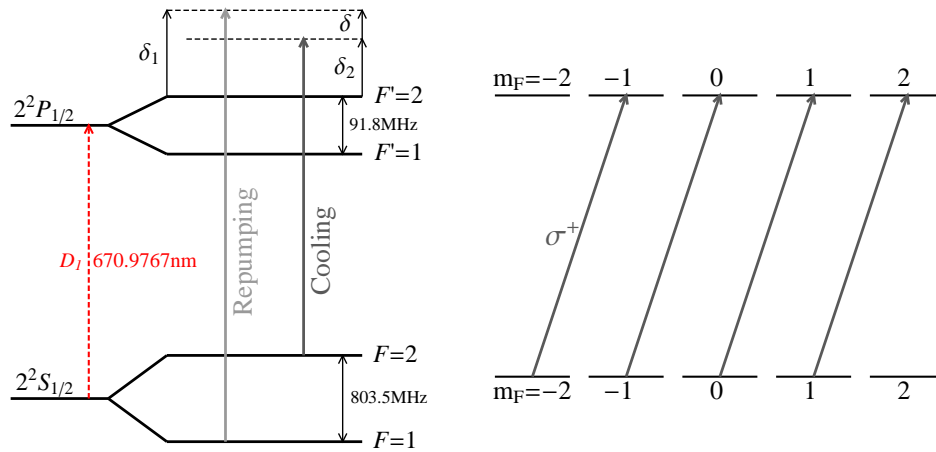


Figure 3.2: Left: Laser scheme used for the D_1 grey molasses cooling on ${}^7\text{Li}$. The cooling scheme has a strong coupling laser (principal beam, black solid arrow) δ_2 blue detuned from the $|F = 2\rangle \rightarrow |F' = 2\rangle$ transition and a weak coupling laser (repumper, grey solid arrow) δ_1 blue detuned from the $|F = 1\rangle \rightarrow |F' = 2\rangle$ transition. Right: example, in the case of σ^+ polarization of the principal cooling light (driving $m_F \rightarrow m_F + 1$ transitions), the dark state is the $|F = 2, m_F = 2\rangle$.

We used the D_1 transition $F = 2 \rightarrow F' = 2$ for the cooling transition, addressed with

^(b)Strictly speaking this is true only for bosonic isotopes, for fermionic isotopes the existence of a dark state depends on the light polarization.

a light frequency ω_2 . Additionally, as is the case for the MOT stage, we need a repumper beam in case the atoms fall into the $F = 1$ manifold^(c), this repumping is done on the $F = 1 \rightarrow F' = 2$ transition with a frequency ω_1 . We note δ_2 the detuning of the cooling light and δ_1 that of the repumper as represented in figure 3.2. The repumping light was obtained by using an electro-optic modulator on the beam path of the cooling light with an adjustable frequency. The cooling beams have a $1/e^2$ radius of 3.5 mm with a peak intensity $I_{\text{max}} = 4.5I_{\text{sat}}$. The intensity of the repumper I_R is much weaker than that of the cooling beam I_C : $I_R/I_C \simeq 0.03$. We have used for the D_1 beams the same directions as the MOT beams, with opposite polarization, we thus have a light wave in three dimensions, with a varying polarization in space.

This grey molasses cooling applied after the CMOT phase results in a successful sub-Doppler cooling of 100% of the atoms to $60 \mu\text{K}$ in less than 2 ms. This temperature is reached for a principal detuning $\delta_2 = 2\pi \times 27 \text{ MHz}$ and when the Raman condition (RC): $\delta_1 = \delta_2$ is respected between the two light frequencies (figure 3.3). The dependence of the temperature on the relative detuning between the two light frequencies $\delta = \delta_1 - \delta_2$ for a fixed principal detuning $\delta_2 = 2\pi \times 27 \text{ MHz}$ is represented in figure 3.3.

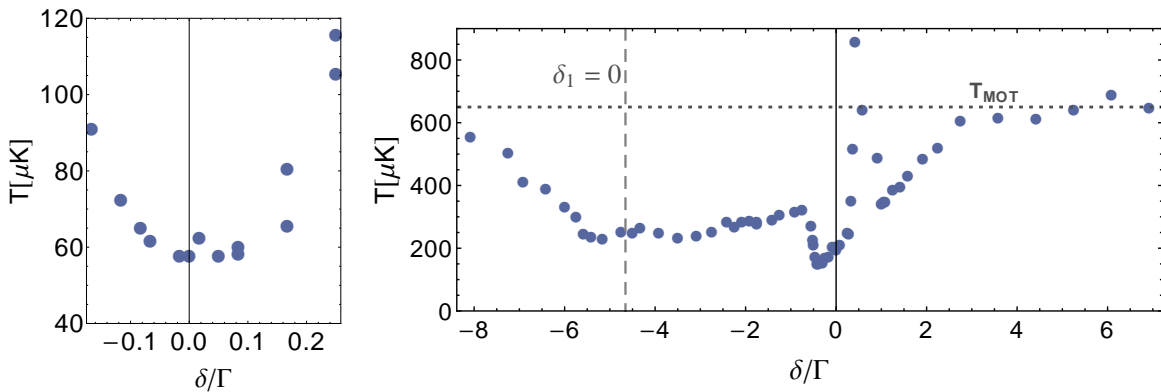


Figure 3.3: Dependence of the temperature on the relative detuning δ between the cooling and repumping frequencies, for a fixed principal detuning $\delta_2 = 2\pi \times 27 \text{ MHz}$. δ is in units of the excited states linewidth: $\Gamma = 2\pi \times 5.9 \text{ MHz}$. Left: results in the optimal beam alignment conditions. Right: on a broad range of detuning with non-optimal alignment, the dotted line indicates the initial temperature after the MOT-CMOT phase and the vertical dashed line indicates the resonance position for the repumping light.

We notice first in figure 3.3 a broad spectrum, with a cooling to a temperature of $250 \mu\text{K}$ obtained between $\delta = -6\Gamma$ and $\delta = -1\Gamma$. Second, we observe a very sharp feature around the Raman condition, with an enhanced cooling at $\delta = 0$ and a strong heating when the repumper is detuned to the blue of the Raman condition $\delta > 0$. In order to understand

^(c)The $F = 1$ manifold constitutes an ensemble of dark states but the coupling by motional coupling or Raman transition out of these states is much too low and we need a repumper.

this sharp feature obtained with such a weak repumper, we have explored theoretically the effects of the Raman configuration. We presents our results in the following.

3.3 | The Λ model.

Our aim is to unravel the effects of the cooler-repumper configuration. So we simplify the situation to a 1D situation and we consider only a three-level Λ model illustrated in figure 3.4. Since the frequency difference (hyperfine splitting of ${}^7\text{Li}$: 803.5 MHz) is small compared to the absolute frequencies, we write two waves of the same frequency $\omega_1 \simeq \omega_2 \simeq \omega = kc$, only spatially dephased by a phase ϕ . The principal cooling transition is labeled here and below as transition 2, between states $|2\rangle$ and $|3\rangle$ with a Rabi frequency $\Omega_2 = \Gamma\sqrt{I_C/2I_{\text{sat}}}$. The repumper transition is labeled 1, between states $|1\rangle$ and $|3\rangle$ with Rabi frequency Ω_1 much weaker than Ω_2 .

We wish to understand the effect of varying the detuning (δ) of transition 1 with respect to the Raman condition with all others parameters fixed.

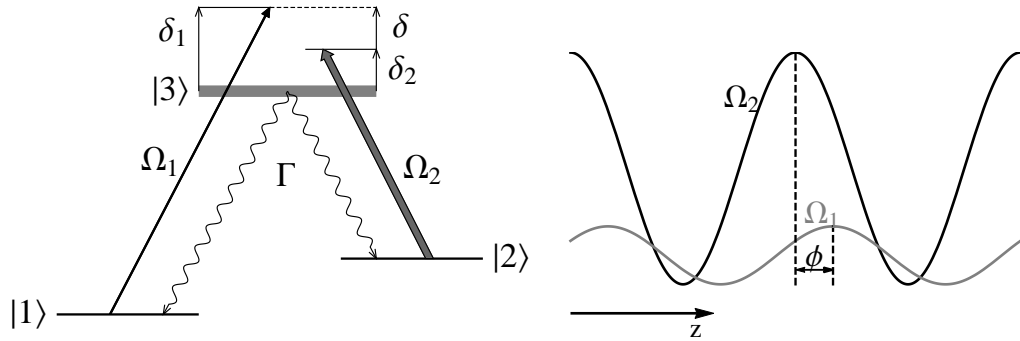


Figure 3.4: The Λ scheme, a simplification of the ${}^7\text{Li}$ level structure, used to understand the effect of the Raman configuration. The cooling (repumping) light is represented by a standing wave with Rabi frequency $\Omega_2(z)$ ($\Omega_1(z)$).

The light-atom interaction in the rotating wave approximation is written :

$$\begin{aligned} \hat{V}_{\text{AL}} = & \hbar\Omega_2 \cos(kz) (|2\rangle \langle 3| + \text{h.c.}) + \hbar\Omega_1 \cos(kz + \phi) (|1\rangle \langle 3| + \text{h.c.}) \\ & + \hbar\delta_1 |2\rangle \langle 2| + \hbar\delta_2 |1\rangle \langle 1| \end{aligned} \quad (3.1)$$

The light force at position z from (3.1) is given by $F = \langle -\nabla \hat{V}_{\text{AL}} \rangle = -\text{Tr} [\hat{\rho} \nabla \hat{V}_{\text{AL}}]$ where $\hat{\rho}$ is the density operator and we get:

$$F = \hbar k (\sin(kz + \phi) \Omega_2 \text{Re } \rho_{23} + \sin(kz) \Omega_1 \text{Re } \rho_{13}), \quad (3.2)$$

where ρ_{ij} are elements of the density matrix, and we can obtain the wavelength-averaged

force \mathcal{F} :

$$\mathcal{F}(v) = \frac{1}{\lambda} \int_0^\lambda dz F(z, v) \quad (3.3)$$

$$\mathcal{F}(v) = \frac{\hbar k^2}{2\pi} \int_0^\lambda dz (\Omega_2 \sin(kz + \phi) \text{Re } \rho_{23} + \Omega_1 \sin(kz) \text{Re } \rho_{13}) \quad (3.4)$$

where $\lambda = \frac{2\pi}{k}$ is the wavelength of the light waves and we have anticipated that the force depends on the atom's velocity as will become clear below.

The usual formalism used to compute the atoms dynamics is to consider the light force as a Langevin force. Its mean value is $\mathcal{F}(v)$, and the fluctuations around this mean will give rise to diffusion in momentum space, characterized by the diffusion coefficient $\mathcal{D}(v) \geq 0$. The velocity distribution of an ensemble of atoms subject to a Langevin force is a stationary solution to the Fokker-Planck equation (FPE) (see appendix A.1). Such a solution can be expressed as a function of \mathcal{F} and \mathcal{D} :

$$P_{st}(v) \propto \frac{1}{\mathcal{D}(v)} \exp\left(m \int_0^v dv' \frac{\mathcal{F}(v')}{\mathcal{D}(v')}\right) \quad (3.5)$$

For a cooling force:

$$\mathcal{F}(v) = -\alpha v, \quad (3.6)$$

where $\alpha > 0$ is the friction coefficient, we identify (3.5) with a Boltzmann distribution to obtain the temperature^(d)

$$k_B T = \mathcal{D}(0)/\alpha. \quad (3.7)$$

To calculate the temperature, one then needs \mathcal{F} and \mathcal{D} . However, in order to reveal the physical mechanisms in action, we only calculate the force $\mathcal{F}(v)$ and the spontaneous emission rate obtained from the excited state population ρ_{33} :

$$\Gamma' = \Gamma \rho_{33}. \quad (3.8)$$

Γ' gives the number of scattered photons as a function of time, each photon leading to a recoil of the emitting atom. Since photons are scattered in a random direction, spontaneous emission can be seen as a random walk in momentum space leading to a broadening of the momentum distribution, thus a heating. Other sources of fluctuations should be taken into account to obtain \mathcal{D} [Cohen-Tannoudji, Claude, 1990], but since our model (3.1) is already a gross simplification of the physical system, we do not expect to be able to quantitatively predict a steady-state temperature. Instead, restricting our analysis to photon scattering rate and the force suffices to determine whether the action of the weak repumper serves to heat or cool the atomic ensemble.

^(d)This is verified only provided that $\mathcal{F}(0) = 0$, $\alpha < 0$ and that the velocity distribution covers a region where the terms $\mathcal{F} = -\alpha v$ and $\mathcal{D} = \mathcal{D}(0)$ are dominant.

The evolution of the density matrix ρ is obtained through the optical Bloch equations (OBE):

$$i \frac{d}{dt} \hat{\rho} = \frac{1}{\hbar} [\hat{V}_{AL}, \hat{\rho}] + i \left(\frac{d\hat{\rho}}{dt} \right)_{\text{spont. emis.}} \quad (3.9)$$

Since the temperature $T = m\langle v^2 \rangle / k_B$ verifies $T \ll \Gamma/k$ in the situation we are considering, (13 mK for lithium), the atomic velocities are such that the dynamics of the center-of-mass is much slower than that of the internal degrees of freedom and we can assume that the internal variables are in quasi-stationary state. We can then replace full time derivatives on the left hand side of (3.9) by a partial spatial derivative times the atomic velocity

$$\frac{d}{dt} \rightarrow v \frac{\partial}{\partial z}.$$

Using $\Omega_i(z) = \Omega_i \cos(kz + \phi_i)$, and setting $\hbar = k = 1$:

$$iv \frac{\partial \rho_{22}}{\partial z} = -2i\Omega_2(z) \text{Im} \rho_{23} + i \frac{\Gamma}{2} \rho_{33} \quad (3.10)$$

$$iv \frac{\partial \rho_{11}}{\partial z} = -2i\Omega_1(z) \text{Im} \rho_{13} + i \frac{\Gamma}{2} \rho_{33} \quad (3.11)$$

$$iv \frac{\partial \rho_{23}}{\partial z} = (\delta_2 - i \frac{\Gamma}{2}) \rho_{23} + \Omega_2(z) (\rho_{33} - \rho_{22}) - \Omega_1(z) \rho_{21} \quad (3.12)$$

$$iv \frac{\partial \rho_{13}}{\partial z} = (\delta_1 - i \frac{\Gamma}{2}) \rho_{13} + \Omega_1(z) (\rho_{33} - \rho_{11}) - \Omega_2(z) \rho_{12} \quad (3.13)$$

$$iv \frac{\partial \rho_{21}}{\partial z} = (\delta_2 - \delta_1) \rho_{21} + \Omega_2(z) \rho_{31} - \Omega_2(z) \rho_{23}. \quad (3.14)$$

I have solved these equations using two different methods, the solutions yield the expression of $\mathcal{F}(v)$ and Γ' . Motivated by the fact that the repumping intensity is much smaller than the principal, we used a perturbative approach using Ω_1 as a small parameter to solve this system, in section 3.4. This approach allows us to understand the mechanisms associated to the presence of the repumper. We further generalize this approach by a non perturbative treatment in terms of continuous fractions based on a previous work [Kosachev and Rozhdestvenskii, 1994, Kosachiov et al., 1997] in section 3.5.

3.4 | The perturbative approach

We perform here a perturbative approach in powers of the repumper Rabi frequency Ω_1 , motivated by the observation that our optimal temperatures were obtained for a weak repumper ($(\Omega_1/\Omega_2)^2 \lesssim .03$). We further simplify it to the case $\phi = 0$, because for a finite phase ϕ , the approximation leads to divergencies at the nodes of wave 2. The validity of our assumptions will be discussed in section 3.5. The expansion of the density matrix reads

$$\rho_{ij} = \sum_l \rho_{ij}^{(l)} (\Omega_1)^l, \quad (3.15)$$

knowing ρ_{ij}^n , we can calculate the force. The friction term corresponds to the first order in an expansion in powers of v and so we write:

$$\rho_{ij} = \sum_{l,k} \rho_{ij}^{(l,k)} (\Omega_1)^l (v)^k. \quad (3.16)$$

Inserting the expansion (3.16) into (3.10-3.14), yields the relations:

$$\frac{\partial \rho_{11}^{(l,k-1)}}{\partial z} = -2 \cos(z) \text{Im} \rho_{13}^{(l-1,k)} + \frac{\Gamma}{2} \rho_{33}^{(l,k)} \quad (3.17)$$

$$\frac{\partial \rho_{22}^{(l,k-1)}}{\partial z} = -2 \Omega_2(z) \text{Im} \rho_{23}^{(l,k)} + \frac{\Gamma}{2} \rho_{33}^{(l,k)} \quad (3.18)$$

$$i \frac{\partial \rho_{13}^{(l,k-1)}}{\partial z} - (\delta_1 - i \frac{\Gamma}{2}) \rho_{13}^{(l,k)} = \cos(z) (\rho_{33}^{(l-1,k)} - \rho_{11}^{(l-1,k)}) - \Omega_2(z) \rho_{12}^{(l,k)} \quad (3.19)$$

$$i \frac{\partial \rho_{23}^{(l,k-1)}}{\partial z} - (\delta_2 - i \frac{\Gamma}{2}) \rho_{23}^{(l,k)} = \Omega_2(z) (\rho_{33}^{(l,k)} - \rho_{22}^{(l,k)}) - \cos(z) \rho_{21}^{(l-1,k)} \quad (3.20)$$

$$\delta \rho_{21}^{(l,k)} + i \frac{\partial \rho_{21}^{(l,k-1)}}{\partial z} = \Omega_2(z) \rho_{31}^{(l,k)} - \cos(z) \rho_{23}^{(l-1,k)}. \quad (3.21)$$

with $\rho_{ij}^{(k,l)} = 0$ if $k < 0$ or $l < 0$. The $\rho_{ij}^{(k,l)}$ coefficients can thus be obtained recursively. To lowest non-vanishing order in Ω_1 , we eventually find:

$$\alpha = -\frac{\Omega_1^2}{2\pi} \int_0^{2\pi} dz \sin(z) \left(\Omega_2 \text{Re} \rho_{23}^{(2,1)} + \text{Re} \rho_{13}^{(1,1)} \right). \quad (3.22)$$

For the spontaneous emission rate we get:

$$\Gamma' = \Gamma \frac{(\Omega_1)^2}{2\pi} \int_0^{2\pi} dz \rho_{33}^{(2,0)}. \quad (3.23)$$

The expressions of $\rho_{33}^{(2,0)}$, $\text{Re} \rho_{23}^{(1,1)}$ and $\text{Re} \rho_{13}^{(2,1)}$ expressed in terms of lower-order coefficients are given in appendix (A.2).

We compare in figure 3.5 the experimental temperature with our findings for the friction coefficient (3.22) and spontaneous emission rate (3.23) as a function of detuning δ for a principal detuning $\delta_2 = 2\pi \times 27$ MHz and in appendix A.3 for 17 MHz and 10 MHz.

An analysis of figure 3.5 yields a first qualitative understanding of the temperature dependence on the Raman detuning δ . First, we notice that the spontaneous emission rate drops at the Raman condition, precisely where the temperature is minimum. Second, we observe two sign reversals in the friction coefficient, one centered around $\delta_1 = 0$, corresponding to the resonance of the probe beam with the $|1\rangle \rightarrow |3\rangle$ transition. A second one is centered on the Raman condition, from cooling ($\alpha > 0$) on the red of this transition to heating ($\alpha < 0$) on the blue (the friction coefficient displays an unphysical divergence on the Raman condition due to the assumptions of our model, that will be resolved in section 3.5). Let us explicit the mechanisms responsible for these features.

First, the decrease in emission rate is due to the existence of a dark state ($|\text{NC}\rangle$) in the three-level system when the two frequencies fulfil the Raman condition $\delta = 0$. This dark state reads:

$$|\text{NC}\rangle = (\Omega_2 |1\rangle - \Omega_1 |2\rangle) / \sqrt{\Omega_1^2 + \Omega_2^2}. \quad (3.24)$$

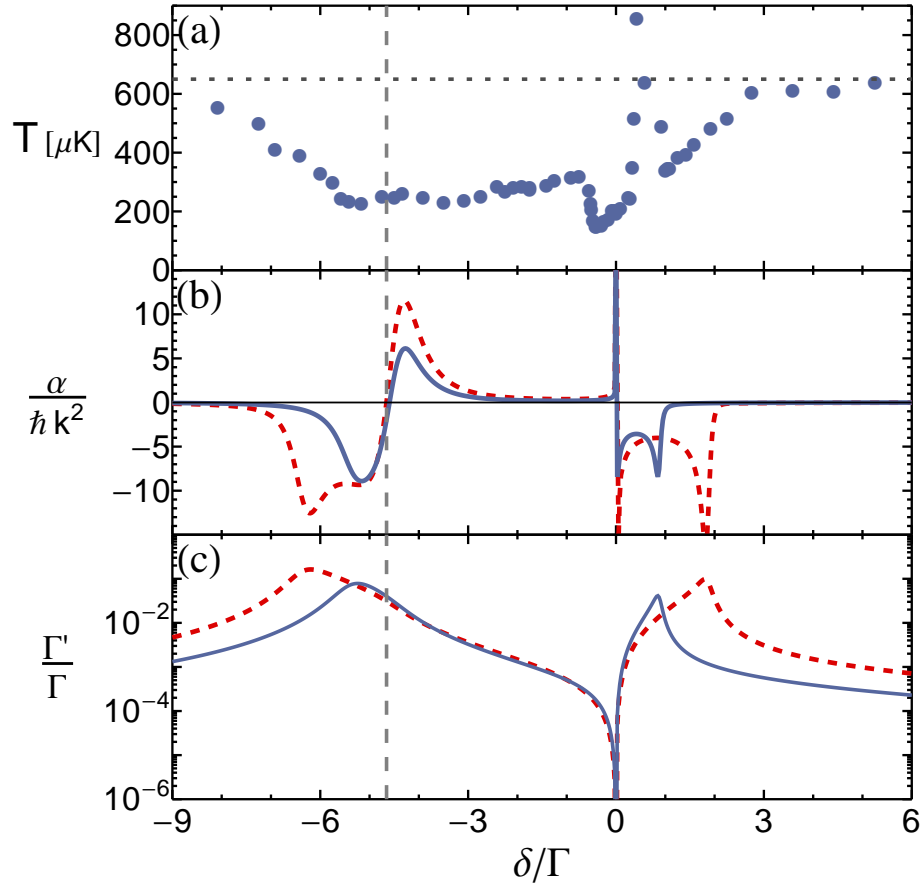


Figure 3.5: Cooling efficiency as a function of the repumper detuning δ . Top: Experimental temperature, same as fig. 3.3. Middle: Friction coefficient α , showing a sign reversal from cooling to heating at $\delta = 0$. Bottom: Spontaneous emission rate $\Gamma' = \Gamma \rho_{33}$, showing a drop around the Raman condition ($\delta = 0$) due to the presence of a dark state. In the middle and bottom panels, we plot our results for two different principal beam Rabi frequency Ω_2 , because we have only an approximate idea of this parameter in the real 3D situation with random relative phase (red solid line $\Omega_2 = 3.4\Gamma$, blue: $\Omega_2 = 2.1\Gamma$).

The presence of this dark state and a reduced spontaneous emission rate indicates that the Raman condition creates a new grey molasses cooling mechanism much like the one described earlier. In addition, we need to understand why the probe's action results in cooling to the red of the Raman condition $\delta < 0$ and turns into a strong heating to the blue $\delta > 0$ ^(e). Since the probe's effect is amplified only close to the Raman condition, we will focus on this range.

For this purpose, we make use again of the dressed-atom picture: since our principal beam is much stronger than the probe, we will consider the levels $|2\rangle$ and $|3\rangle$ dressed by the strong pump beam, and try to understand the effect of the probing of these by the level $|1\rangle$ coupled with the repumper light. The dressing of $|2\rangle$ and $|3\rangle$ by the strong light with Rabi frequency $\Omega_2(z)$ gives rise to an Autler-Townes doublet structure which follows the spatial modulation of the standing wave:

$$|2'\rangle \propto |2\rangle - i\Omega_2(z)/\delta_2 |3\rangle \quad (3.25)$$

$$|3'\rangle \propto -i\Omega_2(z)/\delta_2 |2\rangle + |3\rangle. \quad (3.26)$$

Since our pump beam is far detuned $\delta_2 \gg \Omega_2$, the state $|2'\rangle$ carries very little $|3\rangle$ character while $|3'\rangle$ is mostly comprised of the excited state $|3\rangle$. As a consequence $|3'\rangle$ has a short life time: $\Gamma^{|3'\rangle} \simeq \Gamma$, while $|2'\rangle$ has a long lifetime modulated in space

$$\Gamma^{|2'\rangle} = \Gamma(\Omega_2(z)/\delta_2)^2 \ll \Gamma^{(f)}. \quad (3.27)$$

We note in addition that these two states are light-shifted. Their position in δ are:

$$\delta^{|3'\rangle} \simeq -\delta_2 - \Omega_2(z)^2/\delta_2 \quad (3.28)$$

$$\delta^{|2'\rangle} \simeq \Omega_2(z)^2/\delta_2 \quad (3.29)$$

These dressed states are usually represented in the form of a cascade of states where each doublet is separated by a pump photon (fig. 3.6). Finally we reintroduce by hand the effect of the repumping radiation coupling $|1\rangle$ to the radiative cascade. The coupling rates can be approximated by:

$$\gamma_{|1\rangle \rightarrow |2'\rangle} \sim \frac{\Omega_1(z)^2}{2} \frac{\Gamma^{|2'\rangle}(z)}{(\Gamma^{|2'\rangle}(z)/2)^2 + (\delta - \delta^{|2'\rangle}(z))^2} \quad (3.30)$$

$$\gamma_{|1\rangle \rightarrow |3'\rangle} \sim \frac{\Omega_1(z)^2}{2} \frac{\Gamma}{(\Gamma/2)^2 + (\delta - \delta^{|3'\rangle}(z))^2} \quad (3.31)$$

This approximation treats the three level system like two two-levels systems. ($|1\rangle$ and $|2'\rangle$, and $|1\rangle$ and $|3'\rangle$), it is valid provided many-repumping-photon effects can be neglected which is verified in the range $|\delta| > \Gamma(\Omega_2/\delta_2)^2$ (out of the Raman resonance).

^(e)This situation is somehow inverse from the 'normal' grey molasses cooling mechanism in which one needs a blue detuning $\Delta > 0$ to cool.

^(f)This is an approximation, at the antinodes of the intense wave $\Gamma^{|2'\rangle}$ can be equal to a fraction of Γ .

We can now try to understand how atoms lose or gain energy by cycling through the radiative cascade, as a function of δ . To understand effects on the temperature, we can consider only spontaneous emission events out of $|2'\rangle$ to $|1\rangle$ whose rate is given by (3.27). Indeed a coherent transfer from $|1\rangle$ to $|2'\rangle$ does not extract energy from the atomic ensemble

First, for repumper detunings between $\delta^{|3'\rangle}$ and 0, Fig. 3.6(b), we predict cooling. For this region, the atoms are initially pumped into $|3'\rangle$. Here the light shift modifies the relative detuning, favoring coupling near the nodes of the light. Since $|3'\rangle$ has a very short lifetime, spontaneous decay drops the atoms near to the nodes of the longer-lived $|2'\rangle$, and they travel up the potential hill into regions of larger light shift before decaying, yielding cooling and a positive α . Second, for the case of the repumper tuned slightly blue of the narrow doublet state, $\delta > \delta^{|2'\rangle}$, shown in Fig. 3.6(a), the atoms are pumped directly from $|1\rangle$ into $|2'\rangle$. However, this pumping happens preferentially at the antinodes of the standing wave as the repumper intensity is greatest, the linewidth of $|2'\rangle$ is the largest, and the light shift minimizes the detuning of the repumper from the $|1\rangle \rightarrow |2'\rangle$ transition for the $\phi = 0$ case considered here. On average, the atoms exit this state at a point with a smaller light shift through a spontaneous emission process either into the cascade of dressed states or directly back to $|1\rangle$. As a result, we expect heating and $\alpha < 0$ in this region. The negative sign of α in the region $\delta < \delta^{|3'\rangle}$ can also be easily understood by the same means.

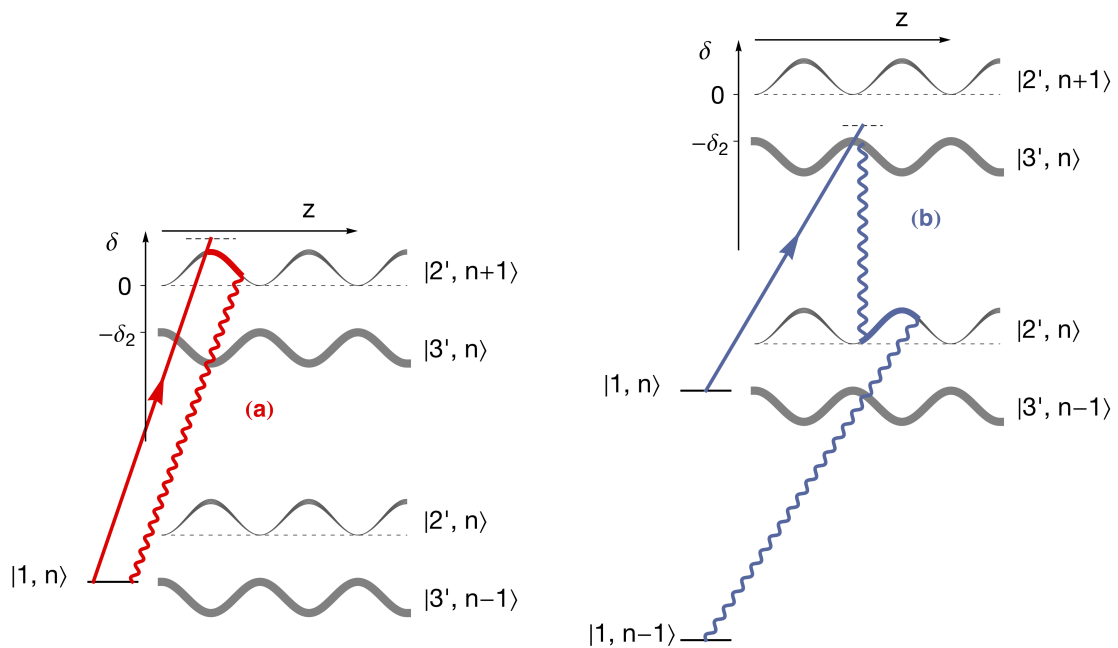


Figure 3.6: The cascade of levels dressed by transition 2, the space-varying light shift and linewidth are represented. Traces show typical cycles of atoms pumped from $|1\rangle$ and back depending on the detuning of wave 1. The detuning of the repumper modulates the entry point into the cascade of the dressed states. Trace (a) represents a typical cycle for $\delta > 0$ leading to heating, on the right, trace (b) shows a cycle for $\delta < 0$ which leads to the cooling feature observed experimentally.

We conclude this section by stating that the experimentally observed change of sign of the force close to the Raman condition is qualitatively well described in our perturbative model. The model further reveals the importance of Raman coherence and the existence of a dark state. The dark state together with the friction coefficient associated with cycles represented in figure 3.6(b) correspond to a cooling mechanism analogous to that of grey molasses. In this way, the bichromatic system provides an additional grey molasses scheme involving both hyperfine states which complements the grey molasses cooling scheme on the principal transition. On the other hand, when the friction coefficient is negative in the vicinity of the two-photon resonance, it turns into a heating mechanism that overcomes the standard grey molasses operating on the $F = 2 \rightarrow F' = 2$ transition.

The perturbative approach analyzed in terms of the dressed cascade has successfully revealed the mechanisms responsible for the experimental temperature. However it also possesses some shortcomings. First α displays a divergence on the Raman condition, this divergence is due to a breakdown of the validity of our perturbative approach at the RC where Ω_1 is not the smallest scale in the problem ($\delta \rightarrow 0$). Second, for the assumption $\Omega_2/\Omega_1 \gg 1$ to hold and the perturbative approach to be valid, we had to make the assumption that the two waves are exactly in phase with each other $\phi = 0$. This is not verified experimentally, where the geometry of our cooling beams (6 counter-propagating beams in 3 dimensions) creates a spatially-varying phase and an atom moving across the laser field will in general experience all possible phases. We wish then to calculate a phase-averaged force:

$$\langle \mathcal{F}(v) \rangle_\phi = \frac{1}{2\pi} \int_0^{2\pi} \mathcal{F}(v, \phi) d\phi. \quad (3.32)$$

Furthermore using (3.24) the dark state is space-dependent for a non-zero phase because the ratio $\Omega_1(z)/\Omega_2(z)$ varies in space. We must then also calculate a phase-average spontaneous emission-rate and check whether the physical picture derived with the perturbative approach still holds.

3.5 | The continued fractions approach

This can be realized using a more general approach based on the projection of the density matrix on the Fourier basis:

$$\rho_{ij} = \sum_{n=-\infty}^{n=+\infty} \rho_{ij}^{(n)} e^{inkz} \quad (3.33)$$

Injecting this expansion in (3.10-3.14) yields recursive relations between different Fourier components of ρ . Kozachiov *et al.* [Kosachev and Rozhdestvenskii, 1994, Kozachiov *et al.*, 1997] express the solutions of these relations for a generalized Λ system in terms of continued fractions. We have used their results to numerically solve the Bloch equations. We then compute the force $\mathcal{F}(v)$ to arbitrary order of Ω_1 and extract α by means of a linear fit to the

small- v region.

First, in figure 3.7 we compare the numerical results for α to our perturbative expansion, for $\phi = 0$, where we see that the features derived above still hold. Additionally the divergence at $\delta = 0$ has been regularized in the numerics. Another noticeable difference we note is that the magnitude of the friction coefficient near the two resonances is reduced in the continued fraction approach whereas away from the resonance the two approaches agree. This points out the importance of many-repumper-photons processes near resonance, processes absent in the perturbative approach.

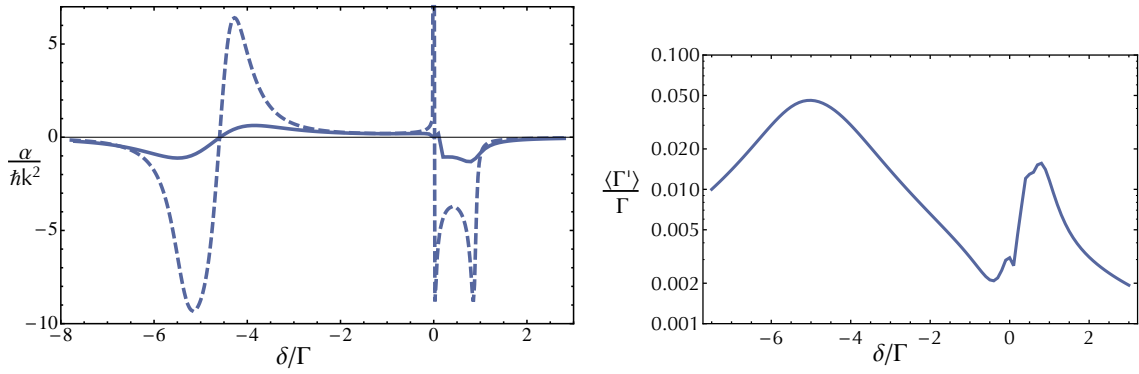


Figure 3.7: Left : Comparison of results using the perturbative calculation (dashed), and the continued fractions (solid) for the $\phi = 0$ case, with the same parameters as in Fig. (3.5) and $\Omega_2 = 2.1\Gamma$. Right: Continued fractions solution of the photon scattering rate $\Gamma' = \Gamma \rho_{33}$ averaged over all relative phases of the repumper and principal standing waves as a function of the two-photon detuning δ . Velocity-dependent effects are taken into account here by computing an average of $\langle \Gamma' \rangle_\phi(v)$ weighed by a Maxwell-Boltzmann velocity distribution at $200 \mu\text{K}$.

Next, in figure 3.7 we plot the spontaneous emission rate calculated by continued fractions. This rate does not reach 0 at the Raman condition because the dark state is space-dependent for a finite dephasing and the atoms can be motionally coupled out of this state. To take into account these velocity-dependent effects we plot Γ' averaged over all relative phases and velocities, weighed by a thermal Maxwell-Boltzmann distribution with temperature $T = 200 \mu\text{K}$. $\langle \Gamma' \rangle$ retains a minimum near the Raman condition, in agreement with our previous findings.

Finally in figure 3.8 we plot $\langle \mathcal{F} \rangle_\phi(v)$ for six different detunings δ . We recall that the force leads to cooling when $(\mathcal{F}(v) \times v) < 0$ for all v in the velocity distribution of the atomic ensemble whose extent is given by the thermal velocity $v_{\text{th}} = \sqrt{k_B T/m}$. We thus plot in figure 3.8 $\langle \mathcal{F} \rangle_\phi(v)$ with v in units of v_{th} . The forces displayed are in good qualitative agreement with the findings of the continued fraction approach, with a cooling character when $\delta < 0$, a sign reversal at $\delta = 0$ and a heating force for $\delta > 0$.

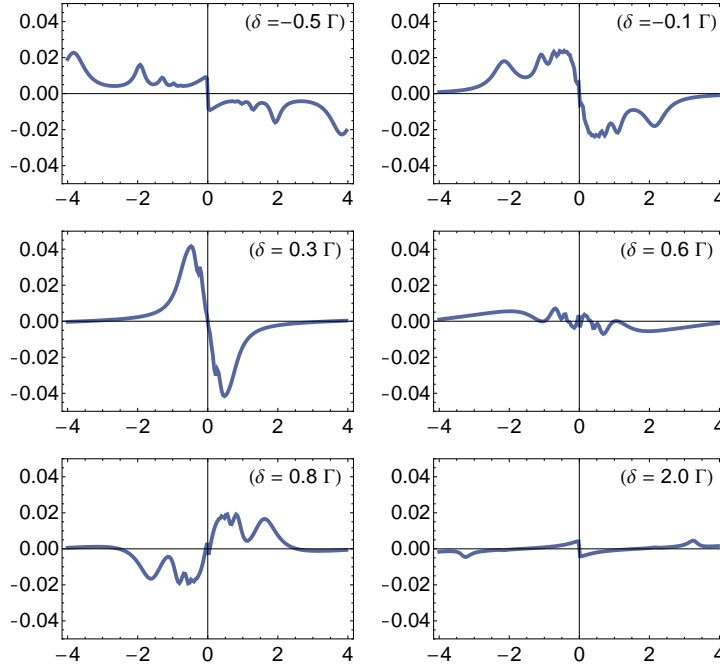


Figure 3.8: $\langle \mathcal{F} \rangle_\phi$ as a function of v for different values of δ around $\delta = 0$. Vertical units: $1/\hbar k \Gamma$, horizontal units: the thermal velocity at $T = 200 \mu\text{K}$, $v_{\text{th}} = \sqrt{k_B T/m}$.

We can now conclude on our theoretical investigation of the effect of the Λ configuration. We have showed that this configuration creates an additional grey-molasses cooling mechanism with a dark state present at the Raman condition, a motional coupling due to the space dependence of this dark state and a cooling mechanism in the radiative cascade for $\delta < 0$. An identical study has been later performed on potassium leading to the same conclusions [Nath *et al.*, 2013]. A complete study, taking into account the Zeeman degeneracy of the hyperfine states can be performed, either by a numerical resolution of the optical Bloch equations for the full system, or by a quantum Monte-Carlo approach [Dalibard *et al.*, 1992], such a work focusing on ${}^6\text{Li}$ is under progress [Sievers, F. and Wu, S., 2014].

Conclusion

As a general conclusion on grey molasses, we note that this method represents a substantial gain in temperature from laser cooling and in the subsequent phase density. Following the work in our group, a number of experimental teams have implemented this scheme [Salomon *et al.*, 2013, Nath *et al.*, 2013, Burchianti *et al.*, 2014], and another technique successfully implementing sisyphus cooling on lithium has reached similar performances, with the possibility to use far-from-resonant light [Hamilton *et al.*, 2014].

The situation on our experiment is special because we need to cool and trap simultaneously ${}^6\text{Li}$ and ${}^7\text{Li}$, while the D_1 line of ${}^7\text{Li}$ is very close to the D_2 line of ${}^6\text{Li}$. This correspondence results in a strong heating of the ${}^6\text{Li}$ cloud when implementing a D_1 molasses on ${}^7\text{Li}$, that cannot be compensated by keeping the ${}^6\text{Li}$ MOT light. It might be solvable by implementing simultaneous D_1 molasses on ${}^7\text{Li}$ and ${}^6\text{Li}$. Otherwise the use of the off-resonant technique of ref. [Hamilton et al., 2014] could allow to avoid exciting the D_2 transition of ${}^6\text{Li}$. We also would like to point-out that the Doppler cooling that we perform in the compressed magnetic trap cools to temperatures comparable or lower than achieved with a cloud cooled by grey molasses before being loaded in the magnetic trap. The advantage of grey molasses is found on our experiment in fact in the transport to the upper appendix, where the cold temperature protects the ${}^7\text{Li}$ cloud from being clipped by the walls of the appendix and we can reach 100 % efficiency for this transport instead of 40% in the absence of D_1 cooling.

The best opportunity opened by grey molasses on lithium is to avoid the magnetic trapping stage to load directly in an optical trap. With a temperature of $60\ \mu\text{K}$ the laser power necessary to realise a sufficient trap depth can be easily achieved as shown recently in [Burchianti et al., 2014, Salomon et al., 2014].

Chapter 4 |

Three-body losses in strongly interacting Bose gases

As discussed in chapter 1.4, dedicated to the physics of interacting Bose gases, one of the main objectives of this research field is to study degenerate Bose gases under resonant interactions. However this task is rendered experimentally challenging by the instability of Bose gases with large scattering length, caused by three-body losses. In this chapter, we present an experimental study of these losses, in the vicinity of a Feshbach resonance.

4.1 | Three-body losses

Three-body losses originate from the recombination of three free atoms into a bound dimer and a free atom (Fig. 4.1). During these inelastic collisions, the binding energy of the dimer is released into kinetic energy of the products. The binding energy is usually higher than the trap depth U_0 and the products evade the trapping potential.

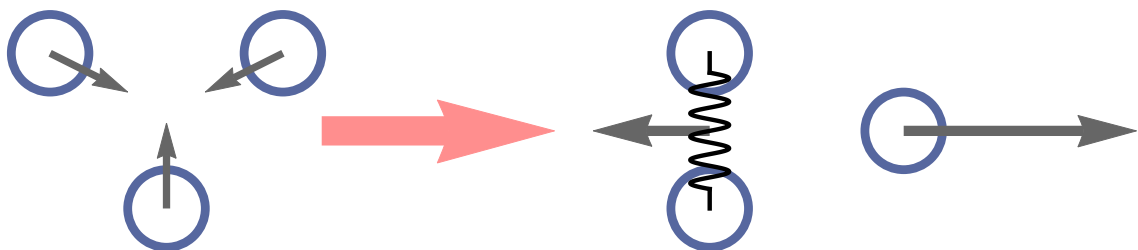


Figure 4.1: Schematical representation of a three-body recombination event. Left, initial state of a 3-body collision involving 3 free atoms. Right, final state corresponding to an inelastic collision forming a free atom and a bound dimer (represented by the spring). Both products carry the binding energy of the dimer as kinetic energy.

If we neglect one- and two- body losses, the local equation for the density n as a function of time in a dilute gas is:

$$\frac{dn}{dt} = -L_3 n^3 \quad (4.1)$$

where L_3 is called the 3-body loss constant. By integration over the volume, we get for the total number of bosons in the trap

$$\frac{dN}{dt} = -L_3 \langle n^2 \rangle N \quad (4.2)$$

where $\langle \dots \rangle$ means an average over the whole gas volume. Considering the case of a gas at zero temperature with universal interactions described solely by the scattering length a , assuming three-body losses are also described by the scattering length, then dimensional analysis yields

$$L_3 \propto \hbar a^4 / m. \quad (4.3)$$

This a^4 scaling was also derived formally in [Fedichev *et al.*, 1996]. So losses are enhanced when increasing a and we expect ultracold gases to be unstable in the vicinity of a Feshbach resonance. Dimensional analysis based on two-body parameters however does not yield the exact expression of L_3 because it is based only on the scattering length. We discussed the case of fermions in chapter 1, the relaxation to deeply-bound dimer states is strongly reduced due to Pauli blocking. Oppositely bosons easily decay to dimer states, the a^4 scaling is correct in a first approximation, but it is modulated as a function of a . This modulation comes from the solution of the three-body problem for resonant two-body scattering. It is illustrated in figure 4.2 extracted from [Gross *et al.*, 2010] where we see data for L_3 (called K_3 in the figure) obtained for ^7Li , the underlying a^4 scaling (dashed line) and the modulated theory (solid red line). Let us explain this modulation of the a^4 scaling.

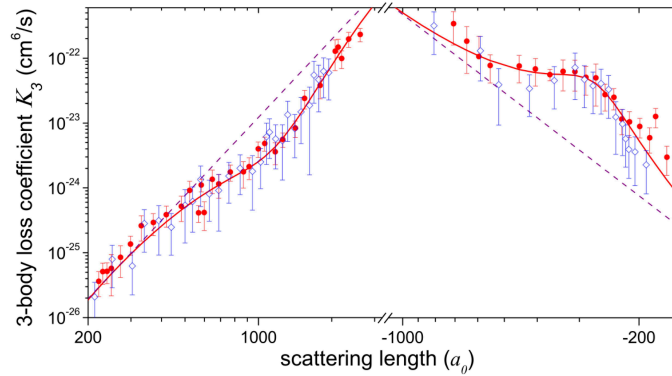


Figure 4.2: Three body recombination constant L_3 (called here K_3) as a function of a through a Feshbach resonance, from [Gross *et al.*, 2010]. Blue and red points show the experimental data. The dashed purple lines show the underlying a^4 scaling and the solid red line show the theory from a solution of the three-body problem, see main text below.

4.2 | A glance at Efimov Physics

The 3-body problem for a resonant short-range 2-body interaction was studied by V. Efimov [Efimov, 1970, Efimov, 1973]. He showed that at unitarity ($1/a = 0$) there exists an infinite

series of trimers (3-body bound states) with energy

$$E_n = -\frac{\hbar^2}{mR_t^2} e^{2\pi n/s_0} \quad (4.4)$$

where n refers to the n -th trimer and $s_0 = 1.00624$. R_t is a length specific to the three-body problem, which characterizes fully the trimer states properties such as energy and spatial extent. The energy of these trimers varies as a function of $1/a$ as represented in figure 4.3, it reaches the free atom continuum at $a = a_n < 0$. The log-periodicity present in the trimer's energies at $1/a = 0$ is reflected in the series a_n :

$$a_{n+1} = a_n e^{\pi/s_0} \simeq 22.7 a_n. \quad (4.5)$$

For $a > 0$, their energy eventually meets the energy of the universal dimer ($-\hbar^2/ma^2$) at $a = a_n^+$ and the trimers become indistinguishable from a free atom and one dimer (fig. 4.3). The resonances of trimers energies with the dimers or with the continuum are responsible for a modulation of the three-body loss constant L_3 [Esry and Greene, 1999, Bedaque et al., 2000, Braaten and Hammer, 2001], which is enhanced for $a = a_n$ and reduced for $a = a_n^+$. These resonances have been measured experimentally [Kraemer et al., 2006], demonstrating the existence of Efimov trimers 30 years after their theoretical prediction.

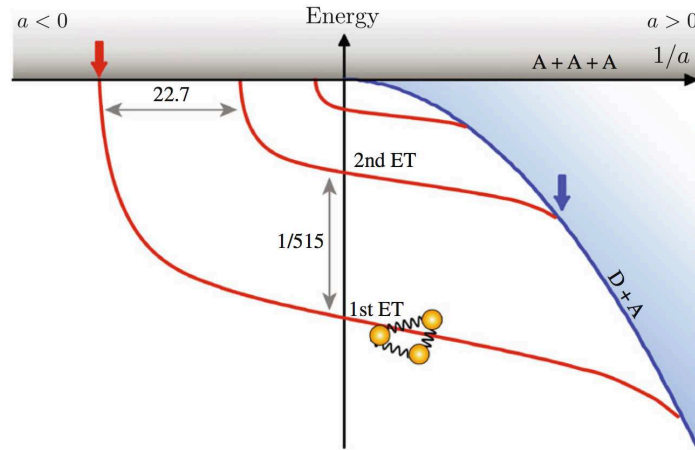


Figure 4.3: Representation of the energy of the Efimov trimers (ET) (red solid lines) and of the universal dimer (blue) as a function of $1/a$ taken from [Ferlandino et al., 2011]. The resonances in three-body recombination happen when the energy of a trimer meets the free atom continuum on the $a < 0$ side (red arrow) and when it joins the dimer energy on the $a > 0$ side (blue arrow). This picture was derived by V. Efimov.

An additional parameter enters the expression of L_3 : the ‘inelasticity parameter’ η_3 . It gives the probability amplitude for recombination (loss) to occur when three atoms are in contact $P_{\text{loss}} = \exp(-2\eta_3)$ so that finally, L_3 depends on three parameters (a, R_t, η_3):

$$L_3 = \frac{\hbar}{m} a^4 C\left(\frac{a}{R_t}, \eta_3\right) \quad (4.6)$$

with $C(a/R_t, \eta_3)$ a log-periodic function: $C(a/R_t, \eta_3) = C(22.7a/R_t, \eta_3)$. The analytical form of C has been derived [Braaten and Hammer, 2001], and using R_t and

η_3 as fit parameters one can predict accurately the three-body recombination rate [Kraemer *et al.*, 2006, Zaccanti *et al.*, 2009, Gross *et al.*, 2010] (solid red line in fig. 4.2). R_t and η_3 are a priori specific to each species and are extracted from the experimental data. Recent theoretical and experimental works though propose a universal description of three-body recombination in terms of the Van der Waals length of the interaction potential and the strength of the Feshbach resonance s_{res} [Wang *et al.*, 2012, Naidon *et al.*, 2014, Wang and Julienne, 2014].

4.3 | Results on the stability of a unitary Bose gas

The theoretical expression (4.6) is valid at zero temperature, that is for $1/k_{\text{th}} > a$ with k_{th} the thermal wave-vector:

$$k_{\text{th}} = \sqrt{mk_{\text{B}}T}/\hbar = \sqrt{2\pi}/\lambda_{\text{dB}}. \quad (4.7)$$

Thus this theory cannot describe three-body losses in a unitary Bose gas at finite temperature ($k_{\text{th}}a \gg 1$). To infer the limit $L_3(a \rightarrow \infty)$, we can make a parallel with the 2-body problem where when a diverges it drops out of the cross-section expression (1.27). It is then replaced by the only length scale left : $1/k_{\text{th}}$. Performing the same replacement for L_3 we obtain:

$$L_3 \underset{ka \gg 1}{=} D(k_{\text{th}}R_t, \eta_3) \frac{\hbar}{mk_{\text{th}}^4} \quad (4.8)$$

where D is now the equivalent to C . We can guess that the transition from (4.6) to (4.8) happens around $k_{\text{th}}a = 1$ but this does not yield an analytical prediction. During the first year of my PhD we studied experimentally the lifetime of a non-condensed (thermal) Bose gas in the strongly interacting and unitary cases, in collaboration with D. Petrov and F. Werner who derived an analytical model extending from $k_{\text{th}}a \ll 1$ to $k_{\text{th}}a \gg 1$ [Rem *et al.*, 2013]. These results have been thoroughly presented in [Rem, 2013] and we will summarize here the main findings.

Our results have been obtained by studying the decay of the atom number in our gases at different scattering lengths and temperatures. The preparation of these gases has been presented in chapter 2, with this preparation we can adjust freely the temperature of the gas and the magnetic field. According to (4.8), three-body losses depend on temperature, so to facilitate the analysis, we ensure that the temperature does not change during the evolution.

A uniform temperature is stabilized by elastic two-body collisions. The collision rate for one atom in the gas is given by $1/\tau_2 = n\sigma v$ where σ is the cross-section and v the velocity of the atom. After a few collision times, equilibrium is reached. Thus the timescale to reach equilibrium is given by $\gamma_2 = \langle n \rangle \sigma \langle v \rangle$. If three-body losses happen faster than this rate, the gas remains out-of-equilibrium during its evolution. The loss rate using (4.2) is:

$$\gamma_3 = -\frac{1}{N} \frac{dN}{dt} = L_3 \langle n^2 \rangle. \quad (4.9)$$

So the equilibrium condition is $\gamma_3/\gamma_2 \ll 1$. For a Boltzmann gas $\langle v \rangle \propto \hbar k_{\text{th}}/m$ and $\langle n \rangle$, $\langle n^2 \rangle$ are easily calculated using (1.16). Furthermore at unitarity, replacing k_{th} by its expression yields without difficulty [Li and Ho, 2012]:

$$\frac{\gamma_3}{\gamma_2} \propto (1 - e^{-4\eta_3}) n \lambda_{\text{dB}}^3 \ll 1 \quad (4.10)$$

So we find that the stability against three-body losses is guaranteed for low phase-space densities $n \lambda_{\text{dB}}^3$, in which case the gas remains in a quasi thermal equilibrium during its evolution.

We verified experimentally that the gases are well described by a Boltzmann distribution (1.16). We could then measure the total number of atoms N and the temperature T , and control a varying the magnetic field B using the Feshbach resonance in the $|1_b\rangle$ state of ${}^7\text{Li}$ at 738 G. The number N as a function of time is given by the solution to (4.2):

$$N(t) = \frac{1}{\sqrt{2t/\tau + N_0^{-2}}} \quad (4.11)$$

$$\tau^{-1} = L_3 \frac{m^3 \bar{\omega}}{24\sqrt{3}\pi^3 (k_{\text{B}}T)^3} \quad (4.12)$$

with N_0 the initial number of atoms and $\bar{\omega}$ the mean trapping frequency. By recording N as a function of time at fixed values of (T, B) and fitting the results with eq. (4.11) we could extract $L_3(a, T)$.

In the case $k_{\text{th}}a \ll 1$ L_3 does not depend on temperature and is constant over the gas. On the other end at unitarity $k_{\text{th}}a \gg 1$, (4.8) yields $L_3 \propto 1/T^2$. The exact expression for (4.8) has been derived by D. Petrov and F. Werner [Rem et al., 2013], it describes $L_3(a, T, R_t, \eta_3)$ for all values of $k_{\text{th}}a$ with $a < 0$. As expected a modulation of the $1/T^2$ scaling due to Efimov Physics is present in the theory but is very weak for our case of equal-mass bosons (variation of about 3%). As a consequence to a good approximation we can neglect this modulation and R_t does not enter in the expression of L_3 , which depends then solely on T and η_3 . This expression reads:

$$L_3 \approx \frac{\hbar^5}{m^3} 36\sqrt{3}\pi^2 \frac{1 - e^{-4\eta_3}}{(k_{\text{B}}T)^2} \quad (4.13)$$

where the numerator $1 - e^{-4\eta_3}$ can be understood as the efficiency for three-body recombination when three atoms are in contact, and the probability of contact varies like $1/T^2$. Measuring $L_3(T)$ at $1/a = 0$ in ${}^7\text{Li}$ gases, we could compare our results with this prediction using the value of η_3 measured in [Gross et al., 2010], with a good agreement as shown in fig. 4.4.

Furthermore, we have extended our studies to observe the saturation of L_3 going the weakly interacting regime to unitarity, in close agreement again with theory, fig. 4.5. On the positive a side of the resonance, three-body recombination can lead to the formation of the shallow dimer with energy $E_b = \hbar^2/ma^2$. For large values of a , this energy is smaller than the trap depth U_0 , this implies that the molecules do not leave the trap. It then becomes

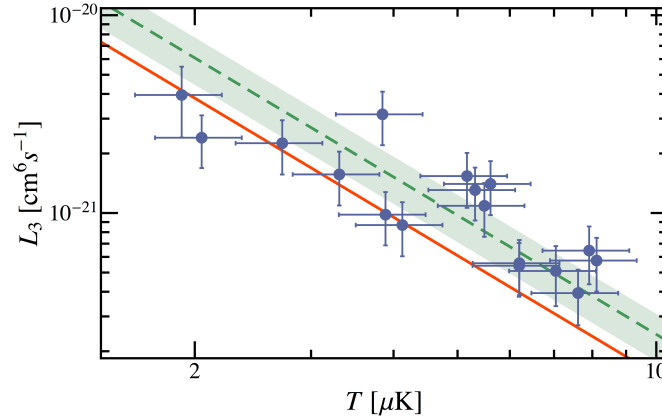


Figure 4.4: Measurements (blue circles) of the three-body recombination constant L_3 as a function of temperature T at unitarity ($1/a = 0$). The green dashed line is a fit with a $L_3(T) = \lambda_3/T^2$ function, yielding $\lambda_3 = 2.5(3)_{\text{stat}}(6)_{\text{syst}} \times 10^{-20} (\mu\text{K})^2 \text{cm}^6 \text{s}$, the green shaded area shows a region with a $1 \times \sigma$ agreement to the fit. The red dashed line is the theoretical prediction (4.13) $\lambda_3 = 1.51 \times 10^{-20} (\mu\text{K})^2 \text{cm}^6 \text{s}$, 40% below the experimental value.

difficult to make a direct relation between losses and three-body recombination rate.

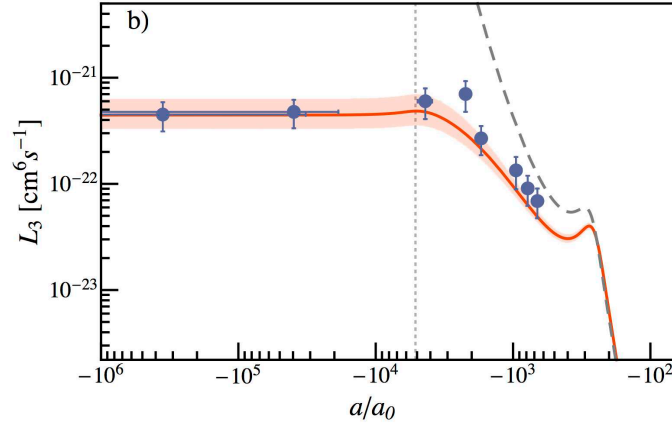


Figure 4.5: Measurements (blue circles) of L_3 as a function of a approaching unitarity, at a temperature of $T = 5.9(6) \mu\text{K}$ (note the log-log scale a_0 is the Bohr radius). The grey dashed line is the zero-temperature theory from [Braaten and Hammer, 2001]. The red solid line is the new theory for L_3 from [Rem et al., 2013], the red shaded area represents the uncertainty due to the spread in the experimental temperature. The grey dotted line shows the value of a for which $a/\lambda_{\text{dB}} = 1$.

Discussion of the constant temperature

The simple model (4.11, 4.12) is based on the assumption (verified experimentally) that the temperature remains constant through time. Let us discuss how this is possible and what it implies. Since the losses increase with density, they occur preferentially at the center of the trap, in this region the atoms have a low potential energy and have a total energy smaller than the ensemble average $E/N = 3k_{\text{B}}T$ for a Boltzmann gas in a harmonic

potential. Thus the remaining atoms have a higher average energy –higher temperature–, so three-body losses in a harmonic trap lead inevitably to heating, as was first shown in [Weber *et al.*, 2003]. This heating is reinforced at unitarity, indeed three-body recombination is momentum-dependent and decreases with increasing kinetic energy of the collision partners. The average energy of an atom lost by three-body recombination is expressed as $\delta k_B T$. δ can be calculated from the density and energy distribution of a Boltzmann ensemble and from the energy dependence of the losses, yielding $\delta = 5/3$ for a unitary Bose gas [Rem *et al.*, 2013]. We have for the total energy $\dot{E}_{3b} = (3 - \delta)k_B T \dot{N}_{3b}$

Thus in the absence of evaporation one expects the gas temperature to increase as atoms are lost from three-body recombination. The aim of our measurements was to measure the temperature-dependence of the losses and to compare independently with theory. We needed a constant temperature to ensure a constant L_3 through time. This is made possible by the fact that our trap has a finite depth U_0 leading to evaporative losses, caused by two-body elastic collisions which we have neglected so far. The average energy lost per atom by evaporation is much higher than the ensemble average leading to cooling, it is expressed as a function of temperature : $\dot{E}_{ev} = (\eta + \kappa)k_B T \dot{N}_{ev}$ where $\eta = U_0/k_B T$, between $\eta = 6$ and $\eta = 8$ on our experiment. κ is the excess energy of an evading atom with respect to the trap depth, it depends on the trap geometry [Cohen-Tannoudji, Claude, 1997]. For our experiment it is evaluated to be $0.68 \lesssim \kappa \lesssim 0.78$ [Rem *et al.*, 2013].

So finally, it can be easily shown that the condition of constant temperature reads

$$\frac{\dot{N}_{ev}}{\dot{N}_{3b}} = \frac{\delta}{\eta + \kappa - 3}, \quad (4.14)$$

and we find that the loss rate due to evaporation is weaker than the one due to recombination. However we note that neglecting evaporation would lead to an over-estimate of L_3 between 30% and 50% and we have corrected our data taking this into account. In this way we assume a temperature dependence of L_3 only to evaluate a correction to our data.

If one assumes in the analysis the temperature dependence of L_3 , a full model can be built taking evaporation into account, with the knowledge of the trap depth. One then obtains coupled-differential equations for temperature and number, the solution of which can be fitted to the experimental data. Such an analysis has been carried out [Laurent, 2013] yielding a more precise measurement of $L_3 T^2$ at unitarity. An article is in preparation with data from our lithium experiment and results obtained on caesium in the group of C. Chin.

4.4 | Conclusion: stability domain of the strongly interacting Bose gas

We have found earlier that the stability against three-body losses is guaranteed for low phase-space density $n\lambda_{\text{dB}}^3$, but to reach the degenerate regime we need $n\lambda_{\text{dB}}^3 > 1$. The only way to stabilize a unitary Bose gas with high phase-space density is then to have a very small η_3 . This η_3 is specific to each species and so far cannot be varied, we give in table 4.1 a list of the known η_3 for the species in which it has been measured, some of them are more favorable than lithium for investigations of the unitary Bose gas. Replacing λ_{dB} by a in (4.10) we can infer the condition for quasi thermal equilibrium for a $T = 0$ Bose gas:

$$\frac{\gamma_3}{\gamma_2} \propto (1 - e^{-4\eta_3})na^3 \ll 1. \quad (4.15)$$

Species	⁸⁵ Rb	⁷ Li	³⁹ K	¹³³ Cs
η_3	0.06	0.21	0.09	0.06

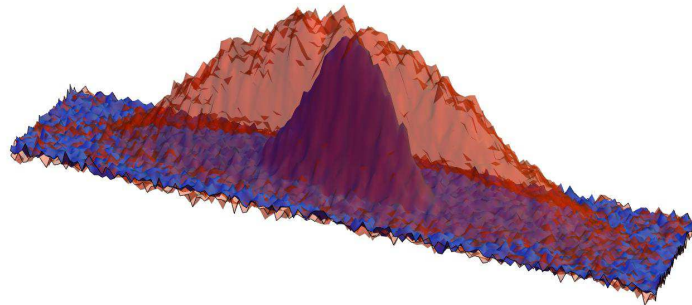
Table 4.1: Inelasticity parameter η_3 for the different species in which it has been measured.

Finally in a degenerate gas at unitarity both a and λ_{dB} diverge and the ratio γ_2/γ_3 may saturate to a density-independent value. This issue has been studied experimentally in [Makotyn *et al.*, 2014] using ⁸⁵Rb, starting from a weakly interacting BEC close to $T = 0$ and ramping the magnetic field rapidly to unitarity. These results indicated that the losses were sufficiently slow as compared to equilibration in the final state, but temperature on this final state was unknown.

To conclude, our results have extended the understanding of three-body recombination near the unitary regime $k_{\text{th}}a > 1$. The universality of these results was confirmed by a similar study on potassium [Fletcher *et al.*, 2013].

Chapter 5 |

Mixtures of Bose and Fermi superfluids



We turn now to the main result of this work, the experimental realization of mixtures of a weakly-interacting Bose-Einstein condensate of ^7Li with a Fermi superfluid of ^6Li in the BEC-BCS crossover. Based on thermometry and other markers, we will demonstrate that the mixtures presented are indeed composed of two superfluids. To the best of our knowledge it is the first production of a system in which a Bose superfluid is mixed with a Fermi superfluid, our results are presented in [Ferrier-Barbut *et al.*, 2014] (in appendix C). We explore this novel system to evidence specific bosons-fermions interaction features. First, using center-of-mass oscillations in the trapping potential, we measure the mean-field interaction between the BEC and the Fermi superfluid. The very long lifetime of these oscillations reveal the superfluid character of the mixture. We further investigate this superfluid feature by driving high-amplitude oscillations where we observe damping above a critical velocity in the relative motion between the superfluids. Extending this study throughout the BEC-BCS crossover uncovers the rich physical content of this novel mixture.

The conditions of existence and stability of a Bose-Fermi superfluid mixture reduce the possible choices of constituents. We have reviewed in the introduction of this work the many different Bose-Fermi mixtures brought to quantum degeneracy thus far, none of them fulfilled all these conditions. In the first section, we analyze the interactions effects and demonstrate that the choice of internal states we have made is indeed suited to realize a stable doubly superfluid mixture.

5.1 | Two-body interactions in the $|1_f\rangle$, $|2_f\rangle$, $|2_b\rangle$ mixture

States	Position (G)	Width (G)	a_{bg} (a_0)
$ 2_b\rangle$	845.5(5)	4.5	-18.24
$ 2_b\rangle$	893.7(4)	-237.8	-18.24
$ 1_f\rangle - 2_f\rangle$	832.18(8)	-262.3(3)	-1582(1)

Table 5.1: Characteristics of the Feshbach resonances in the superfluid mixture.

The doubly-superfluid mixture that we present in the following is composed of ^7Li in the $|2_b\rangle$ state and ^6Li in its two lowest-energy states $|1_f\rangle$ and $|2_f\rangle$, table 5.1 sums up the Feshbach resonances in this mixture. The scattering length in the $|2_b\rangle$ state crosses zero first at 578 G [Shotan *et al.*, 2014] and has two Feshbach resonances, a narrow one centered at 845 G, and a broader one at 894 G. In consequence, a_b is negative for fields $B \leq 578$ G, $B \in [845$ G, 850 G] and $B \geq 894$ G, excepted in these regions, the BEC is stable. The $|1_f\rangle$, $|2_f\rangle$ states have one broad resonance at 832 G, a ^6Li superfluid can be realized around this resonance. The lower magnetic field limit is given by the range of stability of the Feshbach molecules which extends down to $\simeq 600$ G [Jochim *et al.*, 2003a]. For increasing magnetic fields, the limit of superfluidity is due to the exponential drop of T_c on the BCS side, limiting us experimentally to $B \lesssim 890$ G [Navon, 2011]. It turns out that the resonances between ^6Li and ^7Li in this choice of internal states are at too low fields, where $a_b < 0$ and the ^6Li dimers are unstable. Thus the bosons (in $|2_b\rangle$) interact identically weakly with the two fermions states ($|1_f\rangle$, $|2_f\rangle$) with scattering length equal to the background value $a_{bf} = 41 a_0$. Figure 5.1 represents the field dependence of the scattering lengths of interest for our mixture.

Stability against spin-exchange collisions

While Bose-Einstein condensates of ^7Li in the $|2_b\rangle$ state and ^6Li Fermi superfluids in the $|1_f\rangle$, $|2_f\rangle$ states have been obtained and are known to present reasonable lifetimes, a mixture of these three states is not obviously stable. One could think for example of a spin-exchange collision of the sort $|1_f\rangle + |2_b\rangle \rightarrow |2_f\rangle + |1_b\rangle$. The internal energy released in such an event: $E/h \simeq 100$ MHz ($E/k_B \sim 5$ mK) would lead to a direct loss of the products. Calculations by S. Kokkelmans show however that the rate for these processes is rather small: $G \simeq 10^{-16}$ cm³/s with the lifetime of a sample with density n given by $1/\tau = nG$. With our typical densities of the order of 10^{13} cm⁻³, we find $\tau \sim 10^3$ s. Inelastic collisions are not a limiting factor to the lifetime of a $|1_f\rangle$, $|2_f\rangle$, $|2_b\rangle$ mixture. Our experiments confirm the stability of this mixture, with a lifetime of the order of 7 seconds (at 832 G).

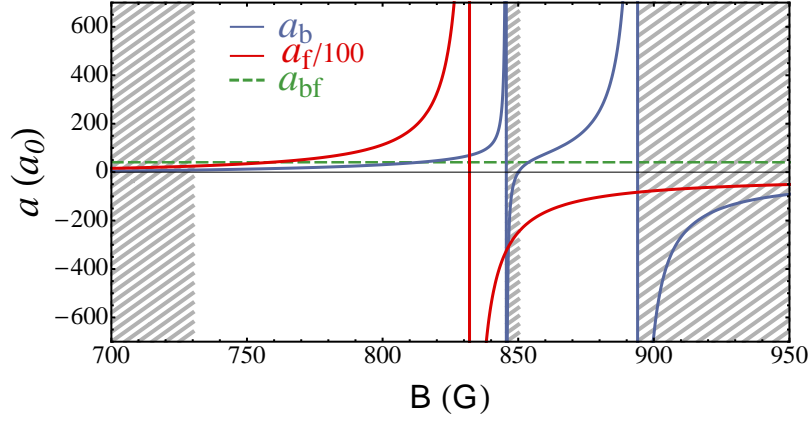


Figure 5.1: Scattering lengths in our superfluid mixture. In blue solid line, the boson-boson scattering length a_b , in red the fermion-fermion a_f (note the 1/100 scaling), and in dashed green the boson-fermion scattering length a_{bf} , which is constant $a_{bf} = 41 a_0$ and identical for both ${}^6\text{Li}$ spin states in the whole region plotted here. The regions of instability of the mixture are hatched, between 845 G and 850 G, and above 894 G the BEC is unstable. Below 730 G the mixture is expected to phase-separate, this limit is only indicative, it is calculated within a mean-field approximation for the ${}^6\text{Li}$ molecular BEC.

5.2 | Mean-field interactions and phase separation

Using the values of the scattering lengths, we can infer the effects of interactions on a superfluid mixture. The weakness of the boson-fermion interaction suggests to describe it by a mean-field approximation as in the weakly-interacting Bose gas case. This approximation reads

$$e(n_b, n_f) = e_f(n_f) + e_b(n_b) + g_{bf} n_f n_b \quad (5.1)$$

where e is the total energy density of the mixture, e_f (e_b) is that of the Fermi (Bose) gas alone and the last term is the mean-field energy density due to the boson-fermion interaction. $g_{bf} = 2\pi\hbar^2 a_{bf}/m_{bf}$ is the boson-fermion coupling constant with $m_{bf} = m_b m_f / (m_b + m_f)$ their reduced mass. Equation 5.1 is the equation of state of the mixture. With $\mu_\alpha = \frac{\partial e}{\partial n_\alpha}$, we obtain

$$\mu_b = g_{bf} n_f + g_b n_b \quad (5.2)$$

$$\mu_f = g_{bf} n_b + \mu_f(n_f), \quad (5.3)$$

where we have taken a mean-field approximation for the boson-boson interaction, and $\mu_f(n_f)$ describes the zero-temperature EoS of the fermions in the absence of bosons which varies in the BEC-BCS crossover as presented in chapter 1. First using (5.2, 5.3) one can infer the mixture's mechanical stability condition against phase separation. It is fulfilled if the compressibility matrix ($\kappa_{ij} = \partial\mu_i/\partial n_j$) has positive eigenvalues, this imposes:

$$\frac{\partial\mu_f}{\partial n_f} \frac{\partial\mu_b}{\partial n_b} \geq \frac{\partial\mu_f}{\partial n_b} \frac{\partial\mu_b}{\partial n_f}. \quad (5.4)$$

Injected into (5.2, 5.3) this yields

$$\frac{\partial \mu_f}{\partial n_f} \geq \frac{g_{bf}^2}{g_b}. \quad (5.5)$$

So from the knowledge of the equation of state of the Fermi superfluid in the BEC-BCS crossover one can predict whether the mixture will phase-separate or if it will remain mixed. One can use the full EoS of the Fermi gas presented in chapter 1, let us rather consider simple limits which are sufficient to demonstrate the stability of the mixture. In the BCS regime where $a_f \rightarrow 0^-$ we have $\mu_f = E_F = \hbar^2(3\pi^2 n_f)^{2/3}/2m_f$, and at unitarity ($1/a_f = 0$) $\mu_f = \xi E_F$. This yields an upper bound on the fermions density, this bound is lowest at unitarity namely $n_f \leq 2.7 \times 10^{16} \text{ cm}^{-3}$ (we have used the bosons scattering length at 832 G). This density is much higher than the typical densities in our samples ($n_{f,b} < 10^{14} \text{ cm}^{-3}$).

Close to the unitary regime of the Fermi gas, approaching from above the zero-crossing of a_b located at 850 G, we see from eq. (5.5) that when $a_b \rightarrow 0^+$ the mixture should phase-separate. The magnetic field range over which this phase separation takes place can be evaluated using the field dependence of a_b and the equation of state of the Fermi superfluid with our typical experimental densities ($n_f \sim 4 \times 10^{12} \text{ cm}^{-3}$). Using LDA we find that it occurs for $a_b \leq 0.5 a_0$ which corresponds to a very narrow field interval above the true zero crossing, less than 50 mG.

On the BEC side, using a MF approximation for the molecular BEC regime: $\mu_d = g_{dd} n_d$ with $g_{dd} = 2\pi\hbar^2 a_d/m_f$, $n_d = n_f/2$, and $\partial \mu_f/\partial n_f = 2\partial \mu_d/\partial n_f$, where the subscript d refers to the dimers ($a_d = 0.6a_f$), we obtain the stability condition for a mixture of a molecular and an atomic BEC: $a_{bf}^2/a_f a_b \leq 0.075$. From the magnetic field dependences of the scattering lengths, we find that this is fulfilled provided $B > 730 \text{ G}$. The lower limit of 730 G is only an indication since it is calculated using the mean-field approximation for a homogeneous system. We conclude that the Bose-Fermi superfluid mixture is stable for $B \in [730 \text{ G}, 845 \text{ G}] \cup [850 \text{ G}, 890 \text{ G}]$, illustrated as the white regions in figure 5.1 (the regions of instability are hatched in grey). This stability is in contrast with liquid helium mixtures where the strong ^4He - ^3He interaction leads to phase separation.

An observation of phase-separation in our system would be a stark signal of the interactions and could allow to gain valuable information for helium mixtures. The region of phase-separation above 850 G is very narrow, below our field stability, furthermore at low scattering length, LDA breaks down and quantum pressure effects further decrease the BEC density. An improved field stability is then necessary to observe phase-separation at the 850 G zero-crossing. It could be however observed for low magnetic fields, the limit of 730 G is approximative but since $a_b > 0$ for $B \geq 578 \text{ G}$ [Shotan *et al.*, 2014] and the molecular BEC is stable for $B \geq 600 \text{ G}$ [Jochim *et al.*, 2003a], we can explore much below this value and the observation of the phase-separation is an interesting prospect.

Using (5.2, 5.3) we can calculate in-trap densities for the Bose and Fermi superfluid in

the presence of the other. Inserting in (5.2, 5.3) the local density approximation ($\mu_\alpha(\mathbf{r}) = \mu_\alpha^0 - V_{\text{ext}}(\mathbf{r})$) yields the solutions for the fermionic and bosonic densities $n_f(\mathbf{r})$, $n_b(\mathbf{r})$. They are found as the solution to the implicit equations:

$$n_f(\mathbf{r}) = n_F \left(\mu_f^0 - \frac{g_{\text{bf}}}{g_b} \mu_b^0 - V_{\text{ext}}(\mathbf{r}) \left(1 - \frac{g_{\text{bf}}}{g_b} \right) + \frac{g_{\text{bf}}^2}{g_b} n_f(\mathbf{r}) \right) \quad (5.6)$$

$$n_b(\mathbf{r}) = \frac{1}{g_b} (\mu_b^0 - V_{\text{ext}}(\mathbf{r})) - \frac{g_{\text{bf}}}{g_b} n_f(\mathbf{r}) \quad (5.7)$$

where $n_F(\mu)$ is the equation of state of the Fermi superfluid. These solutions depend on the atom numbers and on magnetic field. An interesting situation arises when $g_{\text{bf}} = g_b$ where we find that the density of fermions is independent on \mathbf{r} over the extent of the BEC (for $\mu_b(\mathbf{r}) > 0$) [Mølmer, 1998, Delehay, 2012]:

$$n_f = n_F (\mu_f^0 - \mu_b^0 + g_{\text{bf}} n_f). \quad (5.8)$$

The bosons thus create a flat potential for the fermions, offering very interesting prospects. For example in the presence of spin-imbalanced Fermi gases the bosons can modify the critical polarization for superfluidity [Ozawa *et al.*, 2014]. The condition $g_{\text{bf}} = g_b$, is fulfilled for two magnetic fields: $B = 817.1$ G and $B = 854.3$ G.

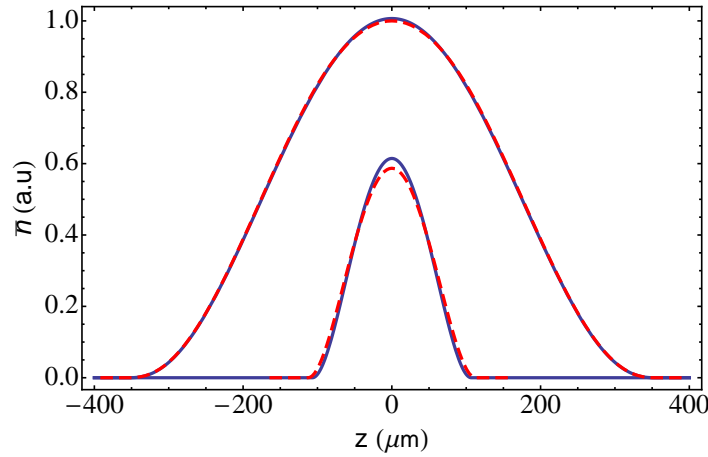


Figure 5.2: Theoretical doubly integrated density profiles of the bosons and one spin state of the fermions, at $B = 832$ G obtained using LDA with $N_f = 300 \times 10^3$ balanced fermions, and $N_b = 30 \times 10^3$ bosons. Solid blue lines: theory neglecting the interspecies interaction. Red dashed lines: theory with the same atom numbers taking the Bose-Fermi coupling into account, see main text.

Last we can infer the experimental signature of the boson-fermion interactions on the in-situ density profiles. The imaging technique does not allow for a measurement of the in-situ density, we rather measure the doubly-integrated density. Figure 5.2 shows doubly-integrated density profiles of bosons and fermions with typical numbers in our experiments calculated for $B = 832$ G. In this figure it is clear that the doubly integrated densities are very weakly perturbed by the presence of the other species. This was indeed

expected considering the weakness of the Bose-Fermi interaction reflected by the parameter $k_{\text{F}}a_{\text{bf}} \simeq 0.01$. Thus in what follows we will analyse the experimental profiles neglecting the inter-isotope interaction.

Having analyzed the interactions in our choice of internal states and demonstrated that a double superfluid is expected to be stable in this system, we now turn to its experimental realization achieved on our apparatus.

5.3 | Evidences for superfluidity

We have presented in details in chapter 2 the experimental preparation of the mixture. The final sequence consists in a dual-isotope forced evaporative cooling close to the Feshbach resonance of ${}^6\text{Li}$ situated at 832 G, driven by the ${}^6\text{Li}$ gas with a high collision rate. At different stages of the evaporation, Fermi degeneracy, Bose superfluidity and then Fermi superfluidity are crossed. While the superfluid transition of the Bose gas is easily observed on its profile as a central peak, on the opposite, that of the Fermi gas does not lead to a stark modification of its distribution. A reliable thermometry in the degenerate regime is then crucial to assess the double superfluidity.

5.3.1 Thermometry of the mixture

Due to strong interactions, temperature is known to be difficult to measure on degenerate spin-balanced Fermi gases on a Feshbach resonance. In previous experiments on our setup, a weakly interacting ${}^7\text{Li}$ gas was used as a thermometer for ${}^6\text{Li}$ samples [Nascimbène *et al.*, 2010]. The internal ${}^7\text{Li}$ state used then ($|1_{\text{b}}\rangle$) has a negative scattering at the magnetic fields of interest so that the Bose gas collapses when reaching the BEC threshold, setting the limit of thermometry. For the present measurements we also use the ${}^7\text{Li}$ gas for thermometry, but in our situation (${}^7\text{Li}$ in the $|2_{\text{b}}\rangle$), the BEC is stable and allows us to push thermometry to lower temperatures. To extract temperature, we use in-situ density images. The Bose gas is a reliable thermometer^(a) even under the critical temperature for BEC, because the temperature can be measured in the thermal wings of the distribution containing the non-condensed fraction. The temperature is extracted by fitting these wings by a Boltzmann distribution, or for a better precision, with the ideal Bose gas equation of state (1.5) taking quantum statistics into account. The final limit of thermometry is reached when the thermal fraction is too small to be observed on the profile, corresponding to $N_0/N \gtrsim 80\%$ given our signal-to noise ratio. This is reached typically at $T = 100$ nK.

^(a)We have checked that this method agrees with the measure using the time-of-flight distribution in the axial direction. We have also verified that at high temperature, for non-degenerate gases, the temperature extracted from the ${}^7\text{Li}$ image is the same as from the ${}^6\text{Li}$ image of the same mixture.

5.3.2 Degeneracy points

Fermi degeneracy of ${}^6\text{Li}$ is crossed at a temperature $T \simeq 2 \mu\text{K}$ and trap depth $U_0 \simeq 15 \mu\text{K}$ and the Bose-Einstein condensation threshold of ${}^7\text{Li}$ is met for $U_0 = 5 \mu\text{K}$. The BEC is signalled by the appearance of a central peak in the in-situ profile as showed in figure 5.3 where we represent the doubly-integrated profile of a Bose gas just under T_c (with T_c defined in (1.13)), fitted with the sum of a thermal profile for the non-condensed part and a Thomas-Fermi profile for the condensed part.

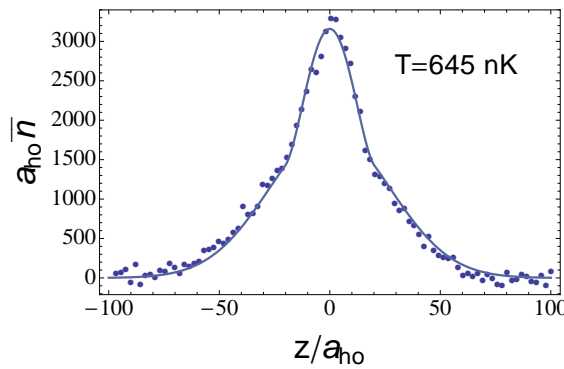


Figure 5.3: Doubly integrated profile of a Bose gas at $T = 0.95 T_c$, in units of the harmonic oscillator length. The solid line is a bimodal fit with a thermal distribution on the wings from which we extract temperature and a central Thomas-Fermi profile. The condensed fraction extracted from this fit is $N_0/N \simeq 0.17(5)$, in agreement with the expected value $1 - (T/T_c)^3 = 0.14$ using the temperature measured on the wings of the distribution.

5.3.3 Superfluidity of ${}^7\text{Li}$

Based on previous studies presented in chapter 1, there is no ambiguity that the ${}^7\text{Li}$ BEC is superfluid. However it is preferable to have a proof of superfluidity of this BEC, and this is provided by its hydrodynamic expansion in time of flight. A hydrodynamic behaviour of the BEC is explained by its superfluidity, and not by a high collision rate γ since we have in the experimental conditions $\gamma \ll \omega_z$ ^(b). It results in an expansion dynamics after release from the trap that differs from the expansion of a non-interacting system. In figure 5.4, we represent the aspect ratio $\eta = R_r/R_z$ where R_r (R_z) is the transverse (axial) radius of a pure ${}^7\text{Li}$ BEC at 835 G. η is represented as a function of time after release from the dipole trap radial confinement, with the magnetic confinement in the axial direction still on^(c). The data is compared with the hydrodynamic equations from [Castin and Dum, 1996] (solid line) with no fit parameters using our trap frequencies $\omega_z = 2\pi \times 16 \text{ Hz}$, $\omega_r = 2\pi \times 500 \text{ Hz}$. For comparison, the expansion dynamics expected for a Boltzmann gas at $T = 100 \text{ nK}$ is shown

^(b)Namely the mean free path is longer than the cloud size.

^(c)The weak radial expelling potential (with frequency $\omega' = 1/2\omega_z$) was neglected here since it plays a little role at these short time scales ($\omega' t \leq 0.45$ here).

as the dot-dashed line. We also plot in dashed line the solution to the Schrödinger equation for a non-interacting wave-packet expanding from the ground state of the harmonic trap. Neither the Boltzmann gas theory nor the Schrödinger equation agrees with our data, this demonstrates the hydrodynamic behavior of the ${}^7\text{Li}$ condensate which can only be explained by its superfluidity.

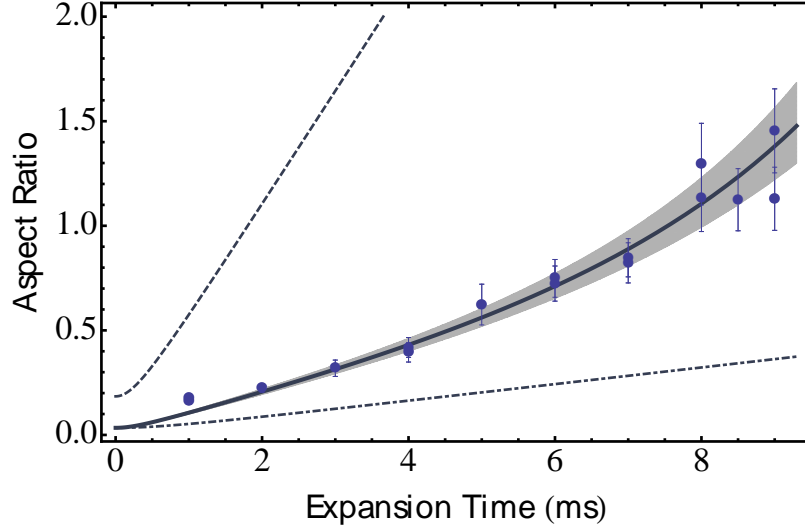


Figure 5.4: Aspect ratio of a ${}^7\text{Li}$ BEC after release from the radial confinement. The solid line shows the result from the hydrodynamic equations with no fit parameters using our trap frequencies and the shaded region shows the uncertainty resulting from the uncertainty on the frequencies. The dashed line shows the solution of the Schrödinger equation of an expanding wave packet, the dot-dashed line that of a Boltzmann gas at 100 nK.

5.3.4 Superfluidity of ${}^6\text{Li}$

Superfluidity in a degenerate Fermi gas is notoriously more difficult to assess. The demonstration of a hydrodynamic behavior is no proof of superfluidity, indeed the very high collision rate of fermions on a Feshbach resonance results in a hydrodynamic behaviour before the superfluid transition is crossed [O'Hara *et al.*, 2002, Bourdel *et al.*, 2003, Wright *et al.*, 2007]. Other signatures of superfluidity of ${}^6\text{Li}$ must be used.

The first way is to prove that the temperature is below the critical temperature for superfluidity of a unitary Fermi gas, $T_{c,f}$. The most precise measurement of $T_{c,f}$ is reported in [Ku *et al.*, 2012] for a homogeneous system, with $T_c = 0.167(13) T_F^{\text{hom}}$ where $T_F^{\text{hom}} = \hbar^2(3\pi^2 n)^{3/2}/2mk_B$. The critical temperature for a trapped gas (that we called $T_{c,f}$ here) can be found using the local-density approximation with the knowledge of the equation of state to calculate the local Fermi energy at the trap bottom. This is done in [Nascimbène *et al.*, 2010] yielding $T_{c,f} = 0.19 T_F^{(d)}$, with $T_F = \hbar\bar{\omega}(3N)^{1/3}/k_B$ the Fermi

^(d)The homogeneous critical temperature was estimated to be $T_c/T_F^{\text{hom}} = 0.157$ for this calculation, $T_{c,f} = 0.19 T_F$ is thus a safe lower bound.

temperature of the trapped gas. Measuring a temperature lower than $T_{c,f}$ using the Bose gas provides a first proof of the superfluidity of the Fermi gas.

For the coldest samples studied in our experiment, the thermal fraction of the BEC is too small to be detected. Nonetheless this still allows us to set an upper bound on temperature, using the lower bound of 80% on the condensed fraction and its expression as a function of temperature $N_0/N = 1 - (T/T_{c,b})^3$. From the knowledge of the atom number of each isotope and the trap frequencies we can calculate $T_{c,b}$, T_F and thus $T_{c,f}$. Our typical numbers in very shallow traps ($\sim 1 \mu\text{K}$) are: $N_b = 30 \times 10^3$, $N_f = 300 \times 10^3$ in a trap with frequencies $\omega_z = 2\pi \times 16 \text{ Hz}$, $\omega_r = 2\pi \times 550 \text{ Hz}$ ^(e). The corresponding critical temperatures are then $T_{c,b} = 240 \text{ nK}$, $T_{c,f} = 160 \text{ nK}$, and the upper bound on the condensed fraction gives a temperature lower bound $T \leq 140 \text{ nK} = 0.16 T_F$ demonstrating that the unitary Fermi gas is in the superfluid regime. Furthermore when the boson-boson scattering length drops to very low values, because the BEC peak is very narrow we are able to observe lower thermal fractions and to extract lower temperatures. This is the case for magnetic fields below 800 G and around the scattering length zero-crossing located at 850 G. We measure typically $T = 80(20) \text{ nK}$, well below the upper limits given above. From this $T/T_{c,f} \simeq 0.5$, and using the value of the condensed fraction as a function of temperature measured in [Sidorenkov *et al.*, 2013], we estimate that the superfluid fraction of our spin-balanced Fermi gas is above 80%. To this regard, the mixture is close to a zero-temperature limit. Table 5.2 summarizes the degeneracy and critical temperatures in the mixture during evaporation.

Point	Temperature	Trap depth	Axial frequency	Radial frequency
$T = T_F$	2(0.5) μK	15(5) μK	23(2) Hz (⁶ Li)	2000(300) Hz (⁶ Li)
$T = T_{c,b}$	700(50) nK	5(2) μK	18(1) Hz (⁷ Li)	1200(100) Hz (⁷ Li)
$T = T_{c,f}$	200(30) nK	2(0.3) μK	18(.5) Hz (⁶ Li)	800(50) Hz (⁶ Li)

Table 5.2: Typical degeneracy and critical points, indicated for the evaporation at 835 G, the isotope for which the frequency is given is indicated in parentheses.

To further demonstrate the superfluidity of the Fermi gas we show that atoms of opposite spin are fully paired in the center of the cloud. This method was used previously at Rice, MIT and in our group [Partridge *et al.*, 2006, Zwierlein *et al.*, 2006, Nascimbène *et al.*, 2009], it is based on the measurement of spin-imbalanced gases profiles in a harmonic trap. In this case the gas forms concentric layers of different polarizations, with in the center where the phase-space density is highest the fully-paired superfluid core. The outermost shell contains only majority atoms ($|\uparrow\rangle$) which then form an ideal Fermi gas. In between these two shells lies a highly polarized phase, in which polarization is too high to allow superfluidity. The minority atoms $|\downarrow\rangle$ dressed by the surrounding majority atoms form a gas of polarons, which turn into

^(e)The indicated frequencies are given for ⁷Li, the frequencies of the same potential seen by ⁶Li are simply higher by a factor $\sqrt{m_7/m_6} = \sqrt{7/6}$.

molecules in the strongly attractive BEC limit [Chevy and Mora, 2010]. Let us show how the imaging of the doubly integrated density profiles of imbalanced gases yields a demonstration of pairing in the center.

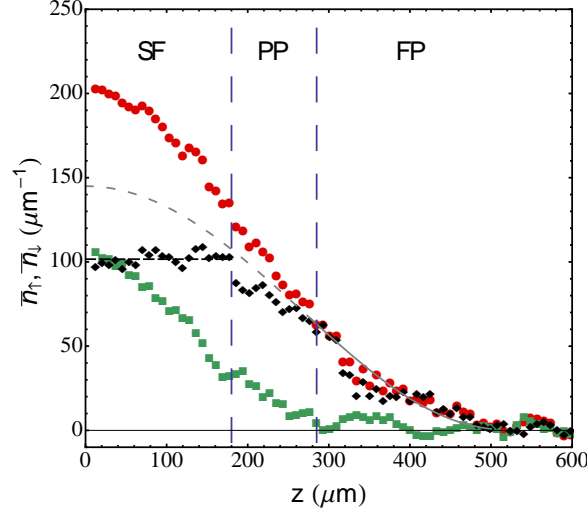


Figure 5.5: Density profiles of an imbalanced Fermi gas at 835 G, containing $N_{\uparrow} = 200 \times 10^3$, $N_{\downarrow} = 100 \times 10^3$ atoms (here $|\uparrow\rangle = |1_f\rangle$, $|\downarrow\rangle = |2_f\rangle$). In red circles we show \bar{n}_{\uparrow} , in green squares: \bar{n}_{\downarrow} , and in black diamonds we show the doubly integrated density difference $\bar{n}_{\uparrow} - \bar{n}_{\downarrow}$. The inner shell extending from $z = 0$ to $z \simeq 180 \mu\text{m}$ is superfluid (SF), indicated by the plateau in the density difference (black dashed line). The second shell consists of the polaron phase, partially polarized (PP) with a non-zero minority density. Finally the outermost shell is fully polarized (FP), the majority atoms form an ideal Fermi gas. The solid grey line is a fit to this profile by a non-interacting zero-temperature EoS, it is extended to the inner shells in dashed grey, the enhanced experimental pressure at the core is a signature of strong attraction between the majority and minority spin components.

In the superfluid core, the density difference between the two states is equal to zero: $n_{\uparrow} - n_{\downarrow} = 0$. We recall that using LDA, on the line $r = 0$ we have

$$\frac{\partial}{\partial \mu_{\uparrow}} = \frac{\partial}{\partial \mu_{\downarrow}} = -(1/m\omega_z^2 z) \frac{\partial}{\partial z}, \quad (5.9)$$

and furthermore $\bar{n}_{\sigma}(z) \propto P_{\sigma}(z, r = 0)$ where \bar{n}_{σ} and P_{σ} are respectively the doubly integrated density and pressure for the spin component σ . Finally using the Gibbs-Duhem formula $n_{\sigma} = \partial P_{\sigma} / \partial \mu_{\sigma}$, we obtain for the superfluid region ($n_{\uparrow} - n_{\downarrow} = 0$):

$$\frac{\partial(\bar{n}_{\uparrow} - \bar{n}_{\downarrow})}{\partial z} = 0. \quad (5.10)$$

This shows that pairing results in a plateau in the difference of doubly-integrated densities $\bar{n}_{\uparrow} - \bar{n}_{\downarrow}$ in the superfluid region. An imbalanced profile is shown in figure 5.5 recorded at 835 G, where we clearly see a plateau in the center and the shell structure. This demonstrates the existence of a fully-paired core. Data taken at MIT in rotating Fermi gases have shown the existence of vortices in the region of equal spin densities [Zwierlein et al., 2006]; implying its superfluidity. The plateau we observe is thus a signal of the superfluidity of the Fermi

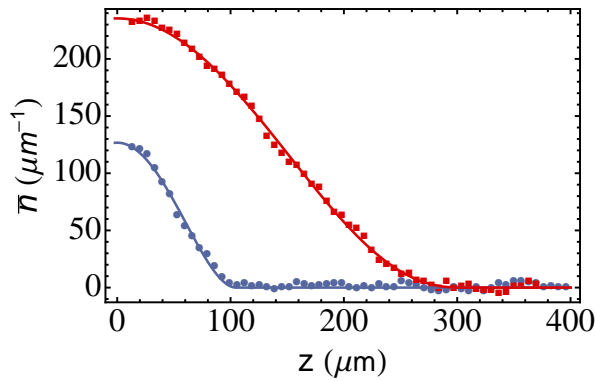


Figure 5.6: Experimental doubly-integrated density profiles in a mixture at 832 G, containing $N_b \simeq 4 \times 10^4$ bosons and $N_f \simeq 3 \times 10^5$ fermions (in a balanced mixture of $|1_f\rangle$ and $|2_f\rangle$). Blue circles: bosons, red squares: fermions (state $|1_f\rangle$). The solid lines are fits with the mean-field equation of state for the BEC and the unitary Fermi gas EoS for the Fermions. The interaction with the other species is neglected in these fits and is expected at the $\sim 1\%$ level as shown earlier.

gas.

The imbalanced Fermi gas of figure 5.5 that exhibits a plateau has been obtained in the presence of a ${}^7\text{Li}$ BEC, that can be imaged in time-of-flight in the axial direction. Our observations demonstrate that our ${}^7\text{Li}$ - ${}^6\text{Li}$ system is a mixture of a Bose superfluid and a Fermi superfluid. As far as we know, it is the first time that such a mixture of Bose-Fermi superfluids is produced. Experimental in-situ profiles of a Bose-Einstein condensate mixed with a unitary Fermi superfluid are presented in figure 5.6. As was discussed in the first chapter of this thesis, superfluidity causes a number of unusual flow properties, among them vortices and frictionless flow. While the observation of vortices requires a specific set-up to set the gas in rotation, counter-flow motion can be easily induced on our experiment.

5.3.5 Frictionless counter-flow

Indeed it is possible to apply a displacement to the center-of-mass (CoM) of the mixture (see section 5.5 for details). When we displace the Bose gas and the Fermi gas individually, they oscillate at the bare frequencies $\omega_b = 2\pi \times 15.3$, $\omega_f = 2\pi \times 16.8$ respectively. This difference is explained by the different masses of ${}^7\text{Li}$ and ${}^6\text{Li}$. Since the potential is the same for both clouds and they have a different mass, their oscillation frequencies are different^(f), and we get $\omega_b = \omega_f \sqrt{6/7}$ in agreement with the experiment.

In the case of the mixture, once the CoM is displaced, the two clouds start to oscillate in the harmonic potential. We observe that the frequencies are not strongly modified with respect to the bare frequency. So after a few oscillations two components get out of phase and

^(f)The potential is not exactly identical, slightly increasing the difference between the trapping frequencies, see 5.5.

flow through each other. We illustrate such a counter-flow motion obtained with oscillations in the axial direction in figure 5.7, and the center-of-mass position of each species monitored during 2 s is shown in figure 5.8.

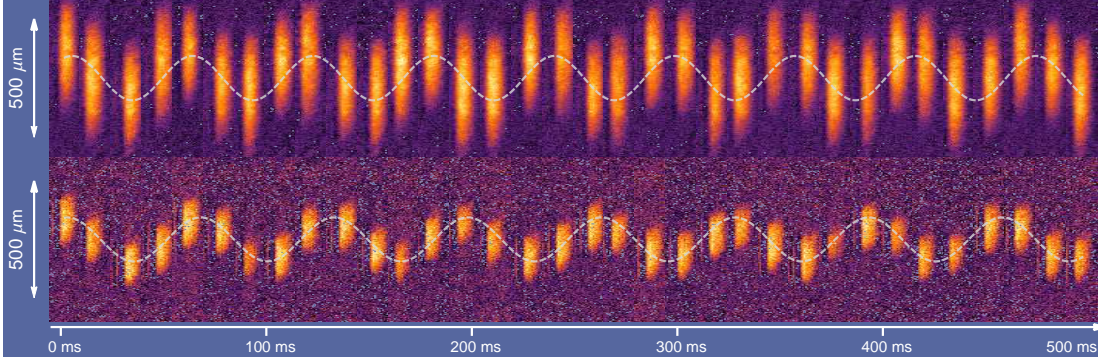


Figure 5.7: Motion of the two superfluids (${}^6\text{Li}$ top, ${}^7\text{Li}$ bottom) in the presence of each other for the first 500 ms with a picture every 15 ms. The dashed white lines are guide to the eye.

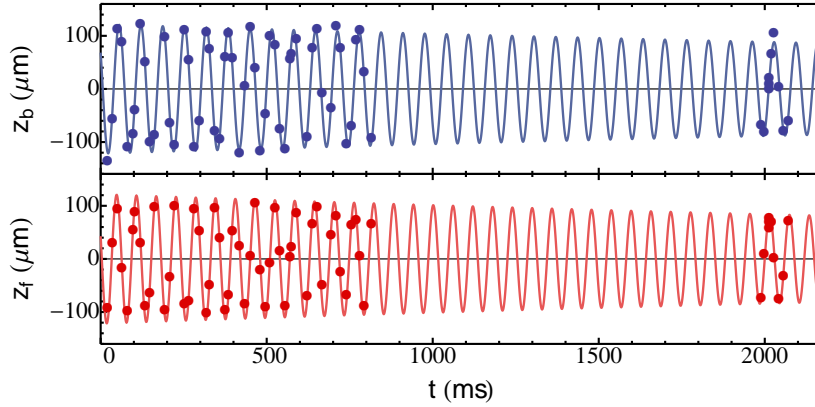


Figure 5.8: Center-of-mass motion of a ${}^7\text{Li}$ cloud (blue circles) and a ${}^6\text{Li}$ cloud (red circles) in a double superfluid at 860 G. The solid lines show fit to the data with exponentially damped sinusoids, yielding a damping rate $\gamma \leq 0.1 \text{ s}^{-1}$. The very-long lifetime of these oscillations show the superfluid character of our mixture.

The fit of the data with a simple exponentially decaying sinusoid (solid lines in figure 5.8) give a decay rate of $\gamma \leq 0.1 \text{ s}^{-1}$. The typical axial frequencies are about $\omega_b \simeq 15.5 \text{ Hz}$ such that the two superfluids oscillate through each-other with a frequency of $\simeq 30 \text{ Hz}$. This frequency is very high compared to the obtained γ , demonstrating a very weak friction. For a better comparison, in a first approximation, we can consider the Bose gas as an impurity oscillating inside the Fermi cloud. In this limit using results from [Ferrari, 1999] we can calculate the damping rate of the oscillations inside a degenerate non-superfluid Fermi gas. In our case the oscillatory motion of the BEC is modulated with high amplitude periods followed by small amplitude ones. To compare our data to theory, we use the mean amplitude of motion, for our temperature we get $\gamma \geq 0.05 n_f^0 \sigma_{bf} v_F$ where $\sigma_{bf} = 4\pi a_{bf}^2$ is the boson-fermion collisional cross-section, n_f^0 the fermion density at center and $v_F = \sqrt{2\hbar\omega(3N_f)^{1/3}/m_f}$ their Fermi velocity. Using our typical parameters $v_F \simeq 50 \text{ mm/s}$ we get $\gamma \gtrsim 0.5 \text{ s}^{-1}$, a factor of five higher than the experimental upper bound,

which is a clear sign of the superfluidity of our mixture.

The excitation of CoM oscillations of the mixture has allowed us to observe frictionless flow, illustrating its superfluidity. These oscillations are called the dipole modes, they are low-energy collective excitations of a gas in a harmonic potential. Being very long-lived in our experiment, they can be used as a sensitive probe of the mixture properties. In what follows we will show that indeed the dipole modes are modified by the interactions with the other species, we calculate this effect with a perturbative approach. Implementing a precise spectroscopy of the dipole modes, we measure this effect, in very good agreement with theory. Finally, having characterized the oscillations in the regime of near-zero viscosity, we will demonstrate that the counter-flow motion follows the general behaviour of superfluid flows with a breakdown of frictionless motion above a critical velocity.

In the past, the dipole modes have been used to study the properties of ultracold gases and in particular ultracold mixtures. Soon after the first realization of Bose-Einstein condensations, mixtures of BECs in two different hyperfine states of the same atomic species were produced [Cornell and Wieman, 2002]. The center-of-mass motion of these mixtures revealed a strong interaction between the two BECs leading to a fast damping [Hall et al., 1998a, Hall et al., 1998b]. This damping was analysed to be due to a coupling of the dipole modes to other collective excitations of the mixture [Sinatra et al., 1999]. Later-on, in order to reduce the coupling between the two gases, their spatial overlap was shrunk using a displacement of the center of the trapping potential for one hyperfine state. The damping was successfully reduced, presenting oscillations over a long time period [Maddaloni et al., 2000, Modugno et al., 2000]. The oscillatory motion of each BEC presented a frequency shift due to interaction with the other component, well described by a time-dependent simulation of the Gross-Pitaevskii equation [Modugno et al., 2001]. In a mixture of two BECs from different atomic species ^{41}K and ^{87}Rb , the scissors mode, a collective mode of a different kind was shown to be excited by interspecies-interactions [Modugno et al., 2002]. Subsequently, dipole mode excitations were used to probe the collisional properties of a mixture of the same two atomic species but with a fermionic isotope of potassium: ^{40}K [Ferlaino et al., 2003]. Since the fermionic component was in a single-spin state, only the bosonic component formed a superfluid in this study. Apart from mixtures of BECs or mixtures of a BEC and a degenerate Fermi gas, the dipole modes have been employed for the study of other systems. For example in a one-dimensional geometry, the excitation of an out-of-phase CoM motion of two condensates in the same internal states allowed to realize a quantum equivalent to Newton's cradle [Kinoshita et al., 2006] and study integrability of a one-dimensional Bose gas. A similar protocol was used to study spin diffusion of a strongly-interacting Fermi gas in three-dimensions [Sommer et al., 2011].

On the theoretical side, different works have investigated dipole oscillations of spin-polarized Bose-Fermi mixtures, [Minguzzi and Tosi, 2000, Capuzzi et al., 2003,

[Maruyama and Bertsch, 2008]. In the following we present such theory of dipole oscillations for our doubly superfluid Bose-Fermi mixture, allowing to understand why the dipole modes are a sensitive probe to the interactions in our system. This theory is then compared with the experimental results obtained.

5.4 | Coupled dipole modes, theory

Considering in the local density approximation that each superfluid sees an effective external potential that is the sum of the trapping potential plus the mean-field boson-fermion interaction, the center-of-mass oscillations should be modified by the presence of the other superfluid. To compute this modification, we first make use of a simple model which follows the approach of [Lobo *et al.*, 2006] developed to calculate the dipole frequency of the polaron in an imbalanced unitary Fermi gas, and further used in our group in the study of the polaron's axial breathing modes [Nascimbène *et al.*, 2009].

5.4.1 Simple model for the BEC dipole frequency shift

This approach is here based on the fact that the samples produced contain a large majority of ${}^6\text{Li}$ ($N_f \gg N_b$). Considering figure 5.6, we see that with our typical parameters, the bosons occupy a small fraction of the volume of the Fermi gas near its center, from which we conclude that the Fermi superfluid sees mostly the unperturbed harmonic confinement and its dipole frequency should be almost unchanged. On the other hand, the bosons are entirely contained in the Fermi superfluid. We treat then the bosons as impurities evolving in the external potential composed of the sum of the trapping potential $V_{\text{ext}}(\mathbf{r})$ and the mean-field term $g_{\text{bf}}n_f(\mathbf{r})$:

$$V_{\text{eff}}(\mathbf{r}) = V_{\text{ext}}(\mathbf{r}) + g_{\text{bf}}n_f(\mathbf{r}). \quad (5.11)$$

Neglecting the effect of the bosons, the fermions density is:

$$n_f(\mathbf{r}) = n_F(\mu_f^0 - V_{\text{ext}}(\mathbf{r})). \quad (5.12)$$

We consider the limit of vanishing amplitude for the oscillation of the BEC, then we can expand n_f around $\mathbf{r} = 0$:

$$n_f(\mathbf{r}) = n_f(0) - V_{\text{ext}}(\mathbf{r}) \left(\frac{dn_F}{d\mu_f} \right)_{r=0}. \quad (5.13)$$

And finally the effective potential acting on the bosons is:

$$V_{\text{eff}}(\mathbf{r}) = V_{\text{ext}}(\mathbf{r}) \left(1 - g_{\text{bf}} \left(\frac{dn_F}{d\mu_f} \right)_{r=0} \right) + g_{\text{bf}}n_f(0). \quad (5.14)$$

This expression shows that the fermions act as a chemical potential shift ($g_{\text{bf}}n_f(0)$), plus a small reduction of the trapping potential. For a harmonic trap, we can easily calculate the

resulting frequency shift:

$$\tilde{\omega}_b = \omega_b \left(1 - \frac{1}{2} g_{bf} \left(\frac{dn_F}{d\mu_f} \right)_{r=0} \right), \quad (5.15)$$

where ω_b is the bare bosons frequency and $\tilde{\omega}_b$ is that in the presence of the Fermi superfluid. We note $\delta\omega_b = \omega_b - \tilde{\omega}_b$, since $\left(\frac{dn_F}{d\mu_f} \right)_{r=0} \geq 0^{(g)}$ and $g_{bf} > 0$, we have $\delta\omega_b > 0$. Using a precise spectroscopy of the center-of-mass oscillation of the BEC, this frequency shift can be measured. Before reporting on our measurements, we develop a theory that takes into account the back-action of the bosons and allows to gain a more complete picture of the dipole oscillations of the mixture. The result can be easily understood as a coupled-oscillators model.

5.4.2 Sum rules and coupled ${}^6\text{Li}$ - ${}^7\text{Li}$ dipole oscillations

The simple model treating the fermions cloud as an effective potential for the bosons indeed does not take into account the bosons' effect on the fermions. We now take it into account using a treatment of the dipole modes applying sum rules. This method is explained in [Pitaevskii and Stringari, 2003, Stringari, 2004]. Here we present how to apply the sum rules to obtain the frequency of the dipole modes in our Bose-Fermi mixture. They allow, using some assumptions, to calculate the response of the mixture to a displacement of the centers-of-mass.

The system is described by the following hamiltonian

$$\hat{H} = \sum_{\alpha,i} \frac{\hat{p}_i^2}{2m_{\alpha,i}} + U(\hat{\mathbf{r}}_{\alpha,i}), \quad (5.16)$$

where $\alpha = f, b$ denotes either fermions or bosons and U is the potential energy comprised of the trapping potential and the interatomic interactions, and i denotes the identical particles. The trapping potential in the z direction reads $m_\alpha \omega_\alpha^2 \hat{z}^2 / 2 = k^2 \hat{z}^2 / 2$ where k is the stiffness of the trapping potential. The sum rules are introduced through the operators $\hat{F}_\alpha = \sum_{i=0}^{N_\alpha} \hat{z}_{\alpha,i}$, where $\hat{z}_{\alpha,i}$ denotes the position along the axial direction of the trap of particle i in species α . Let us take the excitation operator $\hat{F}(b_f, b_b) = b_f \hat{F}_f + b_b \hat{F}_b$, and the associated moments:

$$S_k = \sum_n (E_n - E_0)^k \left| \langle n | \hat{F} | 0 \rangle \right|^2, \quad (5.17)$$

where $\{|n\rangle\}$ is the orthonormal basis of eigenstates with eigenvalues $\{E_n\}$ of \hat{H} , $|0\rangle$ is the ground state and we take its energy to be the reference $E_0 = 0$. Let us explain why these sum rules are useful to our purpose which is to describe the CoM oscillation dynamics of the mixture. First we note that the operator \hat{F} is a displacement operator, that is the hamiltonian $\hat{H}' = \hat{H} - kd\hat{F}$ corresponds to the hamiltonian of the system with the center of the trap for the species α shifted by a distance $d_\alpha = db_\alpha$ in the z direction. Furthermore, we make the assumption which will have to be verified experimentally that the displacement operator couples the ground state $|0\rangle$ to only two eigenmodes of the *unperturbed* hamiltonian

^(g)The mechanical stability of the Fermi gas imposes a positive compressibility.

($\langle 0 | \hat{F} | n \rangle = 0 \forall n \notin \{1, 2\}$), we call the energy of these modes $E_n = \hbar\omega_n$, $n = 1, 2$ with by convention $\omega_1 \leq \omega_2$. Then the sum for all n is to be taken only for $n = 1, 2$ and we find easily that for any value of (b_b, b_f) ,

$$(\hbar\omega_1)^2 \leq \frac{S_1}{S_{-1}} \leq (\hbar\omega_2)^2 \quad (5.18)$$

Thus to find the frequencies of these modes one has to find the extrema of S_1/S_{-1} as a function of b_b, b_f . For this we have to calculate S_1 and S_{-1} explicitly.

Recalling that $\hat{H} = \sum_n E_n |n\rangle \langle n|$ we find $S_1 = \langle 0 | \hat{F} \hat{H} \hat{F} | 0 \rangle = -\frac{1}{2} \langle 0 | [\hat{F}, [\hat{F}, \hat{H}]] | 0 \rangle$, and using the commutation relation $[\hat{z}_{\alpha,l}, \hat{p}_{\beta,j}] = i\hbar \delta_{lj} \delta_{\alpha\beta}$ we get:

$$S_1 = \hbar^2 \sum_{\alpha} \frac{b_{\alpha}^2 N_{\alpha}}{2m_{\alpha}}. \quad (5.19)$$

S_{-1} can be calculated in the following manner: first consider the perturbed hamiltonian $\hat{H}' = \hat{H} - kd\hat{F}$. Using first-order perturbation theory we can calculate the eigenvectors $|n'\rangle$ of \hat{H}' , we find:

$$\langle 0' | \hat{F} | 0' \rangle = \langle 0 | \hat{F} | 0 \rangle + 2 dk \sum_n \frac{|\langle 0 | \hat{F} | n \rangle|^2}{E_n} = \langle 0 | \hat{F} | 0 \rangle + 2 dk S_{-1}. \quad (5.20)$$

To obtain an expression of S_{-1} we can express $\langle 0' | \hat{F} | 0' \rangle$ using a Taylor expansion of the mean position of each species $\langle z'_{\alpha} \rangle = \langle 0' | \hat{z}_{\alpha} | 0' \rangle$:

$$\langle z'_{\alpha} \rangle = \langle 0 | \hat{z}_{\alpha} | 0 \rangle + \sum_{\beta} d_{\beta} \frac{\partial \langle z_{\alpha} \rangle}{\partial d_{\beta}} \quad (5.21)$$

and using the definition of \hat{F} given above we finally obtain

$$S_{-1} = \frac{1}{2k} \sum_{\alpha,\beta} N_{\alpha} b_{\alpha} b_{\beta} \frac{\partial \langle z_{\alpha} \rangle}{\partial d_{\beta}}, \quad (5.22)$$

where $\langle z_{\alpha} \rangle = \langle 0' | \hat{z}_{\alpha} | 0' \rangle$. So using the two relations (5.19, 5.22) one can calculate the two eigenmodes frequency. The expressions of S_1 and S_{-1} (5.19, 5.22), involve only static macroscopic quantities, which can be calculated using the local density approximation with the knowledge of the equation of state of the system and do not require any knowledge of the short-range correlations, showing the power of the sum-rules method for our problem. In the absence of interaction between the species, these modes are simply the dipole mode of the bosons and of the fermions with frequencies ω_f, ω_b . When there is a coupling between bosons and fermions the new modes can be calculated with (5.19, 5.22). The problem is simplified by using the experimental fact $N_b \ll N_f$, furthermore in the limit of a weak coupling the new eigenmodes are close to the non-interacting modes, and the frequencies are readily found using first order perturbation theory, let us detail this in the following.

To this aim, two useful conditions can be derived. First when the trapping potentials for both species are displaced by the same amount $d_{\alpha} = d$, then the mass centers are identically

moved: $\langle z_\alpha \rangle = d$, by differentiating this with respect to d , one gets $1 = \sum_\beta \partial_{d_\beta} \langle z_\alpha \rangle$. Next we recall Hellmann-Feynman's theorem: $\partial_\lambda E = \langle \psi | \partial_\lambda \hat{H} | \psi \rangle$, where λ is a continuous variable. Applied twice with $\lambda = d_\alpha, d_\beta$, in either order, we conclude that the matrix $N_\alpha \partial_{d_\beta} \langle z_\alpha \rangle$ is symmetric.

We can turn now to the calculation of the eigenfrequencies, for this we recast the sum rules ratio in (5.18) as:

$$\frac{S_1}{S_{-1}} = \hbar^2 k \frac{\langle \psi | \psi \rangle}{\langle \psi | \mathcal{M} | \psi \rangle} \quad (5.23)$$

using the definitions: $|\psi\rangle = (b'_f, b'_b)$, $b'_\alpha = b_\alpha \sqrt{N_\alpha/m_\alpha}$, and

$$\mathcal{M}_{\alpha\beta} = \sqrt{m_\alpha m_\beta} \sqrt{\frac{N_\alpha}{N_\beta}} \frac{\partial \langle z_\alpha \rangle}{\partial d_\beta}. \quad (5.24)$$

With these notations the frequencies ω_1, ω_2 are given by $\omega_i = \sqrt{k/\tilde{m}_i}$ where \tilde{m}_i are the eigenvalues of $\mathcal{M}^{(h)}$. The corresponding eigenvectors represent the relative displacements of the two clouds CoM for the given mode, *i.e* if one applies the relative displacements given by the eigenvector ψ_i , then only the corresponding mode with frequency ω_i is excited. In the absence of inter-species interactions ($\partial_{d_\beta} \langle z_\alpha \rangle = 0$) the eigenvalues are m_f, m_b with eigenvectors $(\sqrt{N_f/m_f}, 0), (0, \sqrt{N_b/m_b})$. Finally in the weak-coupling regime, one can write \mathcal{M} as $\mathcal{M} = \mathcal{M}_0 + \mathcal{M}_1$ and treat the boson-fermion interaction (\mathcal{M}_1) as a perturbation. These matrices read:

$$\mathcal{M}_0 = \begin{pmatrix} m_f & 0 \\ 0 & m_b \end{pmatrix} \quad (5.25)$$

$$\mathcal{M}_1 = \begin{pmatrix} -m_f \frac{\partial \langle z_f \rangle}{\partial b_b} & \sqrt{m_f m_b} \sqrt{\frac{N_b}{N_f}} \frac{\partial \langle z_b \rangle}{\partial b_f} \\ \sqrt{m_f m_b} \sqrt{\frac{N_b}{N_f}} \frac{\partial \langle z_b \rangle}{\partial b_f} & -m_b \frac{\partial \langle z_b \rangle}{\partial b_f} \end{pmatrix} \quad (5.26)$$

where we have used the two relations derived earlier. We can apply first-order perturbation theory and identify $\omega_1 (\omega_2)$ with $\tilde{\omega}_b, (\tilde{\omega}_f)$, these new eigenfrequencies are

$$\tilde{\omega}_f \simeq \omega_f \quad (5.27)$$

$$\tilde{\omega}_b \simeq \omega_b \left(1 + \frac{1}{2} \frac{\partial \langle z_b \rangle}{\partial d_f} \right), \quad (5.28)$$

where we have used $N_b \ll N_f$. The frequency shift $\frac{\partial \langle z_b \rangle}{\partial d_f}$ can be calculated explicitly using the LDA with the external potentials $V_b(\mathbf{r}) = V_{\text{ext}}(\mathbf{r})$, $V_f(\mathbf{r}) = V_{\text{ext}}((\mathbf{r} - d_f \mathbf{u}_z))$. We finally get

$$\frac{\delta \omega_b}{\omega_b} = \frac{1}{2} \frac{g_{bf} k}{N_b} \int d^3 \mathbf{r} z^2 \left(\frac{\partial n_b}{\partial \mu_b} \right) \left(\frac{\partial n_f}{\partial \mu_f} \right). \quad (5.29)$$

This expression allows us to calculate the frequency shift of the Bose-Einstein condensate oscillation in the axial direction of the trapping potential. In the limit where the BEC has a

^(h)One can easily show that $m = \frac{\langle \psi | \mathcal{M} | \psi \rangle}{\langle \psi | \psi \rangle}$ is bounded by the two eigenvalues of \mathcal{M} .

small extent inside the Fermi superfluid the value of $\partial n_f / \partial \mu_f$ can be evaluated at $r = 0$ and taken constant over the BEC size. Then the integral is easily calculated using LDA, it yields:

$$\frac{\delta \omega_b}{\omega_b} = \frac{1}{2} g_{bf} \left(\frac{\partial n_f}{\partial \mu_f} \right)_{r=0} \quad (5.30)$$

we recover as expected expression (5.15) obtained treating the fermions as an effective potential. The approximations made to obtain this simple expression are that the BEC has a small extent, that it oscillates with a small amplitude inside the Fermi superfluid and that it modifies weakly its profile. Furthermore we considered that the CoM displacement excites only the dipole modes, these approximations are discussed in paragraph 5.5.4. In this frame, the effect of the BEC is just the reaction to the Fermi superfluid's action.

These reciprocal effects can yield the dynamics of the full system, indeed one can obtain the eigenvectors ψ_1, ψ_2 , ($\psi_i = (b_{f,i}, b_{b,i})$), which correspond to the relative initial displacements to apply to excite the eigenmode with frequency ω_i . In the relevant weak coupling regime these modes are close to the non-interacting ones. Using again perturbation theory they are readily found as $\tilde{\psi}_f = \sqrt{m_f/N_f}(1, \varepsilon)$, $\tilde{\psi}_b = \sqrt{m_b/N_b}(\varepsilon\eta\rho, 1)$ with frequency respectively $\tilde{\omega}_f, \tilde{\omega}_b$, and we define $\rho = N_b/N_f$, $\eta = m_f/m_b$ and

$$\varepsilon = -\frac{2m_b}{m_b - m_f} \frac{\delta \omega_b}{\omega_b}. \quad (5.31)$$

Then the equations of motion for the center-of-mass of the two species: $Z(t) = (z_f(t), z_b(t))$ can be calculated by expressing Z in the $\tilde{\psi}$ basis $Z = \sum_i c_i \tilde{\psi}_i$, at time t we have then $Z(t) = \sum_i c_i \cos(\omega_i t) \tilde{\psi}_i$. To simplify the discussion of the motion, we will use a simple parallel. The equations thus obtained are indeed found to be formally equivalent to the equations of motion of a simple system: Two oscillators of mass $M_f = m_f N_f$ and $M_b = N_b m_b$ with bare frequencies ω_f, ω_b , weakly coupled by a spring with stiffness K_{bf} . This harmonic coupling exerts a force $F_{bf} = -K_{bf}(z_b - z_f)$ on the oscillator of mass M_b and an equal and opposite force on the other one. The equations of motion for this system read:

$$\begin{pmatrix} \ddot{z}_f(t) \\ \ddot{z}_b(t) \end{pmatrix} = - \begin{pmatrix} \omega_f^2 + \frac{K_{bf}}{M_f} & -\frac{K_{bf}}{M_f} \\ -\frac{K_{bf}}{M_b} & \omega_b^2 + \frac{K_{bf}}{M_b} \end{pmatrix} \begin{pmatrix} z_f(t) \\ z_b(t) \end{pmatrix} \quad (5.32)$$

Using first order perturbation theory with K_{bf} as a perturbation and in the limit $M_f \gg M_b$, the eigenfrequencies of this system are found to be

$$\tilde{\omega}_f \simeq \omega_f \quad (5.33)$$

$$\tilde{\omega}_b \simeq \omega_b \left(1 + \frac{1}{2} \frac{K_{bf}}{M_b \omega_b^2} \right). \quad (5.34)$$

So we see that the coupled oscillator model is equivalent to the dipole modes oscillations of our mixture if K_{bf} matches $2M_b \omega_b^2 \frac{\delta \omega_b}{\omega_b}$ with $\frac{\delta \omega_b}{\omega_b}$ defined in (5.29). The eigenmodes of this system are simply the in-phase and out-of-phase oscillations modes.

Finally, taking the limits $m_f \simeq m_b$, $N_f \gg N_b$, we can obtain the position of the center-of-masses as a function of time for the initial conditions $z_b = z_f = d$, $\dot{z}_b = \dot{z}_f = 0$:

$$z_f(t) = d((1 - \rho\varepsilon)\cos(\tilde{\omega}_f t) + \rho\varepsilon\cos(\tilde{\omega}_b t)) \quad (5.35)$$

$$z_b(t) = d(-\varepsilon\cos(\tilde{\omega}_f t) + (1 + \varepsilon)\cos(\tilde{\omega}_b t)), \quad (5.36)$$

where z_α denotes the center-of-mass of species α .

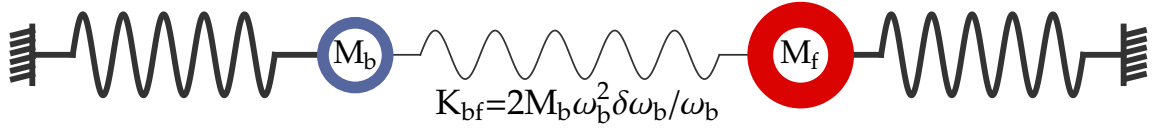


Figure 5.9: Schematic representation of the center-of mass oscillations of the mixture. Each superfluid is seen as an oscillator (fermions: left, bosons: right), and the mean-field interaction between them acts as a weak harmonic coupling.

This coupled-oscillators model illustrated in figure 5.9 explains why we can apply an identical perturbation to both superfluids and still measure a response that depends on their mutual coupling. If the two atoms had the same mass then their oscillators frequencies would be degenerate. In which case for identical initial displacements the two oscillators would never get out of phase and the central spring would never be stretched. This is a consequence of the generalized Kohn's theorem [Dobson, 1994] which states that the center-of-mass motion for an ensemble of particles of the same mass placed in an external potential is described by the classical equation of a particle in the external potential. Owing to the different masses of ${}^6\text{Li}$ and ${}^7\text{Li}$ leading to different frequencies, we can displace them by the same amount and still measure their coupling, such measurements are presented in the following.

5.5 | Coupled dipole modes, experiments

In the experiment, in the regime where both ${}^7\text{Li}$ and ${}^6\text{Li}$ are superfluid, the atoms are radially trapped by the trapping laser, and axially by a magnetic curvature. Since the coils creating the field (the Pinch coils) have large dimensions with respect to the clouds size, they create a very harmonic trapping potential. Our experiments are performed at magnetic fields higher than 700 G, so both isotopes are in the Paschen-Back regime. As a consequence their energy versus field dependence is close to $\frac{\partial E}{\partial B} = \mu_B$ where μ_B is the Bohr magneton⁽ⁱ⁾. Thus the two isotopes see the same harmonic potential in the axial direction $V_{\text{ext},z} = m_b \omega_b z^2 / 2 = m_f \omega_f z^2 / 2 = k z^2 / 2$, the ratio of their trapping frequencies is given by $\omega_f / \omega_b = \sqrt{7/6} \simeq 1.08$. Taking into account the actual field dependence of the energy levels,

⁽ⁱ⁾As was shown in [Jochim et al., 2003b] when the ${}^6\text{Li}$ molecules are strongly bound, they have a magnetic moment that differs from $2\mu_B$, but a relevant discrepancy was observed only for fields lower than 700 G, outside of the range of our experiments.

this ratio is actually $\simeq 1.1$ near 832 G.

5.5.1 Dipole modes excitation

To excite the dipole modes, we make use of the fact that the focal point of the dipole laser is actually not exactly superimposed with the center of the magnetic axial confinement. When the laser is at low power, the resulting axial potential is mainly composed of the magnetic confinement and the atoms lie at its center. When the laser power is increased, the cloud's center is shifted along the z direction by the light potential. Thus, the center-of-mass of the clouds can be displaced by increasing the laser power. To use this as a dipole mode excitation scheme, we must ensure that no other mode is excited. For this, the laser power is ramped-up in a time slow compared to the trap oscillation period, this time is $t_{\text{up}} = 150$ ms, with the typical radial frequencies $\omega_r \sim 2\pi \times 500$ Hz and axial frequencies $\omega_z \sim 2\pi \times 16$ Hz. The CoM in the axial direction is thus adiabatically displaced to a position that we note d , this displacement can be varied at will by varying the laser power at the end of the ramp, for a displacement $d = 100 \mu\text{m}$ the power must be increased by a factor $\simeq 1.3$. To excite dipole oscillations, the ramp-down of the laser power to its initial value has to be done faster than the axial oscillation period. In order not to excite collective oscillations in the radial direction, this time must be slow compared to the radial oscillation periods. To satisfy both these constraints we do this ramp in $t_{\text{down}} = 20$ ms.

5.5.2 Uncoupled oscillations

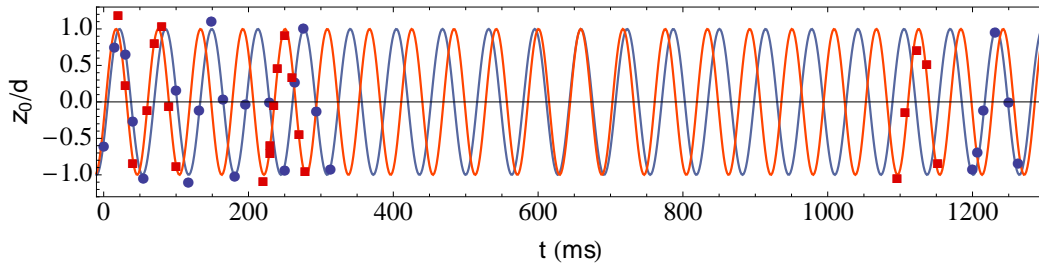


Figure 5.10: Center-of-mass motion of a ${}^7\text{Li}$ cloud (blue circles) and a ${}^6\text{Li}$ cloud (red squares) in the absence of the other species. The solid lines show sine fit to the data allowing to measure, $\omega_b = 2\pi \times 15.68$, $\omega_f = 2\pi \times 17.14$ with a ratio in agreement with the expectations of 1.1 for the magnetic trap.

As a first check, we measure the oscillation of each isotope separately in the trap. Such measurements are presented in figure 5.10 where the motion of a cloud of ${}^6\text{Li}$ in the absence of ${}^7\text{Li}$ and vice versa⁽ⁱ⁾, is monitored for times up to 1.3 s. With the reported data we reach a precision of $\Delta\omega/\omega \lesssim 10^{-2}$, this allows us to verify first the ratio of the bare oscillation frequencies of the two isotopes. We find $\omega_b = 2\pi \times 15.68(10)$ Hz and $\omega_f = 2\pi \times 17.14(10)$ Hz,

⁽ⁱ⁾Since we observe weak fluctuations of the trapping potential over a few hours, to compare two frequencies we interleave their measurements such that they are measured over the same time period of less than 3 hours.

thus the ratio $\omega_b/\omega_f = 1.09(1)$ is in agreement with the expected ratio within the uncertainty. Furthermore we can check the harmonic character of the trap. For this we drive oscillations during a longer time (3.5 s reported for ${}^7\text{Li}$ in figure 5.11), we find the decay time of the oscillations to be $\tau \gtrsim 20$ s which gives a high quality factor for the uncoupled oscillators of $Q = \omega\tau \simeq 2000$, explained by the fact that in this regime the axial trapping is provided solely by the magnetic confinement which is harmonic with a very good approximation due to the dimensions of the coils. These high-quality oscillators represent very sensitive probes for perturbations.

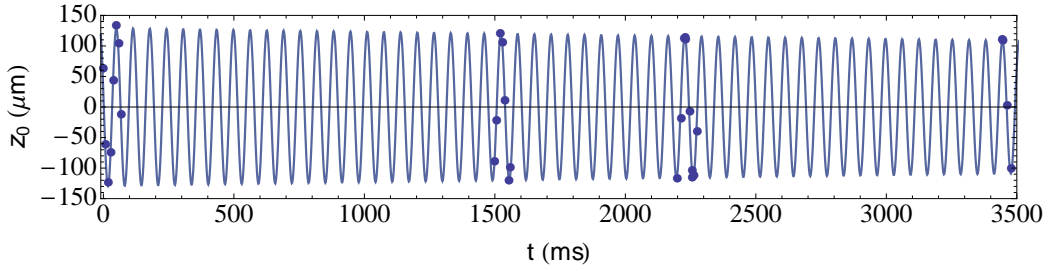


Figure 5.11: Long time oscillations of ${}^7\text{Li}$ alone allowing for a precise frequency measurement. The long damping time observed $\tau \gtrsim 20$ s shows the high quality factor of the magnetic trapping in the axial direction.

5.5.3 Coupled oscillations

Here we report on the observation of the coupling between the two superfluids using dipole oscillations. The oscillations are prepared by the same procedure as described above, with a mixture of superfluids inside the trap. The evolution of the CoM of ${}^7\text{Li}$ and ${}^6\text{Li}$ are represented for $B = 835$ G in figure 5.12, fitted with expressions (5.35,5.36). A first observation is that the motion the two superfluids is undamped for times up to 4 seconds, even when they move through each other. As we discussed earlier, this very low friction reveals the superfluid character of the mixture. Furthermore, it allows for a precise measurement of the frequency of oscillation of each species. A comparison with the bare frequencies gives a measurement of the coupling. We note as above ω_f and ω_b the bare frequencies and $\tilde{\omega}_f$, $\tilde{\omega}_b$ the frequencies in the presence of the other isotope. For a field of 832 G we measure bare and coupled frequencies, the results are:

$$\omega_b = 2\pi \times 15.27(1) \text{ Hz}, \quad \omega_f = 2\pi \times 16.80(50) \text{ Hz} \quad (5.37)$$

$$\tilde{\omega}_b = 2\pi \times 15.00(2) \text{ Hz}, \quad \tilde{\omega}_f = 2\pi \times 16.80(2) \text{ Hz}. \quad (5.38)$$

We focus on the ${}^7\text{Li}$ frequency, it is shifted by $\delta\omega_b/\omega_b = 0.018(1)$. At this field the fermion cloud is a unitary Fermi superfluid with the simple equation of state $\mu_{\text{loc}} = \xi E_{\text{F,loc}}$ with $\xi = 0.37(1)$ the Bertsch parameter. The expected frequency shift can be easily calculated from equation (5.30), we get

$$\frac{\delta\omega_b}{\omega_b} = \frac{13k_{\text{F}}a_{\text{bf}}}{7\pi\xi^{5/4}} \quad (5.39)$$

with $k_F = \sqrt{2m_f\bar{\omega}_f(3N_f)^{1/3}/\hbar}$. Using the experimental parameters ($N_f = 3 \times 10^5$, $\bar{\omega}_f = 2\pi \times 170$ Hz) we get $\delta\omega_b/\omega_b = 0.019(2)$ in excellent agreement with the experimental value of 0.018(1).

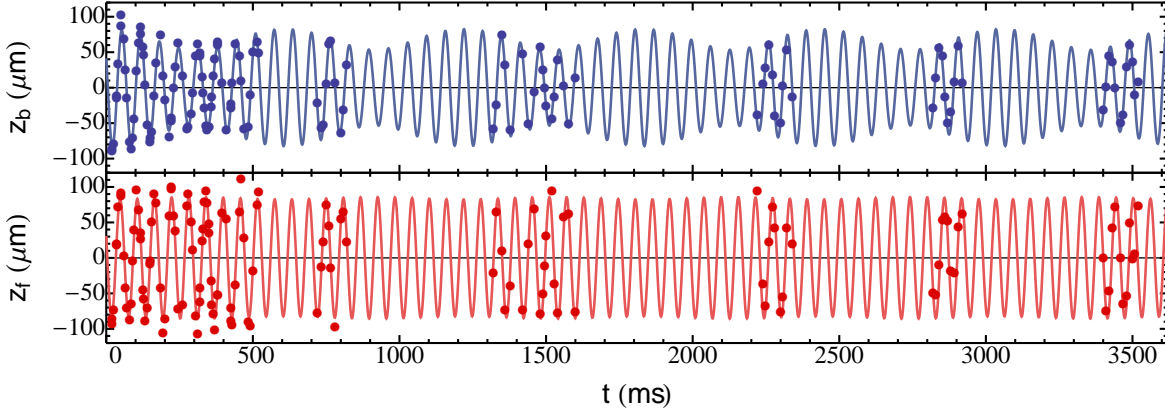


Figure 5.12: Coupled dipole oscillations of the Bose-Fermi superfluid mixture, top: ${}^7\text{Li}$, bottom: ${}^6\text{Li}$. Data taken at 835 G close to unitarity. The coherent energy exchange between the two superfluids and the very weak damping are clearly observed.

The coupling between the two superfluids is also observed in figure 5.12 as an amplitude modulation of the ${}^7\text{Li}$ BEC oscillations. The data are fitted using the coupled-oscillators equations (5.35, 5.36), again in excellent agreement. The relative amplitude modulation of the ${}^7\text{Li}$ BEC is much higher than the relative frequency shift, reflected by the factor $\varepsilon = -14\delta\omega_b/\omega_b$ in equation (5.36). This is due to the near degeneracy of the two oscillator frequencies, resulting in an efficient coherent energy exchange between them despite their weak coupling.

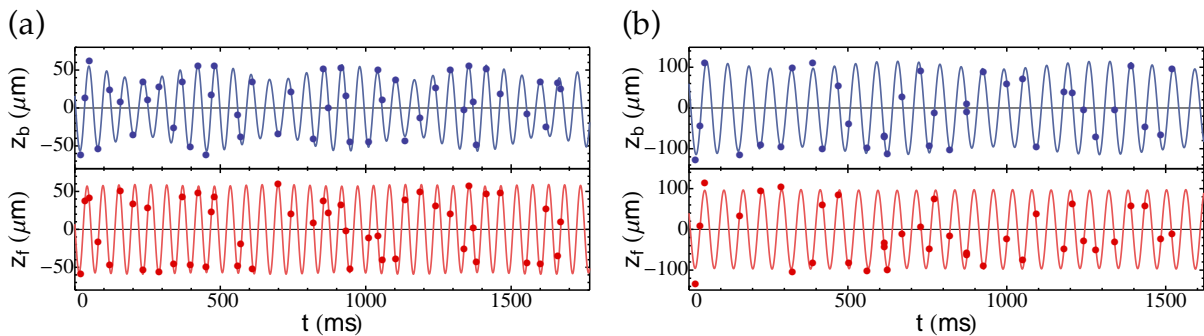


Figure 5.13: Coupled dipole oscillations of the Bose-Fermi superfluid mixture (top: ${}^7\text{Li}$, bottom: ${}^6\text{Li}$) at different magnetic fields: (a): 790 G, on the BEC side of the crossover, (b): 860 G on the BCS side. The efficiency of the coherent energy exchange varies in the crossover due to a variation of the coupling.

The measurement of $\delta\omega_b/\omega_b$ can be extended to the BEC-BCS crossover of the Fermi superfluid by varying the magnetic field. Figure 5.13 shows oscillation measurements at

two different magnetic fields (see appendix 5.7 for more traces through the crossover). From its theoretical expression (5.30) we expect $\delta\omega_b/\omega_b$ to vary in the crossover since the equation of state of the Fermi gas varies. The value of $(\partial n_f/\partial\mu_f)_{r=0}$ depends not only on magnetic field but also on the total fermions number. It can actually be recast as a universal function of the interaction parameter $1/k_F a_f$ where k_F is the Fermi wave-vector of the trapped ${}^6\text{Li}$ gas $k_F = \sqrt{2m_f\bar{\omega}_f(3N_f)^{1/3}/\hbar}$. At zero temperature the equation of state of the homogeneous Fermi gas with density n is indeed a universal function of $1/k_F^{\text{hom}} a_f$ ($k_F^{\text{hom}} = (3\pi^2 n)^{1/3}$), this means that any thermodynamical quantity (here $\partial n/\partial\mu$) is that of a non-interacting Fermi gas times a function of $1/k_F^{\text{hom}} a_f$. This yields $\delta\omega_b/\omega_b = k_F^0 a_{bf} h(k_F^0 a_f)$ where $k_F^0 = (3\pi^2 n_f(0))^{1/3}$ is the local Fermi wave-vector at the center of the trap and $h(k_F^0 a_f)$ is a universal function obtained from the EoS. Using the local density approximation, one can show that $k_F^0 = k_F g(1/k_F a_f)$ with here again $k_F = \sqrt{2m_f\bar{\omega}_f(3N_f)^{1/3}/\hbar}$. Finally the frequency shift can be written as

$$\frac{\delta\omega_b}{\omega_b} = k_F a_{bf} f(1/k_F a_f), \quad (5.40)$$

where f is a universal function which depends on the equation of state of the Fermi superfluid, obtained formally from h and g . From the EoS measured in [Navon *et al.*, 2010] and presented in chapter 1, the function f can be computed numerically.

On the BCS side ($a_f \rightarrow 0^-$), the EoS is that of an ideal Fermi gas, $n_f = (2m_f\mu_f/\hbar^2)^{3/2}/3\pi^2$ yielding

$$\lim_{1/k_F a_f \rightarrow -\infty} f(1/k_F a_f) = \frac{13}{7\pi} \quad (5.41)$$

which is as expected the same as for a unitary Fermi gas but taking $\xi = 1$. On the BEC side, the frequency shift does not go to a constant value. Indeed in the limit of a molecular BEC, the size of the BEC decreases with a_f so that its curvature at center increases and with it the ${}^7\text{Li}$ BEC frequency shift. As a first approximation the molecular BEC can be treated by the mean-field approximation, which yields $\partial\mu_f/\partial n_f = 2m_f/\pi\hbar^2 a_d$ with $a_d = 0.6 a_f$ the dimer-dimer scattering length and so

$$\lim_{1/k_F a_f \rightarrow \infty} f(1/k_F a_f) = 6.19 \frac{1}{k_F a_f}. \quad (5.42)$$

As expected the frequency shift increases on the BEC side, for a better approximation one can take the Lee-Huang-Yang correction into account, this is presented in Appendix 5.7.

Figure 5.14 represents the measurements of $\delta\omega_b/\omega_b k_F a_{bf}$ (red circles) as a function of $1/k_F a_f$, compared to theory in blue line. We also show as a blue triangle the expected value at unitarity calculated from the most recent result on the unitary EoS from [Ku *et al.*, 2012], and the BCS limit of the frequency shift (5.41) in blue dashed line. The agreement between the data and the model is good. This demonstrates that the collective dipole modes are a sensitive probe to both the coupling between the superfluids and the EoS of the Fermi gas.

The frequency shift data displayed in figure 5.14 have been obtained comparing ω_b and $\bar{\omega}_b$. It can also be provided by a single measurement using the measurement of ε . Indeed

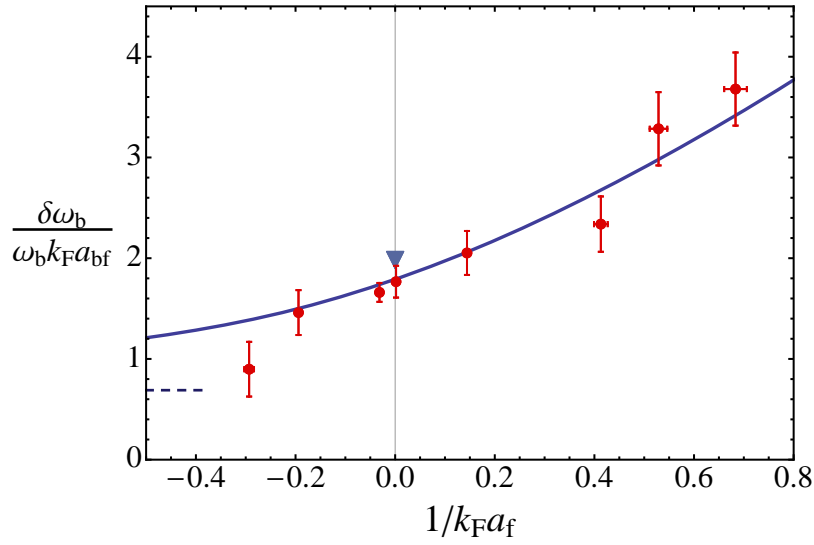


Figure 5.14: Relative frequency shift of the BEC dipole mode in the presence of the Fermi superfluid, through the BEC-BCS crossover. The red points are data measured, the error bars represent the quadrature sum of the different uncertainties: frequency measurements and value of k_F . The blue solid line is the expectation calculated from the EoS presented in Chapter 1, the dashed line shows the BCS limit (5.41 and the blue triangle is the calculated value at unitarity using the measurements of [Ku *et al.*, 2012].

from the fits of the data by equations (5.35, 5.36) displayed as solid lines in figures 5.12, 5.13 and appendix 5.7, the value of ε can be extracted. Since its expression reads $\varepsilon = -14 \delta\omega_b/\omega_b$, the fitted value yields a second measurement of $\delta\omega_b/\omega_b$. In figure 5.13 it appears that indeed the amplitude modulation of the ^7Li BEC oscillations given by ε differs between the BEC and BCS sides as expected. The variation of $\delta\omega_b/\omega_b$ thus measured rescaled in the same units as fig. 5.14 is presented in figure 5.15 in green diamonds. The amplification factor of 14 amplifies the error on $\delta\omega_b/\omega_b$ measured this way. But on the BEC side we observe a disagreement between the green points and theory. The relative amplitude modulation given by ε being very sensitive to the coupling between the two superfluids, we expect it to be the first observable to show departure from the perturbative approach results, which might explain the experimental disagreement with theory. We discuss the limitations of this approach below.

5.5.4 Discussion of the model

To derive the expression of the frequency shift and the coupled oscillators equations, several assumptions were made. One of them is that the initial displacement of the center-of-mass of the mixture excites only the two dipole modes. Experimentally, we observe that during the CoM oscillations, the BEC recovers its full initial amplitude after a cycle of amplitude-modulation, which corresponds to a coherent energy exchange between the fermions and bosons modes. This suggests that the dipole modes are not coupled to additional collective

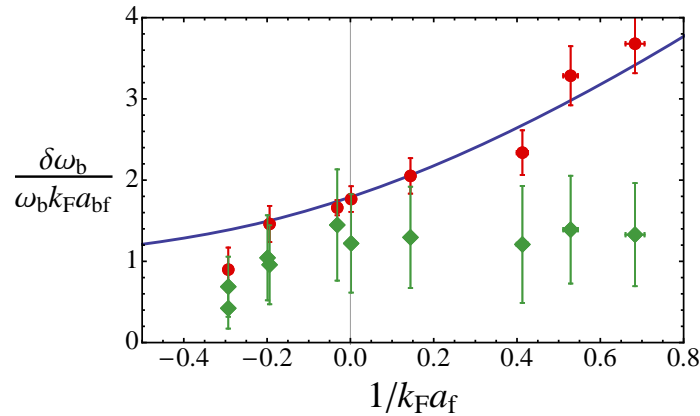


Figure 5.15: Relative frequency shift of the BEC dipole mode in the presence of the Fermi superfluid, measured using the amplitude modulation of the BEC oscillations (green diamonds), compared to the theory presented in main text and to the data from the direct frequency measure (red circles).

modes. To verify this, a signature of the excitation of other collective modes could be a time-modulation of the Thomas-Fermi radii of the two isotopes. Such a modulation is not measurable as exemplified in figure 5.16, it validates the assumption that only two modes are excited.

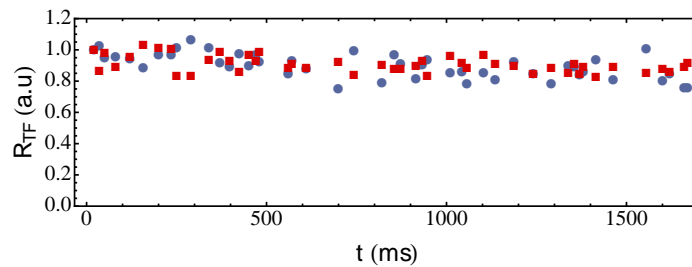


Figure 5.16: Time evolution of the Thomas-Fermi radius of the ^7Li BEC (blue circles) and the ^6Li Fermi superfluid (red squares) during dipole oscillations at 790 G rescaled in arbitrary units. The absence of measurable periodic pattern suggests that no other collective modes than the dipole modes are excited. A weak decrease of both radii is due to residual atom loss during the oscillations.

Also, in the model we considered the BEC as an impurity with a very small extent and negligible effect on the Fermi superfluid. Experimentally the typical ratio of sizes between the Fermi superfluid and the BEC is a factor three. Thus the extent of the BEC is not really negligible. To take the BEC's extent and its effect on the fermions into account, one can calculate the full integral in eq. (5.29). This requires a tedious numerical integration, let us rather discuss qualitatively what we expect. Figure 5.17 represents the theoretical density profiles of a mixture at 832 G along the z direction calculated using the LDA. The fermions density profile is compared to a profile neglecting the effect of the bosons. The effect of the bosons on the fermions is substantial over the size of the BEC, the curvature of the fermions

profile at the center is reduced. It is this curvature that gives the effective potential seen by the bosons, we thus expect a weaker modification of the potential so smaller frequency shift than obtained neglecting the bosons. Finally in some experiments the amplitude of the oscillations was of the order of the BEC size $\simeq 100 \mu\text{m}$, so the approximation of small amplitude oscillations was not verified. In conclusion, though the perturbative model is successful to predict the bosons frequency shift, some of the experiments extended beyond the perturbative regime and a more advanced analysis might reveal interesting dynamics. To obtain a faithful prediction, full hydrodynamics simulations might be necessary. In the remainder of this chapter we present what happens when driving oscillations with an even larger amplitude.

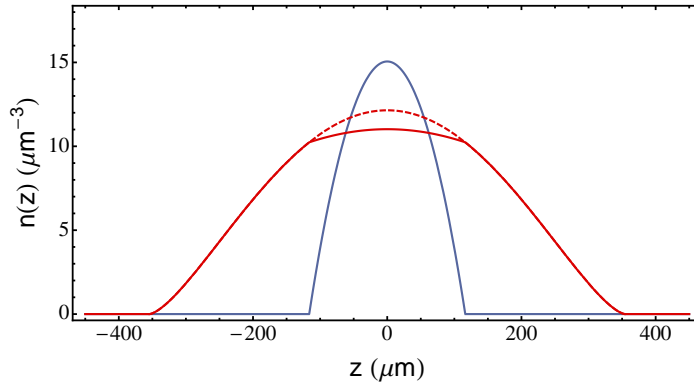


Figure 5.17: Theoretical density profiles on the z axis of a mixture of a ${}^7\text{Li}$ BEC (blue solid line) with a ${}^6\text{Li}$ unitary Fermi superfluid (red solid line). The profile of a Fermi superfluid with the same Thomas-Fermi radius in the absence of ${}^7\text{Li}$ is shown in dashed line, demonstrating that the curvature of the fermions profile is modified in the presence of ${}^7\text{Li}$.

5.6 | Damping of the dipole modes and critical velocity

So far, the dipole oscillations presented are excited with an amplitude $d \leq 110 \mu\text{m}$. Using the equations of motion this corresponds to a maximal relative velocity of $v_{\text{max}} \simeq d(1 + \epsilon)(\tilde{\omega}_f + \tilde{\omega}_b) \simeq 18 \text{ mm/s}$. Below this limit^(k) no damping is observed while the two gases move through each other, a sign of superfluidity of the mixture. Superfluidity is characterized by the absence of dissipation below a certain critical velocity. It is then expected that for higher relative velocities the motion should be damped. This distinctive sign of superfluidity is indeed observed in our experiments, as is presented in the next section starting from the case of a unitary Fermi gas.

^(k)The limit of $d = 110 \mu\text{m}$ is given for a field of 832 G, it varies in the crossover as we discuss below.

5.6.1 Damping at unitarity

When increasing the amplitude of the oscillations, a striking phenomenon is observed: for velocities $v \leq v_{\max}$ we observe a very weak damping, explained by a slight anharmonicity of the trapping potential. Above this limit as represented in figure 5.18, two timescales appear: first a very rapid damping of the BEC oscillations, and following this initial damping, long-lived oscillations at a lower relative velocity. This behaviour is in agreement with the existence of a critical velocity for the relative motion of the two superfluids. At initial times when the two superfluids get out of phase, the velocity passes above the critical value, inducing damping. Once the relative velocity drops below the critical velocity, the motion is long-lived again. In principle the heating caused by the dissipation of the initial motion should create a thermal fraction and induce a friction even at long times. But since the trap is shallow in the radial direction, the clouds can be cooled-down by evaporation. The Fermi superfluid also exhibits a similar behaviour but with a smaller reduction of the oscillation amplitude which can be understood since the drag force created by the BEC is weak relative to its inertia.

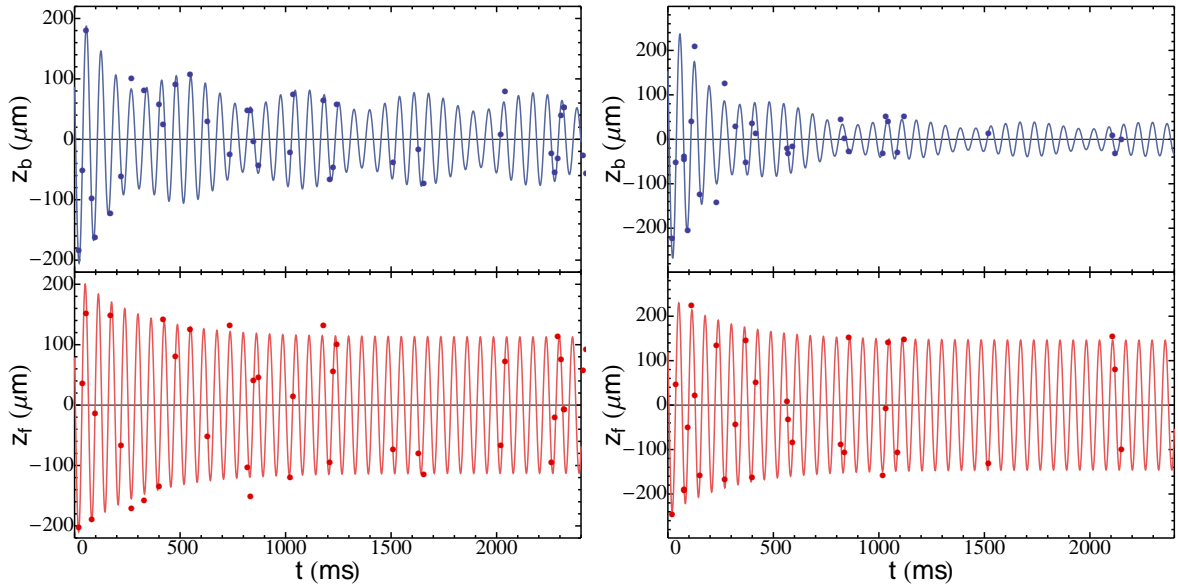


Figure 5.18: Damped oscillations of superfluid mixtures (top: ${}^7\text{Li}$, bottom: ${}^6\text{Li}$), for two different initial displacements, $d = 200 \mu\text{m}$, left, $d = 250 \mu\text{m}$, right. The BEC data clearly show an initial damped motion followed by long-lived oscillations, the Fermi superfluid motion is less reduced by damping, due to a higher mass. The solid lines are fits to the data using equations (5.43, 5.44). On both data we obtain a damping time $\tau \simeq 300 \text{ ms}$.

In principle, the onset of friction above the critical velocity could be seen in a single trace as a reduction in speed. However this requires a high precision on the motion monitoring. To simplify the analysis, we use another measurement. It consists in fitting the experimental data with a phenomenological set of equations, inspired by the observed behaviour. Instead of fitting the motion of the Bose-Einstein condensate and of the Fermi superfluids by

eqs. (5.35, 5.36), we allow for a time-varying amplitude:

$$z'_f(t) = (\delta_f + (1 - \delta_f)e^{-\gamma_f t}) z_f(t) \quad (5.43)$$

$$z'_b(t) = (\delta_b + (1 - \delta_b)e^{-\gamma_b t}) z_b(t), \quad (5.44)$$

where $z_b(t)$ and $z_f(t)$ are as in (5.35, 5.36). These equations are purely phenomenological. The δ_α and γ_α are constants representing the final amplitude of motion relative to the initial one and the initial damping rate of the oscillations. Results of these fits are shown in figure 5.18. Using the obtained $z'_f(t)$, $z'_b(t)$ we can extract the maximal relative velocity during the oscillations.

In figure 5.19 we plot the initial damping rate of the ^7Li BEC γ_b as a function of the maximal relative velocity between the ^7Li and ^6Li superfluids during the oscillations, for a field of 832 G corresponding to unitarity. The maximal relative velocity is rescaled in units of the Fermi velocity of the cloud:

$$v_F = \frac{\hbar k_F}{m_f} = \sqrt{\frac{2\hbar\bar{\omega}(3N_f)^{1/3}}{m_f}}, \quad (5.45)$$

with the typical experimental parameters: $v_F \simeq 48$ mm/s.

In figure 5.19 we observe a sharp onset of damping for relative velocities above $v \simeq 0.4 v_F$. To extract the critical velocity from this data we fit it with an ad-hoc function:

$$\gamma(v) = \Theta(v - v_c) \times (v - v_c)^\alpha, \quad (5.46)$$

using α and v_c as fit parameters, with $\Theta(v)$ the Heaviside function. This fit is shown in solid line in figure 5.19 with the best fit parameters $\alpha = 0.96^{+0.6}_{-0.2}$ and

$$v_c = 0.42(5) v_F. \quad (5.47)$$

This method thus yields a measurement of the critical velocity for the motion of a BEC inside a Fermi superfluid. Assuming the super-critical damping is due to a breakdown of superfluidity and not to other mechanisms such as a dynamical instability, we can discuss the value of v_c in terms of a Landau critical velocity.

First, the sound velocity of the ^7Li BEC at its center $c_{b,0} = \sqrt{g_b n(0)/2m_b} \simeq 3$ mm/s⁽¹⁾ is much lower than the measured critical velocity, thus, superfluidity of ^7Li does not seem to play an obvious role, pointing to a breaking of superfluidity in the fermion gas. As discussed in chapter 1, the simple Landau formula for a massive impurity is

$$v_c = \text{Min}_{s=f,b} \left(\frac{\epsilon_s^F(\mathbf{p})}{p} \right) \quad (5.48)$$

where $\epsilon_{f,b}^F$ denotes the two excitation branches of the ^6Li superfluid. For a unitary Fermi superfluid it gives a critical velocity close to $v_c = c_f$ with c_f the speed of sound of the Fermi

⁽¹⁾The factor $\sqrt{1/2}$ is due to the elongated geometry [Pitaevskii and Stringari, 2003].

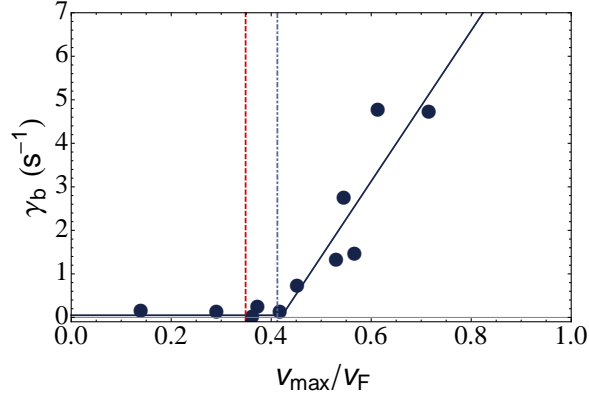


Figure 5.19: Damping rate of the BEC oscillations as a function of the maximal velocity of the BEC inside the Fermi superfluid, rescaled in units of the Fermi velocity, as defined in main text. The solid line shows the fit used to extract the value of v_c . The red dashed line shows the value of the sound velocity at the center of the fermions cloud, and the blue dot-dashed line shows the sum of the two sound velocities $c_b + c_f$ as predicted by [Castin *et al.*, 2014] calculated with the parameters of our experiments.

superfluid ([Combescot *et al.*, 2006] see ch. 1 fig 1.5). For an elongated gas at unitarity, the sound velocity at its center can be shown to be $c_f = \xi^{1/4} v_F / \sqrt{5} = 0.35 v_F$ [Hou *et al.*, 2013] with v_F defined above, in fair agreement with our measurements though slightly smaller. This value is shown in red dashed line in figure 5.19. We have also discussed in chapter 1 the relevant case of a BEC impurity in which the value of the critical velocity reads:

$$v_c = \text{Min}_{p; s=b,f} \frac{\epsilon^B(p) + \epsilon_s^F(p)}{p}, \quad (5.49)$$

where $\epsilon^B(p)$ is the Bogolyubov dispersion relation of the BEC's elementary excitations. Recalling figure 1.6 obtained in [Castin *et al.*, 2014] using the typical parameters of our experiments: $\mu_b \simeq E_F/10$, v_c is the threshold for the emission of sound excitations in both superfluids yielding:

$$v_c = c_b + c_f \quad (5.50)$$

with c_b the sound velocity in the ^7Li BEC. From equation (5.50), v_c is upshifted with respect to c_f . In an elongated BEC, the sound velocity at center is given by $c_b = \sqrt{gn(0)/2m}$. To compare with our measurements we use a mean sound velocity along the z axis, we get $c_b = 0.6(2) v_F$, finally using (5.50) we obtain $v_c = 0.41(3) v_F$ shown as the blue dot-dashed line in figure 5.19, in good agreement with the experimental value.

Other experiments have implemented the motion of an impurity in a Fermi superfluid. In the measurement of v_c using a moving optical lattice, [Miller *et al.*, 2007] and very recently an attractive laser beam [Weimer *et al.*, 2014], the direct comparison with theory is rendered difficult by the fact that the defect probes low-density regions. The value of v_c we report in this thesis is the highest ever measured in a dilute Fermi gas, both in units of v_F and in absolute value. This stresses out the particularity of our experiment, where the perturbation is localized inside the gas and the condition of weak-coupling is readily fulfilled, avoiding the drawbacks of laser impurities, and finally the critical velocity value is possibly enhanced due to the superfluid nature of the impurity.

Contrary to the unitary case, in other regions of the BEC-BCS crossover, the necessity to create two excitations (one in each superfluid) could cause the value of v_c for a BEC impurity to differ strongly from that of a massive impurity as measured with a laser. For instance, the damping of an excitation in the BEC through elementary excitations in the Fermi cloud is expected to differ starkly between the BEC and BCS regimes [Zheng and Zhai, 2014]. For this reason we have extended our measurements of the damping rate of the BEC as a function of v/v_F to the crossover.

5.6.2 Damping in the BEC-BCS crossover

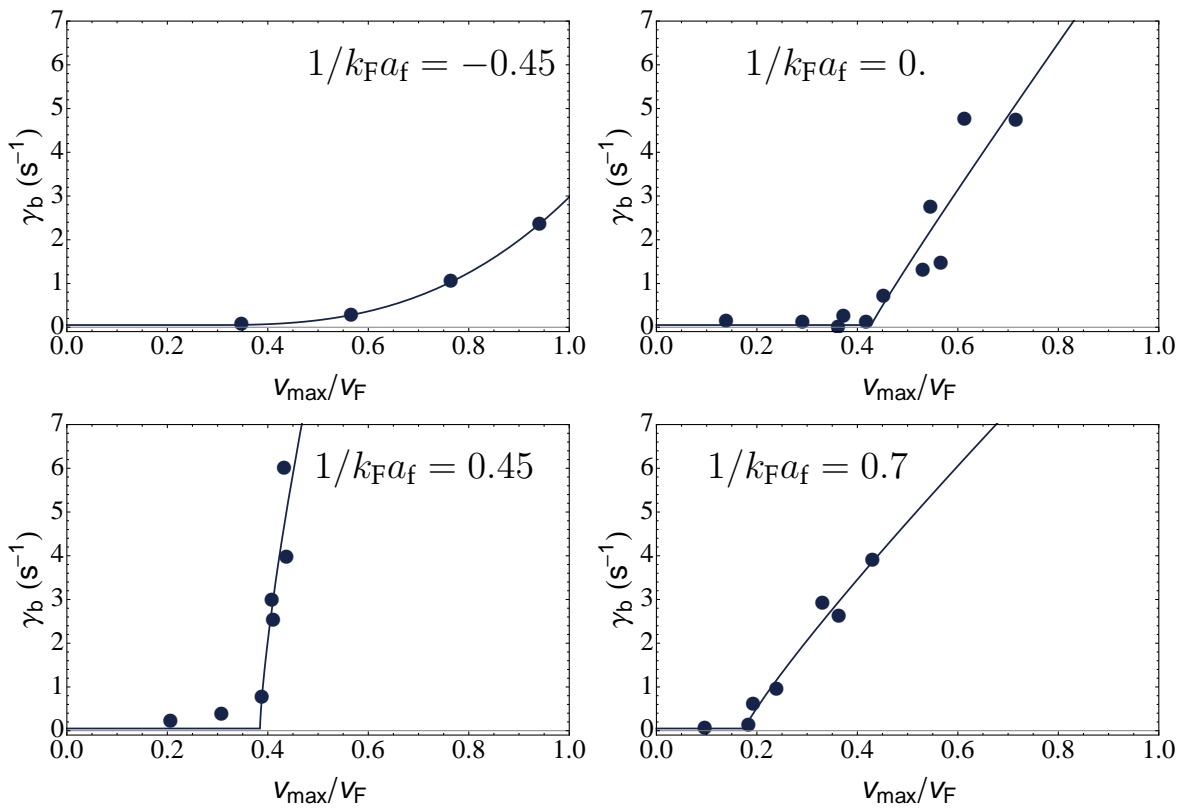


Figure 5.20: Damping of the BEC motion as a function of the relative velocity for four different points in the BEC-BCS crossover. On the BEC side and at unitarity ($1/k_F a_f \geq 0$), a sharp onset of damping is observed for increasing velocity, while friction is strongly reduced on the BCS side. The solid lines are fits with the ad-hoc function (5.46).

The results in the form $\gamma_b = f(v_c)$ are represented in figure 5.20, so far we have been able to repeat the measurements for four different magnetic fields (780, 800, 832, 880 G), corresponding to $1/k_F a_f = (0.7, 0.45, 0, -0.45)$. On the BEC side, a sharp onset of damping is also observed, with at $1/k_F a_f = 0.7$ a striking reduction of the apparent critical velocity to half of its value at unitarity. On the BCS side, the damping rate is strongly reduced, with a slow increase as a function of velocity rendering difficult an extraction of v_c .

Though more measurements are needed, we can already comment on the present ones.

First, for decreasing magnetic fields, the sharp decrease of the apparent v_c on the BEC side is in disagreement with the theories from [Combescot *et al.*, 2006, Castin *et al.*, 2014]. Indeed, both predict a critical velocity close to the sound velocity, which, at $1/k_F a_f = 0.7$ is reduced only by $\sim 5\%$ with respect to its value at unitarity^(m). Since both a_f and a_b decrease while a_{bf} stays constant, the coupling between the superfluids increases and the observed damping could be due in fact to dissipation through other channels than elementary excitations. For instance, it is known that in the case of two BECs close to the phase-separation threshold, relative motion induces phase-separation for velocities much lower than the sound velocity [Law *et al.*, 2001], this leads experimentally to the formation of dark-bright soliton trains observed in [Hamner *et al.*, 2011]. A coupling of the dipole modes to other collective modes leading to a dynamical instability could also explain damping at low amplitudes.

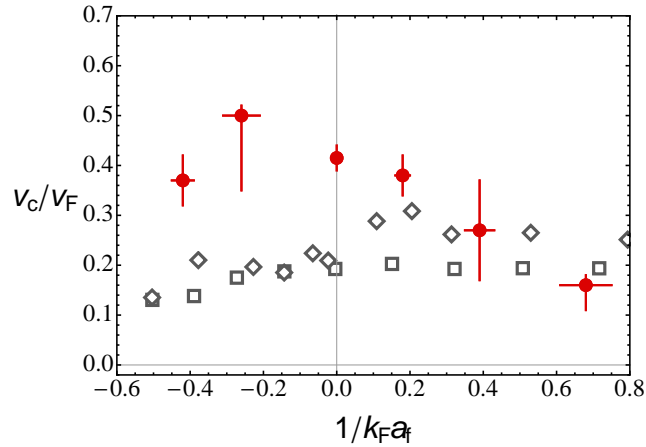


Figure 5.21: Critical velocity v_c in the crossover ($k_F = \sqrt{2m_f \bar{\omega}_f (3N_f)^{1/3} / \hbar}$), the red circles and error bars represent the best value and uncertainty on v_c obtained by fitting the data with the ad-hoc function (5.46). Grey squares show the critical velocity measured in ref [Miller *et al.*, 2007] using a moving optical lattice, Grey diamonds show v_c measured with an attractive tightly focused laser impurity from [Weimer *et al.*, 2014].

On the BCS side of resonance, the strong reduction of the damping could be the signature that a different dissipation mechanism is at work. In this regime, the critical velocity of a moving BEC should differ from that of a massive impurity, and represent an original measurement, but so far our results are preliminary and should be pushed further. We represent the preliminary results on the critical velocity as a function of $1/k_F a_f$ in figure 5.21, together with a summary of the results of fig. 5.20.

The difficulty to extract v_c points out the limits of our measurement method, for more insight, our damping data could be further analyzed if a theory able to predict the drag force above v_c was made available. Some alternative techniques might allow to extract more

^(m)Since the theory is for a homogeneous system, we have calculated the local k_F^0 at the center of the cloud to compare with it.

accurately the value of v_c in the crossover, for example by measuring observables responsive to the energy dissipated like the condensed fraction of the BEC or the number of atoms.

5.6.3 Friction at finite temperature

The observation of a critical velocity is a hallmark of superfluidity. When the temperature increases above T_c , there should be some friction even at vanishingly small relative velocities. It is then interesting to see if such an increase in friction can be observed when increasing temperature. At zero temperature, friction above v_c leads, as we have seen, to a damping of the BEC oscillations. However, as we shall see, a strong friction can lead to unexpected effects and in particular an increase in the lifetime of the BEC oscillations. To model these effects, we use the coupled oscillators model, adding a fluid friction force $f = -\alpha v$ where v is the relative velocity between the two oscillators. This model reads:

$$\begin{pmatrix} \ddot{z}_f \\ \ddot{z}_b \end{pmatrix} = - \begin{pmatrix} \frac{\alpha}{M_f} & -\frac{\alpha}{M_f} \\ -\frac{\alpha}{M_b} & \frac{\alpha}{M_b} \end{pmatrix} \begin{pmatrix} \dot{z}_f \\ \dot{z}_b \end{pmatrix} - \begin{pmatrix} \omega_f^2 + \frac{K_{bf}}{M_f} & -\frac{K_{bf}}{M_f} \\ -\frac{K_{bf}}{M_b} & \omega_b^2 + \frac{K_{bf}}{M_b} \end{pmatrix} \begin{pmatrix} z_f \\ z_b \end{pmatrix}, \quad (5.51)$$

it can easily be solved numerically. Exploring the solutions of (5.51) yields surprising results. Figure 5.22 represents these solutions with the typical parameters of our experiments ($M_f = 10 M_b$, $\omega_f = \sqrt{7/6} \omega_b$) and initial displacement d , for two different friction strengths ($\alpha = 0.2 \omega_b M_b$ and $\alpha = 5 \omega_b M_b$). At zero friction, (not represented) the solutions are the undamped coupled oscillations seen in the precedent sections. For $\alpha = 0.2 \omega_b M_b$, fig. 5.22 (a) the motion of the light oscillator z_b is damped in a time $\tau \simeq 20/\omega_b$. We also observe the amplitude modulation due to coherent coupling between the two oscillators. For the strongest friction represented $\alpha = 5 \omega_b M_b$, fig. 5.22 (b) the result is counter-intuitive: First the motion of the light oscillator is less damped than in the previous case, second the frequency of its oscillations is shifted with respect to the two previous cases, it is locked on the heavy oscillator's frequency.

To understand this behaviour, we perturbatively solve this system in the presence of a strong friction between the oscillators ($\alpha \gg \omega_b M_b$, $\omega_f M_f$). To simplify further the analysis, we neglect the coupling between the oscillators ($K_{bf} = 0$), it plays no major role when friction is strong. First we solve the system in the situation where the two oscillators are degenerate $\omega_f = \omega_b$, looking for solutions in the form $(z_f(t), z_b(t)) = (d_f, d_b) \exp(i\omega t)$, we find one undamped mode with frequency $\omega_1 = \omega_b$ and $d_{f,1} = d_{b,1}$, the other solutions correspond to initial displacements in two opposite directions and are quickly damped. Since in the experiments an identical initial displacement is applied on the two oscillators we are interested in the evolution of the in-phase undamped mode when the degeneracy is lifted ($\omega_f \neq \omega_b$). Then we treat the shift in bare frequency of the two oscillators as a perturbation, expressing $\omega_f^2 = \omega_b^2(1 + \epsilon)$ (in our experimental system $\epsilon = 1/6$). Expanding ω_1 in powers of ϵ : $\omega_1 = \omega_1^{(0)} + \epsilon \omega_1^{(1)} + \epsilon^2 \omega_1^{(2)} + \dots$, we find:

$$\omega_1 = \omega_b \left(1 + \frac{\epsilon}{2(1 + \beta)} - \frac{\epsilon^2}{2(1 + \beta^2)} \right) + i \frac{\epsilon^2 \beta \omega_b^2}{2(1 + \beta)^3 \alpha_b} + \dots, \quad (5.52)$$

with $\alpha_b = \alpha/M_b$ and $\beta = M_b/M_f$. We have found that to second order in ϵ , the eigenfrequency acquires an imaginary term

$$\gamma = \frac{\epsilon^2 \beta \omega_b^2}{2(1 + \beta)^3 \alpha_b} \quad (5.53)$$

which corresponds to the damping rate of this mode. Analysing the expression of γ we see that it decreases with increasing friction (α) as is the case in the numerical solutions. In conclusion an increase in friction results in a decrease in damping rate, and a frequency locking of the two oscillators to $\omega = \text{Re}(\omega_1) \simeq \omega_f/(1 + \beta) \simeq \omega_f$.

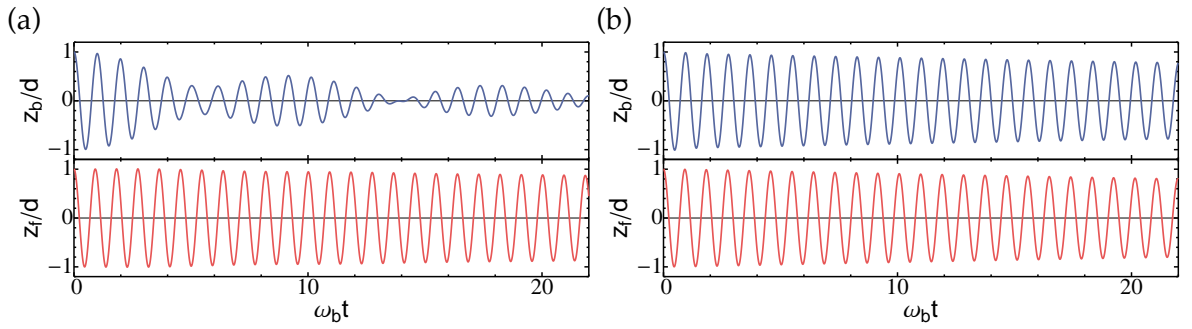


Figure 5.22: Numerical solution to the coupled oscillators model with a friction force $f = -\alpha v$ between the two oscillators. The two cases are $\alpha = 0.2 \omega_b M_b$ (a), $\alpha = 5 \omega_b M_b$ (b). As the friction is increased (between (a) and (b)), the damping of the light oscillator (top) decreases, due to a frequency and phase-locking of the two oscillators.

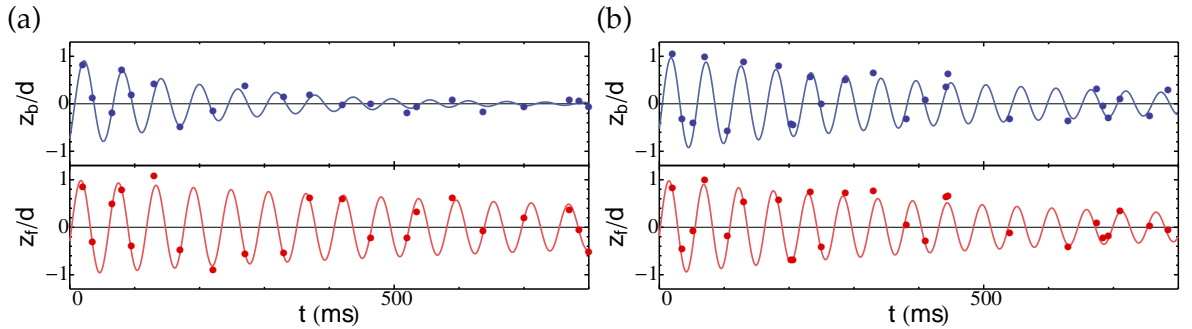


Figure 5.23: Damped oscillations obtained at $T_1 = 0.8 T_{c,b} = 0.4 T_F$ (a) and $T_1 = 1.5 T_{c,b} = 0.5 T_F$ (b). At $T = T_1$ the frequency of the Bose gas oscillations (top) is $\tilde{\omega}_b = 2\pi \times 16.9(2)$ Hz, pushed-up towards the Fermi gas frequency $\tilde{\omega}_f = 2\pi \times 17.3(2)$ Hz. At T_2 we observe an almost perfect locking of the frequencies: $\tilde{\omega}_b = 2\pi \times 18.5(2)$ Hz, $\tilde{\omega}_f = 2\pi \times 18.6(2)$ Hz, associated with a reduction of damping. The initial amplitude of the oscillations is $d = 100 \mu\text{m}$ in both cases.

We have tested this friction model on our experiment, driving oscillations at higher temperature, by stopping the evaporation earlier (at a magnetic field $B = 832$ G). For increasing temperature, the boson-fermion-collision rate rises (see chapter 2), and so the friction between the two gases should grow. We have recorded measurement at two

temperatures : $T_1 \simeq 300\text{nK}$, which corresponds to $T_1 \simeq 0.8 T_{c,b}$ and $T_2 \simeq 0.4 T_F \simeq 2 T_{c,f}$ the results at this temperature are represented in figure 5.23 (a). The second temperature is $T_2 \simeq 600\text{nK}$ corresponding to $T_2 \simeq 1.5 T_{c,b} \simeq 0.5 T_F^{(n)}$, represented in figure 5.23 (b). The data are fitted with simple exponentially damped sinusoids to extract the oscillations frequency and damping time (solid lines). For both data sets, the initial displacement d is $d \simeq 100 \mu\text{m}$, a value for which no damping was observed at zero temperature.

For the first temperature (T_1), initially 50 % of the BEC is condensed while the Fermi gas is entirely in the normal phase. We observe a fast damping of the Bose gas oscillations down to zero amplitude, a sign that the mixture is not superfluid. From the fits we get $\omega_b = 2\pi \times 15.9(2) \text{ Hz}$ (measurement not shown), $\tilde{\omega}_b = 2\pi \times 16.9(2) \text{ Hz}$ $\tilde{\omega}_f = 2\pi \times 17.3(2) \text{ Hz}$, $\tau \simeq 200 \text{ ms}$ with τ the damping time of the Bose gas oscillations. For the higher temperature (T_2) the two gases are fully in the normal phase. The fits yield $\omega_b = 2\pi \times 17.2(2) \text{ Hz}$, $\tilde{\omega}_b = 2\pi \times 18.5(2) \text{ Hz}$ $\tilde{\omega}_f = 2\pi \times 18.6(2) \text{ Hz}$, $\tau \simeq 550 \text{ ms}$.

These results are in qualitative agreement with the friction model: First, in the lower temperature data set the Bose gas frequency is upshifted with respect to the bare one, and for the higher temperature an almost perfect frequency locking with the fermions is observed. Second the damping rate of the Bose gas oscillations is reduced when increasing friction, as expected from the model. Besides the interesting result that these finite-temperature measurement yield, they could represent if repeated at many temperatures a probe of the critical temperature of the Fermi gas in the BEC-BCS crossover.

5.7 | Concluding remarks and prospects with Bose-Fermi superfluid mixtures

In this chapter we have presented experimental results on mixtures of Bose and Fermi superfluids in ${}^7\text{Li}-{}^6\text{Li}$ gases. First we have demonstrated the superfluidity of the two components, before turning to the possible signatures of interactions between the two superfluids. Such signature was found in the spectroscopy of the dipole modes of the mixture in the harmonic trapping potential. The experimental results were found in good agreement with a perturbative model in terms of sum rules. We then explored the damping of the dipole modes in different regimes, first in the zero-temperature doubly-superfluid regime, where damping was observed above a certain velocity for relative motion allowing to study the issue of the critical velocity for counter-flow. Second the damping of the dipole modes was observed at finite temperature demonstrating an interesting frequency-locking effect caused by dissipation. The damping measurement if pushed further could bring

⁽ⁿ⁾The number of atoms was reduced with respect to the usual conditions on the experiment which explains differences in degeneracy with respect to what is given in table 5.2.

precious insight in the critical velocity and damping mechanisms at zero-temperature, and could allow for an original measurement of the critical temperature of the Fermi superfluid.

While we have observed the first markers of interactions between the two superfluids, a number of interesting measurements could be performed with such gases. For instance, since the dipole modes are sensitive to the boson-fermion interaction, they could be used to measure the effective boson-dimer scattering length which can differ from $2a_{bf}$ as was assumed in our mean-field approximation [Cui, 2014, Zhang et al., 2014]. Beyond the low-lying dipole modes, other collective modes of the mixture in a harmonic trap could be investigated. A profusion of theoretical investigations have focused on collective excitations in spin-polarized Bose-Fermi mixtures [Minguzzi and Tosi, 2000, Miyakawa et al., 2000, Yip, 2001, Capuzzi and Hernández, 2001, Sogo et al., 2002, Liu and Hu, 2003, Capuzzi et al., 2003, Sogo et al., 2003, Maruyama et al., 2005, Banerjee, 2007, Maruyama and Yabu, 2009, Maruyama and Yabu, 2013], and their extension to doubly-superfluid mixtures could be of significant interest.

The dipole modes are long-wavelength excitations of the first sound modes. In a Bose-Fermi superfluid mixture, there exist two first sound modes as we have verified experimentally. A hallmark of superfluidity is the existence of second-sound, recently observed in a unitary Fermi gas [Sidorenkov et al., 2013]. In an early theoretical investigation of Bose-Fermi superfluid mixtures dedicated to a potential realization in liquid ^3He - ^4He mixtures, [Volovik et al., 1975] have demonstrated that only one second-sound excitation is expected in the mixture. However this was obtained using the assumption - verified for liquid helium - that the thermal expansion coefficient is small (due to the fact $C_V \simeq C_P$). This is not verified for dilute quantum gases, it is then worthwhile investigating this issue both theoretically and experimentally, with potential measurable effects in a ^6Li - ^7Li mixture. Another hallmark of superfluidity is the existence of vortices in rotating superfluids, the vortex creation dynamics and steady state of rotating Bose-Fermi superfluid mixtures was recently studied in [Wen and Li, 2014], and could be experimentally studied in a ^6Li - ^7Li mixture.

A realistic proposal of interesting experiments with a ^6Li - ^7Li superfluid mixture is given in [Ozawa et al., 2014]. The authors study a mixture of a BEC with a spin-imbalanced Fermi gas, and they demonstrate that the presence of bosons stabilizes superfluidity, raising the critical imbalance for loss of superfluidity (the Clogston-Chandrasekhar limit). They show that an instability can occur, forming measurable spatial structures in trapped mixtures. Furthermore, the imbalanced Fermi gas in a flat potential could display FFLO order at zero temperature [Zwergner, 2012].

Other interesting proposals include simulation of quark matter [Maeda et al., 2009] and the formation of Faraday waves [Abdullaev et al., 2013]. Finally the phase diagram of homogeneous superfluid Bose-Fermi mixtures was studied in [Adhikari and Salasnich, 2008, Ramachandhran et al., 2011]. When placed in a optical lat-

tice this mixture should exhibit an interesting phase diagram with a so-called “super-counter-fluid” phase [Kuklov and Svistunov, 2003], this system has also been studied in [Modak et al., 2011, Bukov and Pollet, 2014].

Some of these theoretical proposals require a stronger or even tunable boson-fermion interaction. The possibility to reduce the boson-boson scattering length in the ${}^6\text{Li}$ - ${}^7\text{Li}$ mixture can allow to amplify the boson-fermion relative effects and makes our mixture a privileged one for the study of double superfluids, but one should also look for other potential mixtures to widen the scope of opportunities.

The only other fermionic atom to have been brought to the superfluid state so far is ${}^{40}\text{K}$. Simultaneous superfluidity could be reached in a ${}^{40}\text{K}$ - ${}^{41}\text{K}$ mixture since bosonic ${}^{41}\text{K}$ has a positive scattering length at the fields of the Feshbach resonances of the fermionic isotope ${}^{40}\text{K}$. The boson-fermion background scattering length in this mixture is $97 a_0$ [Wang et al., 2000, Falke et al., 2008], and ${}^{40}\text{K}$ - ${}^{41}\text{K}$ resonances might allow for a tuneable interaction. ${}^{40}\text{K}$ - ${}^7\text{Li}$ mixture might also offer heteronuclear Feshbach resonances in the range of superfluidity of ${}^{40}\text{K}$ and ${}^7\text{Li}$, to the best of our knowledge no published work exists on the topic, ${}^{39}\text{K}$ - ${}^6\text{Li}$ or ${}^{41}\text{K}$ - ${}^6\text{Li}$ have heteronuclear resonances at too low fields and should not allow for a tunable boson-fermion interaction [Hanna, T. and Tiesinga, E.,]. A mixture of ${}^{23}\text{Na}$ and ${}^{40}\text{K}$, with a large and negative background scattering length $-575 a_0$ [Gerdes et al., 2008], could realize a strong boson-fermion interaction⁽⁶⁾. Finally and most interestingly, it has been shown that broad interspecies Feshbach resonances exist between ${}^{133}\text{Cs}$ and ${}^6\text{Li}$ [Repp et al., 2013, Tung et al., 2013]. With ${}^{133}\text{Cs}$ in its absolute internal ground state $|F = 3, m_F = 3\rangle$ (first excited $|F = 3, m_F = 2\rangle$) and ${}^6\text{Li}$ in $|1_f\rangle$, the resonance is found at $B = 843 \text{ G}$ ($B = 897 \text{ G}$), and with $|2_f\rangle$ at $B = 889 \text{ G}$ ($B = 943 \text{ G}$). These resonances overlap both with the large ${}^6\text{Li}$ resonance that we have used between $|1_f\rangle$ - $|2_f\rangle$ at 832 G and with zero crossings of the boson-boson scattering length of ${}^{133}\text{Cs}$ [Ferlaino et al., 2011], opening hope for resonantly interacting doubly superfluid Bose-Fermi mixtures. These few examples do not constitute a comprehensive record of possibilities and the growing list of elements cooled to quantum degeneracy extends the range of candidate Bose-Fermi superfluid mixtures.

⁽⁶⁾Broad Feshbach resonances exist between these isotopes [Park et al., 2012], it might however be necessary to use radio-frequency or optical dressing to displace these resonances in the range of superfluidity of ${}^{40}\text{K}$.

Conclusions, perspectives

In this thesis work, we have presented several experimental investigations conducted on the lithium set-up at Laboratoire Kastler Brossel, each illustrating a different facet of the achievements and prospects of the field of dilute ultracold gases.

The implementation of D_1 cooling on ^7Li provided insight into experimental laser cooling techniques. The theoretical investigation of the results shed light on the mechanisms at work in this scheme. The application of this technique opened the way to fast cooling of large degenerate samples of lithium and potassium nowadays routinely obtained [Salomon *et al.*, 2014, Burchianti *et al.*, 2014, Ketterle, 2014]. Besides, a particularly interesting prospect of this method is its usage for single-site imaging of lithium isotopes in an optical lattice, helping to observe strongly-correlated phases in a lattice. This method is based on fluorescence of trapped atoms, and necessitates a cooling procedure to counteract the heating caused by spontaneous emission. Since simple Sisyphus cooling is unavailable for lithium, another cooling procedure is necessary and D_1 grey molasses cooling is a possible candidate. This is an illustrative example of how novel techniques used in ultracold gases can lead to the attainment and study of strongly-correlated states of matter.

Using a Feshbach resonance, we have studied three-body losses in a Bose gas with resonant two-body interactions. These results have been compared with a theoretical model showing good agreement, thus extending the understanding of three-body recombination of bosons in the unitary regime of maximal s-wave two-body interactions, a contribution to the field of few-body physics. These results allowed us to conclude on the stability-condition of unitary Bose gases, a benchmark for further experimental studies of this elusive strongly-interacting system.

In the last part, we have presented experimental results on Bose-Fermi superfluid mixtures. To the best of our knowledge, such mixtures have not been observed in any other physical system. Using relative motion of the two superfluids, we have been able to measure their coupling (albeit weak). The observed counter-flow motion possesses the characteristics of superfluid flows, with the absence of friction at low velocities and the onset of dissipation above a critical velocity. The measurement of this critical velocity at unitarity is in agreement with the Landau critical velocity. The extension of these measurements could bring insight in the mechanisms for friction above the critical velocity. Besides, interfaces between bosons and fermions are ubiquitous in nature, from the coupling between photons and electrons giving rise to the Meissner effect in superconductors, to liquid ^3He - ^4He

mixtures. ^3He - ^4He mixtures share many characteristics with our mixtures and the advancement of our research could be mutually advantageous. Possibly, implementing cryogenic cooling techniques used in helium like dilution refrigeration to dilute ultracold gases could allow to reach very low temperatures. On the other hand measurements of the properties of degenerate Bose-Fermi mixtures could help to refine interaction models in helium and experimentalists towards double superfluidity in helium.

Appendix A |

D_1 sub-Doppler cooling of ^7Li

A.1 | The Focker-Planck equation

We consider particles subject to a Langevin force, with equation of motion:

$$m\dot{v} = F(v, t), \quad (\text{A.1})$$

where $F(v, t)$ is the Langevin force, with mean value $\langle F(v, t) \rangle = \mathcal{F}(v)$ and the stochastic character of the force is expressed by the fluctuations $\delta F(v, t)$, $\langle \delta F(v, t) \rangle = 0$. δF decays very rapidly^(a) with t as is usually the case for a Langevin force. See for example [Cohen-Tannoudji, Claude, 1990] for a complete treatment. We will take the case here of $\mathcal{F}(0) = 0$, where the velocity distribution is centered on $v = 0$ for long times. The evolution of the velocity distribution is governed by the Focker-Planck equation. In one dimension it reads :

$$\frac{\partial}{\partial t} P(v, t) = \frac{\partial}{\partial v} (M_1[v]P(v, t)) + \frac{\partial^2}{\partial v^2} (M_2[v]P(v, t)). \quad (\text{A.2})$$

with P the velocity distribution and the M_n coefficients are

$$M_n = \lim_{\Delta t \rightarrow 0} \frac{\langle \Delta v^n \rangle}{\Delta t}. \quad (\text{A.3})$$

using equation (A.1) the M_n coefficients can be calculated, for M_1 we get:

$$\left\langle \frac{d\Delta v}{dt} \right\rangle = \left\langle \frac{dv}{dt} - \frac{d\bar{v}}{dt} \right\rangle = \left\langle \frac{dv}{dt} \right\rangle = \frac{1}{m} \mathcal{F}(v) = M_1 \quad (\text{A.4})$$

$$(\text{A.5})$$

where \bar{v} is the equilibrium mean velocity equal to zero in our case. M_2 can be found similarly:

$$m^2 M_2 = \int_0^\infty d\tau \langle \delta F(v, t) \delta F(v, t + \tau) \rangle = \mathcal{D}(v), \quad (\text{A.6})$$

where $\mathcal{D}(v)$ is the diffusion coefficient, expression (A.6) stands for its definition, for example given in [Cohen-Tannoudji, Claude, 1996].

Finally using (A.2) the equilibrium solution is

$$P_{st}(v) \propto \frac{1}{D(v)} \exp \left(m \int_0^v dv' \frac{F(v')}{D(v')} \right), \quad (\text{A.7})$$

^(a)On time scales much shorter than the evolution driven by $\mathcal{F}(v)$.

which is the expression used in the main text.

A.2 | Expressions of coefficients of the perturbative expansion of the density matrix

Using the perturbative approach presented in the main text, the expressions of the friction coefficient and the spontaneous emission rate are expressed in terms of the three following coefficients:

$$\rho_{33}^{(2,0)} = 2 \cos(z) \text{Im} \rho_{13}^{(1,0)} \quad (\text{A.8})$$

$$\rho_{13}^{(1,1)} = \frac{i}{\delta_1 - \frac{i\Gamma}{2} - \Omega_2^2(z)/\delta} \left[\frac{\partial}{\partial z} + \frac{\Omega_2^2 \cos(z)}{\delta^2} \frac{\partial}{\partial z} (\cos(z) \cdot) \right] \rho_{13}^{(1,0)} \quad (\text{A.9})$$

$$\frac{\Gamma}{2} \text{Re} \rho_{23}^{(2,1)} = -\frac{\partial}{\partial z} \text{Re} \rho_{23}^{(2,0)} + \frac{\delta_2}{\Omega_2} \text{Im} \rho_{13}^{(1,1)} - \frac{\delta_2}{2\Omega_2(z)} \frac{\partial}{\partial z} \left(\rho_{33}^{(2,0)} + 2\rho_{22}^{(2,0)} \right) - \cos(z) \text{Im} \rho_{21}^{(1,1)} \quad (\text{A.10})$$

with $\Omega_i(z) = \Omega_i \cos(z)$ and $\delta = \delta_1 - \delta_2$. The expressions of the above coefficients can be found using the relations:

$$\rho_{13}^{(1,0)} = \frac{\cos(z)}{\delta_1 - \Omega_2(z)^2/\delta - i\Gamma/2} \quad (\text{A.11})$$

$$\text{Re} \rho_{23}^{(2,0)} = \text{Im} \rho_{13}^{(1,0)} \left(\frac{\delta_2}{\Omega_2} + \frac{\cos^2(z)\Omega_2}{\delta} \right) \quad (\text{A.12})$$

$$\text{Im} \rho_{21}^{(1,1)} = -\frac{\Omega_2}{\delta^2} \frac{\partial}{\partial z} \left(\cos(z) \text{Re} \rho_{13}^{(1,0)} \right) - \Omega_2(z) \text{Im} \rho_{13}^{(1,1)} \quad (\text{A.13})$$

$$\rho_{22}^{(2,0)} = \text{Im} \rho_{13}^{(1,0)} \left(\frac{\delta^2 + 1}{\cos(z)\Omega_2^2} + \frac{\delta_2 \cos(z)}{\delta} + 2 \cos(z) \right) - \frac{\cos(z)}{\delta} \text{Re} \rho_{13}^{(1,0)} \quad (\text{A.14})$$

A.3 | Extention of D_1 cooling to other principal detunings

The minimal temperatures are found for the parameters given in the main text and namely, $\delta_2 = 2\pi \times 27 \text{ MHz}$ for the principal detuning. We have further explored the effect of the Λ configuration on the temperature for two other detunings: 17 MHz (fig. A.1) and 10 MHz (fig. A.2). We represent the experimental results and compare with our perturbative resolution of the optical Bloch equations as in main text. In the first case we observe cooling in a narrower band with respect to the case $\delta_2 = 2\pi \times 27 \text{ MHz}$ represented in figure 3.5, and a similar narrow structure around the Raman condition. In the second case $\delta_2 = 2\pi \times 10 \text{ MHz}$ we observe a strong heating on both sides off the RC, absent in the previous cases. We note that the model developed in the main text was based on a far detuned principal beam $\delta_2 > \Gamma$, which is not verified here, this modifies the cascade of states and the effects of the cycles through this cascade.

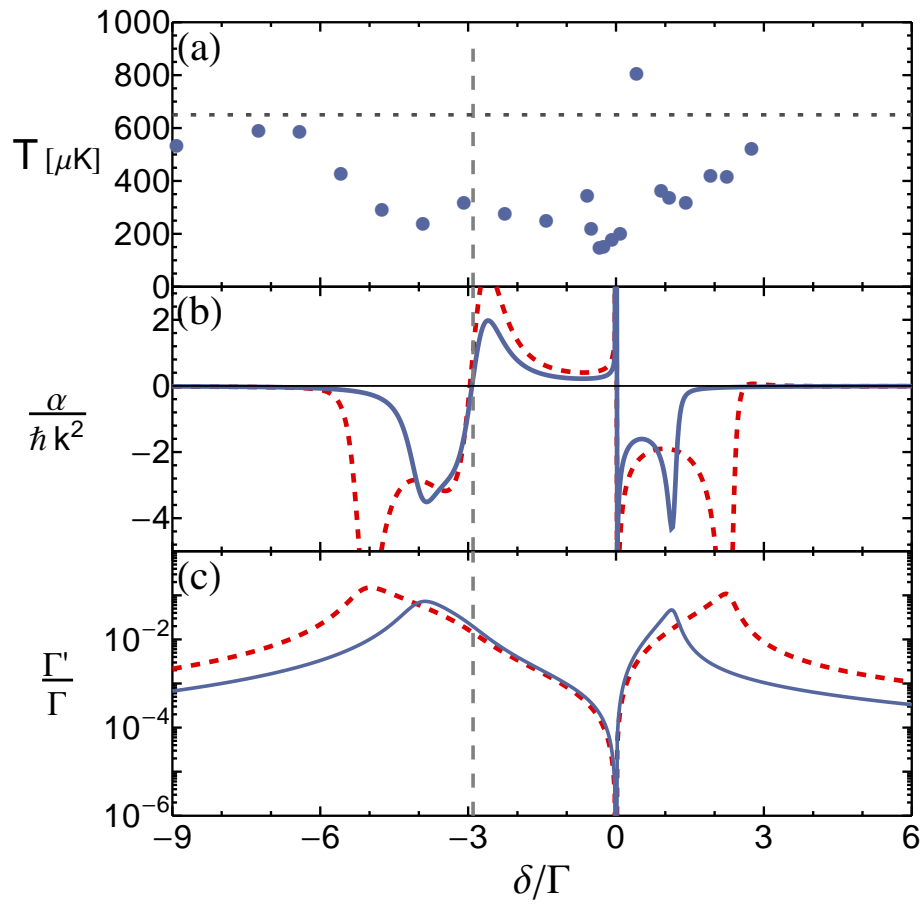


Figure A.1: Cooling efficiency as a function of the repumper detuning δ . Same as figure 3.5 but with $\delta_2 = 2\pi \times 17$ MHz.

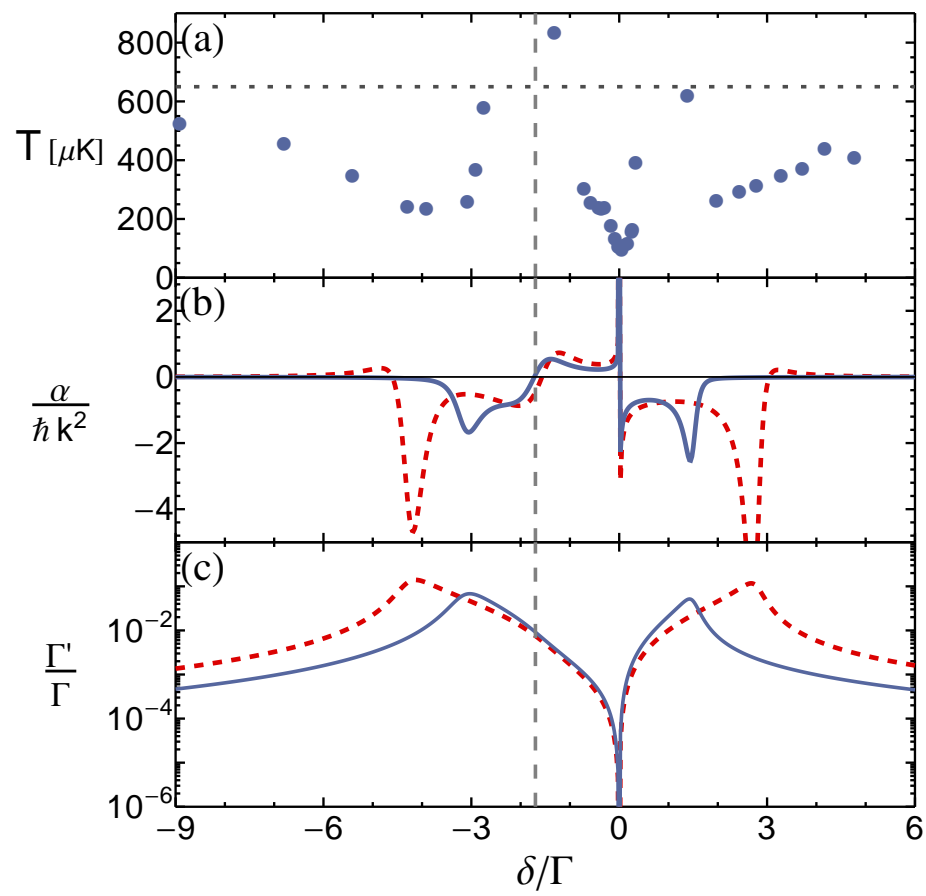


Figure A.2: Cooling efficiency as a function of the repumper detuning δ . Same as figure 3.5 but with $\delta_2 = 2\pi \times 10$ MHz.

Appendix B |

Coupled dipole modes of superfluid mixtures

B.1 | Dipole modes through the crossover.

Measurements of the coupled dipole modes of superfluid mixtures for nine different fields in the crossover.

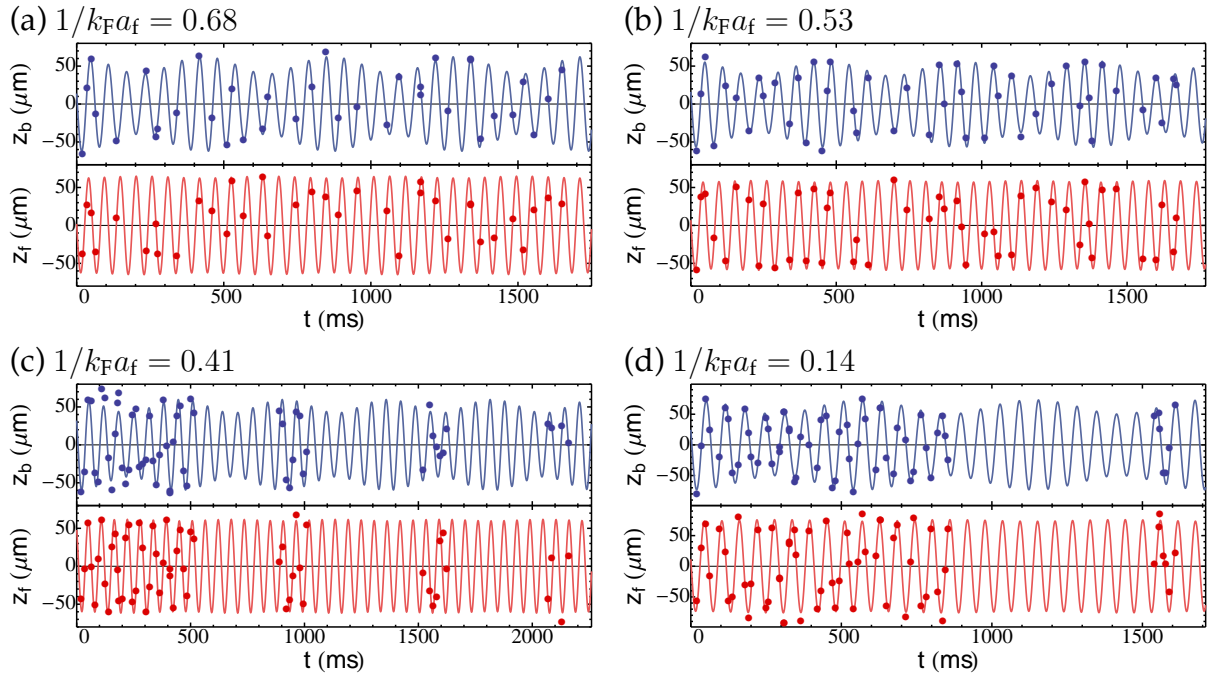


Figure B.1: Oscillations of Bose-Fermi superfluid mixtures, blue: BEC CoM position, red, Fermi superfluid. Solid lines: Fit with equations (5.35, 5.36). (a): data taken at 780 G ($1/k_F a_f = 0.68$), (b): 790 G ($1/k_F a_f = 0.53$), (c): 800 G ($1/k_F a_f = 0.41$), (d): 820 G ($1/k_F a_f = 0.14$).

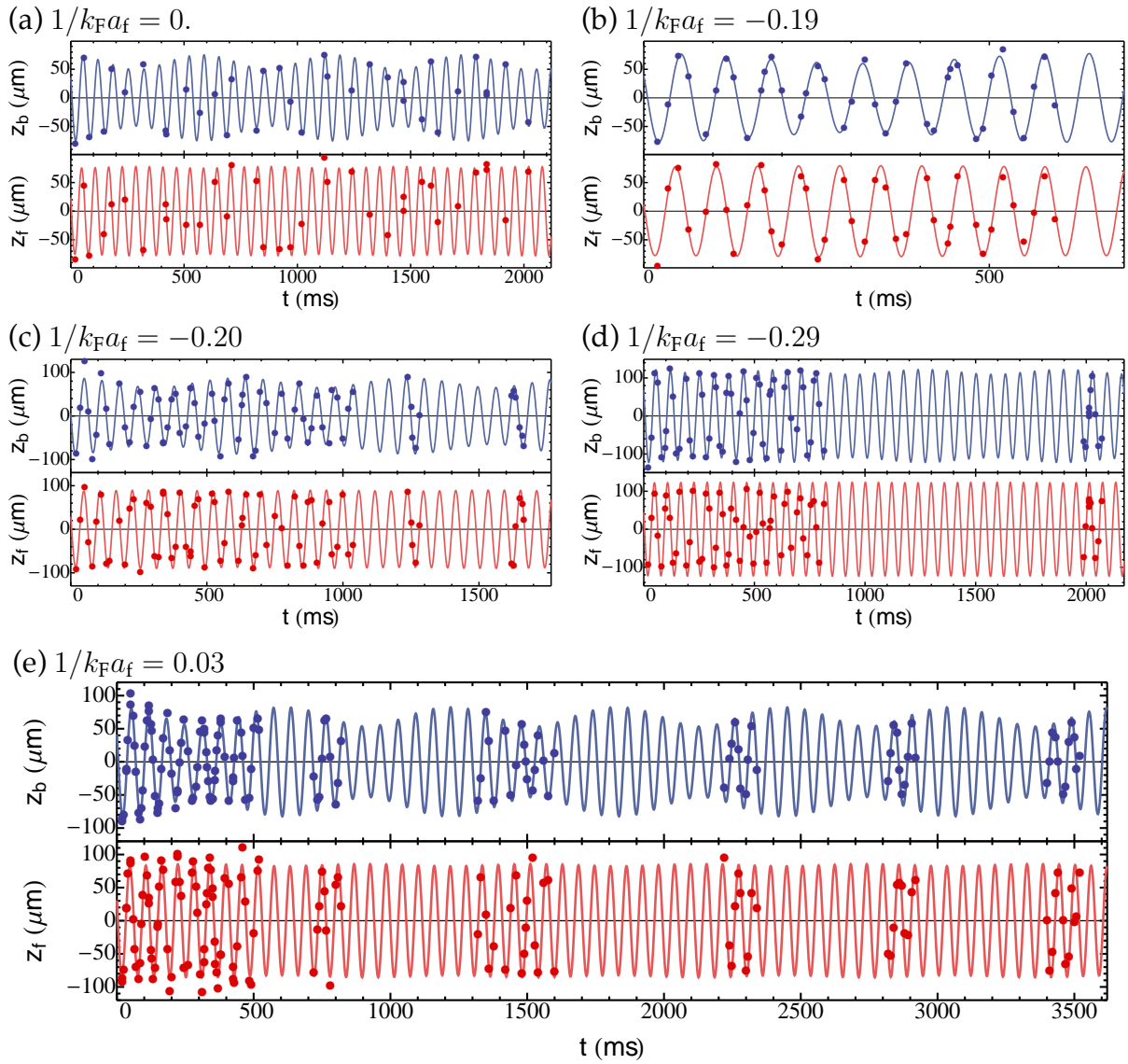


Figure B.2: Same as fig. B.1 (a): data taken at 832 G ($1/k_F a_f = 0.$), (b): 850 G ($1/k_F a_f = -0.19$), (c): 851 G ($1/k_F a_f = -0.20$), (d): 860 G ($1/k_F a_f = -0.29$), (e): 835 G ($1/k_F a_f = -0.03$).

B.2 | BEC limit of the Frequency shift.

Here we evaluate the frequency shift $\delta\omega_b/\omega_b$ given by

$$\frac{\delta\omega_b}{\omega_b} \simeq \frac{1}{2} g_{bf} \left(\frac{dn_f^{(0)}}{d\mu_f} \right)_{r=0}, \quad (\text{B.1})$$

in the limit where the Fermi superfluid is a molecular BEC of composite Fermi-Fermi dimers. The dimers have a mass $m_d = 2m_f$ and a binding energy $E_d = \hbar^2/m_d a_d^2$, where $a_d = 0.6 a_f$ is the dimer-dimer scattering length [Petrov *et al.*, 2004]. The Lee-Huang-Yang EoS for the molecular BEC reads

$$n_d = \frac{\mu_d}{g_d} \left(1 - \frac{32}{3\sqrt{\pi}} \sqrt{\frac{\mu_d a_d^3}{g_{dd}}} \right) \quad (\text{B.2})$$

where $n_d = n_f/2$ is the density of dimers, $\mu_d = 2\mu_f + E_d$ their chemical potential, and $g_{dd} = 4\pi\hbar^2 a_d/m_d$ the coupling constant for the dimer-dimer interaction. Then we have $\frac{d}{d\mu_f} = 2 \frac{d}{d\mu_d}$ and thus

$$\frac{dn_f^{(0)}}{d\mu_f} = \frac{4}{g_d} \left(1 - \frac{16}{\sqrt{\pi}} \sqrt{\frac{\mu_d a_d^3}{g_{dd}}} \right). \quad (\text{B.3})$$

This quantity must be evaluated in the center of the trap ($r = 0$) to infer the frequency shift (B.1). The second term in (B.3) is of first order in $\sqrt{n_d a_d}$. We then evaluate its argument in the mean-field approximation which gives the usual expression for the chemical potential of a BEC in a harmonic trap:

$$(\mu_d)_{r=0} = \frac{\hbar\bar{\omega}_f}{2} \left(15N_d a_d \sqrt{\frac{m_d \bar{\omega}_f}{\hbar}} \right)^{2/5}. \quad (\text{B.4})$$

Using (B.4) and the expression of the Fermi wave-vector:

$$k_F = \sqrt{\frac{m_d \bar{\omega}_f}{\hbar}} (6N_d)^{1/6}, \quad (\text{B.5})$$

with $N_f = 2N_d$, we can recast our expression for the frequency shift (B.3) in the universal units used in the main text (Eq. (10)):

$$\left(\frac{\mu_d a_d^3}{g_d} \right)_{r=0} = \frac{1}{8\pi} \left(\frac{5}{2} \right)^{2/5} (a_d k_F)^{12/5} \quad (\text{B.6})$$

$$\left(\frac{dn_f^{(0)}}{d\mu_f} \right)_{r=0} \simeq \frac{2m_f}{0.6\pi\hbar^2 a_f} \left(1 - 1.172 (k_F a_f)^{6/5} \right) \quad (\text{B.7})$$

$$\frac{\delta\omega_b}{\omega_b} \frac{1}{k_F a_{bf}} \simeq 6.190 \frac{1}{k_F a_f} \left(1 - 1.172 (k_F a_f)^{6/5} \right) \quad (\text{B.8})$$

This limit is shown in green in Fig. B.3. The mean-field approximation (red curve in Fig. B.3) corresponds to the first term in Eq. (B.8).

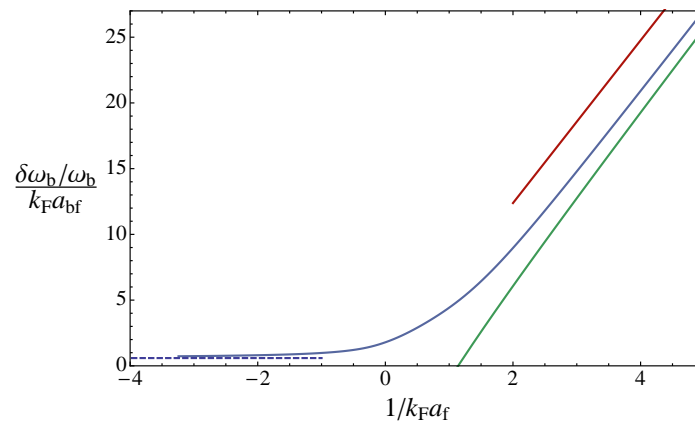


Figure B.3: Predicted frequency shift (blue line) over a broad range of $1/k_F a_f$. The dashed blue line shows the ideal Fermi gas limit. On the BEC side the green line shows the Lee-Huang-Yang prediction (B.8) and the red line the mean-field prediction.

Appendix C |

Publications and Preprints

Lifetime of the Bose Gas with Resonant interactions

B. Rem, A. Grier, I. Ferrier-Barbut, U. Eismann, T. Langen, N. Navon, L. Khaykovich, F. Werner, D.S. Petrov, F. Chevy, C. Salomon

Physical Review Letters **110**, 163202 (2013)

Lifetime of the Bose Gas with Resonant Interactions

B. S. Rem,¹ A. T. Grier,¹ I. Ferrier-Barbut,¹ U. Eismann,¹ T. Langen,² N. Navon,¹ L. Khaykovich,^{1,3} F. Werner,¹
D. S. Petrov,^{4,5} F. Chevy,¹ and C. Salomon¹

¹Laboratoire Kastler-Brossel, École Normale Supérieure, CNRS and UPMC, 24 rue Lhomond, 75005 Paris, France

²Vienna Center for Quantum Science and Technology, Atominstiut, TU Wien, Stadionallee 2, 1020 Wien, Austria

³Department of Physics, Bar-Ilan University, Ramat-Gan, 52900 Israel

⁴Université Paris-Sud, CNRS, LPTMS, UMR8626, Orsay F-91405, France

⁵Russian Research Center Kurchatov Institute, Kurchatov Square, 123182 Moscow, Russia

(Received 20 December 2012; published 16 April 2013)

We study the lifetime of a Bose gas at and around unitarity using a Feshbach resonance in lithium 7. At unitarity, we measure the temperature dependence of the three-body decay coefficient L_3 . Our data follow a $L_3 = \lambda_3/T^2$ law with $\lambda_3 = 2.5(3)_{\text{stat}}(6)_{\text{syst}} \times 10^{-20} (\mu\text{K})^2 \text{cm}^6 \text{s}^{-1}$ and are in good agreement with our analytical result based on zero-range theory. Varying the scattering length a at fixed temperature, we investigate the crossover between the finite-temperature unitary region and the previously studied regime where $|a|$ is smaller than the thermal wavelength. We find that L_3 is continuous across the resonance, and over the whole $a < 0$ range our data quantitatively agree with our calculation.

DOI: 10.1103/PhysRevLett.110.163202

PACS numbers: 34.50.Lf, 03.65.Nk, 31.15.xj, 67.85.-d

Recent advances in manipulating cold atomic vapors have enabled the study of Fermi gases at the unitary limit where the scattering length a describing two-body interactions becomes infinite. It has been demonstrated both experimentally and theoretically that in this limit the system is characterized by a scale invariance leading to remarkably simple scaling laws [1]. In contrast, most experimental results on Bose-Einstein condensates were obtained in the weakly interacting regime. Recent experimental results on bosons near Feshbach resonances have revived the interest in strongly interacting bosons [2]: the development of experimental tools has enabled a precise test of the Lee-Huang-Yang corrections [3,4], and several theoretical papers have studied the hypothetical unitary Bose gas at zero [5–8] or finite [9] temperature. The strongly interacting Bose gas is one of the most fundamental quantum many-body systems, yet many open questions remain. Examples include the prediction of weakly bound Efimovian droplets [10,11], the existence of both atomic and molecular superfluids [12], and the creation of strongly correlated phases through three-body losses [13].

Experimental investigation of ultracold bosons near unitarity has been hampered by the fast increase of the three-body recombination rate close to a Feshbach resonance [14,15]. In this case, the number of trapped atoms $N(t)$ follows the usual three-body law

$$\dot{N} = -L_3 \langle n^2 \rangle N, \quad (1)$$

where $\langle n^2 \rangle = \int d^3r n^3(\mathbf{r})/N$ is the mean square density and L_3 is the three-body loss rate constant. In the zero-temperature limit L_3 increases as $\hbar a^4/m$ [16] multiplied by a dimensionless log-periodic function of a revealing Efimov physics [17–26]. At finite temperature, L_3 saturates when a becomes comparable to the thermal wavelength

$\lambda_{\text{th}} = \hbar/\sqrt{2\pi m k_B T}$, and $L_3 \sim \hbar a^4/m \sim \hbar^5/m^3 (k_B T)^2$ [9,27,28]. This saturation suggests that a non-quantum-degenerate Bose gas near a Feshbach resonance will maintain thermal quasiequilibrium [9]. Indeed, in this regime, $|a| \gtrsim \lambda_{\text{th}}$ and $n\lambda_{\text{th}}^3 \ll 1$. Thus, the elastic collision rate $\gamma_2 \propto \hbar \lambda_{\text{th}} n/m$ is much higher than the three-body loss rate $\gamma_3 = L_3 n^2 \propto \hbar \lambda_{\text{th}}^4 n^2/m$. Experimental and numerical evidence for a saturation of L_3 was reported in Refs. [3,22,27]. A theoretical upper bound compatible with this scaling was derived in Ref. [29] assuming that only the lowest three-body hyperspherical harmonic contributes, an assumption which breaks down when $|a|$ exceeds λ_{th} .

In this Letter, we measure the temperature dependence of the unitary three-body recombination rate and find agreement with a $L_3 \propto 1/T^2$ scaling law. In a second set of measurements performed at constant temperature, we study L_3 versus a . We show how this function smoothly connects to the zero-temperature calculations when $|a| \ll \lambda_{\text{th}}$. These observations are explained by a general theoretical result for $L_3(a, T)$, exact in the zero-range approximation, that we derive in the second part. Our theory allows for a complete analytic description of the unitary case and, in particular, predicts (weak) log-periodic oscillations of the quantity $L_3 T^2$. Our findings quantify the ratio of good-to-bad collisions in the system and provide solid ground for future studies of strongly interacting Bose gases. Furthermore, on the $a < 0$ side, experiments have so far detected a single Efimov trimer [3,23–25,30]. Our analysis predicts that a second Efimov trimer of very large size should be detectable in ${}^7\text{Li}$ at temperatures on the order of a few microkelvins.

Our experimental setup was presented in Ref. [4]. After magneto-optical trapping and evaporation in an Ioffe magnetic trap down to $\approx 30 \mu\text{K}$, $\approx 2 \times 10^6$ ${}^7\text{Li}$ atoms are transferred into a hybrid magnetic and dipole trap in

the state $|1, 1\rangle$. The transverse confinement is obtained by a single laser beam of waist $43(1) \mu\text{m}$ and wavelength 1073 nm , while the longitudinal trapping is enhanced by a magnetic field curvature. The resulting potential has a cylindrical symmetry around the propagation axis of the laser and is characterized by trapping frequencies $0.87 < \omega_\rho/2\pi < 3.07 \text{ kHz}$ and $18 < \omega_z/2\pi < 49 \text{ Hz}$. Further cooling is achieved by applying a homogeneous magnetic field $B \approx 718 \text{ G}$ for which the scattering length is $\approx 200a_0$, and decreasing the depth of the trapping potential down to a variable value U' allowing us to vary the final temperature of the cloud. Afterwards, the dipole trap is recompressed to a value $U > U'$, to prevent significant atom loss due to the enhanced evaporation rate; see below. At each T we choose U so as to maintain the temperature constant during the three-body loss rate measurement. Finally, the magnetic field is ramped in $100\text{--}500 \text{ ms}$ to $B_0 \approx 737.8(3) \text{ G}$, where the scattering length a diverges [4]. We then measure the total atom number N remaining after a variable waiting time t and the corresponding T , using *in situ* imaging of the thermal gas.

Our data are limited to the range of temperature $1 \leq T \leq 10 \mu\text{K}$. For $T \geq 1 \mu\text{K}$, the rate $\gamma_3 = -\dot{N}/N$ remains small with respect to other characteristic rates in our cloud (elastic scattering rate, trapping frequencies), which guarantees that a thermal quasiequilibrium is maintained. We check that for these parameters the *in situ* integrated density profile is indeed Gaussian, and we use it to extract the temperature of the cloud, found to be in agreement with that of time of flight. The peak phase-space density varies within $0.07 \times 10^{-2} < n_0 \lambda_{\text{th}}^3 < 1.1 \times 10^{-2}$. A typical time dependence of N and T is shown in Fig. 1. The time dependence of the atom number is fitted using the usual three-body recombination law Eq. (1) [31]. For a nondegenerate gas of temperature T , the density profile is Gaussian,

and we have $\langle n^2 \rangle = N^2 A(T) = N^2 (m \bar{\omega}^2 / 2\pi \sqrt{3} k_B T)^3$, with $\bar{\omega} = (\omega_\rho^2 \omega_z)^{1/3}$ being the mean trapping frequency. We then have

$$\dot{N} = -L_3(T) A(T) N^3. \quad (2)$$

Assuming constant temperature, integrating Eq. (2) gives

$$N(t) = \frac{N(0)}{\sqrt{1 + 2A(T)L_3(T)N^2(0)t}}, \quad (3)$$

which we use as a fitting function to analyze $N(t)$, and extract $L_3(T)$ as shown in Fig. 1.

Because of their n^3/T^2 dependence, three-body losses preferentially remove atoms of low kinetic energy and those located at the center of the trap where the density is the highest and potential energy is the smallest. As a result, three-body loss events heat up the cloud [16]. We ensure constant temperature by operating with a typical trap depth $U \approx \eta k_B T$ with $6 \leq \eta \leq 8$, for which the residual evaporation then balances recombination heating; see Fig. 1(b). This ensures that L_3 is time independent, but, as a drawback, evaporation contributes to losses. To quantify the relative importance of evaporative and three-body losses, we first note that an atom expelled by evaporation removes on average an energy $\approx (\eta + \kappa) k_B T$, where, taking κ from Ref. [32], we follow Ref. [33]. Typically, we have $\kappa \approx 0.68$ for $\eta = 6$ and $\kappa \approx 0.78$ for $\eta = 8$ [34]. In comparison, each three-body event leaves on average an excess heat of $\delta k_B T$ per particle. Extending the derivation of Ref. [16] to the case of an energy dependent three-body loss rate $\propto E^{-2}$, we obtain $\delta = 5/3$ [34]. The energy balance required to keep the temperature constant thus implies that the evaporation rate is $\approx \delta/(\eta + \kappa - 3)$ times smaller than the three-body loss rate. Neglecting this effect would induce a systematic overestimation of L_3 of about 50% for $\eta = 6$ and 30% for $\eta = 8$. Therefore, we apply this systematic correction to our data.

The temperature dependence of L_3 obtained from our measurements at unitarity is shown in Fig. 2. It is well fit by the scaling law $L_3(T) = \lambda_3/T^2$, with $\lambda_3 = 2.5(3)_{\text{stat}} \times 10^{-20} (\mu\text{K})^2 \text{ cm}^6 \text{ s}^{-1}$ as the best-fit value. In order to discuss the systematic uncertainty of this measurement, we note that the quantity $L_3 T^2$ scales in all experimental parameters identically to the thermodynamic quantity $(\mu^2/P)^2$ of a zero-temperature Bose-Einstein condensate with chemical potential μ and pressure P [34]. We use this relation to calibrate our experimental parameters [4] and obtain a systematic uncertainty on λ_3 of $\leq 25\%$ resulting in $\lambda_3 = 2.5(3)_{\text{stat}}(6)_{\text{syst}} \times 10^{-20} (\mu\text{K})^2 \text{ cm}^6 \text{ s}^{-1}$.

We now study the a dependence of L_3 on both sides of the resonance by employing the same experimental procedure as in the unitary case. We tune the scattering length while keeping the temperature within 10% of $5.9 \mu\text{K}$; see Fig. 3. The excess heat δ entering in the correction now depends on the value of ka . The correction is applied to all data points (filled circles) except in the range $1500a_0 < a < 5000a_0$ (open circles), where the assumptions of our

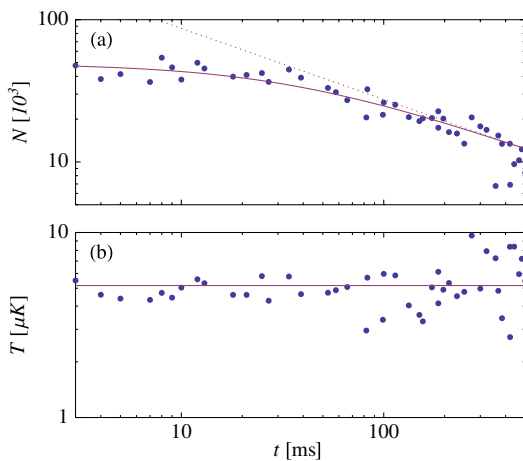


FIG. 1 (color online). Time dependence of the atom number (a) and temperature (b) for $U = \eta k_B T$, with $T = 5.2(4) \mu\text{K}$, $\eta = 7.4$, and (uncorrected) $L_3 = 1.2(2)_{\text{stat}} \times 10^{-21} \text{ cm}^6 \text{ s}^{-1}$. The dotted line shows the long time $t^{-1/2}$ dependence of the number of atoms.

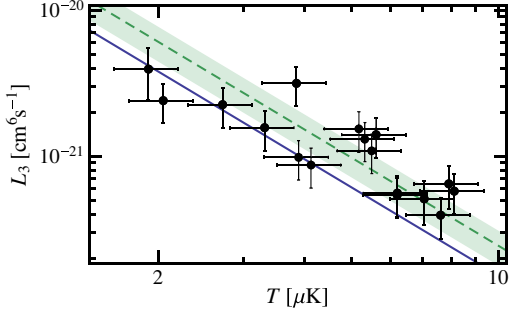


FIG. 2 (color online). Temperature dependence of the three-body loss rate L_3 . Filled circles, experimental data; green dashed line, best fit to the data $L_3(T) = \lambda_3/T^2$ with $\lambda_3 = 2.5(3)_{\text{stat}}(6)_{\text{syst}} \times 10^{-20} (\mu\text{K})^2 \text{cm}^6 \text{s}^{-1}$; the shaded green band shows the 1σ quadrature sum of uncertainties. Solid line, prediction from Eq. (5), $\lambda_3 = 1.52 \times 10^{-20} (\mu\text{K})^2 \text{cm}^6 \text{s}^{-1}$ with $\eta_* = 0.21$ from Refs. [30,39].

model are not applicable [34]. In the limit $|a| \gg \lambda_{\text{th}}$, we observe that $L_3(a)$ saturates to the same value on both sides of the resonance. In the opposite limit $|a| \ll \lambda_{\text{th}}$, our data connect to the zero-temperature behavior [20] studied experimentally in Refs. [22–26]. On the $a < 0$ side, the dashed line is the zero-temperature prediction for L_3 from Ref. [20]. We clearly see that finite temperature reduces the three-body loss rate. On the $a > 0$ side, temperature effects become negligible for $a < 2000a_0$, as testified by our measurements performed on a low-temperature Bose-Einstein condensate (green squares), which agree with the total recombination rate to shallow and deep dimers calculated at $T = 0$ in Ref. [20] (dashed line). The data around unitarity and on the $a < 0$ side are seen to be in excellent agreement with our theory Eq. (4) described below.

In order to understand the dependence $L_3(a, T)$ theoretically, we employ the S -matrix formalism developed in Refs. [20,35,36]. According to the method, at hyperradii $R \gg |a|$ one defines three-atom scattering channels ($i = 3, 4, \dots$) for which the wave function factorizes into a normalized hyperangular part $\Phi_i(\hat{R})$ and a linear superposition of the incoming, $R^{-5/2}e^{-ikR}$, and outgoing, $R^{-5/2}e^{+ikR}$, hyperradial waves. The channel $i = 2$ is defined for $a > 0$ and describes the motion of an atom relative to a shallow dimer. The recombination or relaxation to deep molecular states (with a size of order the van der Waals range R_e) requires inclusion of other atom-dimer channels. In the zero-range approximation, valid when $R_e \ll R_m \equiv \min(1/k, |a|)$, the overall effect of these channels and all short-range physics in general can be taken into account by introducing a single Efimov channel ($i = 1$) defined for $R_e \ll R \ll R_m$: the wave function at these distances is a linear superposition of the incoming, $\Phi_1(\hat{R})R^{-2+i s_0}$, and outgoing, $\Phi_1(\hat{R})R^{-2-i s_0}$, Efimov radial waves. Here $s_0 \approx 1.00624$. The notion “incoming” or “outgoing” is defined with respect to the long-distance region $R_m \lesssim R \lesssim |a|$, so that, for example, the incoming Efimov wave actually propagates towards larger R whereas incoming waves in all other channels propagate

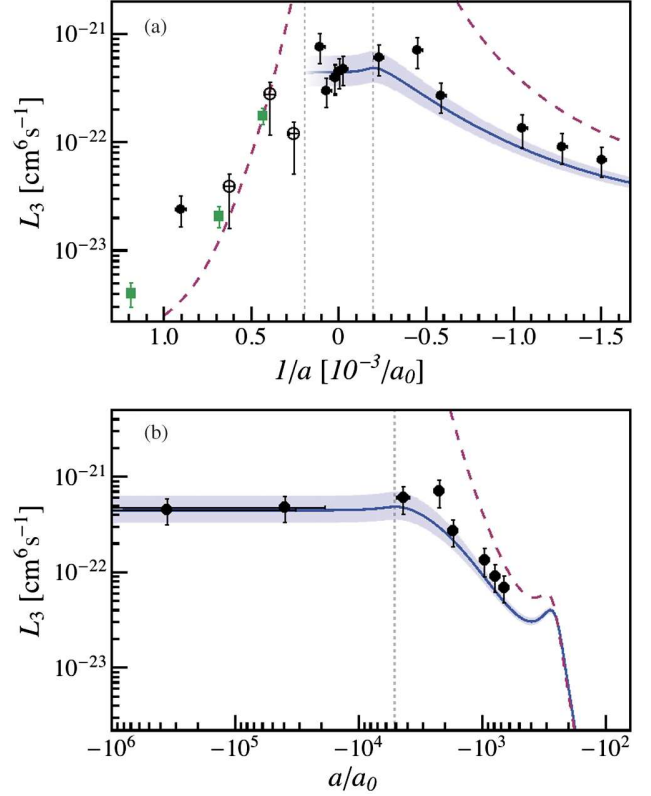


FIG. 3 (color online). (a) ${}^7\text{Li}$ scattering-length dependence of the three-body rate constant $L_3(a)$ for constant $T = 5.9(6) \mu\text{K}$ (filled and open circles). For small positive a , $L_3(a)$ for a low-temperature condensate is also shown (green squares). The solid blue line corresponds to our theoretical prediction Eq. (4) for $T = 5.9 \mu\text{K}$. The blue range is the same theory for 5.3 to 6.5 μK . The dashed lines show the zero-temperature prediction for $L_3(a)$ [20] fitted to the measurements in Refs. [30,39] with the parameters $\eta_* = 0.21$ and $R_0 = 270a_0$. The vertical dotted lines correspond to $|a|/\lambda_{\text{th}} = 1$. The open circles in the range $1500a_0 < a < 5000a_0$ are not corrected for residual evaporation as our model is not applicable. (b) Logarithmic plot of the $a < 0$ side, displaying the two Efimov loss resonances.

towards smaller hyperradii. The matrix s_{ij} relates the incoming amplitude in the i th channel with the outgoing one in the j th channel and describes the reflection, transmission, and mixing of channels in the long-distance region. This matrix is unitary and independent of the short-range physics. The short-range effects are taken into account by fixing the relative phase and amplitude of the incoming and outgoing Efimov waves $R^2\Psi \propto (R/R_0)^{i s_0} - e^{2\eta_*} (R/R_0)^{-i s_0}$, where R_0 is the three-body parameter and the short-range inelastic processes are parametrized by $\eta_* > 0$, which implies that the number of triples going towards the region of $R \sim R_e$ is by the factor $e^{4\eta_*}$ larger than the number of triples leaving this region [37]. Braaten *et al.* [36] have shown that for a given incoming channel $i \geq 2$ the probability of recombination to deeply bound states is $P_i = (1 - e^{-4\eta_*})|s_{i1}|^2 / [1 + (kR_0)^{-2i s_0} e^{-2\eta_*} |s_{11}|^2]$ [38]. For $a < 0$, by using the fact that s_{11} is unitary ($\sum_{i=1}^{\infty} |s_{i1}|^2 = 1$) and averaging over the

Boltzmann distribution, we then obtain the total loss rate constant

$$L_3 = \frac{72\sqrt{3}\pi^2\hbar(1 - e^{-4\eta_*})}{mk_{\text{th}}^6} \times \int_0^\infty \frac{(1 - |s_{11}|^2)e^{-k^2/k_{\text{th}}^2}kdk}{|1 + (kR_0)^{-2is_0}e^{-2\eta_*s_{11}}|^2}, \quad (4)$$

where $k_{\text{th}} = \sqrt{mk_B T}/\hbar$.

Note that in deriving Eq. (4) we closely followed [36] where the scattering length was assumed to be finite. However, we easily generalize this derivation to the case $a = \infty$, in which the channels become decoupled at distances $R \gg 1/k$ and the long-distance region can now be defined by $R \sim 1/k$. A less trivial result of our analysis is that for any ka there exists a unitary transformation of the matrix s_{ij} which leaves the element s_{11} invariant, but all channels with $i > 3$ become decoupled from the Efimov channel [34]. This transformation constructs a new large- R channel characterized by a certain hyperangular wave function $\tilde{\Phi}_3(\hat{R})$. For negative or infinite a this is the only channel that can “talk” to the lossy short-distance Efimov channel via a unitary 2×2 matrix. Therefore, the three-body loss rate cannot exceed the so-called maximum value $L_3^{\text{max}} = 36\sqrt{3}\pi^2\hbar^5(k_B T)^{-2}/m^3$ reached in the case when the outgoing flux in this newly constructed channel vanishes. Previous derivations of L_3^{max} [29] essentially implied that $\tilde{\Phi}_3(\hat{R})$ is the lowest *noninteracting* hyperspherical harmonics. This approximation can be made only for $k|a| \ll 1$. In general, $\tilde{\Phi}_3(\hat{R})$ is *not* an eigenstate of the angular momentum operator. In particular, at unitarity $\tilde{\Phi}_3(\hat{R}) = \Phi_1(\hat{R})$ [34].

The function $s_{11}(ka)$ is calculated in Ref. [34]. At unitarity it equals $s_{11}(\infty) = -e^{-\pi s_0} e^{2i[s_0 \ln 2 + \arg \Gamma(1 + is_0)]}$, and from Eq. (4) one sees that $L_3 T^2$ should be a log-periodic function of T . However, due to the numerically small value of $|s_{11}| \approx 0.04$, in the case of three identical bosons the oscillations are very small and L_3 is well approximated by setting $s_{11} = 0$:

$$L_3 \approx \frac{\hbar^5}{m^3} 36\sqrt{3}\pi^2 \frac{1 - e^{-4\eta_*}}{(k_B T)^2}. \quad (5)$$

This explains the $L_3 \propto T^{-2}$ experimental observation seen in Fig. 2 at unitarity. Taking $\eta_* = 0.21$, which is the average of two measurements made for our ^7Li Feshbach resonance in Refs. [30,39], we get $L_3 = \lambda_3/T^2$ with $\lambda_3 = 1.52 \times 10^{-20} (\mu\text{K})^2 \text{cm}^6 \text{s}^{-1}$. This is 40% below the experimentally determined value without any adjustable parameter and the agreement between theory and experiment is 1.4σ .

We should point out that Eq. (4) can be easily generalized to the case of other three-body systems with smaller s_0 . Then, the terms neglected in Eq. (5) can become important. They also become important in our system of three identical bosons when departing from resonance in the direction of $a < 0$. Then $|s_{11}(ka)|$ monotonically increases as a function of $1/k|a|$ reaching 1 in the limit

$ka \rightarrow 0^-$, the argument of s_{11} also being a monotonic function of $1/k|a|$ [34]. The solid dark gray (blue) line in Fig. 3 is the result obtained from Eq. (4) using the same η_* as above and $R_0 = 270a_0$ also taken from Refs. [30,39]. The shaded blue area reflects our experimental range of temperatures. More or less visible maxima of L_3 appear when the denominator in the integrand of Eq. (4) reaches its minimum, i.e., becomes resonant. The approximate condition for this is $\arg s_{11}(ka) = \pi + 2s_0 \ln kR_0$, and the features become increasingly more pronounced for larger $|s_{11}|$ and smaller η_* . Note that from the viewpoint of the visibility of the maxima, decreasing $|a|$ is equivalent to decreasing \sqrt{T} . Figure 3(b) shows the pronounced resonance at $a = a_- \approx -274a_0$ observed in Refs. [30,39]. This resonance is associated with the passage of an Efimov trimer through the three-atom threshold. Another Efimov trimer, larger in size by a factor of $e^{\pi/s_0} = 22.7$, is expected to go through the threshold at around $a \approx -6350a_0$, leading to another zero energy resonance. As we deduce from Eq. (4) and show in Fig. 3 for $5.9 \mu\text{K}$, the thermally averaged remnants of this predicted resonance lead to a maximum of L_3 at $a \approx -5100a_0$. As seen in Fig. 3(b), the agreement between theory and experiment is very good over the entire $a < 0$ range.

Because of the existence of a shallow dimer state, the case $a > 0$ becomes, in general, a complicated dynamical problem which should take into account the atom-dimer and dimer-dimer relaxation as well as various nonuniversal factors: the finite trap depth, chemical imbalance between trapped shallow dimers and free atoms, and deviations from thermal equilibrium which possibly depend on the preparation sequence. These issues require an extensive discussion beyond the scope of this Letter. The situation obviously simplifies in the case of very small a when the system is purely atomic and the three-body recombination to deep and shallow molecules leads to an immediate loss of three atoms.

Discussing the opposite limit of large $a > 0$, we first note that dimers are well defined when their size $\sim a$ is smaller than $n^{-1/3}$, which we assume in the following (the limit $na^3 \gg 1$ is equivalent to the case $a = \infty$). In the regime $a \gg \lambda_{\text{th}}$ we find using the Skorniakov-Ter-Martirosian equation that $s_{12} \rightarrow 0$ for $ka \rightarrow \infty$, which implies that the atom-dimer relaxation rate vanishes; shallow dimers then remain at chemical quasiequilibrium with the decaying atomic ensemble, with a molecular fraction $\propto n\lambda_{\text{th}}^3 \ll 1$ (for the data of Fig. 3 with $a > \lambda_{\text{th}}$, the molecular fraction is 0.6%) [34]. Shallow dimer formation and breakup are then balanced, so that the atomic decay is just given by Eq. (1). The expression of L_3 for $a > 0$ was obtained in Ref. [36] and reduces to Eq. (4) for $s_{12} \rightarrow 0$. We conclude that the loss rate must be continuous across the resonance, in accordance with our experimental data. Therefore, in Fig. 3(a) the result of Eq. (4) is simply continued to positive a for $a \gg \lambda_{\text{th}}$.

In summary, we have systematically studied the dependence of the three-body loss rate on T and a in a Bose gas

near unitarity. Equation (5) shows that, at unitarity, L_3 never reaches L_3^{\max} , and one can hope to produce quantum degeneracy in a unitary Bose gas using atomic species with a particularly small η_* . Note that the loss mechanism in our system drastically differs from a chemical reaction with finite activation energy ΔE characterized by the well-known Arrhenius law $L_3 \propto \exp(-\Delta E/k_B T)$. In our case, instead of a potential hill there is an effective three-body R^{-2} attraction leading to $\Psi(R) \propto (\lambda_{\text{th}}/R)^2$ at distances $R_e \leq R \leq \lambda_{\text{th}}$, where we normalized the three-body wave function Ψ to unit volume and omitted its log-periodic R dependence. We clearly see that the probability of finding three atoms in the recombination region is enhanced at small temperatures and scales as $|\Psi|^2 \propto \lambda_{\text{th}}^4 \propto 1/T^2$. More subtle is a quantum interference effect in Efimov three-body scattering, which leads to an enhanced decay rate at a negative a , suggesting the possibility to observe the signature of a second Efimov trimer of large size. Another future direction is to explore the approach to the quantum-degenerate regime and test whether the virial expansion of the unitary Bose gas [40] can be measured by using quasiequilibrium thermodynamics [9].

We acknowledge fruitful discussions with G. Shlyapnikov and F. Ferlaino, and support from Région Île de France (IFRAF), EU (ERC advanced grant Ferlodim), Institut Universitaire de France, and the Russian Foundation for Fundamental Research. T.L. acknowledges support by the Austrian Science Fund (FWF) through the Doctoral Programme CoQuS (W1210).

-
- [1] *BCS-BEC Crossover and the Unitary Fermi Gas*, Lecture Notes in Physics Vol. 836, edited by W. Zwerger (Springer, Berlin, 2011).
- [2] S. E. Pollack, D. Dries, M. Junker, Y. P. Chen, T. A. Corcovilos, and R. G. Hulet, *Phys. Rev. Lett.* **102**, 090402 (2009).
- [3] R. J. Wild, P. Makotyn, J. M. Pino, E. A. Cornell, and D. S. Jin, *Phys. Rev. Lett.* **108**, 145305 (2012).
- [4] N. Navon, S. Piatecki, K. Günter, B. Rem, T.-C. Nguyen, F. Chevy, W. Krauth, and C. Salomon, *Phys. Rev. Lett.* **107**, 135301 (2011).
- [5] S. Cowell, H. Heiselberg, I. E. Mazets, J. Morales, V. R. Pandharipande, and C. J. Pethick, *Phys. Rev. Lett.* **88**, 210403 (2002).
- [6] J.-L. Song and F. Zhou, *Phys. Rev. Lett.* **103**, 025302 (2009).
- [7] Yu-Li Lee and Yu-Wen Lee, *Phys. Rev. A* **81**, 063613 (2010).
- [8] D. Borzov, M. S. Mashayekhi, S. Zhang, J.-L. Song, and F. Zhou, *Phys. Rev. A* **85**, 023620 (2012).
- [9] W. Li and T.-L. Ho, *Phys. Rev. Lett.* **108**, 195301 (2012).
- [10] J. von Stecher, *J. Phys. B* **43**, 101002 (2010).
- [11] J. von Stecher, *Phys. Rev. Lett.* **107**, 200402 (2011).
- [12] S. Basu and E. J. Mueller, *Phys. Rev. A* **78**, 053603 (2008).
- [13] N. Syassen, D. M. Bauer, M. Lettner, T. Volz, D. Dietze, J. J. Garcia-Ripoll, J. I. Cirac, G. Rempe, and S. Durr, *Science* **320**, 1329 (2008).
- [14] S. Inouye, M. R. Andrews, J. Stenger, H.-J. Miesner, D. M. Stamper-Kurn, and W. Ketterle, *Nature (London)* **392**, 151 (1998).
- [15] J. L. Roberts, N. R. Claussen, S. L. Cornish, and C. E. Wieman, *Phys. Rev. Lett.* **85**, 728 (2000).
- [16] T. Weber, J. Herbig, M. Mark, H.-C. Nägerl, and R. Grimm, *Phys. Rev. Lett.* **91**, 123201 (2003).
- [17] E. Nielsen and J. H. Macek, *Phys. Rev. Lett.* **83**, 1566 (1999).
- [18] B. D. Esry, C. H. Greene, and J. P. Burke, *Phys. Rev. Lett.* **83**, 1751 (1999).
- [19] P. F. Bedaque, E. Braaten, and H.-W. Hammer, *Phys. Rev. Lett.* **85**, 908 (2000).
- [20] E. Braaten and H.-W. Hammer, *Phys. Rep.* **428**, 259 (2006).
- [21] D. S. Petrov, in *Proceedings of the Les Houches Summer Schools, Session 94*, edited by C. Salomon, G. V. Shlyapnikov, and L. F. Cugliandolo (Oxford University Press, Oxford, England, 2013).
- [22] T. Kraemer, M. Mark, P. Waldburger, J. G. Danzl, C. Chin, B. Engeser, A. D. Lange, K. Pilch, A. Jaakkola, H. C. Nägerl, and R. Grimm, *Nature (London)* **440**, 315 (2006).
- [23] M. Zaccanti, B. Deissler, C. D'Errico, M. Fattori, M. Jona-Lasinio, S. Müller, G. Roati, M. Iguscio, and G. Modugno, *Nat. Phys.* **5**, 586 (2009).
- [24] S. E. Pollack, D. Dries, and R. G. Hulet, *Science* **326**, 1683 (2009).
- [25] N. Gross, Z. Shotan, S. Kokkelmans, and L. Khaykovich, *Phys. Rev. Lett.* **103**, 163202 (2009).
- [26] F. Ferlaino, A. Zenesini, M. Berninger, B. Huang, H. C. Nägerl, and R. Grimm, *Few-Body Syst.* **51**, 113 (2011).
- [27] J. P. D'Incao, H. Suno, and B. D. Esry, *Phys. Rev. Lett.* **93**, 123201 (2004).
- [28] J. P. D'Incao, C. H. Greene, and B. D. Esry, *J. Phys. B* **42**, 044016 (2009).
- [29] N. P. Mehta, S. T. Rittenhouse, J. P. D'Incao, J. von Stecher, and C. H. Greene, *Phys. Rev. Lett.* **103**, 153201 (2009).
- [30] N. Gross, Z. Shotan, S. Kokkelmans, and L. Khaykovich, *Phys. Rev. Lett.* **105**, 103203 (2010).
- [31] We neglect four- and higher-body losses which, dimensionally, are expected to be suppressed by a factor $n_0 \lambda_{\text{th}}^3$ [29].
- [32] O. Luiten, M. Reynolds, and J. T. M. Walraven, *Phys. Rev. A* **53**, 381 (1996).
- [33] L. Luo, B. Clancy, J. Joseph, J. Kinast, A. Turlapov, and J. E. Thomas, *New J. Phys.* **8**, 213 (2006).
- [34] See Supplemental Material at <http://link.aps.org/supplemental/10.1103/PhysRevLett.110.163202> for more information on the calculation of s_{11} ; a discussion of s_{12} , atom-dimer relaxation, and chemical equilibrium in the limit $a \rightarrow \infty$; a construction of the unitary transformation for the matrix s_{ij} ; an interpretation of Eq. (4) in terms of a Fabry-Perot interferometer; and a discussion of evaporation and experimental uncertainties.
- [35] V. Efimov, *Sov. J. Nucl. Phys.* **29**, 546 (1979).
- [36] E. Braaten, H.-W. Hammer, D. Kang, and L. Platter, *Phys. Rev. A* **78**, 043605 (2008).
- [37] E. Braaten, H.-W. Hammer, and M. Kusunoki, *Phys. Rev. A* **67**, 022505 (2003).
- [38] Our s_{11} differs by a phase factor from the one defined in Ref. [36]; see Ref. [34].
- [39] N. Gross, Z. Shotan, O. Machtey, S. Kokkelmans, and L. Khaykovich, *C.R. Physique* **12**, 4 (2011).
- [40] Y. Castin and F. Werner, [arXiv:1212.5512v2](https://arxiv.org/abs/1212.5512v2).

Λ -Enhanced Sub-Doppler Cooling of Lithium Atoms in D_1 Gray Molasses

A. Grier, I. Ferrier-Barbut, B. Rem, M. Delehaye, L. Khaykovich, F. Chevy, C. Salomon

Physical Review A **87**, 063411 (2013)

A-enhanced sub-Doppler cooling of lithium atoms in D_1 gray molassesAndrew T. Grier,^{1,*} Igor Ferrier-Barbut,¹ Benno S. Rem,¹ Marion Delehaye,¹ Lev Khaykovich,² Frédéric Chevy,¹ and Christophe Salomon¹¹Laboratoire Kastler-Brossel, École Normale Supérieure, CNRS and UPMC, 24 rue Lhomond, 75005 Paris, France²Department of Physics, Bar-Ilan University, Ramat-Gan 52900, Israel

(Received 26 April 2013; published 12 June 2013)

Following the bichromatic sub-Doppler cooling scheme on the D_1 line of ^{40}K recently demonstrated in Fernandes *et al.* [Europhys. Lett. **100**, 63001 (2012)], we introduce a similar technique for ^7Li atoms and obtain temperatures of $60\ \mu\text{K}$ while capturing all of the 5×10^8 atoms present from the previous stage. We investigate the influence of the detuning between the two cooling frequencies and observe a threefold decrease of the temperature when the Raman condition is fulfilled. We interpret this effect as arising from extra cooling due to long-lived coherences between hyperfine states. Solving the optical Bloch equations for a simplified Λ -type three-level system we identify the presence of an efficient cooling force near the Raman condition. After transfer into a quadrupole magnetic trap, we measure a phase space density of $\sim 10^{-5}$. This laser cooling offers a promising route for fast evaporation of lithium atoms to quantum degeneracy in optical or magnetic traps.

DOI: 10.1103/PhysRevA.87.063411

PACS number(s): 37.10.De, 32.80.Wr, 67.85.-d

I. INTRODUCTION

Lithium is enjoying widespread popularity in the cold-atom trapping community thanks to the tunability of its two-body interactions and its lightness. Both the fermionic and the bosonic isotopes of lithium feature broad, magnetically tunable Feshbach resonances in a number of hyperfine states [1]. The presence of these broad resonances makes lithium an attractive candidate for studies of both the Fermi- and Bose-Hubbard models [2] and the strongly correlated regime for bulk dilute gases of Fermi [3] or Bose [4–6] character. Its small mass and correspondingly large photon-recoil energy are favorable factors for large area atom interferometers [7] and precision frequency measurements of the recoil energy and fine structure constant [8]. Under the tight-binding lattice model, lithium's large photon-recoil energy leads to a larger tunneling rate and faster time scale for superexchange processes, allowing for easier access to spin-dominated regimes [9]. Finally, lithium's small mass reduces the heating due to nonadiabatic parts of the collision between ultracold atoms and Pauli-trapped ions. This feature, together with Pauli suppression of atom-ion three-body recombination events involving ^6Li [10], potentially allows one to reach the s -wave regime of ion-atom collisions [11].

However, lithium, like potassium, is harder to cool using optical transitions than the other alkali-metal atoms. The excited-state structure of the D_2 transition in lithium lacks the separation between hyperfine states for standard sub-Doppler cooling techniques such as polarization gradient cooling [12–14] to work efficiently. Recently, it has been shown by the Rice group that cooling on the narrow $2S_{1/2} \rightarrow 3P_{3/2}$ transition produces lithium clouds near $60\ \mu\text{K}$, about half the D_2 -line Doppler cooling limit [15], and can be used for fast all-optical production of a ^6Li quantum degenerate Fermi gas. However, this approach requires special optics and a coherent source at 323 nm, a wavelength range where power is still limited. Another route is to use the three-level structure of the atom as implemented previously in neutral atoms

and trapped ions [16–22]. The three-level structure offers the possibility of using dark states to achieve temperatures below the standard Doppler limit, as evidenced by the use of velocity-selective coherent population trapping (VSCPT) to produce atomic clouds with subrecoil temperatures [23]. In another application, electromagnetically induced transparency has been used to demonstrate robust cooling of a single ion to its motional ground state [19,24].

In this paper, we implement three-dimensional bichromatic sub-Doppler laser cooling of ^7Li atoms on the D_1 transition. Figure 1 presents the ^7Li level scheme and the detunings of the two cooling lasers that are applied to the atoms after the magneto-optical trapping phase. Our method combines a gray molasses cooling scheme on the $|F=2\rangle \rightarrow |F'=2\rangle$ transition [25,26] with phase-coherent addressing of the $|F=1\rangle \rightarrow |F'=2\rangle$ transition, creating VSCPT-like dark states at the two-photon resonance. Instead of UV laser sources, the method uses laser light that is conveniently produced at 671 nm by semiconductor laser sources or solid-state lasers [27,28] with sufficient power. This enables us to capture all of the $\simeq 5 \times 10^8$ atoms from a MOT and cool them to $60\ \mu\text{K}$ in a duration of 2 ms.

We investigate the influence of the relative detuning between the two cooling lasers and observe a threefold decrease of the temperature in a narrow frequency range around the exact Raman condition. We show that extra cooling arises due to long-lived coherences between hyperfine states. We develop a simple theoretical model for a sub-Doppler cooling mechanism which occurs in atoms with a Λ -type three-level structure, in this case, the $F=1$, $F=2$, and $F'=2$ manifolds of the D_1 transition in ^7Li . The main physical cooling mechanism is contained in a 1D bichromatic lattice model. We first give a perturbative solution to the model and then verify the validity of this approach with a continued fraction solution to the optical Bloch equations (OBEs).

II. EXPERIMENT

The stage preceding D_1 sub-Doppler cooling is a compressed magneto-optical trap (CMOT) in which, starting from a standard MOT optimized for total atom number, the

*Corresponding author: agrier@lkb.ens.fr

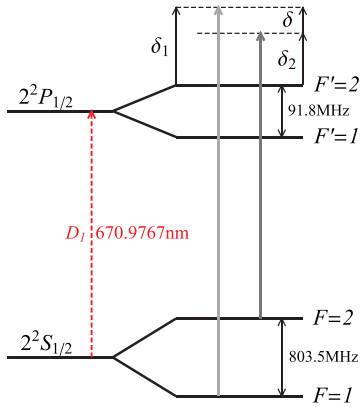


FIG. 1. (Color online) The D_1 line for ${}^7\text{Li}$. The cooling scheme has a strong coupling laser (principal beam, black solid arrow) δ_2 blue detuned from the $|F=2\rangle \rightarrow |F'=2\rangle$ transition and a weak coupling laser (repumper, gray solid arrow) δ_1 blue detuned from the $|F=1\rangle \rightarrow |F'=2\rangle$ transition. The repumper is generated from the principal beam by an electro-optical modulator operating at a frequency $803.5 + \delta/2\pi$ MHz, where $\delta = \delta_1 - \delta_2$.

frequency of the cooling laser is quickly brought close to resonance while the repumping laser intensity is diminished in order to increase the sample's phase space density [29]. The CMOT delivers 5×10^8 ${}^7\text{Li}$ atoms at a temperature of $600 \mu\text{K}$. The atoms are distributed throughout the $F=1$ manifold in a spatial volume of $800 \mu\text{m}$ $1/e$ width. Before starting our D_1 molasses cooling, we wait $200 \mu\text{s}$ to allow any transient magnetic fields to decay to below 0.1 G. The light used for D_1 cooling is generated by a solid-state laser presented in [27]. The laser is locked at frequency ω_2 , detuned from the $|F=2\rangle \rightarrow |F'=2\rangle$ D_1 transition in ${}^7\text{Li}$ by δ_2 . It is then sent through a resonant electro-optical modulator (EOM) operating at a frequency near the hyperfine splitting in ${}^7\text{Li}$, $\nu_{\text{EOM}} = 803.5 \text{ MHz} + \delta/2\pi$. This generates a small-amplitude sideband, typically a few percent of the carrier, at frequency ω_1 . We define the detuning of this frequency from the $|F=1\rangle \rightarrow |F'=2\rangle$ transition as δ_1 (such that $\delta = \delta_1 - \delta_2$), as shown in Fig. 1. Using about 150 mW of 671-nm light we perform a three-dimensional D_1 molasses as in [25], with three pairs of $\sigma^+ - \sigma^-$ counterpropagating beams. The beams are of 3.4-mm waist and the intensity (I) of each beam is $I \gtrsim 45I_{\text{sat}}$, where $I_{\text{sat}} = 2.54 \text{ mW/cm}^2$ is the saturation intensity of the D_2 cycling transition in lithium.

We capture all of the atoms present after the CMOT stage into the D_1 gray molasses. The $1/e$ lifetime of atoms in the molasses is $\geq 50 \text{ ms}$. After being cooled for $1.5\text{--}2.0 \text{ ms}$, the temperature is as low as $40 \mu\text{K}$ without optical pumping or $60 \mu\text{K}$ after optical pumping into the $|F=2, m_F=2\rangle$ state for imaging and subsequent magnetic trapping. In contrast with [25], we find no further reduction in the steady-state temperature by slowly lowering the light intensities after the initial 2.0 ms .

During the molasses phase, we find a very weak dependence on the principal laser detuning for $3\Gamma \leq \delta_2 \leq 6\Gamma$. For the remainder of this article, we use a principal laser detuning of $\delta_2 = 4.5\Gamma = 2\pi \times 26.4 \text{ MHz}$. In Fig. 2(a), the temperature dependence upon the repumper detuning is displayed for

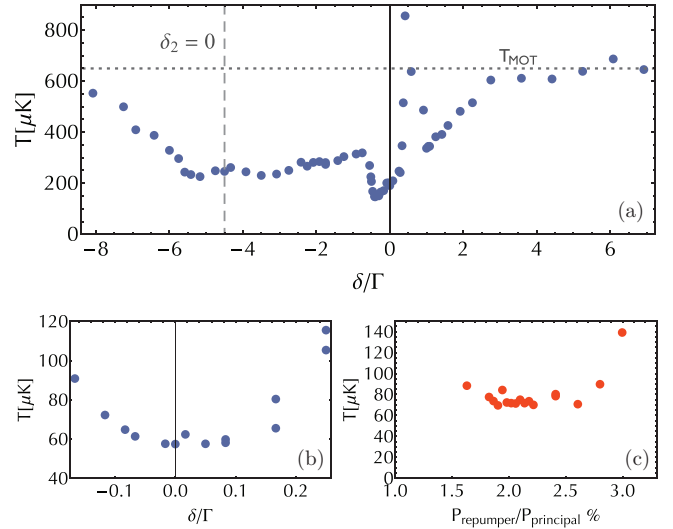


FIG. 2. (Color online) (a) Typical temperature of the cloud as a function of the repumper detuning for a fixed principal beam detuned at $\delta_1 = 4.5\Gamma = 2\pi \times 26.4 \text{ MHz}$. The dashed vertical line indicates the position of the resonance with transition $|F=2\rangle \rightarrow |F'=2\rangle$, the dotted horizontal line shows the typical temperature of a MOT. (b) Magnification of the region near the Raman condition with well-aligned cooling beams and zeroed magnetic offset fields. (c) Minimum cloud temperature as a function of repumper power.

typical conditions. For $-9 \leq \delta/\Gamma \leq -6$, the temperature drops from $600 \mu\text{K}$ (the CMOT temperature) to $200 \mu\text{K}$ as gray molasses cooling gains in efficiency when the weak repumper comes closer to resonance. For $-6 \leq \delta/\Gamma \leq -1$, the cloud temperature stays essentially constant but, in a narrow range near the position of the exact Raman condition ($\delta = 0$), one notices a sharp drop of the temperature. For δ slightly blue of the Raman condition, a strong heating of the cloud occurs, accompanied by a sharp decrease in the number of cooled atoms. Finally for $\delta \geq \Gamma$, the temperature drops again to a level much below the initial MOT temperature until the repumper detuning becomes too large to produce significant cooling below the CMOT temperature.

Figures 2(b) and 2(c) show the sensitivity of the temperature minimum to repumper deviation from the Raman condition and repumper power, respectively. The temperature reaches $60 \mu\text{K}$ in a $\pm 500\text{-kHz}$ interval around the Raman resonance condition. After taking the data for Fig. 2(a), the magnetic field zeroing and beam alignment were improved, which accounts for the frequency offset and higher temperature shown in Fig. 2(a) relative to Figs. 2(b) and 2(c). The strong influence of the repumper around the Raman condition with a sudden change from cooling to heating for small and positive Raman detunings motivated the study of the bichromatic-lattice effects induced by the Λ -type level configuration which is presented in the next section.

III. MODEL FOR HYPERFINE RAMAN COHERENCE EFFECTS ON THE COOLING EFFICIENCY

In order to understand how the addition of the second manifold of ground states modifies the gray molasses scheme,

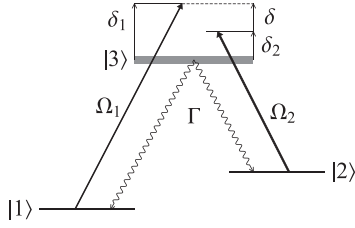


FIG. 3. The Λ level scheme. An intense standing wave with Rabi frequency Ω_2 and a weaker standing wave with Rabi frequency Ω_1 , detuning δ_1 , illuminate an atom with three levels in a Λ configuration.

we analyze a one-dimensional model based on a Λ -type three-level system schematically represented in Fig. 3.

A. The model

This model includes only the $F = 1, 2$ hyperfine ground states and the $F' = 2$ excited state ignoring the Zeeman degeneracy; hence, standard gray molasses cooling [26] does not appear in this model. The states are addressed by two standing waves with nearly the same frequency $\omega_1 \simeq \omega_2 \simeq \omega = kc$ but spatially shifted by a phase ϕ . The principal cooling transition $F = 2 \rightarrow F' = 2$ is labeled here and below as transition 2, between states $|2\rangle$ and $|3\rangle$ with a Rabi frequency $\Omega_2 = \Gamma \sqrt{I/2I_{\text{sat}}}$, where I is the laser light intensity and I_{sat} the saturation intensity on this transition. The repumper transition is labeled 1, between states $|1\rangle$ and $|3\rangle$ with Rabi frequency Ω_1 much smaller than Ω_2 .

The corresponding Hamiltonian for the light-atom interaction in the rotating wave approximation (at ω) is

$$\begin{aligned} \hat{\mathcal{H}}_{\text{a.l.}} &= \hbar\Omega_2 \cos(kz) (|2\rangle\langle 3| + \text{H.c.}) \\ &+ \hbar\Omega_1 \cos(kz + \phi) (|1\rangle\langle 3| + \text{H.c.}) \\ &+ \hbar\delta_2 |2\rangle\langle 2| + \hbar\delta_1 |1\rangle\langle 1|. \end{aligned} \quad (1)$$

The usual formalism used to compute the atom's dynamics is to consider the light force as a Langevin force. Its mean value is $\mathcal{F}(v)$, and the fluctuations around this mean will give rise to diffusion in momentum space, characterized by the diffusion coefficient $\mathcal{D}_p(v) \geq 0$. In order to calculate an equilibrium temperature, one needs $\mathcal{F}(v)$ and $\mathcal{D}_p(v)$. In the limit of small velocities the force reads

$$\mathcal{F}(v) \simeq -\alpha v, \quad (2)$$

with α the friction coefficient. If $\alpha > 0$ the force is a cooling force; in the opposite case it produces heating. For a cooling force the limiting temperature in this regime is given by

$$k_B T \simeq \mathcal{D}_p(0)/\alpha. \quad (3)$$

However, since our model (1) is a gross simplification of the physical system, we do not expect to be able to quantitatively predict a steady-state temperature. Instead, in order to reveal the physical mechanisms in action, we only calculate the force $\mathcal{F}(v)$ and the excited state population ρ_{33} . Restricting our analysis to the force and photon scattering rate, $\Gamma\rho_{33}$, suffices to determine whether the action of the weak repumper serves to heat or cool the atomic ensemble.

From (1) the mean light force on the atoms is computed by taking the quantum average of the gradient of the potential, $F = \langle -\nabla \hat{\mathcal{H}}_{\text{a.l.}} \rangle = -\text{Tr}[\hat{\rho} \hat{\mathcal{H}}_{\text{a.l.}}]$, with ρ the density matrix, yielding the wavelength-averaged force \mathcal{F} ,

$$\mathcal{F}(v) = \frac{k}{2\pi} \int_0^{\frac{2\pi}{k}} dz F(z, v), \quad (4)$$

$$\mathcal{F}(v) = \frac{\hbar k^2}{\pi} \int_0^{\frac{2\pi}{k}} dz \sin(kz) (\Omega_2 \text{Re}\rho_{23} + \Omega_1 \text{Re}\rho_{12}). \quad (5)$$

The spontaneous emission rate averaged over the standing wave is simply given by the linewidth of the excited state multiplied by its population:

$$\Gamma' = \frac{k}{2\pi} \int_0^{\frac{2\pi}{k}} dz \Gamma \rho_{33}. \quad (6)$$

So, both the force and the spontaneous emission rate are functions of the density matrix ρ , the evolution of which is given by the OBEs,

$$i \frac{d}{dt} \rho = \frac{1}{\hbar} [\hat{\mathcal{H}}_{\text{AL}}, \rho] + i \left(\frac{d\rho}{dt} \right)_{\text{spont. emis.}}. \quad (7)$$

As we are focusing on the sub-Doppler regime, we assume

$$v \ll \Gamma/k, \quad (8)$$

with v being the velocity. The inequality holds for $T \ll 13$ mK for lithium. This inequality allows us to replace the full time derivative in the left-hand side of (7) by a partial spatial derivative times the atomic velocity,

$$\frac{d}{dt} \rightarrow v \frac{\partial}{\partial z}.$$

Using the notation $\Omega_i(z) = \Omega_i \cos(z + \phi_i)$ and setting $\hbar = k = 1$ from here on,

$$i v \frac{\partial \rho_{22}}{\partial z} = -2i \Omega_2(z) \text{Im}(\rho_{23}) + i \frac{\Gamma}{2} \rho_{33}, \quad (9)$$

$$i v \frac{\partial \rho_{11}}{\partial z} = -2i \Omega_1(z) \text{Im}(\rho_{13}) + i \frac{\Gamma}{2} \rho_{33}, \quad (10)$$

$$i v \frac{\partial \rho_{23}}{\partial z} = \left(\delta_2 - i \frac{\Gamma}{2} \right) \rho_{23} + \Omega_2(z) (\rho_{33} - \rho_{22}) - \Omega_1(z) \rho_{21}, \quad (11)$$

$$i v \frac{\partial \rho_{13}}{\partial z} = \left(\delta_1 - i \frac{\Gamma}{2} \right) \rho_{13} + \Omega_1(z) (\rho_{33} - \rho_{11}) - \Omega_2(z) \rho_{12}, \quad (12)$$

$$i v \frac{\partial \rho_{21}}{\partial z} = (\delta_2 - \delta_1) \rho_{21} + \Omega_2(z) \rho_{31} - \Omega_2(z) \rho_{23}. \quad (13)$$

The solution of these equations yields the expression of $\mathcal{F}(v)$ and Γ' . This semiclassical model is valid only for velocities above the recoil velocity $v_{\text{rec}} = \hbar k/m$ (corresponding to a temperature $m v_{\text{rec}}/k_B$ of about 6 μK for lithium). Different theoretical studies [17,18,20,22,30,31] as well as experiments [16,32] have been performed on such a Λ configuration in standing waves or similar systems. However, in our ${}^7\text{Li}$ experiment, we have the situation in which the Λ configuration is coupled to a gray molasses scheme which involves a different set of dark states. This fixes the laser light parameters to values that motivate our theoretical exploration. Thus, we

concentrate on the situation corresponding to the conditions of our experiment.

To solve the OBEs (9)–(13), we first introduce a perturbative approach that enables us to point out the relevant physical mechanisms. We further extend the analysis by an exact approach in terms of continued fractions.

B. Perturbative approach

In our perturbative approach we choose a Rabi frequency Ω_2 between 2Γ and 4Γ and $\Omega_1 \ll \Gamma, \Omega_2, \delta_2$ as the ratio of the repumper to principal laser power is very small, typically $(\Omega_1/\Omega_2)^2 \lesssim 0.03$, under our experimental conditions. We further simplify the approach by considering only the in-phase situation $\phi = 0$; any finite phase would lead to divergencies of the perturbative approach at the nodes of wave 1. The validity of these assumptions are discussed in Sec. III C.

We perform an expansion in powers of the Rabi frequency Ω_1 and the atomic velocity such that the complete expansion reads

$$\rho_{ij} = \sum_{n,l} \rho_{i,j}^{(n,l)} (\Omega_1)^n (v)^l. \quad (14)$$

This expansion of ρ allows us to recursively solve the OBEs. Using an expansion similar to Eq. (14) for the force, we find

$$\alpha = - \sum_{n=0}^{\infty} \mathcal{F}^{(n,1)} (\Omega_1)^n. \quad (15)$$

We plug the perturbative solution of the OBEs into Eq. (5) and find, to the lowest order ($n = 2$) in Ω_1 ,

$$\alpha \simeq - \frac{(\Omega_1)^2}{2\pi} \int_0^{2\pi} dz \sin(z) (\Omega_2 \text{Re} \rho_{23}^{(2,1)} + \text{Re} \rho_{13}^{(1,1)}). \quad (16)$$

The spontaneous emission rate to lowest order in v and Ω_1 reads

$$\Gamma' = \Gamma \frac{(\Omega_1)^2}{2\pi} \int_0^{2\pi} dz \rho_{33}^{(2,0)}. \quad (17)$$

Figure 4 presents the results from (15) and (17) compared with the experimental data. It shows that indeed a narrow cooling force appears near the Raman resonance condition and that the photon scattering rate vanishes at exact resonance, hinting at an increase of cooling efficiency with respect to the gray molasses Sisyphus cooling mechanism which achieves a temperature near $200 \mu\text{K}$ over a broad range. The strong heating peak for small, positive repumper detuning is also a consequence of the negative value of α , and the heating peak shifts towards higher frequency and broadens for larger intensities of the principal laser. In contrast, the friction coefficient and scattering rate in the range $-6 \leq \delta/\Gamma \leq -3$, which correspond to a repumper near resonance, do not seem to significantly affect the measured temperature.

To gain further physical insight into this cooling near the Raman condition, it is useful to work in the dressed-atom picture. Given the weak repumping intensity, we first ignore its effect and consider only the dressing of the states $|2\rangle$ and $|3\rangle$ by the strong pump with Rabi frequency Ω_2 . This dressing

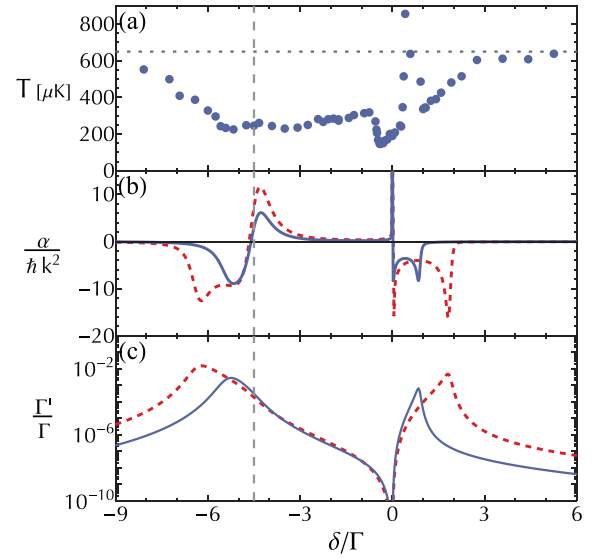


FIG. 4. (Color online) Comparison of experimental data with the perturbative approach results for a detuning of the pump $\delta_2 = 2\pi \times 26.4 \text{ MHz} = 4.5\Gamma$. (a) Temperature versus repumper detuning, experiment; we indicate the MOT temperature by the dotted line. Panels (b) and (c) show, respectively, the friction coefficient α and photon scattering rate Γ' for $\Omega_2 = 3.4\Gamma$ (red dashed curve) and 2.1Γ (blue solid curve). The intensity ratio $(\Omega_1/\Omega_2)^2$ is 0.02. The vertical dashed line indicates the position of $\delta_1 = 0$.

gives rise to an Autler-Townes doublet structure which follows the spatial modulation of the standing wave:

$$|2'\rangle \propto |2\rangle - i\Omega_2(z)/\delta_2|3\rangle, \quad (18)$$

$$|3'\rangle \propto -i\Omega_2(z)/\delta_2|2\rangle + |3\rangle. \quad (19)$$

Since the pump is relatively far detuned (in the conditions of Fig. 4 $\Omega_2/\delta_2 \lesssim 0.45$), the broad state $|3'\rangle$ carries little $|2\rangle$ character. Conversely, the narrow state $|2'\rangle$ is mostly state $|2\rangle$. It follows that $|3'\rangle$ has a lifetime $\Gamma^{(3')} \simeq \Gamma$, while $|2'\rangle$ is relatively long lived with a spatially dependent linewidth $\Gamma^{(2')} = \Gamma(\Omega_2(z)/\delta_2)^2$, which is always $\leq \Gamma/6$ for the parameters chosen here. In order to reintroduce the effects of the repumping radiation, we note that the position in δ of the broad state is $\delta^{(3')} \simeq -\delta_2 - \Omega_2(z)^2/\delta_2$ and the narrow state $\delta^{(2')} \simeq \Omega_2(z)^2/\delta_2$. As coherent population transfer between $|1\rangle$ and $|2'\rangle$ does not change the ensemble temperature, we consider only events which couple atoms out of $|2'\rangle$ to $|1\rangle$ through spontaneous decay and therefore scale with $\Gamma_{|2'\rangle}$. The rates of coupling from $|1\rangle$ into the dressed states can be approximated by the two-level absorption rates:

$$\gamma_{|1\rangle \rightarrow |2'\rangle} \sim \frac{\Omega_1(z)^2}{2} \frac{\Gamma^{(2')}(z)}{[\Gamma^{(2')}(z)/2]^2 + [\delta - \delta^{(2')}(z)]^2}, \quad (20)$$

$$\gamma_{|1\rangle \rightarrow |3'\rangle} \sim \frac{\Omega_1(z)^2}{2} \frac{\Gamma}{(\Gamma/2)^2 + [\delta - \delta^{(3')}(z)]^2}. \quad (21)$$

Finally, these results are valid only in the limit $|\delta| > \Gamma\Omega_2^2/\delta_2^2$ (see, e.g., [33]) when state $|1\rangle$ is weakly coupled to the radiative cascade. Near the Raman resonance, the dressed state family contains a dark state which bears an infinite lifetime under the assumptions made in this section but is, in reality, limited by

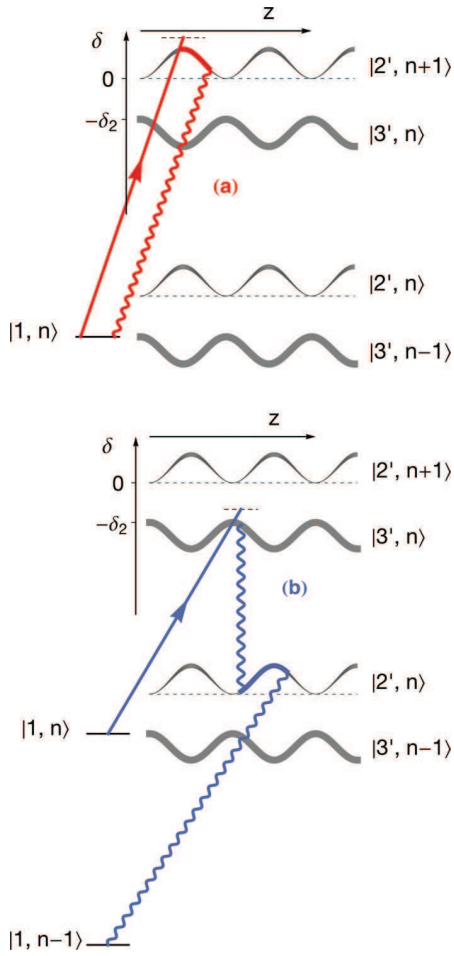


FIG. 5. (Color online) The cascade of levels dressed by transition 2 with a schematical representation of state $|1\rangle$. Traces show typical cycles of atoms pumped from $|1\rangle$ and back depending on the detuning of wave 1. The detuning of the repumper modulates the entry point into the cascade of the dressed states, leading either (a) heating or (b) cooling processes.

off-resonant excitations and motional coupling. This dark state reads

$$|NC\rangle = (\Omega_2|1\rangle - \Omega_1|2\rangle) / \sqrt{\Omega_1^2 + \Omega_2^2}, \quad (22)$$

which we must add in by hand.

Using this toy model, we now explain the features of Fig. 4 and Fig. 2. Figure 5 represents the cascade of dressed levels where each doublet is separated by one pump photon. It gives rise, for example, to the well-known Mollow triplet. Condition (8) states that if an atom falls in state $|3'\rangle$ it will rapidly decay to $|2'\rangle$ without traveling a significant distance. However, the atom will remain in $|2'\rangle$ long enough to sample the spatial variation of the standing wave and gain or lose energy depending on the difference of light shift between the entry and the departure points, as in most sub-Doppler cooling schemes.

Let us first analyze the spontaneous emission rate shown in Fig. 4(c). It reaches two maxima, the first one for $\delta \sim \delta^{(3')}$ and the second one for $\delta \sim \delta^{(2')}$, and it goes to exactly zero at $\delta = 0$. The two maxima are simply due to scattering off the states $|2'\rangle$ and $|3'\rangle$. At $\delta = 0$, Γ' goes to zero due to coherent

population trapping in $|NC\rangle$. It is the presence of this dark state which leads to the reduced scattering rate of photons around $\delta = 0$ and the suppression of the final temperature of the gas in the region around the Raman condition.

The friction coefficient, Fig. 4(b), displays a more complicated structure with variations in δ . It shows a dispersive shape around $\delta^{(3')}$, remains positive in the range $\delta^{(3')} < \delta < 0$, diverges at $\delta = 0$, and reaches negative values for $\delta > 0$ up to $\delta^{(2')}$, where it drops to negligible values. This structure for α can be explained using our toy model. Let us consider the different scenarios corresponding to both sides of δ near 0, they follow formally from Eqs. (20) and (21) and the spatially varying linewidth of $|2'\rangle$.

For the case of the repumper tuned slightly blue of the narrow doublet state, $\delta > \delta^{(2')}$, shown in Fig. 5(a), the atoms are pumped directly from $|1\rangle$ into $|2'\rangle$. However, this pumping happens preferentially at the antinodes of the standing wave as the repumper intensity is greatest, the linewidth of $|2'\rangle$ is the largest, and the light shift minimizes the detuning of the repumper from the $|1\rangle \rightarrow |2'\rangle$ transition for the $\phi = 0$ case considered here. On average, the atoms exit this state at a point with a smaller light shift through a spontaneous emission process either into the cascade of dressed states or directly back to $|1\rangle$. As a result, we expect heating and $\alpha < 0$ in this region.

For repumper detunings between $\delta^{(3')}$ and 0, Fig. 5(b), we predict cooling. For this region, the atoms are initially pumped into $|3'\rangle$. Here the light shift modifies the relative detuning, favoring coupling near the nodes of the light. Spontaneous decay drops the atoms near the nodes of the longer-lived $|2'\rangle$, and they travel up the potential hill into regions of larger light shift before decaying, yielding cooling and a positive α . These sign changes of α and the decreased scattering rate due to $|NC\rangle$ in the vicinity of the Raman condition explain the features of our perturbative model.

We conclude this section by stating that the experimentally observed change of sign of the force close to the Raman condition is well described in our perturbative model. The model further reveals the importance of Raman coherence and the existence of a dark state. The dark state together with the friction coefficient associated with cycles represented in trace 5(b) correspond to a cooling mechanism analogous to that of gray molasses. In this way, the bichromatic system provides an additional gray molasses scheme involving both hyperfine states which complements the gray molasses cooling scheme on the principal transition. On the other hand, when the friction coefficient is negative in the vicinity of the two-photon resonance, it turns into a heating mechanism that overcomes the standard gray molasses operating on the $F = 2 \rightarrow F' = 2$ transition.

The perturbative approach successfully revealed the mechanisms giving rise to the experimentally observed additional cooling. However, it also possesses some shortcomings. First, the divergence of α at $\delta = 0$ is not physical; the assumption that Ω_1 is the smallest scale in the problem breaks down when $\delta \rightarrow 0$. Alternatively, it can be seen as the failure of our model based on nondegenerate perturbative theory in the region where $|1\rangle$ and $|2\rangle$ become degenerate when dressed with ω_1 and ω_2 , respectively. Second, we have only addressed the $\phi = 0$ case. Since the experiment was done in three dimensions with three pairs of counterpropagating beams, the relative phase

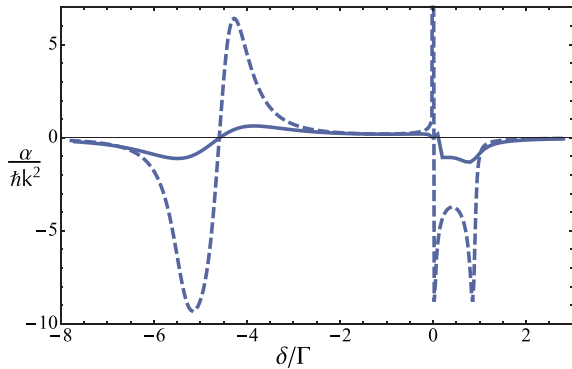


FIG. 6. (Color online) Comparison of results using the perturbative calculation (dashed), and the continued fractions (solid) for the $\phi = 0$ case, with the same parameters as in Fig. 4 and $\Omega_2 = 2.1\Gamma$.

between the two frequencies varies spatially, and we must test if the picture derived at $\phi = 0$ holds when averaging over all phases. In order to address these limitations and confirm the predictions of the perturbative approach, we now present a continued-fractions solution to the OBEs which does not rely on Ω_1 being a small parameter.

C. Continued fractions approach

The limitations listed above can be addressed by using a more general approach, namely, an expansion of the density matrix in Fourier harmonics:

$$\rho_{ij} = \sum_{n=-\infty}^{n=+\infty} \rho_{ij}^{(n)} e^{inkz}. \quad (23)$$

Injecting this expansion in (9)–(13) yields recursive relations between different Fourier components of ρ . Kozachiov *et al.* [17,30] express the solutions of these relations for a generalized Λ system in terms of continued fractions. Here we use their results to numerically solve the Bloch equations. We then compute the force $\mathcal{F}(v)$ to arbitrary order of Ω_1 and extract α by means of a linear fit to the small- v region. We then compute $\mathcal{F}(v)$ and the photon scattering rate Γ' averaged over the phase between the two standing waves.

Figure 6 compares $\alpha(\delta)$ obtained through the continued-fractions approach with the results of the perturbative expansion for the $\phi = 0$ case. The continued-fractions approach has removed the divergence at $\delta = 0$ and α crosses zero linearly. The overall friction coefficient is reduced but the two methods show qualitative agreement in the range of δ considered. At the Raman condition the interaction with light is canceled due to the presence of |NC>; thus, the diffusion coefficient \mathcal{D}_p in momentum space also cancels. To lowest order, the diffusion and friction coefficients scale as

$$\mathcal{D}_p \simeq \delta^2, \quad (24)$$

$$\alpha \simeq \delta; \quad (25)$$

according to (3) the temperature scales as

$$T \simeq \delta. \quad (26)$$

Through this qualitative scaling argument, we show that even though the light action on the atoms is suppressed

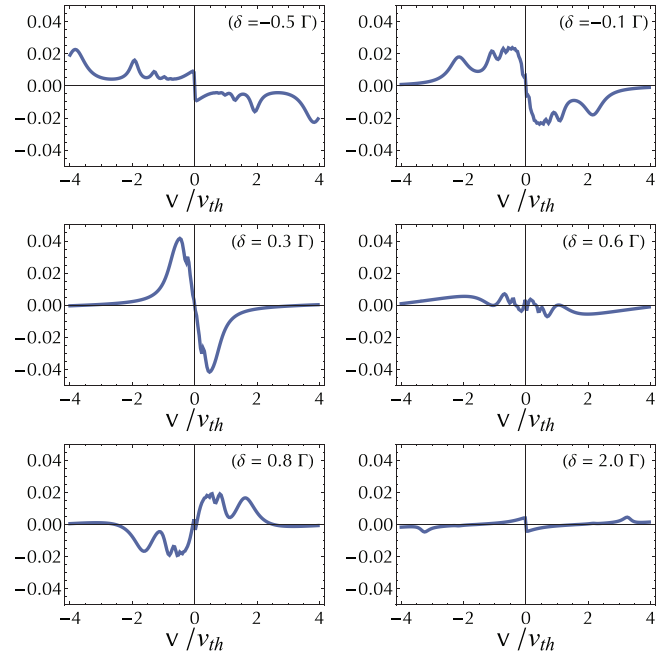


FIG. 7. (Color online) $\langle \mathcal{F} \rangle_\phi$ in units of $1/\hbar k \Gamma$ as a function of v for different values of δ around $\delta = 0$. The horizontal scale is in units of the thermal velocity at $T = 200 \mu\text{K}$, $v_{th} = \sqrt{k_B T/m}$.

when approaching the Raman condition, we expect that the temperature will drop when approaching from the $\delta < 0$ side, completing the physical picture derived in the previous section.

Next, we analyze how a randomized phase between the repumping and principal standing waves, ϕ , modifies $\mathcal{F}(v)$. In order to take this into account, we calculate the phase-averaged force:

$$\langle \mathcal{F}(v) \rangle_\phi = \frac{1}{2\pi} \int_0^{2\pi} \mathcal{F}(v, \phi) d\phi. \quad (27)$$

In Fig. 7, the phase-averaged force is plotted for various detunings near the Raman condition. It can be seen that a cooling force is present for small detunings, qualitatively in agreement with our perturbative model and with the experimental data. The force, however, changes sign to heating for small blue detuning, close to $\delta = 0.6\Gamma$, also in qualitative agreement with the experimental data. We note that the cooling slope very close to zero velocity in the $\delta = 0.8\Gamma$ plot corresponds to a velocity on the order of or below the single-photon recoil velocity, i.e., is nonphysical.

Finally, for the $\phi \neq 0$ case, |NC> varies in space and the motion of the atoms can couple atoms out of |NC> even at the Raman condition. In Fig. 8 we verify that the rate of photon scattering retains a minimum near the $\delta = 0$ region after averaging over ϕ by plotting $\langle \Gamma' \rangle_\phi = \Gamma \langle \rho_{33} \rangle_\phi$ calculated with the continued fractions approach. Overall, the friction coefficient α and photon scattering rate Γ' confirm the existence of a cooling force associated with a decrease in photon scattering in the vicinity of the Raman condition for the 1D bichromatic standing-wave model. Thus, the continued fractions calculation has confirmed the physical mechanisms revealed by the perturbative expansion and that the lowest

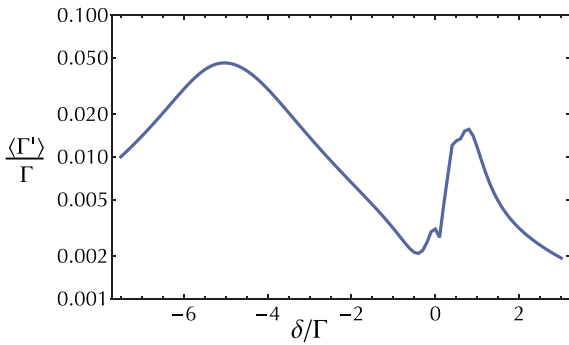


FIG. 8. (Color online) Continued fractions solution of the photon scattering rate $\Gamma' = \Gamma \rho_{33}$ averaged over all relative phases of the repumper and principal standing waves as a function of the two-photon detuning δ . Velocity-dependent effects are taken into account here by computing an average of $\langle \Gamma' \rangle_\phi(v)$ weighed by a Maxwell-Boltzmann velocity distribution at $200 \mu\text{K}$.

temperatures should be expected close to $\delta = 0$, as seen in the experiment.

IV. CONCLUSION

In this study, using bichromatic laser light near 670 nm, we have demonstrated sub-Doppler cooling of ${}^7\text{Li}$ atoms down to $60 \mu\text{K}$ with near unity capture efficiency from a magneto-optical trap. Solving the OBEs for a simplified Λ level structure, we have analyzed the detuning dependence

of the cooling force and photon scattering rate. Our analysis shows that the lowest temperatures are expected for a detuning of the repumping light near the Raman condition, in agreement with our measurements. There the Λ configuration adds a new set of long-lived dark states that strongly enhance the cooling efficiency. For ${}^7\text{Li}$, this addition results in a threefold reduction of the steady-state temperature in comparison with an incoherently repumped gray molasses scheme. This atomic cloud at $60 \mu\text{K}$ is an ideal starting point for direct loading into a dipole trap, where one of the broad Feshbach resonances in the lowest-energy states of ${}^7\text{Li}$ or ${}^6\text{Li}$ could be used to efficiently cool the atoms to quantum degeneracy [15,34]. Alternatively, when the atoms are loaded into a quadrupole magnetic trap, we measure a phase space density of $\simeq 10^{-5}$. This Λ -enhanced sub-Doppler cooling in a D_1 gray molasses is general and should occur in all alkali metals. Notably, we have observed its signature in a number of the alkali-metal isotopes not amenable to polarization gradient cooling: ${}^7\text{Li}$ (this work), ${}^{40}\text{K}$ [25], and ${}^6\text{Li}$ [35].

ACKNOWLEDGMENTS

We acknowledge fruitful discussions with Y. Castin, J. Dalibard S. Wu, F. Sievers, N. Kretzschmar, D. R. Fernandes, M. Schleier-Smith, and I. Leroux and support from Région Île de France (IFRAF-C’Nano), EU (ERC advanced grant Ferlodim), Institut de France (Louis D. Foundation), and Institut Universitaire de France.

-
- [1] C. Chin, R. Grimm, P. Julienne, and E. Tiesinga, *Rev. Mod. Phys.* **82**, 1225 (2010).
 - [2] I. Bloch, J. Dalibard, and W. Zwerger, *Rev. Mod. Phys.* **80**, 885 (2008).
 - [3] S. Nascimbène, N. Navon, K. J. Jiang, F. Chevy, and C. Salomon, *Nature (London)* **463**, 1057 (2010).
 - [4] N. Navon, S. Piatecki, K. Günter, B. Rem, T. C. Nguyen, F. Chevy, W. Krauth, and C. Salomon, *Phys. Rev. Lett.* **107**, 135301 (2011).
 - [5] R. J. Wild, P. Makotyn, J. M. Pino, E. A. Cornell, and D. S. Jin, *Phys. Rev. Lett.* **108**, 145305 (2012).
 - [6] B. S. Rem, A. T. Grier, I. Ferrier-Barbut, U. Eismann, T. Langen, N. Navon, L. Khaykovich, F. Werner, D. S. Petrov, F. Chevy *et al.*, *Phys. Rev. Lett.* **110**, 163202 (2013).
 - [7] S. Lepoutre, A. Gauguier, G. Tréneç, M. Büchner, and J. Vigué, *Phys. Rev. Lett.* **109**, 120404 (2012).
 - [8] R. Bouchendira, P. Cladé, S. Guellati-Khélifa, F. Nez, and F. Biraben, *Phys. Rev. Lett.* **106**, 080801 (2011).
 - [9] T. Esslinger, *Annu. Rev. Condens. Matter Phys.* **1**, 129 (2010).
 - [10] A. Härter, A. Krüchow, A. Brunner, W. Schnitzler, S. Schmid, and J. H. Denschlag, *Phys. Rev. Lett.* **109**, 123201 (2012).
 - [11] M. Cetina, A. T. Grier, and V. Vuletic, *Phys. Rev. Lett.* **109**, 253201 (2012).
 - [12] J. Dalibard and C. Cohen-Tannoudji, *J. Opt. Soc. Am. B* **6**, 2023 (1989).
 - [13] P. D. Lett, W. D. Phillips, S. L. Rolston, C. E. Tanner, R. N. Watts, and C. I. Westbrook, *J. Opt. Soc. Am. B* **6**, 2084 (1989).
 - [14] D. S. Weiss, E. Riis, Y. Shevy, P. J. Ungar, and S. Chu, *J. Opt. Soc. Am. B* **6**, 2072 (1989).
 - [15] P. M. Duarte, R. A. Hart, J. M. Hitchcock, T. A. Corcovilos, T. L. Yang, A. Reed, and R. G. Hulet, *Phys. Rev. A* **84**, 061406 (2011).
 - [16] R. Gupta, C. Xie, S. Padua, H. Batelaan, and H. Metcalf, *Phys. Rev. Lett.* **71**, 3087 (1993).
 - [17] D. V. Kosachiov, Y. V. Rozhdetsvensky, and G. Nienhuis, *J. Opt. Soc. Am. B* **14**, 535 (1997).
 - [18] M. Drewsen, *Phys. Rev. A* **51**, 1407 (1995).
 - [19] C. F. Roos, D. Leibfried, A. Mundt, F. Schmidt-Kaler, J. Eschner, and R. Blatt, *Phys. Rev. Lett.* **85**, 5547 (2000).
 - [20] G. Grynberg and J.-Y. Courtois, *Europhys. Lett.* **27**, 41 (1994).
 - [21] G. Morigi and E. Arimondo, *Phys. Rev. A* **75**, 051404 (2007).
 - [22] J. W. Dunn, J. W. Thomsen, C. H. Greene, and F. C. Cruz, *Phys. Rev. A* **76**, 011401 (2007).
 - [23] A. Aspect, E. Arimondo, R. Kaiser, N. Vansteenkiste, and C. Cohen-Tannoudji, *Phys. Rev. Lett.* **61**, 826 (1988).
 - [24] G. Morigi, J. Eschner, and C. H. Keitel, *Phys. Rev. Lett.* **85**, 4458 (2000).
 - [25] D. R. Fernandes, F. Sievers, N. Kretzschmar, S. Wu, C. Salomon, and F. Chevy, *Europhys. Lett.* **100**, 63001 (2012).

A Mixture of Bose and Fermi Superfluids

I. Ferrier-Barbut, M. Delehaye, S. Laurent, A. Grier, M. Pierce, B. Rem, F. Chevy, C. Salomon

Science **345**, 1035 (2014)

collisions. An analysis with some similarities to ours for the bright debris disk of HD 172555 (20) found that dust created in a hypervelocity impact will have a size slope of ~ -4 , in agreement with the fits of (10) to the IR spectrum of ID8.

After the exponential decay is removed from the data (“detrending”), the light curves at both wavelengths appear to be quasi-periodic. The regular recovery of the disk flux and lack of extraordinary stellar activity essentially eliminate coronal mass ejection (21) as a possible driver of the disk variability. We employed the SigSpec algorithm (22) to search for complex patterns in the detrended, post-impact 2013 light curve. The analysis identified two significant frequencies with comparable amplitudes, whose periods are $P_1 = 25.4 \pm 1.1$ days and $P_2 = 34.0 \pm 1.5$ days (Fig. 3A) and are sufficient to qualitatively reproduce most of the observed light curve features (Fig. 3B). The quoted uncertainties (23) do not account for systematic effects due to the detrending and thus are lower limits to the real errors. Other peaks with longer periods in the periodogram are aliases or possibly reflect long-term deviation from the exponential decay. These artifacts make it difficult to determine whether there are weak real signals near those frequencies.

We now describe the most plausible interpretation of this light curve that we have found. The two identified periods have a peak-to-peak amplitude of $\sim 6 \times 10^{-3}$ in fractional luminosity, which provides a critical constraint for models of the ID8 disk. In terms of sky coverage at the disk distance inferred from the IR SED, such an amplitude requires the disappearance and reappearance every ~ 30 days of the equivalent of an opaque, stellar-facing “dust panel” of radius ~ 110 Jupiter radii. One possibility is that the disk flux periodicity arises from recurring geometry that changes the amount of dust that we can see. At the time of the impact, fragments get a range of kick velocities when escaping into interplanetary space. This will cause Keplerian shear of the cloud (24), leading to an expanding debris concentration along the original orbit (supplementary text). If the ID8 planetary system is roughly edge-on, the longest dimension of the concentration will be parallel to our line of sight at the greatest elongations and orthogonal to the line of sight near conjunctions to the star. This would cause the optical depth of the debris to vary within an orbital period, in a range on the order of 1 to 10 according to the estimated disk mass and particle sizes. Our numerical simulations of such dust concentrations on moderately eccentric orbits are able to produce periodic light curves with strong overtones. P_2 and P_1 should have a 3:2 ratio if they are the first- and second-order overtones of a fundamental, which is consistent with the measurements within the expected larger errors ($< 2\sigma$ or better). In this case, the genuine period should be 70.8 ± 5.2 days (lower-limit errors), a value where it may have been submerged in the periodogram artifacts. This period corresponds to a semimajor axis of ~ 0.33 astronomical units, which is consistent with the temperature and distance suggested by the spectral models (10).

Despite the peculiarities of ID8, it is not a unique system. In 2012 and 2013, we monitored four other “extreme debris disks” (with disk fractional luminosity $\geq 10^{-2}$) around solar-like stars with ages of 10 to 120 My. Various degrees of IR variations were detected in all of them. The specific characteristics of ID8 in the time domain, including the yearly exponential decay, additional more rapid weekly to monthly changes, and color variations, are also seen in other systems. This opens up the time domain as a new dimension for the study of terrestrial planet formation and collisions outside the solar system. The variability of many extreme debris disks in the era of the final buildup of terrestrial planets may provide new possibilities for understanding the early solar system and the formation of habitable planets (25).

REFERENCES AND NOTES

1. R. Helled *et al.*, in *Protostars and Planets VI*, H. Beuther, R. Klessen, C. Dullemond, T. Henning, Eds. (Univ. of Arizona Press, Tucson, AZ, 2014), in press; available at <http://arxiv.org/abs/1311.1142>.
2. M. C. Wyatt, *Annu. Rev. Astron. Astrophys.* **46**, 339–383 (2008).
3. K. Righter, D. P. O'Brien, *Proc. Natl. Acad. Sci. U.S.A.* **108**, 19165–19170 (2011).
4. S. N. Raymond, E. Kokubo, A. Morbidelli, R. Morishima, K. J. Walsh, in *Protostars and Planets VI*, H. Beuther, R. Klessen, C. Dullemond, T. Henning, Eds. (Univ. of Arizona Press, Tucson, AZ, 2014), in press; available at <http://arxiv.org/abs/1312.1689>.
5. R. M. Canup, *Annu. Rev. Astron. Astrophys.* **42**, 441–475 (2004).
6. M. Ćuk, S. T. Stewart, *Science* **338**, 1047–1052 (2012).
7. R. M. Canup, *Science* **338**, 1052–1055 (2012).
8. H. Y. A. Meng *et al.*, *Astrophys. J.* **751**, L17–L21 (2012).
9. D. R. Soderblom, L. A. Hillenbrand, R. D. Jeffries, E. E. Marnajek, T. Naylor, in *Protostars and Planets VI*, H. Beuther, R. Klessen, C. Dullemond, T. Henning, Eds. (Univ. of Arizona Press, Tucson, AZ, 2014), in press; available at <http://arxiv.org/abs/1311.7024>.
10. J. Olofsson *et al.*, *Astron. Astrophys.* **542**, 90–115 (2012).
11. P. Artymowicz, *Astrophys. J.* **335**, L79–L82 (1988).
12. G. G. Fazio *et al.*, *Astrophys. J. Suppl. Ser.* **154**, 10–17 (2004).
13. D. Jewitt, H. Matthews, *Astron. J.* **117**, 1056–1062 (1999).
14. J. A. M. McDonnell *et al.*, *Nature* **321**, 338–341 (1986).
15. D. Perez-Becker, E. Chiang, *Mon. Not. R. Astron. Soc.* **433**, 2294–2309 (2013).
16. P. H. Warren, *Geochim. Cosmochim. Acta* **72**, 3562–3585 (2008).
17. B. C. Johnson, H. J. Melosh, *Icarus* **217**, 416–430 (2012).
18. M. C. Wyatt, W. R. F. Dent, *Mon. Not. R. Astron. Soc.* **334**, 589–607 (2002).
19. B. Zuckerman, I. Song, *Astrophys. J.* **758**, 77–86 (2012).
20. B. C. Johnson *et al.*, *Astrophys. J.* **761**, 45–57 (2012).
21. R. Osten *et al.*, *Astrophys. J.* **765**, L44–L46 (2013).
22. P. Reegen, *Astron. Astrophys.* **467**, 1353–1371 (2007).
23. T. Kallinger, P. Reegen, W. W. Weiss, *Astron. Astrophys.* **481**, 571–574 (2008).
24. S. J. Kenyon, B. C. Bromley, *Astron. J.* **130**, 269–279 (2005).
25. S. Elser, B. Moore, J. Stadel, R. Morishima, *Icarus* **214**, 357–365 (2011).
26. T. Naylor *et al.*, *Mon. Not. R. Astron. Soc.* **335**, 291–310 (2002).
27. R. D. Jeffries, T. Naylor, C. R. Devey, E. J. Totten, *Mon. Not. R. Astron. Soc.* **351**, 1401–1422 (2004).

ACKNOWLEDGMENTS

H.Y.A.M., K.Y.L.S., and G.H.R. thank R. Malhotra and A. Gáspár for valuable discussions. This work is based on observations made with the Spitzer Space Telescope, which is operated by the Jet Propulsion Laboratory (JPL), California Institute of Technology, under a contract with NASA. Support for this work was provided by NASA through an award issued by JPL/Caltech and by NASA grant NNX13AE74G. All data are publicly available through the NASA/IPAC Infrared Science Archive.

SUPPLEMENTARY MATERIALS

www.sciencemag.org/content/345/6200/1032/suppl/DC1
Supplementary Text
Figs. S1 to S4
References (28–45)

23 April 2014; accepted 15 July 2014
10.1126/science.1255153

SUPERFLUIDITY

A mixture of Bose and Fermi superfluids

I. Ferrier-Barbut,* M. Delehay, S. Laurent, A. T. Grier,† M. Pierce, B. S. Rem,‡ F. Chevy, C. Salomon

Superconductivity and superfluidity of fermionic and bosonic systems are remarkable many-body quantum phenomena. In liquid helium and dilute gases, Bose and Fermi superfluidity has been observed separately, but producing a mixture in which both the fermionic and the bosonic components are superfluid is challenging. Here we report on the observation of such a mixture with dilute gases of two lithium isotopes, lithium-6 and lithium-7. We probe the collective dynamics of this system by exciting center-of-mass oscillations that exhibit extremely low damping below a certain critical velocity. Using high-precision spectroscopy of these modes, we observe coherent energy exchange and measure the coupling between the two superfluids. Our observations can be captured theoretically using a sum-rule approach that we interpret in terms of two coupled oscillators.

In recent years, ultracold atoms have emerged as a unique tool to engineer and study quantum many-body systems. Examples include weakly interacting Bose-Einstein condensates (1, 2), two-dimensional gases (3), and the superfluid-Mott insulator transition (4) in the case of bosonic atoms, and the crossover between Bose-Einstein condensation (BEC) and fermionic superfluidity described by the theory of Bardeen, Cooper, and Schrieffer (BCS) for fermionic atoms (5). Mix-

tures of Bose-Einstein condensates were produced shortly after the observation of BEC (2), and a BEC mixed with a single-spin state Fermi sea was originally observed in (6, 7). However, realizing a mixture in which both fermionic and bosonic species are superfluid has been experimentally challenging. This has also been a long-sought goal in liquid helium, where superfluidity was achieved separately in both bosonic ^4He and fermionic ^3He . The double superfluid should undergo a transition

between s-wave and p-wave Cooper pairs as the ^3He dilution is varied (8). However, because of strong interactions between the two isotopes, ^3He - ^4He mixtures contain only a small fraction of ^3He (typically 6%) which, so far, has prevented attainment of simultaneous superfluidity for the two species (8, 9).

Here we report on the production of a Bose-Fermi mixture of quantum gases in which both species are superfluid. Our system is an ultracold gas of fermionic ^6Li in two spin states mixed with ^7Li bosons and confined in an optical dipole trap. Using radio-frequency pulses, we prepare ^6Li atoms in their two lowest hyperfine states $|1_f\rangle$ and $|2_f\rangle$, whereas ^7Li is spin polarized in the second-to-lowest state $|2_b\rangle$ (10). For this combination of states, in the vicinity of the ^6Li Feshbach resonance at a magnetic field of 832 G (11), the scattering length of the bosonic isotope $a_b = 70a_0$ (a_0 is the Bohr radius) is positive, preventing collapse of the BEC. The boson-fermion interaction is characterized by a scattering length $a_{bf} = 40.8a_0$ that does not depend on magnetic field in the parameter range studied here. At resonance, the Fermi gas exhibits a unitary limited collision rate, and lowering the optical dipole trap depth leads to extremely efficient evaporation. Owing to a large excess of ^6Li atoms with respect to ^7Li , the Bose gas is sympathetically driven to quantum degeneracy.

The two clouds reach the superfluid regime after a 4-s evaporation ramp (10). As the ^7Li Bose gas is weakly interacting, the onset of BEC is detected by the growth of a narrow peak in the density profile of the cloud. From previous studies on atomic Bose-Einstein condensates, we conclude that the ^7Li BEC is in a superfluid phase. Superfluidity in a unitary Fermi gas is notoriously more difficult to detect because of the absence of any qualitative modification of the density profile at the phase transition. To demonstrate the superfluidity of the fermionic component of the cloud, we slightly imbalance the two spin populations. In an imbalanced gas, the cloud is organized in concentric layers, with a fully paired superfluid region at its center, where Cooper pairing maintains equal spin populations. This ^6Li superfluid core can be detected by the presence of a plateau in the doubly integrated density profiles of the bosonic and fermionic superfluids are shown in Fig. 1, where both the Bose-Einstein condensate (blue circles) and the plateau (black diamonds in the inset) are clearly visible. Our coldest samples contain $N_b = 4 \times 10^4$ ^7Li atoms and $N_f = 3.5 \times 10^5$ ^6Li atoms. The absence of a thermal fraction in the bosonic cloud indicates a temperature below $0.5T_{c,b}$, where $k_B T_{c,b} = 0.94\hbar\bar{\omega}_b N_b^{1/3}$ is the critical temperature of the ^7Li bosons, and $\bar{\omega}_b$ ($\bar{\omega}_f$) is the geometric

mean trapping frequency for ^7Li (^6Li). Combined with the observation of the ^6Li plateau, this implies that the Fermi cloud is also superfluid with a temperature below $0.8T_{c,f}$. Here, $T_{c,f}$ is the critical temperature for superfluidity of a spin-balanced, harmonically trapped Fermi gas at unitarity, $T_{c,f} = 0.19T_F$ (13), and $k_B T_F = \hbar\bar{\omega}_f(3N_f)^{1/3}$ is the Fermi temperature. The superfluid mixture is very stable, with a lifetime exceeding 7 s for our coldest samples.

As seen in Fig. 1, the Bose-Fermi interaction is too weak to alter significantly the density profiles of the two species (14). To probe the interaction between the two superfluids, we study the dynamics of the mass centers of the two isotopes (dipole modes), a scheme used previously for the study of mixtures of Bose-Einstein condensates (15, 16), mixtures of Bose-Einstein condensates and spin-polarized Fermi seas (17), spin diffusion in Fermi gases (18), or integrability in one-dimensional systems (19). In a purely harmonic trap and in the absence of interspecies interactions, the dipole mode of each species is undamped and can therefore be measured over long time spans to achieve a high-frequency resolution and detect small perturbations of the system. We excite the dipole modes by shifting the initial position of the ^6Li and ^7Li clouds by a displacement d along the weak direction z of the trap (10). We then release them and let them evolve during a variable time t , after which we measure their positions. By monitoring the cloud oscillations during up to 4 s, we determine their frequencies with high precision ($\frac{\Delta\omega}{\omega} \lesssim 2 \times 10^{-3}$). In the absence of the other species, the oscillation frequencies of ^6Li and ^7Li are, respectively, $\omega_f = 2\pi \times 16.80(2)$ Hz and $\omega_b =$

$2\pi \times 15.27(1)$ Hz. In the axial direction, the confinement is mostly magnetic, and at high magnetic field, both species are in the Paschen-Back regime, where the electronic and nuclear spin degrees of freedom are decoupled. In this regime, the magnetic confinement mostly results from the electronic spin and is therefore almost identical for the two isotopes. The ratio ω_f/ω_b is then very close to the expected value $\sqrt{7/6} \approx 1.08$ based on the ratio of the atomic masses (20).

Contrary to the large damping observed in the Bose-Bose mixtures (15), we observe long-lived oscillations of the Bose-Fermi superfluid mixture at frequencies $(\bar{\omega}_b, \bar{\omega}_f)$. These oscillations extend over more than 4 s with undetectable damping (Fig. 2 and fig. S2). This very weak dissipation is only observed when the initial displacement d is below 100 μm , corresponding to a maximum relative velocity $v_{\text{max}} = (\bar{\omega}_b + \bar{\omega}_f)d$ below 18 mm/s $\approx 0.4 v_F$, where $v_F = \sqrt{2k_B T_F/m_f}$. In this situation, the BEC explores only the central part of the much broader Fermi cloud. When $v_{\text{max}} > v_c = 0.42_{-0.11}^{+0.05} v_F = 20_{-5}^{+2}$ mm/s, we observe a sharp onset of damping and heating of the BEC compatible with the Landau criterion for breakdown of superfluidity (Fig. 2C) (10). For comparison, the sound velocity of an elongated Fermi gas at its center is $v'_s = \xi^{1/4} v_F / \sqrt{5} = 17$ mm/s (21), where $\xi = 0.38$ is the Bertsch parameter (5, 13). The measured critical velocity v_c is very close to v'_s and is clearly above the BEC sound velocity of ≈ 5 mm/s at its center.

Two striking phenomena are furthermore observed. First, whereas the frequency $\bar{\omega}_f$ of ^6Li oscillations is almost unchanged from the value in the absence of ^7Li , that of ^7Li is downshifted

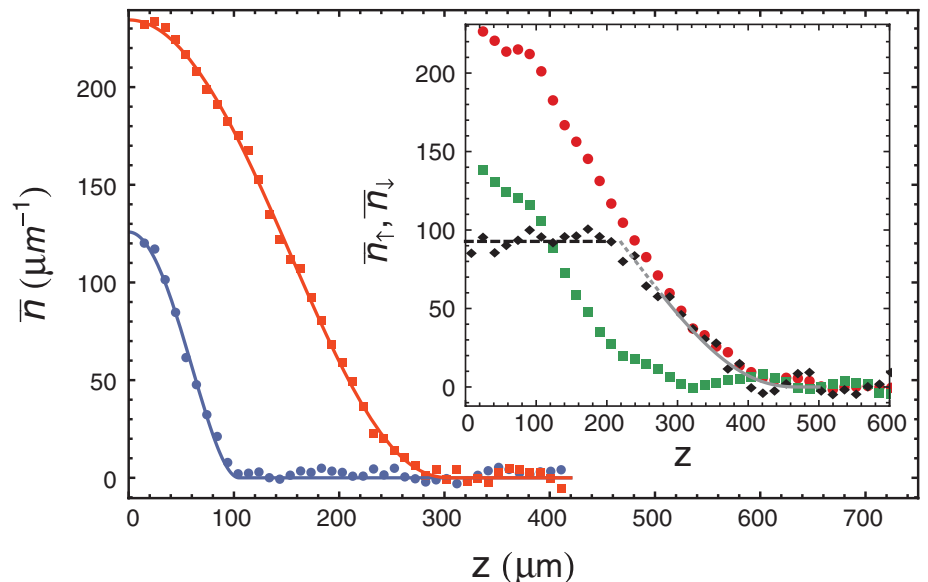


Fig. 1. Density profiles in the double superfluid regime. $N_b = 4 \times 10^4$ ^7Li atoms and $N_f = 3.5 \times 10^5$ ^6Li atoms are confined in a trap at a temperature below 130 nK. The density profiles \bar{n}_b (blue circles) and $\bar{n}_{f,\uparrow}$ (red squares) are doubly integrated over the two transverse directions. The blue (red) solid line is a fit to the ^7Li (^6Li) distribution by a mean-field (unitary Fermi gas) EoS in the Thomas-Fermi approximation. Inset: Spin-imbalanced Fermi gas ($N_{f,\uparrow} = 2 \times 10^5$, $N_{f,\downarrow} = 8 \times 10^4$) in thermal equilibrium with a BEC. Red circles: $\bar{n}_{f,\uparrow}$; green squares: $\bar{n}_{f,\downarrow}$; black diamonds: difference $\bar{n}_{f,\uparrow} - \bar{n}_{f,\downarrow}$. The plateau (black dashed line) indicates superfluid pairing (12). Gray solid line: Thomas-Fermi profile of a noninteracting Fermi gas for the fully spin-polarized outer shell prolonged by the partially polarized normal phase (gray dashed line).

Laboratoire Kastler-Brossel, École Normale Supérieure, Collège de France, CNRS and UPMC, 24 rue Lhomond, 75005 Paris, France.

*Corresponding author. E-mail: iferrer@kb.ens.fr †Present address: Van Swinderen Institute, University of Groningen, Faculty of Mathematics and Natural Sciences, Zernikelaan 25, 9747 AA Groningen, Netherlands. ‡Present address: Institut für Laserphysik, Universität Hamburg, Luruper Chaussee 149, Building 69, D-22761 Hamburg, Germany.

to $\tilde{\omega}_b = 2\pi \times 15.00(2)$ Hz. Second, the amplitude of oscillations of the bosonic species displays a beat at a frequency $\simeq(\tilde{\omega}_f - \tilde{\omega}_b)/(2\pi)$, revealing coherent energy transfer between the two clouds (Fig. 2B). To interpret the frequency shift of the ${}^7\text{Li}$ atoms, we note that $N_b \ll N_f$, which allows us to treat the BEC as a mesoscopic impurity immersed in a Fermi superfluid. Similarly to the Fermi polaron case (22), the effective potential seen by the bosons is the sum of the trapping potential $V(r)$ and the mean-field interaction $g_{\text{bf}}n_f(r)$, where n_f is the total fermion density, $g_{\text{bf}} = 2\pi\hbar^2 a_{\text{bf}}/m_{\text{bf}}$, and $m_{\text{bf}} = \frac{m_b m_f}{m_b + m_f}$ is the ${}^6\text{Li}/{}^7\text{Li}$ reduced mass. Neglecting at first the back-action of the bosons on the fermions, we can assume that n_f is given by the local-density-approximation result $n_f(r) = n_f^{(0)}(\mu_f^{(0)} - V(r))$, where $n_f^{(0)}(\mu)$ is the stationary equation of state (EoS) of the Fermi gas. Because the Bose-Einstein condensate is much smaller than the Fermi cloud (Fig. 2A), $V(r)$ is smaller than $\mu_f^{(0)}$ over the BEC volume. We can thus expand $n_f^{(0)}$, and we get

$$V_{\text{eff}}(r) = g_{\text{bf}}n_f(0) + V(r) \left[1 - g_{\text{bf}} \left(\frac{dn_f^{(0)}}{d\mu_f} \right)_{r=0} \right] \quad (1)$$

We observe that the effective potential is still harmonic and the rescaled frequency is given by

$$\tilde{\omega}_b \simeq \omega_b \left(1 - \frac{1}{2} g_{\text{bf}} \left(\frac{dn_f^{(0)}}{d\mu_f} \right)_{r=0} \right) \quad (2)$$

For a unitary Fermi gas, the chemical potential is related to the density by $\mu_f = \xi \hbar^2 (3\pi^2 n_f)^{2/3} / 2m_f$.

In the weakly coupled limit, we get $\frac{\delta\omega_b}{\omega_b} = \frac{\omega_b - \tilde{\omega}_b}{\omega_b} = \frac{13k_{\text{F}} a_{\text{bf}}}{7\pi\xi^{5/4}}$, where $\hbar k_{\text{F}} = \sqrt{2\hbar m_f \bar{\omega}_f (3N_f)^{1/3}}$ is the Fermi momentum of a noninteracting harmonically trapped Fermi gas. Using our experimental parameters $k_{\text{F}} = 4.6 \times 10^6 \text{ m}^{-1}$, we predict a value $\tilde{\omega}_b \simeq 2\pi \times 14.97$ Hz, in very good agreement with the observed value $15.00(2)$ Hz.

To understand the amplitude modulation, we now take into account the back-action on the fermions. A fully quantum formalism using a sum-rule approach (23–25) leads to a coupled oscillator model in which the positions of the two clouds obey the following equations (10)

$$M_f \ddot{z}_f = -K_f z_f - K_{\text{bf}}(z_f - z_b) \quad (3)$$

$$M_b \ddot{z}_b = -K_b z_b - K_{\text{bf}}(z_b - z_f) \quad (4)$$

where $M_b = N_b m_b$ ($M_f = N_f m_f$) is the total mass of the ${}^7\text{Li}$ (${}^6\text{Li}$) cloud, $K_b = M_b \omega_b^2$ ($K_f = M_f \omega_f^2$) is the spring constant of the axial magnetic confinement, and K_{bf} is a phenomenological (weak) coupling constant describing the mean-field in-

teraction between the two isotopes. To recover the correct frequency shift (Eq. 2), we take $K_{\text{bf}} = 2K_b \frac{\delta\omega_b}{\omega_b}$. Solving these equations with the initial condition $z_f(0) = z_b(0) = d$, and defining $\rho = N_b/N_f$ and $\varepsilon = \frac{2m_b}{m_b - m_f} \left(\frac{\omega_b - \omega_f}{\omega_b} \right)$, in the limit $\rho, \varepsilon \ll 1$ we get

$$z_f = d[(1 - \varepsilon\rho)\cos(\tilde{\omega}_f t) + \varepsilon\rho\cos(\tilde{\omega}_b t)] \quad (5)$$

$$z_b = d[-\varepsilon\cos(\tilde{\omega}_f t) + (1 + \varepsilon)\cos(\tilde{\omega}_b t)] \quad (6)$$

The predictions of Eqs. 5 and 6 agree well with experiment (Fig. 2B). Interestingly, the peak-to-peak modulation of the amplitude of ${}^7\text{Li}$ is much larger than the relative frequency shift, a consequence of the almost exact tuning of the two oscillators (up to a factor $\sqrt{6/7}$). Thus, the mass prefactor in the expression for ε is large (=14) and leads to $\varepsilon \simeq 0.25$ at unitarity. This results in efficient energy transfer between the two modes despite their weak coupling, as observed.

We now extend our study of the Bose-Fermi superfluid mixture to the BEC-BCS crossover by tuning the magnetic field away from the resonance value $B_f = 832$ G. We explore a region from 860 G down to 780 G where $1/k_{\text{F}} a_{\text{f}}$ spans the interval $[-0.4, +0.8]$. In this whole domain, except in a narrow region between 845 and 850 G where the boson-boson scattering length

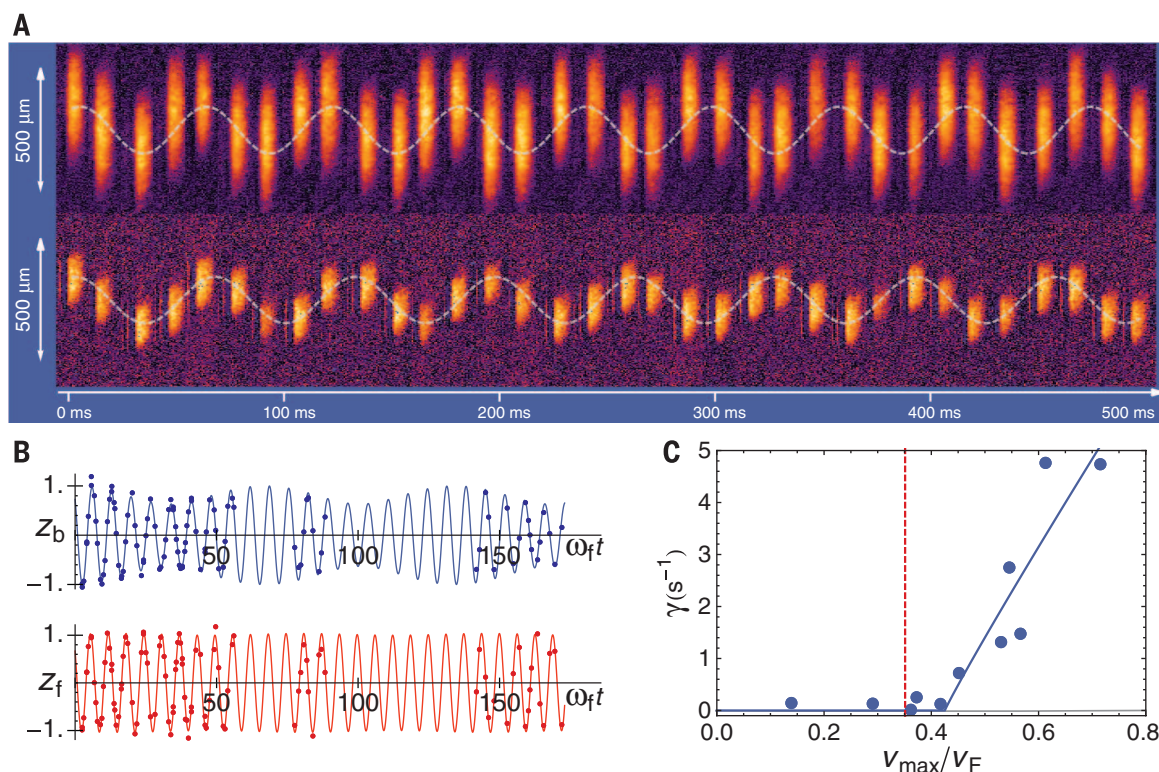


Fig. 2. Coupled oscillations of the superfluid mixture. (A) Center-of-mass oscillations. The oscillations are shown over the first 500 ms at a magnetic field of 835 G for a Fermi superfluid (top) and a Bose superfluid (bottom). The oscillation period of ${}^6\text{Li}$ (${}^7\text{Li}$) is 59.7(1) ms [66.6(1) ms], leading to a dephasing of π near 300 ms. These oscillations persist for more than 4 s with no visible damping. The maximum relative velocity between the two clouds is 1.8 cm/s. (B) Coupled oscillations. Symbols: Center-of-mass oscillation of ${}^7\text{Li}$ (top) and ${}^6\text{Li}$ (bottom) displaying coherent energy exchange between both

superfluids. Solid lines: Theory for an initial displacement d of 100 μm at a magnetic field of 835 G; see text. (C) Critical damping. Symbols: Damping rate (blue circles) of the amplitude of the center-of-mass oscillations of the ${}^7\text{Li}$ BEC as a function of the maximal relative velocity between the two superfluids normalized to the Fermi velocity of the ${}^6\text{Li}$ gas. Data taken at 832 G. From these data and using a fit function given in (10) (solid line), we extract $v_c = 0.42_{-0.11}^{+0.05} v_{\text{F}}$. The red dashed line shows the speed of sound of an elongated unitary Fermi superfluid $v_s = \xi^{1/4} v_{\text{F}} / \sqrt{5} = 0.35 v_{\text{F}}$ (20).

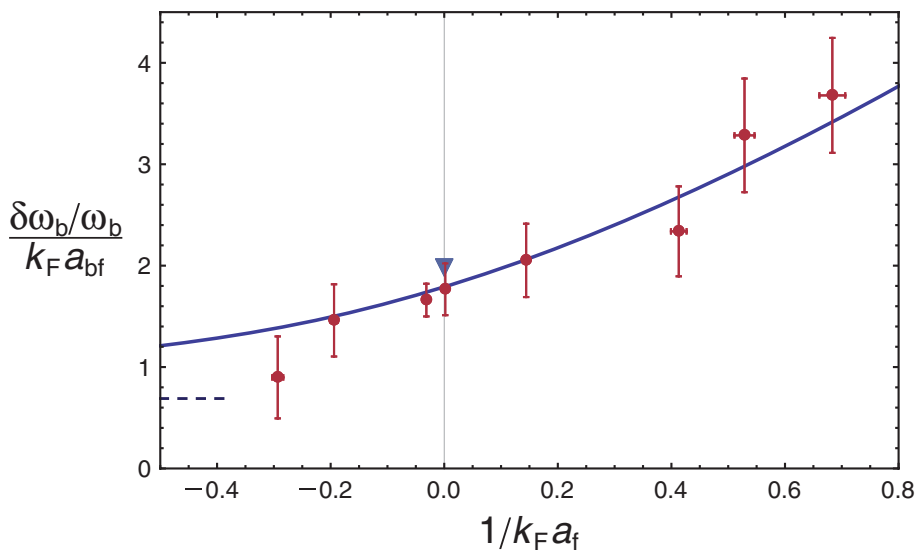


Fig. 3. Dipole mode frequency shift in the BEC-BCS crossover. Red circles: Experiment. Blue line: zero-temperature prediction from the equation of state of (26); dashed line: ideal Fermi gas. Blue triangle: prediction from (13). Error bars include systematic and statistical errors at 1 SD.

is negative, the mixture is stable and the damping extremely small.

The frequency shift of the BEC (Eq. 2) now probes the derivative of the EoS $n_f(\mu_f)$ in the BEC-BCS crossover. In the zero-temperature limit and under the local density approximation, Eq. 2 obeys the universal scaling $\frac{\delta\omega_b}{\omega_b} = k_F a_{bf} f\left(\frac{1}{k_F a_f}\right)$.

In Fig. 3, we compare our measurements to the prediction for the function f obtained from the zero-temperature EoS measured in (26). On the BCS side, $(1/k_F a_f < 0)$, the frequency shift is reduced and tends to that of a noninteracting Fermi gas. Far on the BEC side $(1/k_F a_f \gg 1)$, we can compute the frequency shift using the EoS of a weakly interacting gas of dimers. Within the mean-field approximation, we have $\frac{dn_f}{d\mu_f} = \frac{2m_f}{\pi\hbar^2 a_{dd}}$, where $a_{dd} = 0.6a_f$ is the dimer-dimer scattering length. This expression explains the increase in the frequency shift when a_f is reduced, i.e., moving toward the BEC side [see (10) for the effect of Lee-Huang-Yang quantum correction].

The excellent agreement between experiment and our model confirms that precision measurements of collective modes are a sensitive dynamical probe of equilibrium properties of many-body quantum systems (27). Our approach can be extended to the study of higher-order excitations. In particular, although there are two first sound modes, one for each atomic species, we expect only one second sound for the superfluid mixture (28) if cross-thermalization is fast enough. In addition, the origin of the critical velocity for the relative motion of Bose and Fermi superfluids is an intriguing question that can be further explored in our system. Finally, a richer phase diagram may be revealed when N_b/N_f is increased (29) or when the superfluid mixture is loaded in an optical lattice (30).

REFERENCES AND NOTES

1. W. Ketterle, *Rev. Mod. Phys.* **74**, 1131–1151 (2002).
2. E. A. Cornell, C. E. Wieman, *Rev. Mod. Phys.* **74**, 875–893 (2002).
3. Z. Hadzibabic, P. Krüger, M. Cheneau, B. Battelier, J. Dalibard, *Nature* **441**, 1118–1121 (2006).

4. M. Greiner, O. Mandel, T. Esslinger, T. W. Hänsch, I. Bloch, *Nature* **415**, 39–44 (2002).
5. W. Zwerger, Ed., *The BCS-BEC Crossover and the Unitary Fermi Gas*, vol. 836 of *Lecture Notes in Physics* (Springer, Berlin, 2012).
6. F. Schreck et al., *Phys. Rev. Lett.* **87**, 080403 (2001).
7. A. G. Truscott, K. E. Strecker, W. I. McAlexander, G. B. Partridge, R. G. Hulet, *Science* **291**, 2570–2572 (2001).
8. J. Rysti, J. Tuoriniemi, A. Salmela, *Phys. Rev. B* **85**, 134529 (2012).
9. J. Tuoriniemi et al., *J. Low Temp. Phys.* **129**, 531–545 (2002).
10. See supplementary materials on Science Online.
11. G. Zürn et al., *Phys. Rev. Lett.* **110**, 135301 (2013).
12. T. De Silva, E. Mueller, *Phys. Rev. A* **73**, 051602 (2006).
13. M. J. H. Ku, A. T. Sommer, L. W. Cheuk, M. W. Zwierlein, *Science* **335**, 563–567 (2012).

14. K. Molmer, *Phys. Rev. Lett.* **80**, 1804–1807 (1998).
15. D. S. Hall, M. R. Matthews, J. R. Ensher, C. E. Wieman, E. A. Cornell, *Phys. Rev. Lett.* **81**, 1539–1542 (1998).
16. P. Maddaloni, M. Modugno, C. Fort, F. Minardi, M. Inguscio, *Phys. Rev. Lett.* **85**, 2413–2417 (2000).
17. F. Ferlaino et al., *J. Opt. B Quantum Semiclassical Opt.* **5**, S3–S8 (2003).
18. A. Sommer, M. Ku, G. Roati, M. W. Zwierlein, *Nature* **472**, 201–204 (2011).
19. T. Kinoshita, T. Wenger, D. S. Weiss, *Nature* **440**, 900–903 (2006).
20. Because of a slight deviation from the Paschen-Back regime for ^7Li , this ratio is 1.1 instead of 1.08.
21. Y. Hou, L. Pitaevskii, S. Stringari, *Phys. Rev. A* **88**, 043630 (2013).
22. C. Lobo, A. Recati, S. Giorgini, S. Stringari, *Phys. Rev. Lett.* **97**, 200403 (2006).
23. S. Stringari, *J. Phys. IV France* **116**, 47–66 (2004).
24. T. Miyakawa, T. Suzuki, H. Yabu, *Phys. Rev. A* **62**, 063613 (2000).
25. A. Banerjee, *Phys. Rev. A* **76**, 023611 (2007).
26. N. Navon, S. Nascimbène, F. Chevy, C. Salomon, *Science* **328**, 729–732 (2010).
27. M. K. Tey et al., *Phys. Rev. Lett.* **110**, 055303 (2013).
28. G. Volovik, V. Mineev, I. Khalatnikov, *Sov. Phys. JETP* **69**, 675 (1975).
29. T. Ozawa, A. Recati, S. Stringari, <http://arxiv.org/abs/1405.7187> (2014).
30. A. B. Kuklov, B. V. Svistunov, *Phys. Rev. Lett.* **90**, 100401 (2003).

ACKNOWLEDGMENTS

We thank S. Stringari and Y. Castin for fruitful discussions and S. Balibar, J. Dalibard, F. Gerbier, S. Nascimbène, C. Cohen-Tannoudji, and M. Schleier-Smith for critical reading of the manuscript. We acknowledge support from the European Research Council Ferlodim and Thermodynamix, the Ile de France Nano-K (contract Atomix), and Institut de France Louis D. Prize.

SUPPLEMENTARY MATERIALS

www.sciencemag.org/content/345/6200/1035/suppl/DC1
Materials and Methods
Figs. S1 to S4
References (31–34)

29 April 2014; accepted 30 June 2014
Published online 17 July 2014;
10.1126/science.1255380

EARTHQUAKE DYNAMICS

Strength of stick-slip and creeping subduction megathrusts from heat flow observations

Xiang Gao¹ and Kelin Wang^{2,3*}

Subduction faults, called megathrusts, can generate large and hazardous earthquakes. The mode of slip and seismicity of a megathrust is controlled by the structural complexity of the fault zone. However, the relative strength of a megathrust based on the mode of slip is far from clear. The fault strength affects surface heat flow by frictional heating during slip. We model heat-flow data for a number of subduction zones to determine the fault strength. We find that smooth megathrusts that produce great earthquakes tend to be weaker and therefore dissipate less heat than geometrically rough megathrusts that slip mainly by creeping.

Subduction megathrusts that primarily exhibit stick-slip behavior can produce great earthquakes, but some megathrusts are observed to creep while producing small and moderate-size earthquakes. The relationship between seismogenesis and strength of subduction megathrust is far from clear. Faults that produce great earthquakes are commonly thought of as being stronger than those that creep (1).

Megathrusts that are presently locked to build up stress for future great earthquakes are thus described as being “strongly coupled.” However, some studies have proposed strong creeping megathrusts because of the geometric irregularities of very rugged subducted sea floor (2, 3).

Contrary to a widely held belief, geodetic and seismic evidence shows that very rough subducting sea floor promotes megathrust creep (2). All

The Landau Critical Velocity for a Particle in a Fermi Superfluid
La Vitesse Critique de Landau d'une Particule dans un
Superfluide de Fermions

Y. Castin, I. Ferrier-Barbut, C. Salomon

arXiv:1408.1326, Submitted to Comptes Rendus Physique

La vitesse critique de Landau d'une particule dans un superfluide de fermions

The Landau critical velocity for a particle in a Fermi superfluid

Yvan Castin^a, Igor Ferrier-Barbut^a, Christophe Salomon^a

^aLaboratoire Kastler Brossel, École normale supérieure, CNRS et UPMC, Paris, France

Abstract

We determine à la Landau the critical velocity v_c^L of a moving impurity in a Fermi superfluid, that is by restricting to the minimal excitation processes of the superfluid. v_c^L is then the minimal velocity at which these processes are energetically allowed. The Fermi superfluid actually exhibits two excitation branches : one is the fermionic pair-breaking excitation, as predicted by BCS theory ; the other one is bosonic and sets pairs into motion, as predicted by Anderson's RPA. v_c^L is the smallest of the two corresponding critical velocities $v_{c,f}^L$ and $v_{c,b}^L$. In the parameter space (superfluid interaction strength, fermion-to-impurity mass ratio), we identify two transition lines, corresponding to a discontinuity of the first-order and second-order derivatives of v_c^L . These two lines meet in a triple point and split the plane in three domains. We briefly extend this analysis to the very recently realized case at ENS, where the moving object in the Fermi superfluid is a weakly interacting Bose superfluid of impurities, rather than a single impurity. For a Bose chemical potential much smaller than the Fermi energy, the topology of the transition lines is unaffected ; a key result is that the domain $v_c^L = c$, where c is the sound velocity in the Fermi superfluid, is turned into a domain $v_c^L = c + c_B$, where c_B is the sound velocity in the Bose superfluid, with slightly shifted boundaries.

Keywords : Fermi gases ; superfluidity ; critical velocity ; Landau criterion ; ultracold atoms

Résumé

Nous déterminons la vitesse critique v_c^L d'une impureté en mouvement dans un superfluide de fermions par un raisonnement à la Landau, c'est-à-dire en nous limitant aux processus d'excitation minimale du superfluide par la particule. v_c^L est alors la plus petite des vitesses auxquelles ces processus sont énergétiquement permis. Comme le superfluide de fermions possède deux branches d'excitation, l'une fermionique prédite par la théorie de BCS et consistant à briser des paires de fermions, l'autre bosonique prédite par la RPA d'Anderson et consistant à les mettre en mouvement, il y a une vitesse critique de Landau $v_{c,f}^L$ et $v_{c,b}^L$ associée à chaque branche et v_c^L est la plus petite des deux. Dans l'espace des paramètres (force des interactions dans le superfluide, masse relative fermion-impureté), nous trouvons deux lignes de transition, correspondant respectivement à la discontinuité des différentielles première et seconde de v_c^L . Ces deux lignes se rejoignent en un point triple et partitionnent le plan en trois domaines. Nous étendons succinctement cette analyse au cas, très récemment réalisé à l'ENS, où l'objet en mouvement dans le superfluide de fermions est un superfluide d'impuretés bosoniques en interaction faible, plutôt qu'une impureté seule. Lorsque le potentiel chimique des bosons reste petit devant l'énergie de Fermi, la topologie des lignes de transition sur v_c^L ne change pas ; un résultat marquant est alors qu'au domaine $v_c^L = c$, où c est la vitesse du son dans le superfluide de fermions, correspond maintenant un domaine $v_c^L = c + c_B$, où c_B est la vitesse du son dans le superfluide de bosons, avec des frontières légèrement déplacées.

Mots-clés : gaz de fermions ; superfluidité ; vitesse critique ; critère de Landau ; atomes froids

1. Introduction, rappels et motivations

Les gaz dégénérés d'atomes neutres fermioniques de spin 1/2, supposés ici non polarisés c'est-à-dire avec des populations égales dans les deux états internes, sont réalisables en laboratoire depuis 2002 [1]. Ils présentent, en dessous d'une température critique, deux propriétés quantiques macroscopiques remarquables et bien distinctes. La

première est la présence d'un condensat de paires, c'est-à-dire l'existence d'un mode macroscopiquement peuplé de l'opérateur densité à deux corps [2], et qui se traduit physiquement par une longueur de cohérence macroscopique pour le champ de paires, limitée donc seulement par la taille du système. Cet « ordre à longue portée », est en principe mesurable directement par interférométrie [3], mais c'est pour l'instant la fraction de paires condensées f_c que l'on sait mesurer [4]. La seconde propriété, celle qui nous intéresse ici, est la superfluidité. Elle a la réputation d'être plus subtile, puisqu'elle met en jeu un ensemble de phénomènes complémentaires, dont certains reposent sur la métastabilité plutôt que sur des propriétés à l'équilibre. Nous en retiendrons ici deux aspects, en passant sous silence les réseaux de tourbillons quantiques [5] et les courants permanents.

Le premier aspect met en jeu la notion de fraction superfluide f_s : pour des conditions aux limites périodiques cubiques de période L , c'est la fraction du gaz qui n'est pas entraînée par un potentiel extérieur en mouvement, même au bout d'un temps arbitrairement long permettant au système d'atteindre l'équilibre thermique dans le repère en mouvement. Si le potentiel extérieur se déplace selon la direction Ox , à la vitesse v , la fraction normale $f_n = 1 - f_s$ du gaz est par définition entraînée à cette même vitesse, si bien que

$$1 - f_s = \lim_{N \rightarrow \infty, \rho = \text{ct}} \lim_{v \rightarrow 0} \lim_{\eta \rightarrow 0} \frac{\langle P_x \rangle}{Nmv} \quad (1)$$

où le gaz, composé de N atomes de masse m et de densité $\rho = N/L^3$, possède à l'équilibre une impulsion moyenne totale $\langle P_x \rangle$ selon Ox en présence du potentiel extérieur. La triple limite doit être prise dans cet ordre, afin que la fraction normale soit une quantité intrinsèque. On fait d'abord tendre vers zéro l'amplitude η du potentiel extérieur, afin que f_n ne dépende pas de la forme du potentiel. Puis l'on fait tendre la vitesse d'entraînement vers zéro, avant de prendre la limite thermodynamique, de façon que l'on ait toujours

$$v \ll \frac{2\pi\hbar}{mL} \quad (2)$$

En effet, prendre v égale au quantum de vitesse $2\pi\hbar/(mL)$ permettrait, par invariance galiléenne des conditions aux limites périodiques à cette vitesse, de conclure que le gaz est au repos dans le référentiel du potentiel extérieur, ce qui conduirait à $\langle P_x \rangle = Nmv$ dans le référentiel du laboratoire, et donc au résultat invariable (et non physique) $f_n = 1$. La fraction superfluide f_s du gaz de fermions de spin $1/2$ non polarisé a été très récemment mesurée dans le régime d'interaction forte, en fonction de la température T [6], et a permis de vérifier que la transition de phase superfluide se produit à la même température que celle de la condensation de paires [4] et que celle déduite des singularités des grandeurs thermodynamiques [7]. Une propriété importante attendue, et confirmée expérimentalement sur d'autres systèmes, est que $f_s \rightarrow 1$ à température nulle.

Le deuxième aspect de la superfluidité, limité en toute rigueur au cas d'une température nulle, est l'existence d'une vitesse critique v_c en dessous de laquelle un objet traversant le gaz ne subit aucune force de friction et ne peut y déposer de l'énergie, donc y a un mouvement non amorti. Cet aspect a bien été observé dans les gaz d'atomes froids fermioniques pour un réseau optique unidimensionnel en mouvement [8]. Le calcul de la vitesse critique est souvent ardu, et le résultat dépend en général des caractéristiques de l'objet et de son couplage au gaz [9]. Cependant, pour un couplage arbitrairement *faible*¹, dans l'esprit de la définition (1), on peut se limiter, comme l'a fait Landau [10], à la première étape dans la dissipation de l'énergie cinétique de l'objet, à savoir la création d'une (et une seule) excitation élémentaire dans le gaz. Formellement, ceci revient à calculer l'amplitude de diffusion de l'objet sur le gaz dans l'approximation de Born, au premier ordre en la constante de couplage gaz-objet, ou à évaluer le taux d'émission d'excitation par l'objet selon la règle d'or de Fermi, au second ordre en la constante de couplage. Dans les deux cas apparaît en facteur une distribution de Dirac assurant la conservation de l'énergie non perturbée. Dans ce travail, l'objet est, sauf en section 5, une particule de masse M , discernable des atomes du gaz, de vitesse initiale v donc d'énergie cinétique initiale $\frac{1}{2}Mv^2$. Après émission d'une excitation de vecteur d'onde \mathbf{q} et d'énergie $\epsilon_{\mathbf{q}}$, sa vitesse vaut $\mathbf{v} - \hbar\mathbf{q}/M$, par conservation de l'impulsion totale, d'où

$$\hbar\mathbf{q} \cdot \mathbf{v} = \frac{\hbar^2 q^2}{2M} + \epsilon_{\mathbf{q}} \quad (3)$$

1. Ce couplage peut être un couplage effectif : pour un objet quasi-punctuel, il est proportionnel à sa longueur de diffusion dans l'onde s avec les atomes du gaz.

par conservation de l'énergie. Comme $|\mathbf{q} \cdot \mathbf{v}| \leq qv$, cette condition n'est satisfaite pour aucun \mathbf{q} si v est inférieure à la vitesse critique de Landau

$$v_c^L = \inf_{\mathbf{q}} v_{\mathbf{q}} \quad \text{avec} \quad v_{\mathbf{q}} = \frac{\hbar^2 q^2}{2M} + \epsilon_{\mathbf{q}} / \hbar q \quad (4)$$

Un calcul de v_c^L pour une particule de masse $M \rightarrow +\infty$ a été effectué dans la référence [11] avec la théorie approchée de BCS et de la RPA ; il a fallu pour cela prendre en compte les deux branches d'excitation du superfluide de fermions, la branche fermionique avec bande interdite, décrivant la brisure des paires de Cooper de fermions, et la branche bosonique sans bande interdite mais de départ phononique en $\mathbf{q} = \mathbf{0}$, décrivant la mise en mouvement des paires. On obtient ainsi [11]

$$v_c^L(\alpha = 0) = \min([\mu^2 + \Delta^2]^{1/2} - \mu)/m]^{1/2}, c) \quad (5)$$

où c est la vitesse du son dans le superfluide de fermions de potentiel chimique μ et de gap Δ , et l'on note le rapport de masse

$$\alpha = \frac{m}{M} \quad (6)$$

Le fait que la vitesse critique soit non nulle pour $M \rightarrow +\infty$ semble contredire le raisonnement qui suit l'équation (2), l'effet d'un objet de masse infinie sur le superfluide pouvant être assimilé à celui d'un potentiel extérieur défilant à vitesse constante : on devrait donc avoir $v_c \leq 2\pi\hbar/(mL) \rightarrow 0$ à la limite thermodynamique. C'est bien la notion (subtile) de métastabilité qui permet de donner un sens au raisonnement de Landau et de croire à la vitesse critique prédite v_c^L pour des temps assez courts : lorsque $v < v_c^L$, le premier pas vers la dissipation est bloqué par une barrière d'énergie, mais rien n'empêche que le système puisse franchir cette barrière par des processus d'ordre arbitrairement élevé en le couplage gaz-objet, correspondant à une énergie d'excitation $\epsilon_{\mathbf{q}}$ bien différente de celle des excitations élémentaires de l'équation (4). Ainsi, le processus improbable d'ordre N mettant en mouvement l'ensemble du gaz à la vitesse $2\pi\hbar/(mL)$ selon Ox , par translation en impulsion de chacun de ses atomes de $2\pi\hbar/L$ selon cette direction, correspond à $q = 2\pi N/L$ et $\epsilon_{\mathbf{q}} = N(2\pi\hbar)^2/(2mL^2)$, donc à une vitesse critique $v_{\mathbf{q}} = 2\pi\hbar/(2mL)$ qui s'annule bien à la limite thermodynamique², pourvu que $M \gg Nm$.

L'objectif du présent travail est d'étendre les calculs de la référence [11] au cas d'une masse M finie. Il y a pour cela une très forte motivation expérimentale : la prédiction de Landau pour la vitesse critique d'une impureté atomique dans un condensat de Bose-Einstein a été confirmée au MIT [13], et pourrait bientôt être mesurée dans un superfluide de fermions, grâce au mélange de bosons et de fermions superfluides récemment obtenu à l'ENS [14]. Le calcul de v_c^L pour une particule de masse M est effectué ici en trois étapes : on détermine successivement la vitesse critique $v_{c,f}^L$ due à la branche d'excitation fermionique de BCS en section 2, celle $v_{c,b}^L$ due à la branche bosonique de la RPA en section 3, la plus petite des deux vitesses donnant finalement v_c^L en section 4. Comme la référence [14] met en mouvement dans le superfluide de fermions un condensat de Bose-Einstein plutôt qu'une impureté seule, il convient de modifier la formule de Landau (4) pour prendre en compte l'effet des interactions entre les impuretés, ce qui est fait en section 5. Nous concluons en section 6.

2. Vitesse critique sur la branche fermionique

On pourrait croire naïvement que la vitesse critique $v_{c,f}^L$ associée à la branche d'excitation fermionique du superfluide se déduit de l'expression générale (4) en prenant pour $\mathbf{k} \mapsto \epsilon_{\mathbf{k}}$ la relation de dispersion correspondante $\mathbf{k} \mapsto \epsilon_{f,\mathbf{k}}$ des quasi-particules fermioniques. Cependant, ce serait à tort, car ce serait faire fi des contraintes imposées par la conservation du nombre total de fermions. En réalité, l'impureté de masse M ne peut, par interaction avec le superfluide initialement dans le vide de quasi-particules, faire apparaître qu'un nombre *pair* d'excitations fermioniques. Ceci est particulièrement clair dans le cadre de la théorie de BCS : le Hamiltonien d'interaction entre l'impureté et les fermions fait apparaître les champs fermioniques $\hat{\psi}_{\sigma}(\mathbf{r})$, $\sigma = \pm 1/2$, seulement par des termes quadratiques de la forme $\hat{\psi}_{\sigma}^{\dagger} \hat{\psi}_{\sigma'}$; or chaque $\hat{\psi}_{\sigma}(\mathbf{r})$ est une combinaison linéaire d'opérateurs d'annihilation $\hat{b}_{\mathbf{k}\sigma}$ et de création $\hat{b}_{\mathbf{k}-\sigma}^{\dagger}$ de

2. Il est plus habituel d'invoquer comme excitation macroscopique la création par l'objet en mouvement d'un anneau de vorticit  dans le gaz. Lorsque le rayon de l'anneau est de l'ordre du diam tre du gaz, on aboutit cependant aux m mes lois d' chelle en N et L pour q , $\epsilon_{\mathbf{q}}$ et $v_{\mathbf{q}}$,   un facteur $\ln L$ pr s dans $\epsilon_{\mathbf{q}}$ [12].

quasi-particules, qui changent la parité de leur nombre. Dans le raisonnement à la Landau, il faut donc supposer que l'impureté crée au minimum deux quasi-particules fermioniques, de vecteurs d'onde \mathbf{k}_1 et \mathbf{k}_2 . L'impureté subit alors un changement d'impulsion de $-\hbar(\mathbf{k}_1 + \mathbf{k}_2)$ et acquiert une énergie de recul de $\hbar^2(\mathbf{k}_1 + \mathbf{k}_2)^2/(2M)$, ce qui conduit à la vitesse critique³

$$v_{c,f}^L = \inf_{\mathbf{k}_1, \mathbf{k}_2} \frac{\frac{\hbar^2(\mathbf{k}_1 + \mathbf{k}_2)^2}{2M} + \epsilon_{f, \mathbf{k}_1} + \epsilon_{f, \mathbf{k}_2}}{\hbar|\mathbf{k}_1 + \mathbf{k}_2|} \quad (7)$$

Comme rien n'empêche d'effectuer la minimisation sur \mathbf{k}_1 et \mathbf{k}_2 d'abord sur \mathbf{k}_1 à $\mathbf{q} = \mathbf{k}_1 + \mathbf{k}_2$ fixé, puis sur \mathbf{q} , on peut se ramener à une écriture plus opérationnelle et formellement équivalente à celle de l'équation (4) :

$$v_{c,f}^L = \inf_{\mathbf{q}} v_{f, \mathbf{q}} \text{ avec } v_{f, \mathbf{q}} = \frac{\frac{\hbar^2 q^2}{2M} + \epsilon_{f, \mathbf{q}}^{\text{eff}}}{\hbar q}, \quad (8)$$

où $\epsilon_{f, \mathbf{q}}^{\text{eff}}$ est le bord inférieur du continuum à deux quasi-particules fermioniques au vecteur d'onde total fixé \mathbf{q} :

$$\epsilon_{f, \mathbf{q}}^{\text{eff}} \equiv \inf_{\mathbf{k}_1} \epsilon_{f, \mathbf{k}_1} + \epsilon_{f, \mathbf{k}_2 = \mathbf{q} - \mathbf{k}_1} \quad (9)$$

Comme la relation de dispersion $\mathbf{k} \mapsto \epsilon_{f, \mathbf{k}}$ est une fonction lisse du vecteur d'onde, divergente à l'infini, la borne inférieure est atteinte en un point de stationnarité, c'est-à-dire de gradient nul par rapport à \mathbf{k}_1 , de la fonction à minimiser. Comme la relation de dispersion est de plus isotrope,

$$\epsilon_{f, \mathbf{k}} = \epsilon_f(k), \quad (10)$$

le gradient est nul si et seulement si

$$\epsilon'_f(k_1)\hat{\mathbf{k}}_1 = \epsilon'_f(k_2)\hat{\mathbf{k}}_2 \quad (11)$$

avec $\hat{\mathbf{k}}_i$ la direction \mathbf{k}_i/k_i du vecteur \mathbf{k}_i , $\epsilon'_f(k)$ la dérivée de la fonction $\epsilon_f(k)$, et où l'on a toujours $\mathbf{k}_2 = \mathbf{q} - \mathbf{k}_1$. Il y a donc en général quatre branches de stationnarité possibles :

$$(i) : \mathbf{k}_1 = \mathbf{k}_2 = \mathbf{q}/2, \quad (ii) : \hat{\mathbf{k}}_1 = \hat{\mathbf{k}}_2, k_1 \neq k_2, \quad (iii) : \hat{\mathbf{k}}_1 = -\hat{\mathbf{k}}_2, \quad (iv) : \epsilon'_f(k_1) = \epsilon'_f(k_2) = 0 \quad (12)$$

Dans les deux cas intermédiaires, les dérivées $\epsilon'_f(k_1)$ et $\epsilon'_f(k_2)$ sont, bien entendu, respectivement égales et opposées.

Particularisons cette discussion au cas de la théorie de BCS, de relation de dispersion

$$\epsilon_{f, \mathbf{k}} = \epsilon_f(k) = \left[\left(\frac{\hbar^2 k^2}{2m} - \mu \right)^2 + \Delta^2 \right]^{1/2} \quad (13)$$

Pour un potentiel chimique $\mu > 0$, elle présente une forme de chapeau mexicain, donc un caractère fermionique bien affirmé, avec une bande interdite de largeur le gap Δ . La fonction $\epsilon_f(k)$ est alors concave décroissante jusqu'au point d'inflexion k_{inflex} , puis convexe décroissante jusqu'à la position k_{min} de son minimum,

$$k_{\text{min}} = \frac{(2m\mu)^{1/2}}{\hbar} \quad (14)$$

et enfin convexe croissante au-delà. Les quatre branches de stationnarité peuvent alors être réalisées. Contrairement à la branche (i), les autres branches n'existent que pour q assez faible. Pour explorer la branche (ii), on peut se limiter à $k_1 \in [0, k_{\text{inflex}}]$ et $k_2 \in [k_{\text{inflex}}, k_{\text{min}}]$, et l'on trouve que $q = k_1 + k_2$ décrit $[k_{\text{min}}, 2k_{\text{inflex}}]$; de même, pour la branche

3. Dans le cas d'un objet en mouvement de masse infinie, on trouve pourtant dans la littérature la formule habituelle $v_{c,f}^{\text{hab}} = \inf_q \epsilon_f(q)/(\hbar q)$ [11], avec $\epsilon_f(q) = \epsilon_{f, \mathbf{q}}$, ce qui semble relever de l'erreur naïve susmentionnée. En réalité, notre équation (7) redonne bien $v_{c,f}^{\text{hab}}$ lorsque $M \rightarrow +\infty$. D'une part, $v_{c,f}^L \leq v_{c,f}^{\text{hab}}$ puisque dans l'équation (7) apparaissent en particulier les configurations $\mathbf{k}_1 = \mathbf{k}_2$. D'autre part, la minimisation sur les directions de \mathbf{k}_1 et \mathbf{k}_2 à modules fixés est immédiate lorsque $M = \infty$, il faut prendre les vecteurs d'onde colinéaires et de même sens, et il reste $v_{c,f}^L = \inf_{k_1, k_2} \frac{k_1 \epsilon_f(k_1) + k_2 \epsilon_f(k_2)}{k_1 + k_2}$, qui est $\geq v_{c,f}^{\text{hab}}$ puisque $\epsilon_f(k_i) \geq k_i v_{c,f}^{\text{hab}}$ pour tout k_i .

(iii), on peut prendre $0 \leq k_1 \leq k_{\min} \leq k_2$, et l'on trouve que $q = k_2 - k_1$ décrit $[0, k_{\min}]$.⁴ Finalement, la branche (iv) correspond simplement à $k_1 = k_2 = k_{\min}$, et à $q = |\mathbf{k}_1 + \mathbf{k}_2|$ variant de 0 à $2k_{\min}$. Sur son domaine d'existence, la branche (iv) est clairement celle d'énergie minimale, puisque les vecteurs d'onde \mathbf{k}_1 et \mathbf{k}_2 des deux quasi-particules sont au fond de la rigole du chapeau mexicain. Au-delà, les branches (ii) et (iii) n'existent plus donc l'énergie minimale est obtenue sur la branche (i). Cette discussion est illustrée sur la figure 1. Nous retenons donc, pour $\mu > 0$,

$$\epsilon_f^{\text{eff}}(q) \stackrel{q \leq 2k_{\min}}{\underset{\text{branche (iv)}}{=}} 2\Delta, \quad \epsilon_f^{\text{eff}}(q) \stackrel{q \geq 2k_{\min}}{\underset{\text{branche (i)}}{=}} 2\epsilon_f(q/2) \quad (15)$$

en accord avec la référence [11]. Pour un potentiel chimique $\mu < 0$, lorsque les paires de Cooper atomiques tendent à se bosoniser, la relation de dispersion (13) est une fonction convexe, avec une bande interdite de largeur $(\Delta^2 + \mu^2)^{1/2}$. Comme $\epsilon_f(k)$ est alors strictement croissante pour $k > 0$, seule la branche (i) est réalisée.

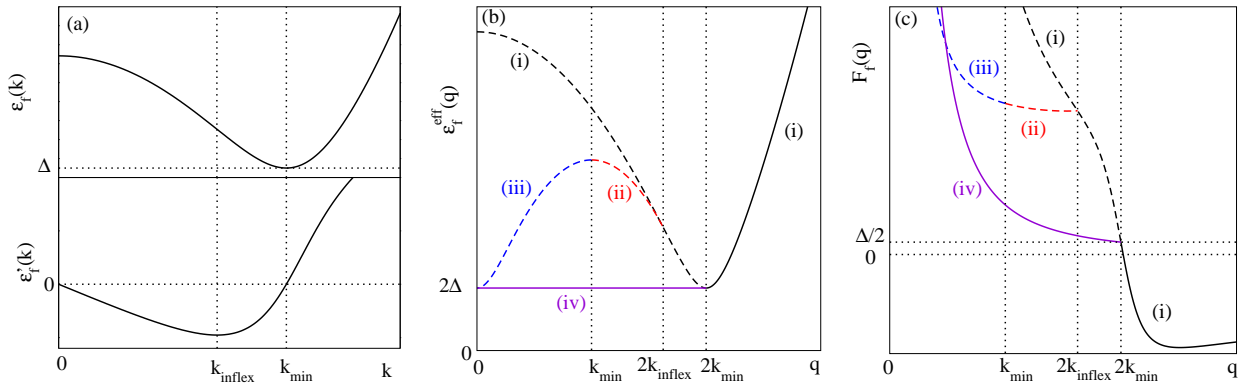


FIGURE 1: Pour la branche d'excitation fermionique de la théorie de BCS à potentiel chimique $\mu > 0$, (a) relation de dispersion $\epsilon_f(k)$ et sa dérivée première, utiles à la discussion des branches de stationnarité (12); (b) les branches en question en fonction de q , en trait plein si d'énergie minimale, en tireté sinon; (c) fonction $F_f(\check{q})$ permettant de minimiser $v_f(q)$ par discussion graphique, voir l'équation (16). Les quantités sur les axes sont adimensionnées comme il est précisé dans le texte.

Pour obtenir la contribution de la branche fermionique de BCS à la vitesse critique de Landau, il reste à minimiser la fonction $v_{f,q} = v_f(q)$ dans l'équation (8). Comme cette fonction diverge en $q = 0$ et en $q = \infty$, elle atteint son minimum avec une dérivée nulle en un point q_0 , $v_f'(q_0) = 0$. On adimensionne le problème, en exprimant les nombres d'onde q et q_0 en unités de $(2m|\mu|)^{1/2}/\hbar$ (c'est-à-dire k_{\min} si $\mu > 0$), les énergies ϵ_f^{eff} et Δ en unités de $|\mu|$ et les vitesses $v_f(q)$ et $v_{c,f}^L$ en unités de $[|\mu|/(2m)]^{1/2}$, ce qui conduit à la jolie équation implicite

$$\alpha = F_f(\check{q}_0) \text{ avec } F_f(\check{q}) = \frac{d}{d\check{q}} \left(-\frac{\check{\epsilon}_f^{\text{eff}}(\check{q})}{\check{q}} \right) \text{ et } \check{v}_{c,f}^L = \alpha \check{q}_0 + \frac{\check{\epsilon}_f^{\text{eff}}(\check{q}_0)}{\check{q}_0} \quad (16)$$

Ici, le symbole suscrit repère les variables sans dimension et α est donné par l'équation (6). Une discussion graphique de l'équation est facile à effectuer. Dans le cas le plus riche $\mu > 0$, les différentes branches de la fonction F_f , correspondant aux branches (12) de la fonction ϵ_f^{eff} , sont représentées sur la figure 1c; seules les lignes en trait plein sont à prendre en compte, puisqu'elles correspondent aux branches d'énergie minimale. On voit donc que, pour $\alpha > \check{\Delta}/2$, la vitesse critique est réalisée sur la branche (iv), avec $\check{q}_0 = (2\check{\Delta}/\alpha)^{1/2}$ et

$$\check{v}_{c,f}^L \underset{\text{branche(iv)}}{=} 2(2\check{\Delta}\alpha)^{1/2}, \quad (17)$$

4. Ceci résulte du fait que $k_1 + k_2$ pour (ii) et $k_2 - k_1$ pour (iii) sont des fonctions croissantes de k_1 . Les branches (ii) et (iii) se raccordent de façon lisse (C^∞) en $q = k_{\min}$, comme on peut le voir en introduisant la quantité algébrique $\bar{k}_1 \in]-k_{\min}, k_{\text{inflex}}]$ et l'extension correspondante $\phi(\bar{k}_1) = \epsilon_{f,\bar{k}_1} \bar{k}_1$ de $\epsilon_f(k_1)$ aux valeurs négatives. L'unique solution $k_2 > k_{\text{inflex}}$ de $\phi'(k_2) = \phi'(\bar{k}_1)$ permet alors un paramétrage lisse $q = \bar{k}_1 + k_2(\bar{k}_1)$ de l'ensemble (ii) plus (iii). En revanche, (i) et (ii) se raccordent de façon C^1 seulement en $q = 2k_{\text{inflex}}$.

Pour $\alpha < \check{\Delta}/2$, elle est réalisée sur la branche (i), et correspond à la plus grande des racines de l'équation polynômiale de degré quatre en \check{v}^2 , en principe exprimable par radicaux⁵ :

$$\check{v}^8 + 8(1 - \alpha^2)\check{v}^6 + \check{v}^4[\check{\Delta}^2(16\alpha^4 - 80\alpha^2 - 8) + 16\alpha^4 - 128\alpha^2 + 16] + \check{v}^2[32\check{\Delta}^2(4\alpha^2 - 1)(5\alpha^2 + 1) + 128\alpha^2(5\alpha^2 - 1)] - 16(4\alpha^2 - 1)[4\alpha^2(1 + \check{\Delta}^2) - \check{\Delta}^2]^2 = 0 \quad (18)$$

À la limite $\alpha \rightarrow 0$, on retrouve le premier terme du second membre de l'équation (5), qui provient effectivement de la branche d'excitation fermionique [11]. Il reste à caractériser la nature de la transition lorsque, par variation continue du rapport de masse α ou du gap réduit $\check{\Delta}$ (c'est-à-dire par variation des interactions dans le gaz de fermions), la vitesse critique $v_{c,f}^L$ passe de la branche (iv) à la branche (i). Comme on le voit bien par discussion graphique, \check{q}_0 est continu à la transition donc $\check{v}_{c,f}^L$ aussi. Or, en dérivant une fois la troisième équation de (16) par rapport à α par exemple, à $\check{\Delta}$ fixé, on trouve, compte tenu de la première équation de (16), que la dérivée première de $\check{v}_{c,f}^L$ est également continue :

$$\frac{d}{d\alpha} \check{v}_{c,f}^L = \check{q}_0 \quad (19)$$

C'est donc la dérivée seconde de $\check{v}_{c,f}^L$ qui doit être discontinue : en dérivant (19) et la première équation de (16) par rapport à α , ainsi que la fonction F sur les branches (iv) et (i), on obtient

$$\left[\frac{d^2}{d\alpha^2} \check{v}_{c,f}^L \left(\alpha = \frac{\check{\Delta}^+}{2} \right) \right]^{-1} - \left[\frac{d^2}{d\alpha^2} \check{v}_{c,f}^L \left(\alpha = \frac{\check{\Delta}^-}{2} \right) \right]^{-1} = \frac{1}{4} \check{\xi}_f'' (\check{k} = 1) \quad (20)$$

et la vitesse critique $\check{v}_{c,f}^L$ présente une transition du second ordre sur la ligne $\alpha = \check{\Delta}/2$, voir figure 2a. Dans le cas moins riche d'un potentiel chimique $\mu < 0$, $v_{c,f}^L$ est toujours réalisée sur la branche (i) et ne peut présenter aucune transition.

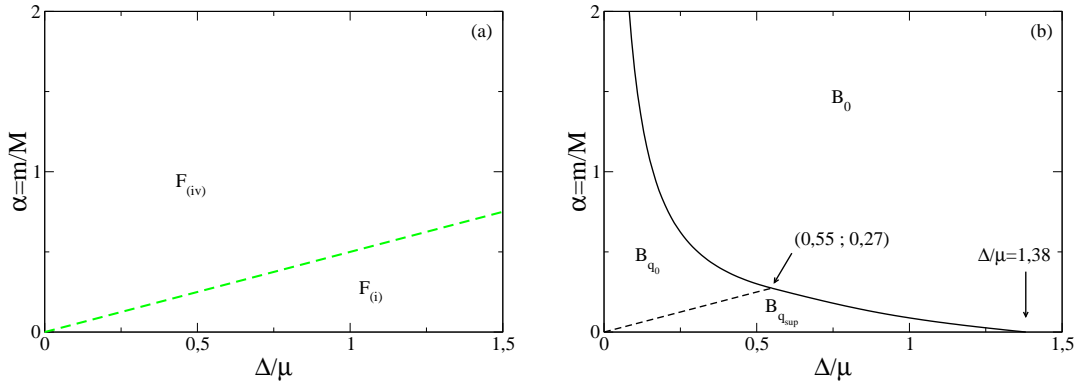


FIGURE 2: Diagramme dans le plan ($\check{\Delta} = \Delta/\mu$, $\alpha = m/M$), $\mu > 0$, indiquant (a) pour la branche d'excitation fermionique du superfluide, sur quelle branche de stationnarité de l'équation (12) la vitesse critique $v_{c,f}^L$ est réalisée (avec les notations limpides $F_{(i)}$ et $F_{(iv)}$), et (b) pour la branche d'excitation bosonique, si la vitesse critique $v_{c,b}^L$ est atteinte en la borne inférieure $q = 0$ (zone B_0), en la borne supérieure $q = q_{\text{sup}}$ (zone $B_{q_{\text{sup}}}$) ou à l'intérieur de son intervalle d'existence, $q = q_0 \in]0, q_{\text{sup}}[$ (zone B_{q_0}). Les lignes en trait plein (en tireté) signalent une transition du premier ordre (du second ordre) sur $v_{c,f}^L$ ou sur $v_{c,b}^L$, c'est-à-dire avec une dérivée première (seconde) discontinue.

3. Vitesse critique sur la branche bosonique

La conservation du nombre de fermions n'empêche bien entendu pas l'impureté, en se déplaçant dans le superfluide, d'y créer un seul quantum sur sa branche d'excitation bosonique, puisqu'il s'agit d'une mise en mouvement

5. Après regroupement astucieux de termes et élévations au carré dans les deux équations extrêmes de (16), on est ramené à deux équations polynômiales sur \check{q}_0 . \check{v} doit en annuler le résultant, dont le polynôme en \check{v} de l'équation (18) est un diviseur.

$1/(k_F a)$	Δ/μ	\mathcal{D}	forme de $\epsilon_b(q)$
$> 0, 161$	$> 1, 729$ ou < 0	$[0, +\infty[$	convexe
$\in [0; 0, 161]$	$\in [1, 162; 1, 729]$	$[0, q_{\text{sup}}] \cup [q_{\text{inf}}, +\infty[$	convexe si $\Delta/\mu > 1, 71$
< 0	$< 1, 162$	$[0, q_{\text{sup}}]$	concave si $\Delta/\mu < 0, 88$

TABLE 1: Domaine d'existence \mathcal{D} de la branche d'excitation bosonique du superfluide, d'après la RPA de la référence [11], et (de notre cru) convexité de la relation de dispersion $q \mapsto \epsilon_b(q)$. La perte de convexité (de concavité) est due à l'apparition d'une partie concave (convexe) aux grands (faibles) vecteurs d'onde q . Sur la composante $[q_{\text{inf}}, +\infty[$ lorsqu'elle existe, il y a toujours convexité. En $q = q_{\text{sup}}$ et $q = q_{\text{inf}}$, la branche bosonique rejoint le continuum à deux excitations fermioniques au vecteur d'onde total considéré, c'est-à-dire que $\epsilon_b(q) = \epsilon_f^{\text{eff}}(q)$. Un résultat important de la référence [11] est qu'on a toujours $q_{\text{sup}} > 2k_{\text{min}}$ défini dans l'équation (14). Le paramètre $1/(k_F a)$ plus habituellement utilisé que Δ/μ pour mesurer la force des interactions, voir le texte, est déduit ici de l'équation d'état de BCS [11]. $1/(k_F a) = 0$ est la limite unitaire, atteinte en $\Delta/\mu = 1, 162 \dots$, et $\mu < 0$ si et seulement si $1/(k_F a) > 0, 553 \dots$. On notera le paradoxe de notation $q_{\text{sup}} < q_{\text{inf}}$.

collective, de type onde sonore, des paires de Cooper atomiques. La vitesse critique associée à la branche bosonique est donc donnée comme dans l'équation (4) par

$$v_{c,b}^L = \inf_{q \in \mathcal{D}} v_{b,q} \quad \text{avec} \quad v_{b,q} = \frac{\hbar^2 q^2}{2M} + \epsilon_{b,q} / \hbar q \quad (21)$$

La relation de dispersion des quasi-particules bosoniques $\mathbf{q} \mapsto \epsilon_{b,q} = \epsilon_b(q)$ est cependant plus difficile à cerner que celle des quasi-particules fermioniques. Son domaine d'existence \mathcal{D} dans l'espace des vecteurs d'onde, sur lequel il faut minimiser $v_{b,q}$ dans l'équation (21), est lui-même à déterminer. Comme l'a montré la référence [11], il n'est pas nécessairement compact ni connexe. On sait seulement de manière générale, grâce à l'hydrodynamique des superfluides, que la branche atteint la limite des faibles nombres d'onde $q \rightarrow 0$ de manière linéaire en q ,

$$\epsilon_b(q) \underset{q \rightarrow 0}{\sim} \hbar c q, \quad (22)$$

le coefficient c n'étant autre que la vitesse du son dans le superfluide de fermions, déductible de l'équation d'état par l'expression bien connue $mc^2 = \rho \frac{d\mu}{d\rho}$. On sait aussi que $\epsilon_b(q)$ doit être inférieur au bord $\epsilon_f^{\text{eff}}(q)$ du continuum à deux excitations fermioniques au vecteur d'onde total \mathbf{q} considéré. Sinon, le mouvement collectif des paires peut s'amortir et son énergie, définie comme un pôle du facteur de structure dynamique, devient complexe [15].

On peut obtenir numériquement $\epsilon_b(q)$ à un ordre d'approximation compatible avec la théorie de BCS utilisée en section 2 grâce à la RPA [16], mise en œuvre de façon très fouillée dans la référence [11], non seulement dans le régime d'interaction faible [15] mais pour des interactions arbitrairement fortes au sein du superfluide.⁶ Les résultats correspondants sur le domaine d'existence sont résumés dans la table 1 ; y est introduit, en sus de Δ/μ , l'habituel paramétrage des interactions par $1/(k_F a)$, où a est la longueur de diffusion dans l'onde s entre deux fermions de spins opposés et $k_F = (3\pi^2 \rho)^{1/3}$ est le nombre d'onde de Fermi du gaz parfait non polarisé de spin 1/2 de même densité totale ρ que le superfluide. Il reste à minimiser la fonction $v_b(q)$ sur le domaine d'existence \mathcal{D} , en distinguant les différentes formes.

Lorsque la branche bosonique existe à tout nombre d'onde, par exemple pour $\mu < 0$, il se trouve que la relation de dispersion $q \mapsto \epsilon_b(q)$ est convexe donc toujours au-dessus de sa tangente en l'origine. Alors $\epsilon_b(q) \geq \hbar c q$ pour tout q , le minimum absolu de $v_b(q)$ est atteint en $q = 0$ et $v_{c,b} = c$. Dans la suite de la discussion, on peut donc se restreindre au cas $\mu > 0$.

La minimisation de $v_b(q)$ sur la seconde composante connexe de \mathcal{D} , à savoir $[q_{\text{inf}}, +\infty[$, lorsqu'elle existe, est également assez simple. On trouve que l'énergie $\epsilon_b(q)$ y est « collée au plafond », c'est-à-dire partout extrêmement proche de $\epsilon_f^{\text{eff}}(q)$; comme q_{inf} est toujours supérieur au point d'annulation de $F_f(q)$ [voir figure 1], les trois fonctions $q \mapsto \epsilon_f^{\text{eff}}(q)/q$, $q \mapsto \epsilon_b(q)/q$ et $q \mapsto v_b(q)$ sont croissantes pour $q \geq q_{\text{inf}}$. On vérifie alors numériquement que le minimum $v_b(q_{\text{inf}})$ de $v_b(q)$ sur cette seconde composante connexe est toujours supérieur à la vitesse du son donc non pertinent.

6. En pratique, nous résolvons par dichotomie une équation sur $\omega = \epsilon_b(q)/\hbar$ de la forme $\chi(\omega, q) = 1$, où $\chi = I_{11} I_{22} / (\omega^2 I_{12}^2)$ est une fonction décroissante de ω à q fixé. Les intégrales doubles I_{12} , I_{11} et I_{22} sont celles (15), (16) et (17) de la référence [11].

Il reste à minimiser $v_b(q)$ sur l'intervalle d'existence $[0, q_{\text{sup}}]$, ce qui peut conduire en général à trois cas de figure : le minimum absolu est (a) en $q = 0$, (b) en $q = q_{\text{sup}}$ ou (c) en un point q_0 strictement à l'intérieur de l'intervalle. Il faut d'abord étudier les minima locaux de $v_b(q)$ suivant ces trois cas, puis les comparer.

Les minima locaux : Pour progresser, nous introduisons les mêmes adimensionnement, fonction auxiliaire $F(q)$ et discussion graphique que pour la branche fermionique :

$$\check{v}_b(\check{q}) = \alpha\check{q} + \frac{\check{\epsilon}_b(\check{q})}{\check{q}} \text{ et } F_b(\check{q}) = \frac{d}{d\check{q}} \left(-\frac{\check{\epsilon}_b(\check{q})}{\check{q}} \right), \text{ si bien que } \frac{d}{d\check{q}} \check{v}_b(\check{q}) = \alpha - F_b(\check{q}) \quad (23)$$

On constate d'abord que $F_b(0) = 0$ donc que $v_b(q)$ a toujours un minimum en $q = 0$, car la première correction au terme linéaire dans l'équation (22) est cubique, le développement de Taylor de $[\epsilon_b(q)]^2$ ne contenant, d'après la RPA, que des puissances paires de q . Ensuite, la fonction $v_b(q)$ admet un minimum en $q = q_{\text{sup}}$ à la simple condition que $\alpha > F_b(\check{q}_{\text{sup}})$. Finalement, $v_b(q)$ admet un minimum local en $q_0 \in]0, q_{\text{sup}}[$ si sa dérivée première s'annule en q_0 et si sa dérivée seconde y est positive. Graphiquement, ceci signifie que la courbe $\check{q} \mapsto F_b(\check{q})$ croise la droite horizontale d'ordonnée α en un point à l'intérieur de l'intervalle et avec une dérivée négative, c'est-à-dire *de haut en bas*. Pour que ce soit possible pour une certaine valeur de α , il faut et il suffit que la fonction $F_b(q)$ présente un maximum sur $]0, q_{\text{sup}}[$ à valeur strictement positive, comme sur la figure 3.

Le minimum global $v_{c,b}$: Les valeurs $v_b(0) = c$ et $v_b(q_{\text{sup}})$ peuvent être comparées directement, après calcul numérique de c et q_{sup} , puisque ϵ_b et ϵ_f^{eff} (connu analytiquement) coïncident en q_{sup} . Lorsqu'il existe, le minimum local de $v_b(q)$ en $q_0 \in]0, q_{\text{sup}}[$ est en pratique inférieur à $v_b(q_{\text{sup}})$, puisque $F_b(q)$ reste sous la droite d'ordonnée α sur l'intervalle $[q_0, q_{\text{sup}}]$ donc $v_b(q)$ y est croissante. Il est aussi facilement comparable à la vitesse du son : par intégration de la troisième équation de (23), on trouve que

$$\check{v}_b(\check{q}_0) - \check{c} = \int_0^{\check{q}_0} d\check{q} [\alpha - F_b(\check{q})] = A_+ - A_- \quad (24)$$

où A_+ et A_- sont les aires (comptées positivement) des zones hachurées sur la figure 3.

Le résultat final est indiqué sur la figure 2b. La ligne de séparation entre les zones où $v_{c,b} = v_b(q_{\text{sup}})$ et $v_{c,b} = v_b(q_0)$ correspond au cas limite $q_0 \rightarrow q_{\text{sup}}$, c'est-à-dire à l'équation $\alpha = F_b(\check{q}_{\text{sup}})$; elle conduit donc, comme dans le cas de $v_{c,f}$ [voir (19)], à une transition du second ordre pour $v_{c,b}$, autrement dit à une discontinuité de la dérivée seconde dans la direction normale à la ligne. Les autres lignes de séparation conduisent à des transitions du premier ordre sur $v_{c,b}$, puisque la position du minimum de $v_b(q)$ saute de 0 à $q_0 > 0$ ou à q_{sup} . Leurs équations respectives sont $A_+ = A_-$ dans l'équation (24), et $v_b(q_{\text{sup}}) = c$. On notera l'existence d'un point triple à la confluence des trois zones.

4. Synthèse : vitesse critique globale de la particule

La vitesse critique globale de Landau pour la particule en mouvement dans le superfluide est donnée par la plus petite des deux vitesses $v_{c,f}^L$ et $v_{c,b}^L$ des sections précédentes. Pour $\mu < 0$, on a toujours $v_{c,b}^L = c < v_{c,f}^L$, si bien que $v_{c,b}^L$, identiquement égale à la vitesse du son, est d'origine bosonique. Pour $\mu > 0$, le diagramme dans le plan $(\Delta/\mu, \alpha = m/M)$ de la figure 4a montre que la vitesse critique est d'origine fermionique ($v_{c,f}^L < v_{c,b}^L$) dans une sorte de triangle à un côté incurvé et dont la base repose sur l'axe $\alpha = 0$ où l'impureté est de masse infinie ; son extension maximale sur cet axe correspond bien au point de croisement $\Delta/\mu \approx 1,38$ des deux termes au second membre de (5). Elle est partout ailleurs d'origine bosonique.

Il reste à voir dans quelle mesure la ou les lignes de transition de phase prédites sur $v_{c,f}^L$ et $v_{c,b}^L$, voir la figure 2, subsistent sur la vitesse critique globale v_c^L , ou sont au contraire masquées parce que la vitesse critique issue de la branche d'excitation concurrente est plus faible. Nous avons représenté la ligne de transition de $v_{c,f}^L$ [entre les branches de stationnarité (i) et (iv)], $\alpha = \check{\Delta}/2$, par un tireté vert sur la figure 4a. La portion correspondant à $\check{\Delta} > 0,55$ est entièrement masquée par la vitesse critique bosonique et est donc omise ; mais, de façon remarquable et peut-être inattendue, la portion correspondant à $\check{\Delta} < 0,55$ est indiscernable, à la résolution de la figure, de la frontière entre le domaine bosonique et le domaine fermionique ! De même, nous avons représenté les lignes de transition de $v_{c,b}^L$ [suivant que $v_b(q)$ soit minimale en $q = 0$, $q = q_{\text{sup}}$ ou strictement entre ces deux valeurs] par un trait noir, plein ou tireté selon que la transition est du premier ou du second ordre. Deux autres faits remarquables apparaissent. D'une

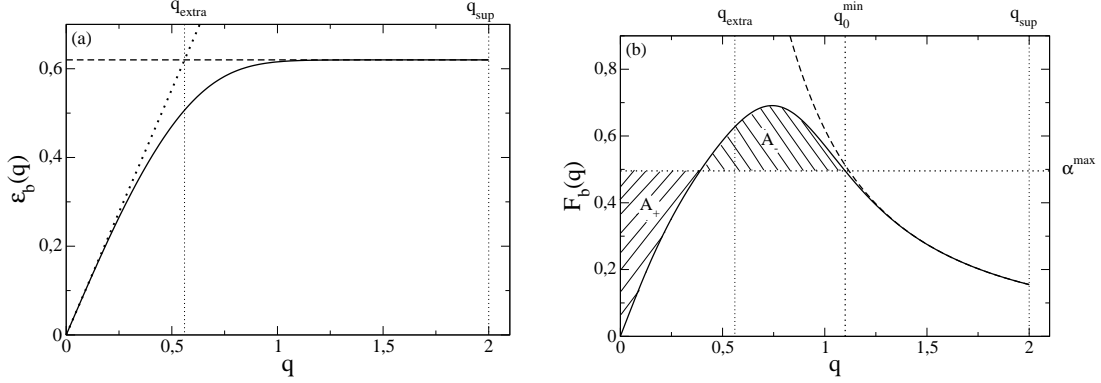


FIGURE 3: Pour la valeur $\Delta/\mu = 0,31$ choisie à titre d'exemple : (a) relation de dispersion adimensionnée $\check{\epsilon}_b(\check{q})$ de la branche bosonique (trait plein), de départ phononique (gros pointillé) mais plafonnée par le bord du continuum à deux excitations fermioniques $\check{\epsilon}_f^{\text{eff}}(\check{q})$ au vecteur d'onde total considéré (tireté), et (b) fonction $F_b(\check{q})$ auxiliaire de discussion graphique pour la minimisation de $v_b(q)$. Ici, la branche bosonique existe seulement sur l'intervalle compact $[0, q_{\text{sup}}]$ et $v_b(q)$ admet un minimum local en q_0 à l'intérieur de l'intervalle ssi le rapport de masse α est compris entre les valeurs $F_b(q_{\text{sup}})$ et $\sup_{\check{q}} F_b(\check{q})$. Le tireté en (b) correspond à l'approximation $F_b(\check{q}) \approx F_f^{(iv)}(\check{q}) = 2\check{\Delta}/\check{q}^2$; elle est légitime assez près de $q = q_{\text{sup}}$ et lorsque $\check{\Delta}$ est assez faible. C'est bien le cas ici, même pour la valeur minimale de \check{q}_0 (c'est-à-dire la valeur maximale de α) accessible dans la zone B_{q_0} à $\check{\Delta}$ fixé, donc telle que $A_+ = A_-$ dans l'équation (24).

part, le tireté noir est en pratique indiscernable du tireté vert, et se trouve donc lui aussi à la frontière entre les domaines bosonique et fermionique. D'autre part, la portion de trait plein de $\check{\Delta} > 0,55$ semble coïncider parfaitement avec la frontière entre les domaines bosonique et fermionique. Finalement, la portion de trait plein aux abscisses $\check{\Delta} < 0,55$ est immergée dans le domaine bosonique, et le partage en deux sous-domaines B_1 et B_2 séparés par une transition de phase du premier ordre sur $v_{c,b}^L$. Nous allons maintenant énoncer quelques faits simples permettant de comprendre une partie de ces constatations.

Des zones d'origine prévisible : Le domaine $B_{q_{\text{sup}}}$ où $v_{c,b}^L = v_b(q_{\text{sup}})$ conduit nécessairement à $v_{c,b}^L \geq v_{c,f}^L$ donc est, dans le diagramme final sur $v_{c,b}^L$, entièrement masqué par la vitesse critique issue de la branche d'excitation fermionique. En effet, en $q = q_{\text{sup}}$, la branche d'excitation bosonique rejoint le « plafond » $\epsilon_f^{\text{eff}}(q)$ à deux excitations fermioniques, donc $v_b(q_{\text{sup}}) = v_f(q_{\text{sup}}) \geq \inf_q v_f(q) = v_{c,f}^L$. On en déduit que la frontière entre B_1 et F est *au-dessus* de la ligne de transition entre les zones B_{q_0} [où $v_{c,b}^L = v_b(q_0)$] et $B_{q_{\text{sup}}}$ [où $v_{c,b}^L = v_b(q_{\text{sup}})$], c'est-à-dire au-dessus du tireté noir sur la figure 4a.

De façon symétrique, le domaine $F_{(iv)}$ de $v_{c,f}^L$ correspondant à la branche de stationnarité (iv), c'est-à-dire à $\alpha > \check{\Delta}/2$, ne peut qu'être entièrement masqué par la contribution de la branche d'excitation bosonique. En effet, sur la branche (iv), le minimum de $v_f(q)$ est atteint sur l'intervalle $q \in [0, 2k_{\text{min}}]$. Or, sur cet intervalle, la branche d'excitation bosonique existe bien, puisque $q_{\text{sup}} > 2k_{\text{min}}$ comme l'a montré la référence [11], et y conduit à une vitesse $v_b(q)$ en tout point inférieure à la vitesse $v_f(q)$, puisque on a toujours $\epsilon_b(q) \leq \epsilon_f^{\text{eff}}(q)$. Alors, $v_{c,b}^L$ est inéluctablement inférieure à $v_{c,f}^{(iv)} = \inf_{q \in [0, 2k_{\text{min}}]} v_f(q)$, et la frontière entre B_1 et F est *en dessous* de la ligne de transition entre les zones $F_{(iv)}$ et $F_{(i)}$ sur $v_{c,f}^L$, c'est-à-dire en dessous du tireté vert sur la figure 4a.

Pour résumer, la frontière entre B_1 et F doit passer entre le plafond tireté vert, d'équation $\alpha = F_f(2) = \check{\Delta}/2$, et le plancher tireté noir, d'équation $\alpha = \lim_{\check{q}_0 \rightarrow \check{q}_{\text{sup}}} F_b(\check{q}_0) = F_b(\check{q}_{\text{sup}})$. Or, comme le montre le calcul numérique, la quantité $F_b(\check{q}_{\text{sup}})$, considérée comme une fonction de $\check{\Delta}$, est extrêmement proche de $\check{\Delta}/2$ jusqu'à $\check{\Delta} \approx 0,6$, valeur au-delà de laquelle son graphe commence à s'incurver vers le bas. Ainsi, pour $\check{\Delta} < 0,55$, l'écart est inférieur à quatre pour mille, et q_{sup} y diffère d'ailleurs de $2k_{\text{min}}$ de moins d'un pour mille. Aussi la frontière entre B_1 et F , le tireté vert et le tireté noir sont-ils en pratique confondus sur la figure 4a, et l'on a la coïncidence remarquable de deux zones du plan $(\check{\Delta}, \alpha)$:

$$B_{q_0} \simeq B_1 \quad (25)$$

Explication de cette coïncidence à la frontière $B_1 - F$: Aux faibles valeurs de Δ/μ , on peut comprendre physiquement

pourquoi les tiretés vert et noir sont presque confondus : le départ linéaire de $\epsilon_b(q)$ aux faibles q , si on l'extrapole linéairement, atteint le plafond à deux excitations fermioniques $\epsilon_f^{\text{eff}}(q) \simeq 2\Delta$ en un point $q_{\text{extra}} \approx 2\Delta/(\hbar c) \ll 2k_{\text{min}}$ puisque $c \simeq (2\mu/3m)^{1/2}$ dans cette limite. En réalité, la branche d'excitation bosonique s'infléchit autour de $q = q_{\text{extra}}$ puis longe le plafond de très près jusqu'à l'atteindre en le point q_{sup} , qui est ici extrêmement proche de $2k_{\text{min}}$. On peut donc s'attendre à pouvoir identifier $\epsilon_b(q)$ et $\epsilon_f^{\text{eff}}(q)$, donc les fonctions $F_f(\check{q})$ et $F_b(\check{q})$, sur un voisinage assez étendu de q_{sup} ou de \check{q}_{sup} , la fonction $F_f(\check{q})$ étant assimilable à son expression $\frac{d}{d\check{q}}(-2\check{\Delta}/\check{q}) = 2\check{\Delta}/\check{q}^2$ sur la branche de stationnarité (iv), voir les équations (15) et (16) : en un mot,

$$F_b(\check{q}) \simeq \frac{2\check{\Delta}}{\check{q}^2} \text{ pour } \check{\Delta} \ll \check{q} \text{ et } \check{\Delta} \ll 1 \quad (26)$$

Ces idées sont illustrées avec succès sur la figure 3. Ceci explique donc pourquoi $F_b(\check{q}_{\text{sup}}) \simeq \check{\Delta}/2$ aux faibles $\check{\Delta}$. Ce qui est remarquable cependant est que, de ce point de vue, la valeur $\check{\Delta} = 0,55$ reste faible.

Quasi-coïncidence de $v_{c,f}^L$ et $v_{c,b}^L$ sur la zone B_1 : On peut se demander si l'approximation précédente (26) reste bonne non seulement en $\check{q} = \check{q}_{\text{sup}}$ mais aussi, dans la zone B_{q_0} de la figure 2b, en la position q_0 du minimum absolu de $v_b(q)$. À $\check{\Delta}$ fixé, il suffit de le vérifier pour la valeur minimale accessible q_0^{min} de q_0 , correspondant à la valeur maximale de α atteinte dans cette zone et telle que $A_+ = A_-$ dans l'équation (24). On trouve par le calcul numérique que c'est bien le cas, \check{q}_0^{min} restant en définitive suffisamment loin à droite de la position du maximum de $F_b(\check{q})$, maximum bien sûr non décrit par (26). On en déduit le résultat remarquable que, dans la zone B_{q_0} , donc en pratique dans la zone B_1 :

$$\forall(\check{\Delta}, \alpha) \in B_1, v_c^L = v_{c,b}^L \simeq v_{c,f}^L \quad (27)$$

où l'on peut utiliser l'équation (17) pour évaluer $v_{c,f}^L$.

La ligne $v_{c,f}^L = c$ est remarquable : Une fois établie la nature bosonico-fermionique de la zone B_1 , c'est-à-dire la validité de l'approximation (27), il est simple d'évaluer la position de la frontière entre les zones B_1 et B_2 par résolution de l'équation

$$v_{c,f}^L = c \quad (28)$$

Le gros pointillé noir correspondant, sur la figure 4a, tombe bien (presque) sur le trait plein noir pour $\check{\Delta} < 0,55$. Mieux encore, dans la partie à $\check{\Delta} > 0,55$ où $v_{c,f}^L$ provient maintenant de la branche de stationnarité (i), il reproduit *exactement* la frontière entre les zones B_2 et F . En effet, on a ici $\alpha < \check{\Delta}/2$, donc $v_{c,f}^L$ provient de la branche de stationnarité (i) ; or $v_b(q_{\text{sup}}) = v_f(q_{\text{sup}}) \geq v_{c,f}^L$ comme nous l'avons vu, donc la zone $B_{q_{\text{sup}}}$ est hors-jeu, et la transition $F - B_2$ est nécessairement une transition $F - B_0$.

Une quasi-coïncidence à la frontière $B_2 - F$: En définitive, il nous reste à expliquer la quasi-coïncidence des frontières $F - B_2$ et $B_{q_{\text{sup}}} - B_0$. Cette quasi-coïncidence est cependant plus approximative que les autres, et probablement plus accidentelle. Il se trouve qu'au point de la frontière $F - B_2$ d'abscisse $\check{\Delta} = 0,55$, q_{sup} est très proche de la position $q = 2k_{\text{min}}$ du minimum de $v_f(q)$; de même, au point terminal de cette frontière d'abscisse $\check{\Delta} \simeq 1,38$, $\check{q}_{\text{sup}} \simeq 2,59$ est, ce que nous n'expliquons pas, très proche de la position $\check{q} \simeq 2,61$ du minimum de $v_f(q)$. Aussi les frontières $F - B_2$ et $B_{q_{\text{sup}}} - B_0$ se touchent-elles (presque) en leurs extrémités. Dans leur région intermédiaire cependant, $0,55 < \check{\Delta} < 1,38$, leur écart devient perceptible sur la figure 4a ; le calcul numérique confirme que q_{sup} peut y dévier significativement de la position du minimum de $v_f(q)$, d'au moins 5%, mais ceci conduit somme toute à un faible écart entre $v_b(q_{\text{sup}}) = v_f(q_{\text{sup}})$ et $\inf_q v_f(q)$ puisque $v_f(q)$ varie seulement au second ordre autour de son minimum.

5. Vitesse critique relative d'un superfluide de bosons et d'un superfluide de fermions

Il est fort probable qu'une vérification expérimentale de la vitesse critique de Landau ici prédite aura lieu pour un grand nombre d'impuretés, plutôt qu'une seule. Comme il est souhaitable d'envoyer dans le superfluide de fermions un ensemble monocinétique d'impuretés, on est naturellement conduit à utiliser un condensat de Bose-Einstein de telles impuretés, avec des interactions en général non négligeables, comme c'est le cas dans la référence [14].

Il faut donc généraliser le raisonnement à la Landau au cas d'un superfluide de bosons en mouvement à la vitesse v dans le superfluide de fermions. Le superfluide de bosons est initialement à température nulle dans le référentiel de

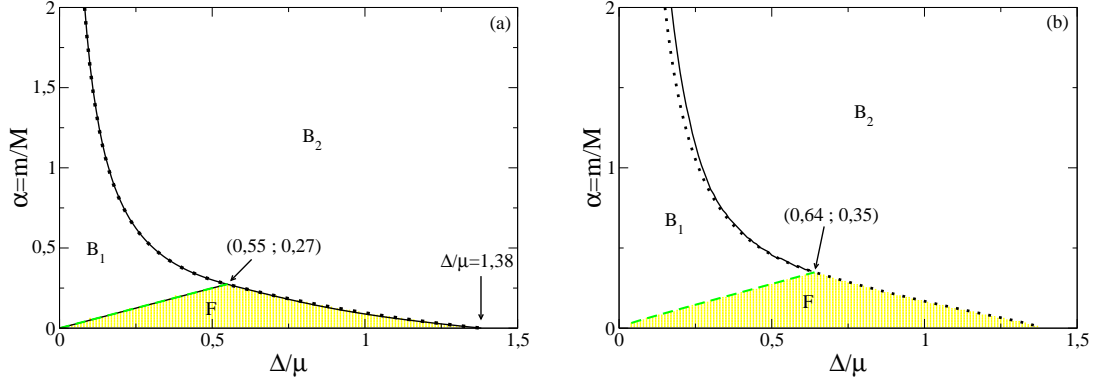


FIGURE 4: (a) Diagramme dans le plan $(\check{\Delta} = \Delta/\mu, \alpha = m/M)$, $\mu > 0$, indiquant dans quelle zone la vitesse critique globale v_c^L de l'impureté de masse M a une origine bosonique (cas $v_{c,b}^L < v_{c,f}^L$, repéré par la lettre B et un fond uni blanc) ou une origine fermionique (cas $v_{c,f}^L < v_{c,b}^L$, repéré par la lettre F et un fond à rayures jaunes). Le domaine bosonique est séparé en deux sous-domaines B_1 et B_2 par la ligne de transition du premier ordre entre les zones B_0 et B_{q_0} [trait plein noir aux abscisses $\check{\Delta} < 0,55$] de la figure 2b. De façon inattendue, la frontière entre B_2 et F semble coïncider en pratique avec la ligne de transition du premier ordre entre les zones $B_{q_{sup}}$ et B_0 [trait plein noir aux abscisses $\check{\Delta} > 0,55$] de la figure 2b. Autre fait remarquable, la partie non masquée de la ligne de transition du second ordre sur $v_{c,f}^L$ [tireté vert] et la ligne de transition du second ordre entre les zones B_{q_0} et $B_{q_{sup}}$ [tireté noir] sont en pratique indiscernables et situées précisément à la frontière entre B_1 et F . Dernier point notable, la ligne $v_{c,f}^L = c$ [gros pointillé noir] reproduit non seulement la frontière entre B_2 et F , comme il se doit, mais aussi fort bien celle entre B_2 et B_1 . (b) Généralisation du diagramme précédent au cas d'un superfluide d'impuretés bosoniques en mouvement dans le superfluide de fermions, à rapport fixée $\mu_B/E_F = 0,1$ entre le potentiel chimique des bosons dans le référentiel de leur centre de masse et l'énergie de Fermi. La nouvelle vitesse critique v_c^L présente elle aussi une partition en trois zones, séparées par une discontinuité de sa différentielle seconde (frontière $F - B_1$) ou première (frontières $F - B_2$ et $B_1 - B_2$) : la zone F (à rayures jaunes), où $v_c^L = v_{c,f}^L$, et les zones B_1 et B_2 , où $v_c^L = v_{c,b}^L$. La frontière $F - B_1$ est très proche de la frontière $F_{(i)} - F_{(iv)}$ à la valeur de μ_B considérée [tireté vert, interrompu lorsqu'il atteint la zone B_2]. La frontière $F - B_2$ est bien donnée, comme il se doit, par le gros pointillé $v_{c,f} = c + c_B$, où c (c_B) est la vitesse du son dans le superfluide de fermions (bosons), à droite du point triple. La frontière $B_1 - B_2$, qui est simplement la frontière $B_{q_0} - B_0$ à la valeur de μ_B considérée [trait plein noir], dévie au contraire du pointillé lorsqu'on s'éloigne du point triple sur sa gauche.

son centre de masse. L'interaction bosons-fermions crée au minimum une excitation élémentaire dans le superfluide de bosons, de quantité de mouvement $\hbar\mathbf{q}$ et d'énergie $\epsilon_{B,\mathbf{q}} - \hbar\mathbf{q} \cdot \mathbf{v}$, $\mathbf{q} \mapsto \epsilon_{B,\mathbf{q}} = \epsilon_B(q)$ étant la relation de dispersion pour un superfluide au repos⁷. De manière concomitante, une paire d'excitations fermioniques de vecteurs d'onde \mathbf{k}_1 et \mathbf{k}_2 et d'énergie $\epsilon_{f,\mathbf{k}_1} + \epsilon_{f,\mathbf{k}_2}$, avec $\mathbf{q} = -(\mathbf{k}_1 + \mathbf{k}_2)$, ou une excitation bosonique de vecteur d'onde $-\mathbf{q}$ et d'énergie $\epsilon_{b,-\mathbf{q}}$, apparaît dans le superfluide. Ce processus minimal d'excitation ne peut cependant conserver l'énergie si la vitesse relative v des deux superfluides est inférieure aux vitesses critiques de Landau

$$v_{c,f}^L = \inf_{\mathbf{q}} v_f(q) \quad \text{avec} \quad v_f(q) = \frac{\epsilon_B(q) + \epsilon_f^{\text{eff}}(q)}{\hbar q} \quad (29)$$

$$v_{c,b}^L = \inf_{\mathbf{q}} v_b(q) \quad \text{avec} \quad v_b(q) = \frac{\epsilon_B(q) + \epsilon_b(q)}{\hbar q}, \quad (30)$$

c'est-à-dire à v_c^L , la plus petite des deux vitesses. Dans la suite, nous utiliserons la forme de Bogoliubov

$$\epsilon_B(q) = \left[\frac{\hbar^2 q^2}{2M} \left(\frac{\hbar^2 q^2}{2M} + 2\mu_B \right) \right]^{1/2} \quad (31)$$

où μ_B est le potentiel chimique (positif) du superfluide de bosons au repos et M la masse d'un boson. Les expressions précédentes (8) et (21) correspondent comme il se doit au cas limite $\mu_B \rightarrow 0$.

7. Ceci découle des propriétés suivantes de la transformation unitaire $T_i(\mathbf{v})$ représentant le changement de référentiel galiléen à la vitesse \mathbf{v} , $T_i(\mathbf{v}) = \exp[-i \sum_j \mathbf{v} \cdot \mathbf{p}_j / \hbar] \exp[i \sum_j m_B \mathbf{v} \cdot \mathbf{r}_j / \hbar]$, la somme portant sur les N_B bosons, de masse $m_B = M$ et d'opérateurs position \mathbf{r}_j et impulsion \mathbf{p}_j : $T_i^\dagger(\mathbf{v}) H_B T_i(\mathbf{v}) = H_B + \mathbf{v} \cdot \mathbf{P}_B + N_B m_B v^2 / 2$ et $T_i^\dagger(\mathbf{v}) \mathbf{P}_B T_i(\mathbf{v}) = \mathbf{P} + N_B m_B \mathbf{v}$, où H_B est le Hamiltonien des bosons et \mathbf{P}_B leur opérateur quantité de mouvement totale. Il reste alors à comparer les énergies et impulsions de $T_i(\mathbf{v})|\Psi_0\rangle$ et $T_i(\mathbf{v})|\Psi_1^{\mathbf{k}}\rangle$, où les vecteurs d'état $|\Psi_0\rangle$ et $|\Psi_1^{\mathbf{k}}\rangle$ sont ceux du superfluide au repos dans son état fondamental ou en présence d'une excitation élémentaire de vecteur d'onde \mathbf{k} .

L'étude de la vitesse critique $v_{c,f}^L$ issue de la branche fermionique peut se faire analytiquement, après adimensionnement comme dans l'équation (16) et en introduisant la largeur \check{Q}_B de $\check{\epsilon}_B(\check{q})/\check{q}$, donnée par

$$\check{Q}_B^2 = \frac{2M}{m} \frac{\mu_B}{|\mu|} = \frac{2\check{\mu}_B}{\alpha} \quad (32)$$

On cherche d'abord les minima locaux, de dérivée nulle :

$$\check{v}_f(\check{q}) = \alpha(\check{q}^2 + \check{Q}_B^2)^{1/2} + \frac{\check{\epsilon}_f^{\text{eff}}(\check{q})}{\check{q}}, \quad \text{si bien que} \quad \frac{d}{d\check{q}}\check{v}_f(\check{q}) = \frac{\alpha\check{q}}{(\check{q}^2 + \check{Q}_B^2)^{1/2}} - F_f(\check{q}) \quad (33)$$

expression dont la racine se trouve sur la branche de stationnarité (iv) [plutôt que sur la branche (i)] ssi la fonction croissante $\check{q} \mapsto \alpha\check{q}/(\check{q}^2 + \check{Q}_B^2)^{1/2}$ atteint la valeur $\check{\Delta}/2$ sur $\check{q} \in [0, 2]$ donc ssi

$$\frac{2\alpha}{(4 + \check{Q}_B^2)^{1/2}} \geq \frac{\check{\Delta}}{2}, \quad (34)$$

comme le montre une discussion graphique à l'aide de la figure 1. Le plan $(\check{\Delta}, \alpha)$ est donc séparé à nouveau en deux domaines $F_{(i)}$ et $F_{(iv)}$, à la frontière desquels $\check{v}_{c,f}$ présente une transition du second ordre.

L'étude de la vitesse critique $v_{c,b}^L$ issue de la branche bosonique est faite numériquement. On trouve, comme dans le cas à une impureté, une partition du plan $(\check{\Delta}, \alpha)$ en trois domaines, suivant que le minimum absolu de $v_b(q)$ est atteint au bord inférieur, au bord supérieur ou à l'intérieur de l'intervalle d'existence $[0, q_{\text{sup}}]$ de la branche bosonique en question. Les frontières diffèrent peu de celles à une impureté seule, puisqu'on a pris ici un potentiel chimique des bosons petit devant l'énergie de Fermi. On notera le résultat simple mais important que $v_{c,b} = c + c_B$ dans toute la zone B_0 , c et c_B étant les vitesses du son dans les superfluides fermionique et bosonique.

Le diagramme de phase de la vitesse critique globale v_c^L est présenté sur la figure 4b et est décrit en détail dans la légende. Les résultats et leur discussion sont d'ailleurs proches du cas à une impureté, voir la section précédente, aussi nous contentons-nous de signaler ici une différence notable : le pointillé d'équation $v_{c,f} = c + c_B$ ne donne plus une bonne approximation de la frontière $B_1 - B_2$, sauf près du point triple.

6. Conclusion

Nous avons étendu le calcul de la vitesse critique de Landau dans un superfluide de fermions non polarisé au cas où l'objet en mouvement est (a) une impureté de masse *finie* M , puis (b) un superfluide bosonique de telles impuretés, avec prise en compte des excitations du superfluide de fermions à la BCS par brisure des paires (branche d'excitation fermionique) et à la RPA par leur mise en mouvement (branche d'excitation bosonique) comme dans la référence [11].

Lorsque le potentiel chimique des fermions est négatif, $\mu < 0$, nous trouvons que la vitesse critique est déterminée par la partie phononique de la branche bosonique et vaut donc simplement (a) la vitesse du son c dans le superfluide de fermions, puis (b) la somme $c + c_B$, où c_B est la vitesse du son dans le superfluide de bosons.

Lorsque le potentiel chimique des fermions est positif, $\mu > 0$, ces résultats ne valent que dans une certaine zone B_2 du plan $(\Delta/\mu, m/M)$, où Δ et m sont le gap et la masse d'une particule du superfluide de fermions. Pour (a) aussi bien que pour (b), au moins dans le régime d'un potentiel chimique μ_B petit devant l'énergie de Fermi, il existe alors deux autres zones, une zone B_1 où la vitesse critique est déterminée par la partie intermédiaire, non phononique, de la branche bosonique et une zone F où la vitesse critique vaut celle $v_{c,f}^L$ associée à la branche fermionique. La vitesse critique a une différentielle seconde discontinue à la frontière $F - B_1$, et une différentielle première discontinue en $F - B_2$ et en $B_1 - B_2$, les trois frontières étant concourantes en un point triple. La frontière $F - B_2$ s'obtient, de manière exacte, en résolvant l'équation $v_{c,f}^L = c$ [cas (a)] ou $v_{c,f}^L = c + c_B$ [cas (b)]. La frontière $B_1 - B_2$ est, de même, exactement sur la ligne d'égalité entre les vitesses critiques issues des parties phononique et intermédiaire de la branche bosonique ; dans le cas (a), on l'obtient avec une bonne approximation en résolvant l'équation plus simple $v_{c,f}^L = c$, parce que la vitesse critique dans B_1 est en réalité proche de $v_{c,f}^L$; dans le cas (b), cette approximation est nettement moins bonne, sauf près du point triple. Finalement, la frontière $F - B_1$ peut être identifiée, avec une bonne

approximation dans les deux cas (a) et (b), à une portion de la ligne de discontinuité de la différentielle seconde de $v_{c,f}^L$, donnée par l'équation $m/M = \Delta/(2\mu)$ pour le cas (a), et par l'égalité dans l'inégalité (34) pour le cas (b).

Ces prédictions pourraient être vérifiées expérimentalement avec le mélange de superfluides des isotopes bosonique ^7Li et fermionique ^6Li du lithium récemment préparé à l'ENS [14]. Ainsi, la transition du premier ordre à la frontière $B_1 - B_2$ prédite ici pourrait être révélée en faisant varier la longueur de diffusion entre fermions de spins opposés, donc $\tilde{\Delta}$, grâce à une résonance de Feshbach, et en mesurant la vitesse critique correspondante; on devrait alors observer une rupture de pente dans la vitesse critique en fonction de la force des interactions, au passage de la ligne $B_1 - B_2$. En revanche, la valeur du rapport de masse $m/M \simeq 6/7$, imposée, ne permet pas de franchir les autres frontières.

Il serait envisageable de prolonger la présente étude théorique à ce qui a été directement mesuré dans la référence [14], à savoir le taux d'amortissement des oscillations du superfluide de bosons dans le superfluide de fermions harmoniquement piégé, en prenant en compte d'éventuels effets de température non nulle. Il faudrait aussi voir si l'interaction entre fermions et bosons est suffisamment faible pour qu'on puisse restreindre l'analyse, comme le fit Landau et comme ce fut fait ici, au nombre *minimal* possible d'excitations élémentaires, et obtenir la même barrière d'énergie (empêchant l'amortissement du mouvement des impuretés dans le superfluide de fermions) que dans l'expérience. Toutes questions que nous espérons inspiratrices de travaux ultérieurs, aussi bien théoriques qu'expérimentaux.

Remerciements

Notre équipe, qui est aussi affiliée à l'IFRAF, remercie pour son soutien financier l'IFRAF Dim-nanoK, sur le projet ATOMIX. Nous remercions les membres de l'équipe « fermions froids » ainsi que Xavier Leyronas pour d'utiles discussions.

Références

- [1] M. Inguscio, W. Ketterle, C. Salomon, « Ultracold Fermi Gases » (Società italiana di fisica, Bologne, Italie, 2007); S. Giorgini, L.P. Pitaevskii, S. Stringari, « Theory of ultracold atomic Fermi gases », Rev. Mod. Phys. **80**, 1215 (2008); W. Zwirger, « The BCS-BEC Crossover and the Unitary Fermi Gas » (Springer Verlag, 2012).
- [2] A.J. Leggett, « Quantum Liquids », section 2.4 (Oxford University Press, Oxford, 2006).
- [3] I. Carusotto, Y. Castin, « Atom interferometric detection of the pairing order parameter in a Fermi gas », Phys. Rev. Lett. **94**, 223202 (2005).
- [4] M. Zwierlein, C. Stan, C. Schunck, S. Raupach, A. Kerman, W. Ketterle, « Condensation of Pairs of Fermionic Atoms near a Feshbach Resonance », Phys. Rev. Lett. **92**, 120403 (2004); S. Jochim, M. Bartenstein, A. Altmeyer, G. Hendl, Cheng Chin, J. Hecker Denschlag, R. Grimm, « Pure Gas of Optically Trapped Molecules Created from Fermionic Atoms », Phys. Rev. Lett. **91**, 240402 (2003).
- [5] M. Zwierlein, J.R. Abo-Shaeer, A. Schirotzek, C.H. Schunck, W. Ketterle, « Vortices and superfluidity in a strongly interacting Fermi gas », Nature **435**, 1047 (2005).
- [6] L.A. Sidorenkov, Meng Khoon Tey, R. Grimm, Yan-Hua Hou, L. Pitaevskii, S. Stringari, « Second sound and the superfluid fraction in a Fermi gas with resonant interactions », Nature **498**, 78 (2013).
- [7] S. Nascimbène, N. Navon, K.J. Jiang, F. Chevy, C. Salomon, « Exploring the thermodynamics of a universal Fermi gas », Nature **463**, 1057 (2010); Mark J.H. Ku, A.T. Sommer, Lawrence W. Cheuk, M. Zwierlein, « Revealing the Superfluid Lambda Transition in the Universal Thermodynamics of a Unitary Fermi Gas », Science **335**, 563 (2012).
- [8] D. Miller, J. Chin, C. Stan, Y. Liu, W. Setiawan, C. Sanner, W. Ketterle, « Critical Velocity for Superfluid Flow across the BEC-BCS Crossover », Phys. Rev. Lett. **99**, 070402 (2007).
- [9] T. Frisch, Y. Pomeau, S. Rica, « Transition to dissipation in a model of superflow », Phys. Rev. Lett. **69**, 1644 (1992).
- [10] L. Landau, J. Phys. (URSS) **5**, 71 (1941).
- [11] R. Combescot, M. Yu. Kagan, S. Stringari, « Collective mode of homogeneous superfluid Fermi gases in the BEC-BCS crossover », Phys. Rev. A **74**, 042717 (2006).
- [12] B. Svistunov, E. Babaev, N. Prokof'ev, « Superfluid States of Matter », chapitre 1, p. 42 (CRC Press, 2014).
- [13] A.P. Chikkatur, A. Görlitz, D.M. Stamper-Kurn, S. Inouye, S. Gupta, W. Ketterle, « Suppression and enhancement of impurity scattering in a Bose-Einstein condensate », Phys. Rev. Lett. **85**, 483 (2000).
- [14] I. Ferrier-Barbut, M. Delehaye, S. Laurent, A. T. Grier, M. Pierce, B.S. Rem, F. Chevy, C. Salomon, « A Mixture of Bose and Fermi Superfluids », arXiv :1404.2548
- [15] A. Minguzzi, G. Ferrari, Y. Castin, « Dynamic structure factor of a superfluid Fermi gas », Eur. Phys. J. D **17**, 49 (2001).
- [16] P.W. Anderson, « Random-Phase Approximation in the Theory of Superconductivity », Phys. Rev. **112**, 1900 (1958).

References

- [Abdullaev et al., 2013] Abdullaev, F. K., Ögren, M., and Sørensen, M. (2013). Faraday waves in quasi-one-dimensional superfluid Fermi-Bose mixtures. *Phys. Rev. A*, 87(2):023616. Cited p. 125
- [Adhikari and Salasnich, 2008] Adhikari, S. and Salasnich, L. (2008). Superfluid Bose-Fermi mixture from weak coupling to unitarity. *Phys. Rev. A*, 78(4):043616. Cited p. 125
- [Allen and Misener, 1938] Allen, J. F. and Misener, A. D. (1938). Flow of Liquid Helium II. *Nature*, 141(3):75. Cited pp. 9 and 34
- [Allum et al., 1976] Allum, D., Bowley, R., and McClintock, P. (1976). Evidence for Roton Pair Creation in Superfluid ^4He . *Phys. Rev. Lett.*, 36(22):1313–1316. Cited p. 38
- [Allum et al., 1977] Allum, D. R., McClintock, P. V. E., and Phillips, A. (1977). The Break-down of Superfluidity in Liquid He: An Experimental Test of Landau’s Theory. *Philosophical Transactions of the Royal Society A: Mathematical, Physical and Engineering Sciences*, 284(1320):179–224. Cited p. 38
- [Anderson et al., 1995] Anderson, M. H., Ensher, J. R., Matthews, M. R., Wieman, C. E., and Cornell, E. A. (1995). Observation of Bose-Einstein Condensation in a Dilute Atomic Vapor. *Science*, 269(5221):198–201. Cited p. 11
- [Astrakharchik et al., 2004] Astrakharchik, G. E., Boronat, J., Casulleras, J., and Giorgini, S. (2004). Equation of State of a Fermi Gas in the BEC-BCS Crossover: A Quantum Monte Carlo Study. *Phys. Rev. Lett.*, 93(2):200404. Cited p. 32
- [Banerjee, 2007] Banerjee, A. (2007). Collective oscillations of a Bose-Fermi mixture: Effect of unequal masses of Bose and Fermi particles. *Phys. Rev. A*, 76(2):023611. Cited p. 125
- [Bardeen et al., 1967] Bardeen, J., Baym, G., and Pines, D. (1967). Effective Interaction of ^3He Atoms in Dilute Solutions of ^3He in ^4He at Low Temperatures. *Phys. Rev.*, 156(1):207–221. Cited p. 11
- [Bardeen et al., 1957a] Bardeen, J., Cooper, L., and Schrieffer, J. (1957a). Microscopic Theory of Superconductivity. *Phys. Rev.*, 106(1):162–164. Cited pp. 10 and 31
- [Bardeen et al., 1957b] Bardeen, J., Cooper, L. N., and Schrieffer, J. R. (1957b). Theory of Superconductivity. *Phys. Rev.*, 108(5):1175–1204. Cited pp. 10 and 31
- [Bardeen and Pines, 1955] Bardeen, J. and Pines, D. (1955). Electron-phonon interaction in metals. *Phys. Rev.*, 99(4):1140. Cited p. 30

- [Baym et al., 2001] Baym, G., Blaizot, J. P., Holzmann, M., Laloë, F., and Vautherin, D. (2001). Bose-Einstein transition in a dilute interacting gas. *The European Physical Journal B-Condensed Matter and Complex Systems*, 24(1):107–124. *Cited p. 33*
- [Beattie et al., 2013] Beattie, S., Moulder, S., Fletcher, R. J., and Hadzibabic, Z. (2013). Persistent currents in spinor condensates. *Phys. Rev. Lett.*, 110(2):025301. *Cited p. 34*
- [Bedaque et al., 2000] Bedaque, P., Braaten, E., and Hammer, H. W. (2000). Three-body Recombination in Bose Gases with Large Scattering Length. *Phys. Rev. Lett.*, 85(5):908–911. *Cited p. 85*
- [Bennemann and Ketterson, 2013] Bennemann, K.-H. and Ketterson, J. B. (2013). *Novel Superfluids*. Oxford University Press. *Cited p. 11*
- [Best et al., 2009] Best, T., Will, S., Schneider, U., Hackermüller, L., van Oosten, D., Bloch, I., and Lühmann, D. S. (2009). Role of Interactions in Rb87-K40 Bose-Fermi Mixtures in a 3D Optical Lattice. *Phys. Rev. Lett.*, 102(3):030408. *Cited p. 13*
- [Boiron et al., 1995] Boiron, D., Triché, C., Meacher, D., Verkerk, P., and Grynberg, G. (1995). Three-dimensional cooling of cesium atoms in four-beam gray optical molasses. *Phys. Rev. A*, 52(5):R3425–R3428. *Cited p. 67*
- [Bourdel et al., 2003] Bourdel, T., Cubizolles, J., Khaykovich, L., Magalhães, K. M. F., Kokkelmans, S. J. J. M. F., Shlyapnikov, G. V., and Salomon, C. (2003). Measurement of the Interaction Energy near a Feshbach Resonance in a ^6Li Fermi Gas. *Phys. Rev. Lett.*, 91(2):020402. *Cited pp. 29 and 98*
- [Bourdel et al., 2004] Bourdel, T., Khaykovich, L., Cubizolles, J., Zhang, S., Chevy, F., Teichmann, M., Tarruell, L., Kokkelmans, S. J. J. M. F., and Salomon, C. (2004). Experimental Study of the BEC-BCS Crossover Region in Lithium 6. *Phys. Rev. Lett.*, 93(5):050401. *Cited p. 30*
- [Braaten and Hammer, 2001] Braaten, E. and Hammer, H. W. (2001). Three-Body Recombination into Deep Bound States in a Bose Gas with Large Scattering Length. *Phys. Rev. Lett.*, 87(1):160407. *Cited pp. 85 and 88*
- [Bukov and Pollet, 2014] Bukov, M. and Pollet, L. (2014). Mean-field phase diagram of the Bose-Fermi Hubbard model. *Phys. Rev. B*, 89(9):094502. *Cited p. 126*
- [Burchianti et al., 2014] Burchianti, A., Valtolina, G., Seman, J. A., Pace, E., De Pas, M., Inguscio, M., Zaccanti, M., and Roati, G. (2014). Efficient all-optical production of large Li6 quantum gases using D1 gray-molasses cooling. *Phys. Rev. A*, 90(4):043408. *Cited pp. 47, 80, 81, and 127*
- [Capuzzi and Hernández, 2001] Capuzzi, P. and Hernández, E. (2001). Zero-sound density oscillations in Fermi-Bose mixtures. *Phys. Rev. A*, 64(4):043607. *Cited p. 125*

- [Capuzzi et al., 2003] Capuzzi, P., Minguzzi, A., and Tosi, M. (2003). Collective excitations of a trapped boson-fermion mixture across demixing. *Phys. Rev. A*, 67(5):053605. Cited pp. 104 and 125
- [Castin and Dum, 1996] Castin, Y. and Dum, R. (1996). Bose-Einstein Condensates in Time Dependent Traps. *Phys. Rev. Lett.*, 77(27):5315–5319. Cited p. 97
- [Castin et al., 2014] Castin, Y., Ferrier-Barbut, I., and Salomon, C. (2014). The Landau critical velocity for a particle in a Fermi superfluid. *ArXiv*, 1408.1326. Cited pp. 36, 38, 119, and 121
- [Chevy and Mora, 2010] Chevy, F. and Mora, C. (2010). Ultra-cold polarized Fermi gases. *Rep. Prog. Phys.*, 73(11):112401. Cited p. 100
- [Chikkatur et al., 2000] Chikkatur, A., Görlitz, A., Stamper-Kurn, D., Inouye, S., Gupta, S., and Ketterle, W. (2000). Suppression and Enhancement of Impurity Scattering in a Bose-Einstein Condensate. *Phys. Rev. Lett.*, 85(3):483–486. Cited p. 39
- [Chin et al., 2010] Chin, C., Grimm, R., Julienne, P., and Tiesinga, E. (2010). Feshbach resonances in ultracold gases. *Rev. Mod. Phys.*, 82(2):1225–1286. Cited pp. 21, 22, and 23
- [Cohen and van Leeuwen, 1961] Cohen, E. G. D. and van Leeuwen, J. M. J. (1961). On supermobility in an isotopic mixture of a hard sphere Bose and Fermi gas at $T = 0$. *Physica*, 27(12):1157–1160. Cited p. 11
- [Cohen-Tannoudji, Claude, 1990] Cohen-Tannoudji, Claude (1990). Atomic motion in laser light. *Fundamental systems in quantum optics*, pages 1–164. Cited pp. 72 and 129
- [Cohen-Tannoudji, Claude, 1996] Cohen-Tannoudji, Claude (1995–1996). Lecture notes at Collège de France. Cited pp. 67 and 129
- [Cohen-Tannoudji, Claude, 1997] Cohen-Tannoudji, Claude (1996–1997). Lecture notes at Collège de France. Cited p. 89
- [Cohen-Tannoudji, Claude, 1999] Cohen-Tannoudji, Claude (1998–1999). Lecture notes at Collège de France. Cited p. 20
- [Combescot et al., 2006] Combescot, R., Kagan, Y., and Stringari, S. (2006). Collective mode of homogeneous superfluid Fermi gases in the BEC-BCS crossover. *Phys. Rev. A*, 74(4):042717. Cited pp. 36, 37, 40, 119, and 121
- [Cooper, 1956] Cooper, L. (1956). Bound Electron Pairs in a Degenerate Fermi Gas. *Phys. Rev.*, 104(4):1189–1190. Cited p. 30
- [Cornell and Wieman, 2002] Cornell, E. A. and Wieman, C. E. (2002). Nobel Lecture: Bose-Einstein condensation in a dilute gas, the first 70 years and some recent experiments. *Rev. Mod. Phys.*, 74(3):875–893. Cited p. 103
- [Cui, 2014] Cui, X. (2014). Atom-dimer scattering and stability of Bose and Fermi mixtures. *Phys. Rev. A*, 90(4):041603. Cited p. 125

- [Dalibard et al., 1992] Dalibard, J., Castin, Y., and Mølmer, K. (1992). Wave-function approach to dissipative processes in quantum optics. *Phys. Rev. Lett.*, 68(5):580–583. Cited p. 80
- [Dalibard and Cohen-Tannoudji, 1989] Dalibard, J. and Cohen-Tannoudji, C. (1989). Laser cooling below the Doppler limit by polarization gradients: Simple theoretical models. *Journal of the Optical Society of America B: Optical Physics*, 6(1):2023–2045. Cited p. 67
- [Davis et al., 1995] Davis, K., Mewes, M., Andrews, M., van Druten, N., Durfee, D., Kurn, D., and Ketterle, W. (1995). Bose-Einstein Condensation in a Gas of Sodium Atoms. *Phys. Rev. Lett.*, 75(22):3969–3973. Cited p. 11
- [Deh et al., 2010] Deh, B., Gunton, W., Klappauf, B., Li, Z., Semczuk, M., Van Dongen, J., and Madison, K. (2010). Giant Feshbach resonances in ${}^6\text{Li}$ - ${}^{85}\text{Rb}$ mixtures. *Phys. Rev. A*, 82(2):020701. Cited p. 12
- [Deh et al., 2008] Deh, B., Marzok, C., Zimmermann, C., and Courteille, P. (2008). Feshbach resonances in mixtures of ultracold ${}^6\text{Li}$ and ${}^{87}\text{Rb}$ gases. *Phys. Rev. A*, 77(1):010701. Cited p. 12
- [Delehaye, 2012] Delehaye, M. (2012). Internship report. Cited p. 95
- [DeMarco, 1999] DeMarco, B. (1999). Onset of Fermi Degeneracy in a Trapped Atomic Gas. *Science*, 285(5434):1703–1706. Cited p. 11
- [Desbuquois et al., 2012] Desbuquois, R., Chomaz, L., Yefsah, T., Léonard, J., Beugnon, J., Weitenberg, C., and Dalibard, J. (2012). Superfluid behaviour of a two-dimensional Bose gas. *Nature Physics*, 8(9):645–648. Cited p. 39
- [Desbuquois et al., 2014] Desbuquois, R., Yefsah, T., Chomaz, L., Weitenberg, C., Cormann, L., Nascimbène, S., and Dalibard, J. (2014). Determination of Scale-Invariant Equations of State without Fitting Parameters: Application to the Two-Dimensional Bose Gas Across the Berezinskii-Kosterlitz-Thouless Transition. *Phys. Rev. Lett.*, 113(2):020404. Cited p. 18
- [Dobson, 1994] Dobson, J. F. (1994). Harmonic-potential theorem: Implications for approximate many-body theories. *Phys. Rev. Lett.*, 73(1):2244–2247. Cited p. 109
- [Duarte et al., 2011] Duarte, P., Hart, R., Hitchcock, J., Corcovilos, T., Yang, T. L., Reed, A., and Hulet, R. (2011). All-optical production of a lithium quantum gas using narrow-line laser cooling. *Phys. Rev. A*, 84(6):061406. Cited p. 47
- [Dyke et al., 2013] Dyke, P., Pollack, S. E., and Hulet, R. G. (2013). Finite-range corrections near a Feshbach resonance and their role in the Efimov effect. *Phys. Rev. A*, 88(2):023625. Cited p. 23
- [Edwards et al., 1965] Edwards, D., Brewer, D., Seligman, P., Skertic, M., and Yaqub, M. (1965). Solubility of ${}^3\text{He}$ in Liquid ${}^4\text{He}$ at 0 °K. *Phys. Rev. Lett.*, 15(20):773–775. Cited p. 10

- [Edwards and Daunt, 1961] Edwards, D. and Daunt, J. (1961). Phase Separation in ^3He - ^4He Mixtures near Absolute Zero. *Phys. Rev.*, 124(3):640–642. Cited p. 10
- [Efimov, 1970] Efimov, V. (1970). Energy levels arising from resonant two-body forces in a three-body system. *Physics Letters B*, 33(8):563–564. Cited p. 84
- [Efimov, 1973] Efimov, V. (1973). Energy levels of three resonantly interacting particles. *Nuclear Physics A*, 210(1):157–188. Cited p. 84
- [Engels and Atherton, 2007] Engels, P. and Atherton, C. (2007). Stationary and Nonstationary Fluid Flow of a Bose-Einstein Condensate Through a Penetrable Barrier. *Phys. Rev. Lett.*, 99(16):160405. Cited p. 39
- [Esry and Greene, 1999] Esry, B. D. and Greene, C. H. (1999). Recombination of Three Atoms in the Ultracold Limit. *Phys. Rev. Lett.*, 83(9):1751–1754. Cited p. 85
- [Esslinger et al., 1996] Esslinger, T., Sander, F., Hemmerich, A., Hänsch, T. W., Ritsch, H., and Weidemüller, M. (1996). Purely optical dark lattice. *Optics Letters*, 21(1):991–993. Cited p. 67
- [Esteve et al., 2006] Esteve, J., Trebbia, J. B., Schumm, T., Aspect, A., Westbrook, C., and Bouchoule, I. (2006). Observations of Density Fluctuations in an Elongated Bose Gas: Ideal Gas and Quasicondensate Regimes. *Phys. Rev. Lett.*, 96(13):130403. Cited p. 18
- [Falke et al., 2008] Falke, S., Knöckel, H., Friebe, J., Riedmann, M., Tiemann, E., and Lisdat, C. (2008). Potassium ground-state scattering parameters and Born-Oppenheimer potentials from molecular spectroscopy. *Phys. Rev. A*, 78(1):012503. Cited p. 126
- [Fedichev et al., 1996] Fedichev, P. O., Reynolds, M. W., and Shlyapnikov, G. V. (1996). Three-body recombination of ultracold atoms to a weakly bound s level. *Phys. Rev. Lett.*, 77(14):2921–2924. Cited pp. 28 and 84
- [Fedichev and Shlyapnikov, 2001] Fedichev, P. O. and Shlyapnikov, G. V. (2001). Critical velocity in cylindrical Bose-Einstein condensates. *Phys. Rev. A*, 63(4):045601. Cited p. 38
- [Ferlaino et al., 2003] Ferlaino, F., Brecha, R. J., Hannaford, P., Riboli, F., Roati, G., Modugno, G., and Inguscio, M. (2003). Dipolar oscillations in a quantum degenerate Fermi-Bose atomic mixture. *Journal of Optics B: Quantum and Semiclassical Optics*, 5(2):S3. Cited p. 103
- [Ferlaino et al., 2006] Ferlaino, F., D’Errico, C., Roati, G., Zaccanti, M., Inguscio, M., Modugno, G., and Simoni, A. (2006). Feshbach spectroscopy of a K-Rb atomic mixture. *Phys. Rev. A*, 73(4):040702. Cited p. 12
- [Ferlaino et al., 2011] Ferlaino, F., Zenesini, A., Berninger, M., Huang, B., Nägerl, H. C., and Grimm, R. (2011). Efimov Resonances in Ultracold Quantum Gases. *Few-Body Syst*, 51(2-4):113–133. Cited pp. 85 and 126

- [Ferrari, 1999] Ferrari, G. (1999). Collisional relaxation in a fermionic gas. *Phys. Rev. A*, 59(6):R4125–R4128. Cited p. 102
- [Ferrari, 2000] Ferrari, G. (2000). *Piégeage simultané des isotopes fermionique et bosonique du lithium. Étude théorique de la relaxation collisionnelle dans un gaz de Fermi dégénéré*. PhD thesis, Université Paris 6. Cited p. 43
- [Ferrier-Barbut et al., 2014] Ferrier-Barbut, I., Delehay, M., Laurent, S., Grier, A. T., Pierce, M., Rem, B. S., Chevy, F., and Salomon, C. (2014). A mixture of Bose and Fermi superfluids. *Science*, 345(6200):1035–1038. Cited p. 91
- [Feynman, 1955] Feynman, R. P. (1955). Application of quantum mechanics to liquid helium. *Progress in low temperature physics*, 1:17–53. Cited p. 39
- [File and Mills, 1963] File, J. and Mills, R. (1963). Observation of Persistent Current in a Superconducting Solenoid. *Phys. Rev. Lett.*, 10(3):93–96. Cited p. 34
- [Fletcher et al., 2013] Fletcher, R. J., Gaunt, A. L., Navon, N., Smith, R. P., and Hadzibabic, Z. (2013). Stability of a Unitary Bose Gas. *Phys. Rev. Lett.*, 111(12):125303. Cited p. 90
- [Frisch et al., 1992] Frisch, T., Pomeau, Y., and Rica, S. (1992). Transition to dissipation in a model of superflow. *Phys. Rev. Lett.*, 69(11):1644–1647. Cited pp. 38 and 39
- [Frohlich, 1952] Frohlich, H. (1952). Interaction of Electrons with Lattice Vibrations. *Proceedings of the Royal Society A: Mathematical, Physical and Engineering Sciences*, 215(1122):291–298. Cited p. 30
- [Gaunt et al., 2013] Gaunt, A. L., Schmidutz, T. F., Gotlibovych, I., Smith, R. P., and Hadzibabic, Z. (2013). Bose-Einstein Condensation of Atoms in a Uniform Potential. *Phys. Rev. Lett.*, 110(20):200406. Cited p. 39
- [Gerdes et al., 2008] Gerdes, A., Hobein, M., Knöckel, H., and Tiemann, E. (2008). Ground state potentials of the NaK molecule. *Eur. Phys. J. D*, 49(1):67–73. Cited p. 126
- [Giorgini et al., 1999] Giorgini, S., Boronat, J., and Casulleras, J. (1999). Ground state of a homogeneous Bose gas: A diffusion Monte Carlo calculation. *Phys. Rev. A*, 60(6):5129–5132. Cited p. 23
- [Goosen et al., 2010] Goosen, M. R., Tiecke, T. G., Vassen, W., and Kokkelmans, S. J. J. M. F. (2010). Feshbach resonances in $^3\text{He}^*$ - $^4\text{He}^*$ mixtures. *Phys. Rev. A*, 82(4):042713. Cited p. 12
- [Greiner et al., 2003] Greiner, M., Regal, C. A., and Jin, D. S. (2003). Emergence of a molecular Bose-Einstein condensate from a Fermi gas. *Nature*, 426(6966):537–540. Cited p. 30
- [Grier et al., 2013] Grier, A. T., Ferrier-Barbut, I., Rem, B. S., Delehay, M., Khaykovich, L., Chevy, F., and Salomon, C. (2013). Λ -enhanced sub-Doppler cooling of lithium atoms in D_1 gray molasses. *Phys. Rev. A*, 87(6):063411. Cited pp. 67 and 69

- [Grimm et al., 2000] Grimm, R., Weidemüller, M., and Ovchinnikov, Y. B. (2000). Optical dipole traps for neutral atoms. volume 42 of *Advances In Atomic, Molecular, and Optical Physics*, pages 95 – 170. Academic Press. *Cited p. 51*
- [Gross et al., 2010] Gross, N., Shotan, Z., Kokkelmans, S. J. J. M. F., and Khaykovich, L. (2010). Nuclear-Spin-Independent Short-Range Three-Body Physics in Ultracold Atoms. *Phys. Rev. Lett.*, 105(1):103203. *Cited pp. 84, 86, and 87*
- [Gross et al., 2011] Gross, N., Shotan, Z., Machtey, O., Kokkelmans, S. J. J. M. F., and Khaykovich, L. (2011). Study of Efimov physics in two nuclear-spin sublevels of 7 Li. *Comptes Rendus Physique*, 12(1):4–12. *Cited p. 23*
- [Grynberg and Courtois, 1994] Grynberg, G. and Courtois, J.-Y. (1994). Proposal for a Magneto-Optical Lattice for Trapping Atoms in Nearly-Dark States. *EPL (Europhysics Letters)*, 27(1):41. *Cited p. 67*
- [Günter et al., 2006] Günter, K., Stöferle, T., Moritz, H., Köhl, M., and Esslinger, T. (2006). Bose-Fermi Mixtures in a Three-Dimensional Optical Lattice. *Phys. Rev. Lett.*, 96(18):180402. *Cited p. 13*
- [Hadzibabic et al., 2002] Hadzibabic, Z., Stan, C. A., Dieckmann, K., Gupta, S., Zwierlein, M. W., Görlitz, A., and Ketterle, W. (2002). Two-species mixture of quantum degenerate Bose and Fermi gases. *Phys. Rev. Lett.*, 88(16). *Cited p. 12*
- [Hall et al., 1998a] Hall, D. S., Matthews, M. R., Ensher, J. R., Wieman, C. E., and Cornell, E. A. (1998a). Dynamics of Component Separation in a Binary Mixture of Bose-Einstein Condensates. *Phys. Rev. Lett.*, 81(8):1539–1542. *Cited p. 103*
- [Hall et al., 1998b] Hall, D. S., Matthews, M. R., Wieman, C. E., and Cornell, E. A. (1998b). Measurements of Relative Phase in Two-Component Bose-Einstein Condensates. *Phys. Rev. Lett.*, 81(8):1543–1546. *Cited p. 103*
- [Hamilton et al., 2014] Hamilton, P., Kim, G., Joshi, T., Mukherjee, B., Tiarks, D., and Müller, H. (2014). Sisyphus cooling of lithium. *Phys. Rev. A*, 89(2):023409. *Cited pp. 80 and 81*
- [Hamner et al., 2011] Hamner, C., Chang, J. J., Engels, P., and Hofer, M. A. (2011). Generation of Dark-Bright Soliton Trains in Superfluid-Superfluid Counterflow. *Phys. Rev. Lett.*, 106(6):065302. *Cited p. 121*
- [Hanna, T. and Tiesinga, E.,] Hanna, T. and Tiesinga, E. private communication. *Cited p. 126*
- [Hansen et al., 2011] Hansen, A. H., Khramov, A., Dowd, W. H., Jamison, A. O., Ivanov, V. V., and Gupta, S. (2011). Quantum degenerate mixture of ytterbium and lithium atoms. *Phys. Rev. A*, 84(1):011606. *Cited p. 12*

- [Hara et al., 2011] Hara, H., Takasu, Y., Yamaoka, Y., Doyle, J. M., and Takahashi, Y. (2011). Quantum Degenerate Mixtures of Alkali and Alkaline-Earth-Like Atoms. *Phys. Rev. Lett.*, 106(20):205304. *Cited p. 12*
- [Heavner et al., 2001] Heavner, T., Jefferts, S., and Dunn, G. (2001). Atomic mass of ${}^6\text{Li}$ using a Penning-ion-trap mass spectrometer. *Phys. Rev. A*, 64(6):062504. *Cited p. 43*
- [Hou et al., 2013] Hou, Y.-H., Pitaevskii, L. P., and Stringari, S. (2013). First and second sound in a highly elongated Fermi gas at unitarity. *Phys. Rev. A*, 88(4):043630. *Cited p. 119*
- [Hu et al., 2010] Hu, H., Taylor, E., Liu, X.-J., Stringari, S., and Griffin, A. (2010). Second sound and the density response function in uniform superfluid atomic gases. *New J. Phys.*, 12(4):043040. *Cited p. 41*
- [Hung et al., 2011] Hung, C.-L., Zhang, X., Gemelke, N., and Chin, C. (2011). Observation of scale invariance and universality in two-dimensional Bose gases. *Nature*, 470(7333):236–239. *Cited p. 18*
- [Inouye et al., 2004] Inouye, S., Goldwin, J., Olsen, M., Ticknor, C., Bohn, J., and Jin, D. S. (2004). Observation of Heteronuclear Feshbach Resonances in a Mixture of Bosons and Fermions. *Phys. Rev. Lett.*, 93(18):183201. *Cited p. 12*
- [Inouye et al., 2001] Inouye, S., Gupta, S., Rosenband, T., Chikkatur, A., Görlitz, A., Gustavson, T., Leanhardt, A., Pritchard, D., and Ketterle, W. (2001). Observation of Vortex Phase Singularities in Bose-Einstein Condensates. *Phys. Rev. Lett.*, 87(8):080402. *Cited p. 39*
- [Jiang et al., 2014] Jiang, S.-J., Liu, W.-M., Semenov, G. W., and Zhou, F. (2014). Universal Bose gases near resonance: A rigorous solution. *Phys. Rev. A*, 89(3):033614. *Cited p. 28*
- [Jochim et al., 2003a] Jochim, S., Bartenstein, M., Altmeyer, A., Hendl, G., Chin, C., Denschlag, J. H., and Grimm, R. (2003a). Pure Gas of Optically Trapped Molecules Created from Fermionic Atoms. *Phys. Rev. Lett.*, 91(24):240402. *Cited pp. 92 and 94*
- [Jochim et al., 2003b] Jochim, S., Bartenstein, M., Altmeyer, A., Hendl, G., Riedl, S., Chin, C., Hecker Denschlag, J., and Grimm, R. (2003b). Bose-Einstein Condensation of Molecules. *Science*, 302(5):2101–2104. *Cited pp. 30 and 109*
- [Julienne and Hutson, 2014] Julienne, P. S. and Hutson, J. M. (2014). Contrasting the wide Feshbach resonances in Li_6 and Li_7 . *Phys. Rev. A*, 89(5):052715. *Cited p. 23*
- [Kamerlingh Onnes, 1913] Kamerlingh Onnes, H. (1913). Investigations into the properties of substances at low temperatures, which have led, amongst other things, to the preparation of liquid helium. *Nobel lecture*, 4. *Cited pp. 9 and 34*
- [Kapitza, 1938] Kapitza, P. (1938). Viscosity of Liquid Helium below the λ -Point. *Nature*, 141(3):74. *Cited pp. 9 and 34*
- [Ketterle, 2014] Ketterle, W. (2014). private communication. *Cited p. 127*

- [Kinoshita et al., 2006] Kinoshita, T., Wenger, T., and Weiss, D. S. (2006). A quantum Newton's cradle. *Nature*, 440(7086):900–903. *Cited p. 103*
- [Kosachev and Rozhdestvenskii, 1994] Kosachev, D. V. and Rozhdestvenskii, Y. V. (1994). Theory of sub-Doppler cooling of three-level Λ atoms in standing light waves. *Journal of Experimental and Theoretical Physics*, 106:1588–1605. *Cited pp. 73 and 78*
- [Kosachiov et al., 1997] Kosachiov, D. V., Rozhdestvensky, Y. V., and Nienhuis, G. (1997). Laser cooling of three-level atoms in two standing waves. *JOSA B*, 14(3):535–543. *Cited pp. 73 and 78*
- [Kraemer et al., 2006] Kraemer, T., Mark, M., Waldburger, P., Danzl, J. G., Chin, C., Engeser, B., Lange, A. D., Pilch, K., Jaakkola, A., Nägerl, H. C., and Grimm, R. (2006). Evidence for Efimov quantum states in an ultracold gas of caesium atoms. *Nature*, 440(7082):315–318. *Cited pp. 85 and 86*
- [Ku et al., 2012] Ku, M. J. H., Sommer, A. T., Cheuk, L. W., and Zwierlein, M. W. (2012). Revealing the Superfluid Lambda Transition in the Universal Thermodynamics of a Unitary Fermi Gas. *Science*, 335(6):563. *Cited pp. 18, 31, 33, 98, 113, and 114*
- [Kuklov and Svistunov, 2003] Kuklov, A. B. and Svistunov, B. V. (2003). Counterflow Superfluidity of Two-Species Ultracold Atoms in a Commensurate Optical Lattice. *Phys. Rev. Lett.*, 90(10):100401. *Cited p. 126*
- [Laburthe-Tolra, 2014] Laburthe-Tolra, B. (2014). private communication. *Cited p. 12*
- [Landau, 1941a] Landau, L. (1941a). The Theory of Superfluid Helium II. *J. Phys. USSR*, 5:70. *Cited pp. 34 and 35*
- [Landau, 1941b] Landau, L. (1941b). Theory of the Superfluidity of Helium II. *Phys. Rev.*, 60(4):356–358. *Cited pp. 34 and 35*
- [Landau and Lifchitz, 1966a] Landau, L. and Lifchitz, S. (1966a). *Quantum Mechanics, non relativistic theory*. Mir Editions. *Cited pp. 20 and 27*
- [Landau and Lifchitz, 1966b] Landau, L. and Lifchitz, S. (1966b). *Statistical Physics*. Mir Editions. *Cited p. 16*
- [Laurent, 2013] Laurent, S. (2013). Internship report. *Cited p. 89*
- [Law et al., 2001] Law, C., Chan, C., Leung, P., and Chu, M. C. (2001). Critical velocity in a binary mixture of moving Bose condensates. *Phys. Rev. A*, 63(6):063612. *Cited p. 121*
- [Lee et al., 1957] Lee, T., Huang, K., and Yang, C. (1957). Eigenvalues and Eigenfunctions of a Bose System of Hard Spheres and Its Low-Temperature Properties. *Phys. Rev.*, 106(6):1135–1145. *Cited p. 27*
- [Leggett, 2001] Leggett, A. (2001). Bose-Einstein condensation in the alkali gases: Some fundamental concepts. *Rev. Mod. Phys.*, 73(2):307–356. *Cited p. 34*

- [Leggett, 1980] Leggett, A. J. (1980). Cooper pairing in spin-polarized Fermi systems. *J. Phys. Colloques*, 41(C7):C7-19-C7-26. *Cited p. 29*
- [Leggett, 2006] Leggett, A. J. (2006). *Quantum Liquids: Bose condensation and Cooper pairing in condensed-matter systems*. Oxford University Press. *Cited p. 40*
- [Lett et al., 1988] Lett, P., Watts, R., Westbrook, C., Phillips, W., Gould, P., and Metcalf, H. (1988). Observation of Atoms Laser Cooled below the Doppler Limit. *Phys. Rev. Lett.*, 61(2):169-172. *Cited p. 67*
- [Leyronas and Combescot, 2007] Leyronas, X. and Combescot, R. (2007). Superfluid Equation of State of Dilute Composite Bosons. *Phys. Rev. Lett.*, 99(17):170402. *Cited p. 30*
- [Li and Ho, 2012] Li, W. and Ho, T.-L. (2012). Bose Gases near Unitarity. *Phys. Rev. Lett.*, 108(1):195301. *Cited pp. 28 and 87*
- [Liu and Hu, 2003] Liu, X.-J. and Hu, H. (2003). Collisionless and hydrodynamic excitations of trapped boson-fermion mixtures. *Phys. Rev. A*, 67(2):023613. *Cited p. 125*
- [Lobo et al., 2006] Lobo, C., Recati, A., Giorgini, S., and Stringari, S. (2006). Normal State of a Polarized Fermi Gas at Unitarity. *Phys. Rev. Lett.*, 97(20):200403. *Cited pp. 34 and 104*
- [Lu et al., 2012] Lu, M., Burdick, N. Q., and Lev, B. L. (2012). Quantum Degenerate Dipolar Fermi Gas. *Phys. Rev. Lett.*, 108(21):215301. *Cited p. 12*
- [Maddaloni et al., 2000] Maddaloni, P., Modugno, M., Fort, C., Minardi, F., and Inguscio, M. (2000). Collective Oscillations of Two Colliding Bose-Einstein Condensates. *Phys. Rev. Lett.*, 85(12):2413-2417. *Cited p. 103*
- [Madison et al., 2000] Madison, K., Chevy, F., Wohlleben, W., and Dalibard, J. (2000). Vortex Formation in a Stirred Bose-Einstein Condensate. *Phys. Rev. Lett.*, 84(5):806-809. *Cited p. 40*
- [Maeda et al., 2009] Maeda, K., Baym, G., and Hatsuda, T. (2009). Simulating Dense QCD Matter with Ultracold Atomic Boson-Fermion Mixtures. *Phys. Rev. Lett.*, 103(8):085301. *Cited p. 125*
- [Makotyn et al., 2014] Makotyn, P., Klauss, C. E., Goldberger, D. L., Cornell, E. A., and Jin, D. S. (2014). Universal dynamics of a degenerate unitary Bose gas. *Nature Physics*, 10(2):116-119. *Cited p. 90*
- [Maruyama and Bertsch, 2008] Maruyama, T. and Bertsch, G. (2008). Dipole oscillations in Bose-Fermi mixtures in the time-dependent Gross-Pitaevskii and Vlasov equations. *Phys. Rev. A*, 77(6):063611. *Cited p. 104*
- [Maruyama and Yabu, 2009] Maruyama, T. and Yabu, H. (2009). Quadrupole oscillations in Bose-Fermi mixtures of ultracold atomic gases made of Yb atoms in the time-dependent Gross-Pitaevskii and Vlasov equations. *Phys. Rev. A*, 80(4):043615. *Cited p. 125*

- [Maruyama and Yabu, 2013] Maruyama, T. and Yabu, H. (2013). Longitudinal and transverse breathing oscillations in Bose–Fermi mixtures of Yb atoms at zero temperature in the largely prolate deformed traps. *J. Phys. B: At. Mol. Opt. Phys.*, 46(5):055201. Cited p. 125
- [Maruyama et al., 2005] Maruyama, T., Yabu, H., and Suzuki, T. (2005). Monopole oscillations and dampings in a boson and fermion mixture in the time-dependent Gross-Pitaevskii and Vlasov equations. *Phys. Rev. A*, 72(1):013609. Cited p. 125
- [McNamara et al., 2006] McNamara, J., Jeltsov, T., Tychkov, A., Hogervorst, W., and Vassen, W. (2006). Degenerate Bose-Fermi Mixture of Metastable Atoms. *Phys. Rev. Lett.*, 97(8):080404. Cited p. 12
- [Miller et al., 2007] Miller, D., Chin, J., Stan, C., Liu, Y., Setiawan, W., Sanner, C., and Ketterle, W. (2007). Critical Velocity for Superfluid Flow across the BEC-BCS Crossover. *Phys. Rev. Lett.*, 99(7):070402. Cited pp. 40, 119, and 121
- [Minguzzi and Tosi, 2000] Minguzzi, A. and Tosi, M. P. (2000). Schematic phase diagram and collective excitations in the collisional regime for trapped boson–fermion mixtures at zero temperature. *Physics Letters A*, 268(1-2):142–148. Cited pp. 104 and 125
- [Miyakawa et al., 2000] Miyakawa, T., Suzuki, T., and Yabu, H. (2000). Sum-rule approach to collective oscillations of a boson-fermion mixed condensate of alkali-metal atoms. *Phys. Rev. A*, 62(6):063613. Cited p. 125
- [Modak et al., 2011] Modak, S., Tsai, S. W., and Sengupta, K. (2011). Renormalization group approach to spinor Bose-Fermi mixtures in a shallow optical lattice. *Phys. Rev. B*, 84(13):134508. Cited p. 126
- [Modugno et al., 2002] Modugno, G., Modugno, M., Riboli, F., Roati, G., and Inguscio, M. (2002). Two Atomic Species Superfluid. *Phys. Rev. Lett.*, 89(19):190404. Cited pp. 12 and 103
- [Modugno et al., 2000] Modugno, M., Dalfovo, F., Fort, C., Maddaloni, P., and Minardi, F. (2000). Dynamics of two colliding Bose-Einstein condensates in an elongated magnetostatic trap. *Phys. Rev. A*, 62(6):063607. Cited p. 103
- [Modugno et al., 2001] Modugno, M., Fort, C., Maddaloni, P., Minardi, F., and Inguscio, M. (2001). Damping and frequency shift in the oscillations of two colliding Bose-Einstein condensates. *Eur. Phys. J. D*, 17(3):345–349. Cited p. 103
- [Mølmer, 1998] Mølmer, K. (1998). Bose Condensates and Fermi Gases at Zero Temperature. *Phys. Rev. Lett.*, 80(9):1804–1807. Cited p. 95
- [Nagy et al., 2006] Nagy, S., Fritioff, T., Suhonen, M., Schuch, R., Blaum, K., Björkhage, M., and Bergström, I. (2006). New Mass Value for ^7Li . *Phys. Rev. Lett.*, 96(16):163004. Cited p. 43
- [Naidon et al., 2014] Naidon, P., Endo, S., and Ueda, M. (2014). Microscopic Origin and Universality Classes of the Efimov Three-Body Parameter. *Phys. Rev. Lett.*, 112(1):105301. Cited p. 86

- [Nascimbène, 2010] Nascimbène, S. (2010). *Thermodynamics of ultracold Fermi gases*. PhD thesis, Université Paris 6. Cited pp. 33 and 62
- [Nascimbène et al., 2010] Nascimbène, S., Navon, N., Jiang, K. J., Chevy, F., and Salomon, C. (2010). Exploring the thermodynamics of a universal Fermi gas. *Nature*, 463(7284):1057–1060. Cited pp. 18, 31, 33, 96, and 98
- [Nascimbène et al., 2009] Nascimbène, S., Navon, N., Jiang, K. J., Tarruell, L., Teichmann, M., McKeever, J., Chevy, F., and Salomon, C. (2009). Collective Oscillations of an Imbalanced Fermi Gas: Axial Compression Modes and Polaron Effective Mass. *Phys. Rev. Lett.*, 103(17):170402. Cited pp. 34, 99, and 104
- [Nascimbène et al., 2011] Nascimbène, S., Navon, N., Pilati, S., Chevy, F., Giorgini, S., Georges, A., and Salomon, C. (2011). Fermi-Liquid Behavior of the Normal Phase of a Strongly Interacting Gas of Cold Atoms. *Phys. Rev. Lett.*, 106(21):215303. Cited p. 33
- [Nath et al., 2013] Nath, D., Easwaran, R. K., Rajalakshmi, G., and Unnikrishnan, C. S. (2013). Quantum-interference-enhanced deep sub-Doppler cooling of 39K atoms in gray molasses. *Phys. Rev. A*, 88(5):53407. Cited pp. 47 and 80
- [Navon, 2011] Navon, N. (2011). *Thermodynamics of ultracold Bose and Fermi gases*. PhD thesis, Université Paris 6. Cited pp. 32, 33, 62, and 92
- [Navon et al., 2010] Navon, N., Nascimbène, S., Chevy, F., and Salomon, C. (2010). The Equation of State of a Low-Temperature Fermi Gas with Tunable Interactions. *Science*, 328(5979):729–732. Cited pp. 18, 30, 32, and 113
- [Navon et al., 2013] Navon, N., Nascimbène, S., Leyronas, X., Chevy, F., and Salomon, C. (2013). Condensation energy of a spin-1/2 strongly interacting Fermi gas. *Phys. Rev. A*, 88(6):63614. Cited p. 33
- [Navon et al., 2011] Navon, N., Piatecki, S., Günter, K., Rem, B., Nguyen, T. C., Chevy, F., Krauth, W., and Salomon, C. (2011). Dynamics and Thermodynamics of the Low-Temperature Strongly Interacting Bose Gas. *Phys. Rev. Lett.*, 107(13):135301. Cited pp. 18, 23, and 28
- [Neely et al., 2010] Neely, T. W., Samson, E. C., Bradley, A. S., Davis, M. J., and Anderson, B. P. (2010). Observation of Vortex Dipoles in an Oblate Bose-Einstein Condensate. *Phys. Rev. Lett.*, 104(16):160401. Cited p. 39
- [Nozières and Schmitt-Rink, 1985] Nozières, P. and Schmitt-Rink, S. (1985). Bose condensation in an attractive fermion gas: From weak to strong coupling superconductivity. *J Low Temp Phys*, 59(3-4):195–211. Cited p. 29
- [Oh et al., 1994] Oh, G. H., Ishimoto, Y., Kawae, T., Nakagawa, M., Ishikawa, O., Hata, T., Kodama, T., and Ikehata, S. (1994). Cooling of ^3He - ^4He dilute solution down to 97 μK . Thermal boundary resistance between dilute solution and metal powder. *J Low Temp Phys*, 95(3-4):525–546. Cited p. 11

- [O'Hara et al., 2002] O'Hara, K. M., Hemmer, S. L., Gehm, M. E., Granade, S. R., and Thomas, J. E. (2002). Observation of a Strongly Interacting Degenerate Fermi Gas of Atoms. *Science*, 298(5):2179–2182. *Cited p. 98*
- [Onofrio et al., 2000] Onofrio, R., Raman, C., Vogels, J. M., Abo-Shaeer, J. R., Chikkatur, A. P., and Ketterle, W. (2000). Observation of superfluid flow in a Bose-Einstein condensed gas. *Phys. Rev. Lett.*, 85(11):2228–2231. *Cited p. 39*
- [Osheroff et al., 1972] Osheroff, D., Richardson, R., and Lee, D. (1972). Evidence for a New Phase of Solid ^3He . *Phys. Rev. Lett.*, 28(14):885–888. *Cited p. 9*
- [Ospelkaus et al., 2006a] Ospelkaus, S., Ospelkaus, C., Humbert, L., Sengstock, K., and Bongs, K. (2006a). Tuning of Heteronuclear Interactions in a Degenerate Fermi-Bose Mixture. *Phys. Rev. Lett.*, 97(12):120403. *Cited p. 12*
- [Ospelkaus et al., 2006b] Ospelkaus, S., Ospelkaus, C., Wille, O., Succo, M., Ernst, P., Sengstock, K., and Bongs, K. (2006b). Localization of Bosonic Atoms by Fermionic Impurities in a Three-Dimensional Optical Lattice. *Phys. Rev. Lett.*, 96(18):180403. *Cited p. 13*
- [Ozawa et al., 2014] Ozawa, T., Recati, A., Delehay, M., Chevy, F., and Stringari, S. (2014). Chandrasekhar-Clogston limit and critical polarization in a Fermi-Bose superfluid mixture. *Phys. Rev. A*, 90(4):043608. *Cited pp. 95 and 125*
- [Papp et al., 2008] Papp, S. B., Pino, J. M., Wild, R. J., Ronen, S., Wieman, C. E., Jin, D. S., and Cornell, E. A. (2008). Bragg Spectroscopy of a Strongly Interacting Rb85 Bose-Einstein Condensate. *Phys. Rev. Lett.*, 101(1):135301. *Cited p. 28*
- [Park et al., 2012] Park, J. W., Wu, C.-H., Santiago, I., Tiecke, T. G., Will, S., Ahmadi, P., and Zwierlein, M. W. (2012). Quantum degenerate Bose-Fermi mixture of chemically different atomic species with widely tunable interactions. *Phys. Rev. A*, 85(5):051602. *Cited pp. 12 and 126*
- [Partridge et al., 2006] Partridge, G. B., Li, W., Kamar, R. I., Liao, Y.-a., and Hulet, R. G. (2006). Pairing and Phase Separation in a Polarized Fermi Gas. *Science*, 311(5760):503–505. *Cited pp. 34 and 99*
- [Petrov et al., 2004] Petrov, D. S., Salomon, C., and Shlyapnikov, G. V. (2004). Weakly Bound Dimers of Fermionic Atoms. *Phys. Rev. Lett.*, 93(9):090404. *Cited pp. 29, 30, and 135*
- [Piatecki and Krauth, 2014] Piatecki, S. and Krauth, W. (2014). Efimov-driven phase transitions of the unitary Bose gas. *Nature Communications*, 5:3503. *Cited p. 28*
- [Pires et al., 2014] Pires, R., Ulmanis, J., Häfner, S., Repp, M., Arias, A., Kuhnle, E. D., and Weidemüller, M. (2014). Observation of Efimov Resonances in a Mixture with Extreme Mass Imbalance. *Phys. Rev. Lett.*, 112(25):250404. *Cited p. 12*
- [Pitaevskii and Stringari, 2003] Pitaevskii, L. and Stringari, S. (2003). *Bose-Einstein Condensation*. Clarendon Press. *Cited pp. 17, 27, 65, 105, and 118*

- [Ramachandhran et al., 2011] Ramachandhran, B., Bhongale, S. G., and Pu, H. (2011). Finite-temperature study of Bose-Fermi superfluid mixtures. *Phys. Rev. A*, 83(3). Cited p. 125
- [Raman et al., 1999] Raman, C., Köhl, M., Onofrio, R., Durfee, D., Kuklewicz, C., Hadzibabic, Z., and Ketterle, W. (1999). Evidence for a Critical Velocity in a Bose-Einstein Condensed Gas. *Phys. Rev. Lett.*, 83(13):2502–2505. Cited p. 39
- [Raman et al., 2001] Raman, C., Onofrio, R., Vogels, J. M., Abo-Shaeer, J. R., and Ketterle, W. (2001). Dissipationless Flow and Superfluidity in Gaseous Bose-Einstein Condensates - Springer. *J Low Temp Phys*, 122(1/2):99–116. Cited p. 39
- [Randeria et al., 1989] Randeria, M., Duan, J.-M., and Shieh, L.-Y. (1989). Bound states, Cooper pairing, and Bose condensation in two dimensions. *Phys. Rev. Lett.*, 62(9):981–984. Cited p. 31
- [Regal et al., 2004a] Regal, C. A., Greiner, M., and Jin, D. S. (2004a). Lifetime of Molecule-Atom Mixtures near a Feshbach Resonance in ^{40}K . *Phys. Rev. Lett.*, 92(8):083201. Cited p. 29
- [Regal et al., 2004b] Regal, C. A., Greiner, M., and Jin, D. S. (2004b). Observation of Resonance Condensation of Fermionic Atom Pairs. *Phys. Rev. Lett.*, 92(4):040403. Cited p. 30
- [Rem, 2013] Rem, B. S. (2013). *The Road to the Unitary Bose Gas*. PhD thesis, École Normale Supérieure. Cited pp. 28, 55, and 86
- [Rem et al., 2013] Rem, B. S., Grier, A. T., Ferrier-Barbut, I., Eismann, U., Langen, T., Navon, N., Khaykovich, L., Werner, F., Petrov, D. S., Chevy, F., and Salomon, C. (2013). Lifetime of the Bose Gas with Resonant Interactions. *Phys. Rev. Lett.*, 110(16):163202. Cited pp. 55, 86, 87, 88, and 89
- [Repp et al., 2013] Repp, M., Pires, R., Ulmanis, J., Heck, R., Kuhnle, E. D., Weidemüller, M., and Tiemann, E. (2013). Observation of interspecies ^6Li - ^{133}Cs Feshbach resonances. *Phys. Rev. A*, 87(1):010701. Cited pp. 12 and 126
- [Riedl et al., 2008] Riedl, S., Sánchez Guajardo, E., Kohstall, C., Altmeyer, A., Wright, M., Denschlag, J., Grimm, R., Bruun, G., and Smith, H. (2008). Collective oscillations of a Fermi gas in the unitarity limit: Temperature effects and the role of pair correlations. *Phys. Rev. A*, 78(5):053609. Cited p. 65
- [Rio Fernandes et al., 2012] Rio Fernandes, D., Sievers, F., Kretschmar, N., Wu, S., Salomon, C., and Chevy, F. (2012). Sub-Doppler laser cooling of fermionic 40K atoms in three-dimensional gray optical molasses. *EPL (Europhysics Letters)*, 100(6):63001. Cited pp. 47 and 67
- [Roati et al., 2002] Roati, G., Riboli, F., Modugno, G., and Inguscio, M. (2002). Fermi-Bose Quantum Degenerate K40-R87b Mixture with Attractive Interaction. *Phys. Rev. Lett.*, 89(15):150403. Cited p. 12

- [Rossi et al., 2014] Rossi, M., Salasnich, L., Ancilotto, F., and Toigo, F. (2014). Monte Carlo simulations of the unitary Bose gas. *Phys. Rev. A*, 89(4):41602. Cited p. 28
- [Rysti, 2013] Rysti, J. (2013). *Microscopic and Macroscopic Studies of Liquid and Solid Helium Mixtures*. PhD thesis, Aalto University. Cited p. 10
- [Rysti et al., 2012] Rysti, J., Tuoriniemi, J., and Salmela, A. (2012). Effective ^3He interactions in dilute ^3He - ^4He mixtures. *Phys. Rev. B*, 85(13):134529. Cited p. 11
- [Ryu et al., 2007] Ryu, C., Andersen, M., Cladé, P., Natarajan, V., Helmerson, K., and Phillips, W. (2007). Observation of Persistent Flow of a Bose-Einstein Condensate in a Toroidal Trap. *Phys. Rev. Lett.*, 99(26):260401. Cited p. 34
- [Sá de Melo et al., 1993] Sá de Melo, C., Randeria, M., and Engelbrecht, J. (1993). Crossover from BCS to Bose superconductivity: Transition temperature and time-dependent Ginzburg-Landau theory. *Phys. Rev. Lett.*, 71(19):3202–3205. Cited p. 31
- [Salomon et al., 2014] Salomon, G., Fouché, L., Lepoutre, S., Aspect, A., and Bourdel, T. (2014). All-optical cooling of K 39 to Bose-Einstein condensation. *Phys. Rev. A*. Cited pp. 81 and 127
- [Salomon et al., 2013] Salomon, G., Fouché, L., Wang, P., Aspect, A., Bouyer, P., and Bourdel, T. (2013). Gray-molasses cooling of 39K to a high phase-space density. *Europhysics Letters*, 104(6):63002. Cited pp. 47 and 80
- [Sansonetti et al., 2011] Sansonetti, C. J., Simien, C. E., Gillaspay, J. D., Tan, J. N., Brewer, S. M., Brown, R. C., Wu, S., and Porto, J. V. (2011). Absolute Transition Frequencies and Quantum Interference in a Frequency Comb Based Measurement of the $^{6,7}\text{Li}$ D Lines. *Phys. Rev. Lett.*, 107(2):023001. Cited p. 44
- [Schreck, 2002] Schreck, F. (2002). *Mixtures of ultracold gases: Fermi sea and Bose-Einstein condensate of lithium isotopes*. PhD thesis, Université Paris 6. Cited p. 43
- [Schreck et al., 2001a] Schreck, F., Ferrari, G., Corwin, K. L., Cubizolles, J., Khaykovich, L., Mewes, M.-O., and Salomon, C. (2001a). Sympathetic cooling of bosonic and fermionic lithium gases towards quantum degeneracy. *Phys. Rev. A*, 64(1):011402. Cited p. 11
- [Schreck et al., 2001b] Schreck, F., Khaykovich, L., Corwin, K. L., Ferrari, G., Bourdel, T., Cubizolles, J., and Salomon, C. (2001b). Quasipure Bose-Einstein Condensate Immersed in a Fermi Sea. *Phys. Rev. Lett.*, 87(8):080403. Cited pp. 11 and 12
- [Shotan et al., 2014] Shotan, Z., Machtey, O., Kokkelmans, S. J. J. M. F., and Khaykovich, L. (2014). Three-Body Recombination at Vanishing Scattering Lengths in an Ultracold Bose Gas. *Phys. Rev. Lett.*, 113(5):053202. Cited pp. 92 and 94
- [Sidorenkov et al., 2013] Sidorenkov, L. A., Tey, M. K., Grimm, R., Hou, Y.-H., Pitaevskii, L., and Stringari, S. (2013). Second sound and the superfluid fraction in a Fermi gas with resonant interactions. *Nature*, 498(7452):78–81. Cited pp. 41, 99, and 125

- [Sievers, F. and Wu, S., 2014] Sievers, F. and Wu, S. (2014). private communication. *Cited p. 80*
- [Silber et al., 2005] Silber, C., Günther, S., Marzok, C., Deh, B., Courteille, P., and Zimmermann, C. (2005). Quantum-Degenerate Mixture of Fermionic Lithium and Bosonic Rubidium Gases. *Phys. Rev. Lett.*, 95(17):170408. *Cited p. 12*
- [Sinatra et al., 1999] Sinatra, A., Fedichev, P. O., Castin, Y., Dalibard, J., and Shlyapnikov, G. V. (1999). Dynamics of Two Interacting Bose-Einstein Condensates. *Phys. Rev. Lett.*, 82(2):251–254. *Cited p. 103*
- [Smith et al., 2014] Smith, D. H., Braaten, E., Kang, D., and Platter, L. (2014). Two-Body and Three-Body Contacts for Identical Bosons near Unitarity. *Phys. Rev. Lett.*, 112(11):110402. *Cited p. 28*
- [Smith et al., 2011] Smith, R., Tammuz, N., Campbell, R., Holzmann, M., and Hadzibabic, Z. (2011). Condensed Fraction of an Atomic Bose Gas Induced by Critical Correlations. *Phys. Rev. Lett.*, 107(19):190403. *Cited p. 33*
- [Sogo et al., 2002] Sogo, T., Miyakawa, T., Suzuki, T., and Yabu, H. (2002). Random-phase approximation study of collective excitations in the Bose-Fermi mixed condensate of alkali-metal gases. *Phys. Rev. A*, 66(1):013618. *Cited p. 125*
- [Sogo et al., 2003] Sogo, T., Suzuki, T., and Yabu, H. (2003). Transition of fermionic spectra and monopole oscillations under phase separation in the atomic Bose-Fermi mixture. *Phys. Rev. A*, 68(6):063607. *Cited p. 125*
- [Sommer et al., 2011] Sommer, A., Ku, M. J. H., Roati, G., and Zwierlein, M. W. (2011). Universal spin transport in a strongly interacting Fermi gas. *Nature*, 472(7342):201–204. *Cited p. 103*
- [Stan et al., 2004] Stan, C. A., Zwierlein, M. W., Schunck, C. H., Raupach, S. M. F., and Ketterle, W. (2004). Observation of Feshbach Resonances between Two Different Atomic Species. *Phys. Rev. Lett.*, 93(14):143001. *Cited p. 12*
- [Stellmer et al., 2013] Stellmer, S., Grimm, R., and Schreck, F. (2013). Production of quantum-degenerate strontium gases. *Phys. Rev. A*, 87(1):013611. *Cited p. 12*
- [Stießberger and Zwerger, 2000] Stießberger, J. and Zwerger, W. (2000). Critical velocity of superfluid flow past large obstacles in Bose-Einstein condensates. *Phys. Rev. A*, 62(6):061601. *Cited p. 39*
- [Stringari, 1998] Stringari, S. (1998). Dynamics of Bose-Einstein condensed gases in highly deformed traps. *Phys. Rev. A*, 58(3):2385–2388. *Cited p. 38*
- [Stringari, 2004] Stringari, S. (2004). Sum rules and the collective oscillations of a quantum gas. *J. Phys. IV France*, 116:47–66. *Cited p. 105*

- [Sugawa et al., 2011] Sugawa, S., Inaba, K., Taie, S., Yamazaki, R., Yamashita, M., and Takahashi, Y. (2011). Interaction and filling-induced quantum phases of dual Mott insulators of bosons and fermions. *Nature Physics*, 7(8):642–648. Cited pp. 12 and 13
- [Taglieber et al., 2008] Taglieber, M., Voigt, A. C., Aoki, T., Hänsch, T., and Dieckmann, K. (2008). Quantum Degenerate Two-Species Fermi-Fermi Mixture Coexisting with a Bose-Einstein Condensate. *Phys. Rev. Lett.*, 100(1):010401. Cited p. 12
- [Tarruell, 2009] Tarruell, L. (2009). *Superfluidité dans un gaz de fermions ultrafroids*. PhD thesis, Université Paris 6. Cited pp. 43, 46, and 50
- [Tey et al., 2010] Tey, M. K., Stellmer, S., Grimm, R., and Schreck, F. (2010). Double-degenerate Bose-Fermi mixture of strontium. *Phys. Rev. A*, 82(1):011608. Cited p. 12
- [Truscott et al., 2001] Truscott, A. G., Strecker, K. E., McAlexander, W. I., B, P. G., and Hulet, R. (2001). Observation of Fermi Pressure in a Gas of Trapped Atoms. *Science*, 291(5513):2570–2572. Cited pp. 11 and 12
- [Tung et al., 2014] Tung, S.-K., Jimenez-Garcia, K., Johansen, J., Parker, C. V., and Chin, C. (2014). Observation of geometric scaling of Efimov states in a Fermi-Bose Li-Cs mixture. *arXiv*, 1402.5943. Cited p. 12
- [Tung et al., 2013] Tung, S.-K., Parker, C., Johansen, J., Chin, C., Wang, Y., and Julienne, P. S. (2013). Ultracold mixtures of atomic ^6Li and ^{133}Cs with tunable interactions. *Phys. Rev. A*, 87(1):010702. Cited pp. 12 and 126
- [Tuoriniemi et al., 2002] Tuoriniemi, J., Martikainen, J., Pentti, E., Sebedash, A., Boldarev, S., and Pickett, G. (2002). Towards Superfluidity of ^3He Diluted by ^4He . *J Low Temp Phys*, 129(5/6):531–545. Cited p. 11
- [Van Houcke et al., 2012] Van Houcke, K., Werner, F., Kozik, E., Prokof'ev, N., Svistunov, B., Ku, M. J. H., Sommer, A. T., Cheuk, L. W., Schirotzek, A., and Zwierlein, M. W. (2012). Feynman diagrams versus Fermi-gas Feynman emulator. *Nature Physics*, 8(5):366–370. Cited pp. 31 and 33
- [Volovik et al., 1975] Volovik, G. E., Mineev, V. P., and Khalatnikov, I. M. (1975). Theory of solutions of a superfluid Fermi liquid in a superfluid Bose liquid. *Zh. Eksp. Teor. Fiz*, 69:675–687. Cited p. 125
- [von Kempen et al., 2004] von Kempen, E. G. M., Marcelis, B., and Kokkelmans, S. J. J. M. F. (2004). Formation of fermionic molecules via interisotope Feshbach resonances. *Phys. Rev. A*, 70(5):050701. Cited p. 25
- [Wang et al., 2000] Wang, H., Nikolov, A., Ensher, J., Gould, P., Eyler, E., Stwalley, W., Burke, J., Bohn, J., Greene, C. H., Tiesinga, E., Williams, C., and Julienne, P. (2000). Ground-state scattering lengths for potassium isotopes determined by double-resonance photoassociative spectroscopy of ultracold ^{39}K . *Phys. Rev. A*, 62(5):052704. Cited p. 126

- [Wang et al., 2012] Wang, J., D’Incao, J. P., Esry, B. D., and Greene, C. H. (2012). Origin of the Three-Body Parameter Universality in Efimov Physics. *Phys. Rev. Lett.*, 108(2):263001. *Cited p. 86*
- [Wang and Julienne, 2014] Wang, Y. and Julienne, P. S. (2014). Universal van der Waals physics for three cold atoms near Feshbach resonances. *Nature Physics*. *Cited p. 86*
- [Watanabe et al., 2009] Watanabe, G., Dalfovo, F., Piazza, F., Pitaevskii, L. P., and Stringari, S. (2009). Critical velocity of superfluid flow through single-barrier and periodic potentials. *Phys. Rev. A*, 80(5):053602. *Cited p. 39*
- [Weber et al., 2003] Weber, T., Herbig, J., Mark, M., Nägerl, H.-C., and Grimm, R. (2003). Three-Body Recombination at Large Scattering Lengths in an Ultracold Atomic Gas. *Phys. Rev. Lett.*, 91(12):123201. *Cited pp. 54 and 89*
- [Weidemüller et al., 1994] Weidemüller, M., Esslinger, T., Ol’Shanii, M. A., Hemmerich, A., and Hänsch, T. W. (1994). A Novel Scheme for Efficient Cooling below the Photon Recoil Limit. *EPL (Europhysics Letters) (EPL)*, 27:109–114. *Cited p. 67*
- [Weimer et al., 2014] Weimer, W., Morgener, K., Singh, V. P., Siegl, J., Hueck, K., Luick, N., Mathey, L., and Moritz, H. (2014). The critical velocity in the BEC-BCS crossover. *ArXiv*, 1408.5239. *Cited pp. 40, 119, and 121*
- [Wen and Li, 2014] Wen, L. and Li, J. (2014). Structure and dynamics of a rotating superfluid Bose-Fermi mixture. *Phys. Rev. A*, 90(5):053621. *Cited p. 125*
- [Wilks and Betts, 1987] Wilks, J. and Betts, D. S. (1987). *An introduction to liquid Helium*. Oxford Science Publication. *Cited p. 38*
- [Wright et al., 2013] Wright, K. C., Blakestad, R. B., Lobb, C. J., Phillips, W. D., and Campbell, G. K. (2013). Threshold for creating excitations in a stirred superfluid ring. *Phys. Rev. A*, 88(6):063633. *Cited p. 39*
- [Wright et al., 2007] Wright, M. J., Riedl, S., Altmeyer, A., Kohstall, C., Guajardo, E. R. S., Denschlag, J. H., and Grimm, R. (2007). Finite-Temperature Collective Dynamics of a Fermi Gas in the BEC-BCS Crossover. *Phys. Rev. Lett.*, 99(1):150403. *Cited p. 98*
- [Wu et al., 2012] Wu, C.-H., Park, J. W., Ahmadi, P., Will, S., and Zwerlein, M. W. (2012). Ultracold fermionic Feshbach molecules of Na 23 K 40. *Phys. Rev. Lett.*, 109(8):085301. *Cited p. 12*
- [Wu et al., 2011] Wu, C.-H., Santiago, I., Park, J. W., Ahmadi, P., and Zwerlein, M. W. (2011). Strongly interacting isotopic Bose-Fermi mixture immersed in a Fermi sea. *Phys. Rev. A*, 84(1):011601. *Cited p. 12*
- [Yefsah et al., 2011] Yefsah, T., Desbuquois, R., Chomaz, L., Günter, K. J., and Dalibard, J. (2011). Exploring the Thermodynamics of a Two-Dimensional Bose Gas. *Phys. Rev. Lett.*, 107(13):130401. *Cited p. 18*

- [Yin and Radzihovsky, 2013] Yin, X. and Radzihovsky, L. (2013). Quench dynamics of a strongly interacting resonant Bose gas. *Phys. Rev. A*, 88(6):063611. *Cited p. 28*
- [Yip, 2001] Yip, S. (2001). Collective modes in a dilute Bose-Fermi mixture. *Phys. Rev. A*, 64(2):023609. *Cited p. 125*
- [Zaccanti et al., 2009] Zaccanti, M., Deissler, B., D’Errico, C., Fattori, M., Jona-Lasinio, M., Müller, S., Roati, G., Inguscio, M., and Modugno, G. (2009). Observation of an Efimov spectrum in an atomic system. *Nature Physics*, 5(8):586–591. *Cited p. 86*
- [Zaccanti et al., 2006] Zaccanti, M., D’Errico, C., Ferlaino, F., Roati, G., Inguscio, M., and Modugno, G. (2006). Control of the interaction in a Fermi-Bose mixture. *Phys. Rev. A*, 74(4):041605. *Cited p. 12*
- [Zaremba, 1998] Zaremba, E. (1998). Sound propagation in a cylindrical Bose-condensed gas. *Phys. Rev. A*, 57(1):518–521. *Cited p. 38*
- [Zhang et al., 2005] Zhang, J., Van Kempen, E. G. M., Bourdel, T., Khaykovich, L., Cubizolles, J., Chevy, F., Teichmann, M., Tarruell, L., Kokkelmans, S. J. J. M. F., and Salomon, C. (2005). Expansion of a lithium gas in the BEC-BCS crossover. In *ATOMIC PHYSICS 19: XIX International Conference on Atomic Physics; ICAP 2004*, pages 228–237. AIP. *Cited pp. 12 and 25*
- [Zhang et al., 2014] Zhang, R., Zhang, W., Zhai, H., and Zhang, P. (2014). Calibration of Interaction Energy between Bose and Fermi Superfluids. *arXiv*, 1409.0282. *Cited p. 125*
- [Zheng and Zhai, 2014] Zheng, W. and Zhai, H. (2014). Quasi-particle Lifetime in a Mixture of Bose and Fermi Superfluids. *arXiv*, 1408.6419. *Cited p. 120*
- [Zürn et al., 2013] Zürn, G., Lompe, T., Wenz, A. N., Jochim, S., Julienne, P. S., and Hutson, J. M. (2013). Precise Characterization of ^6Li Feshbach Resonances Using Trap-Sideband-Resolved RF Spectroscopy of Weakly Bound Molecules. *Phys. Rev. Lett.*, 110(13):135301. *Cited p. 23*
- [Zwerger, 2012] Zwerger, W. (2012). *The BCS-BEC Crossover and the Unitary Fermi Gas*. Lecture Notes in Physics. Springer, Berlin. *Cited pp. 29, 32, and 125*
- [Zwierlein et al., 2005] Zwierlein, M. W., Abo-Shaeer, J. R., Schirotzek, A., Schunck, C. H., and Ketterle, W. (2005). Vortices and superfluidity in a strongly interacting Fermi gas. *Nature*, 435(7045):1047–1051. *Cited p. 40*
- [Zwierlein et al., 2006] Zwierlein, M. W., Schirotzek, A., Schunck, C. H., and Ketterle, W. (2006). Fermionic Superfluidity with Imbalanced Spin Populations. *Science*, 311(5760):492–496. *Cited pp. 34, 99, and 100*
- [Zwierlein et al., 2003] Zwierlein, M. W., Stan, C., Schunck, C., Raupach, S., Gupta, S., Hadzibabic, Z., and Ketterle, W. (2003). Observation of Bose-Einstein Condensation of Molecules. *Phys. Rev. Lett.*, 91(25):250401. *Cited p. 30*

Abstract

Manifestations of Quantum Physics at the thermodynamical level are found in a broad range of physical systems. A famous example is superfluidity, discovered at the beginning of the 20th century and found in many different situations, from liquid helium to neutron stars. Dilute ultracold gases offer a unique versatility to engineer quantum many-body systems, which can be directly compared with theory thanks to the controllability of their environment. In this thesis we present several experimental investigations led on ultracold lithium gases. Lithium provides the possibility to study ensembles of bosons and fermions, with controllable interactions between the constituents. We present experimental techniques for preparation and studies of degenerate gases of lithium, with prospects for improvement of the existing methods. We first report on an investigation of three-body recombination of bosons under a resonant two-body interaction. This study, quantitatively compared with theory constitutes a benchmark for further studies of the unitary Bose gas. Finally, we present the first experimental realization of a mixture of a Bose superfluid with a Fermi superfluid. We demonstrate that both components are in the superfluid regime, and that the counter-flow motion between them possesses the characteristics of superfluid flow, with the absence of viscosity below a critical velocity, and an onset of friction above. Using collective oscillations of the mixture, we measure the coupling between the two superfluids in close agreement with a theoretical model.

Keywords: quantum gases, superfluidity, Bose-Fermi mixtures, unitary gases, three-body recombination, laser cooling, grey molasses.

Résumé

On trouve des manifestations de la physique quantique au niveau thermodynamique dans de nombreux systèmes. Un exemple marquant est la superfluidité, découverte au début du 20^{ème} siècle, que l'on retrouve de l'hélium aux étoiles à neutrons. Les gaz dilués ultra-froids offrent une polyvalence unique pour étudier des systèmes quantiques macroscopiques, pouvant directement tester les théories grâce à un environnement contrôlé. Dans cette thèse, nous présentons plusieurs études expérimentales de gaz froids de lithium. Le lithium fournit la possibilité de réaliser des ensembles de bosons et de fermions, avec des interactions contrôlables entre les constituants. Nous présentons les techniques utilisées pour préparer et étudier des gaz dégénérés de lithium, et une amélioration possible des méthodes existantes. Nous décrivons premièrement une étude de la recombinaison à trois bosons avec une interaction à deux corps résonante. Comparés quantitativement à la théorie, ces résultats fournissent une référence pour les études futures du gaz de Bose unitaire. Pour finir, nous présentons la première observation expérimentale d'un mélange de superfluides de Bose et de Fermi. Nous démontrons que les deux composants sont superfluides et que leur écoulement relatif vérifie les propriétés des écoulement superfluides, avec une absence de viscosité en dessous d'une vitesse critique puis la présence de dissipation au-delà. En utilisant des excitations collectives de ce mélange, nous mesurons l'interaction entre les deux superfluides, en accord avec un modèle théorique.

Mots-clés: gaz quantiques, superfluidité, mélanges de bosons et de fermions, gaz unitaires, recombinaison à trois corps, refroidissement laser, mélasses grises.